BremHLR
Kompetenzzentrum für Höchstleistungsrechnen Bremen

Statusbericht 2020

des

Kompetenzzentrums

für

Höchstleistungsrechnen Bremen

–BremHLR–

Bremen, September 2021

Universität Bremen
JACOBS UNIVERSITY
ALFRED-WEGENER-INSTITUT HELMHOLTZ-ZENTRUM FÜR POLAR- UND MEERESFORSCHUNG
Hochschule Bremerhaven

HLRN
Norddeutscher Verbund für Hoch- und Höchstleistungsrechnen

www.bremhlr.uni-bremen.de

Das Berichtsjahr 2020 in Stichpunkten

- Erfolgreicher Umstieg der Bremer Anwendungen auf die neuen HLRN-IV Systeme
- Weiter ansteigende Bremer Nutzung der Ressourcen des Norddeutschen Verbunds für Hoch- und Höchstleistungsrechnen (HLRN)
- Inbetriebnahme der zweiten Ausbaustufe des neuen Rechnersystems HLRN-IV in Göttingen

Inhaltsverzeichnis

1 BremHLR: Aufgaben und organisatorische Struktur

1.1 Aufgaben

Das Land Bremen beteiligt sich am Norddeutschen Verbund für Hoch- und Höchstleistungsrechnen – HLRN – um an dem rasanten Fortschritt der Computer- und Softwaretechnologie Teil zu haben. Das Kompetenzzentrum für Höchstleistungsrechnen Bremen – BremHLR – unterstützt dazu Wissenschaftler im wissenschaftlichen Rechnen insbesondere im Land Bremen. Die Fachberater des BremHLR leisten Unterstützung für Projekte sowohl in der Konzeption, der Antragstellung als auch der Durchführung. Der Schwerpunkt der Unterstützung liegt hierbei auf Projekten auf dem HLRN-System. Seit 2005 wurde die Betreuung aber auch auf Rechenprojekte an den nationalen Höchstleistungsrechenzentren wie z. B. dem Jülich Supercomputing Centre (JSC) ausgeweitet.

Als Bestandteil im Kompetenznetzwerk des HLRN beteiligt sich BremHLR unter anderem an der fachspezifischen Nutzerberatung, der Pflege von Software-Paketen und der Veranstaltung überregionaler Nutzerworkshops. Die Geschäftsstelle des BremHLR ist an der Universität Bremen im Zentrum für Technomathematik angesiedelt.

Das BremHLR wurde am 1. Juli 2003 als Kooperation zwischen der Universität Bremen (UB), der Jacobs University Bremen (JUB) und dem Alfred-Wegener-Institut Helmholtz-Zentrum für Polar- und Meeresforschung (AWI) gegründet. Seit April 2008 ist auch die Hochschule Bremerhaven (HBHV) Kooperationspartner des BremHLR. Das Kompetenzzentrum wird von den beteiligten Kooperationspartnern sowie der Bremer Senatorin für Wissenschaft und Häfen (SWH) anteilig finanziell getragen. Seit Januar 2014 ist die JUB als ideelles Mitglied beitragsfrei gestellt. Zum Jahr 2019 konnte eine Weiterfinanzierung des BremHLR bis Ende 2021 sicherstellt werden.

1.2 Struktur

Dem Lenkungsausschuss des BremHLR als oberstes beschlussfassendes und steuerndes Gremium gehörten in der Berichtsperiode folgende Vertreter der kooperierenden Einrichtungen an. Im Einzelnen sind dies:

- Prof. Dr. Alfred Schmidt (UB/Zentrum für Technomathematik ZeTeM)
- Prof. Dr.StephanFrickenhaus (AWI/Rechenzentrum, UB/FB3)
- Prof. Dr. Ulrich Kleinekathöfer (JUB)
- Prof. Dr. Henrik Lipskoch (HBHV)
- Dr. Jörg Hofmann (SWH)

Die fachspezifische Betreuung der Projekte am Norddeutschen Verbund für Hoch- und Höchstleistungsrechnen (HLRN) sowie von Projekten an anderen nationalen Höchstleistungsrechenzentren wird von den Fachberatern des BremHLR geleistet, die ebenfalls den Einrichtungen der Kooperationspartner angehören. Im Berichtszeitraum waren folgende Fachberater tätig:

- Dr. Lars Nerger (AWI/Rechenzentrum, UB/ZeTeM, Leiter Geschäftsstelle)
- Thorsten Coordes (UB/ZARM)
- Dr. Achim Geleßus (JUB/CLAMV)
- Dr. Natalja Rakowsky (AWI/Rechenzentrum)

Die Geschäftsstelle ist verantwortlich für die Organisation der Workshops (siehe Abschnitt Veranstaltungen) und die Unterstützung der Nutzer, insbesondere im Antragsverfahren. Bis zum 15.12.2020 wurde das Sekretariat der Geschäftsstelle betreut von

- Julitta von Deetzen.

Zum 15.12.2020 ist Frau von Deetzen in den Ruhestand gegangen. Bis die Sekretariatsstelle neu besetzt werden kann, soll diese komissarisch besetzt werden.

2 Tätigkeitsprofil des BremHLR im Berichtszeitraum

2.1 Unterstützung der HLRN-Nutzung im Land Bremen

Ein Schwerpunkt der Aktivitäten des BremHLR lag auch in diesem Berichtszeitraum in der Unterstützung der HLRN-Nutzung. Neben den Tätigkeiten von Prof. Dr. Stephan Frickenhaus als Mitglied der Technischen Kommission sowie Prof. Dr. Alfred Schmidt als Mitglied des Wissenschaftlichen Ausschusses bestand die Unterstützung des HLRN durch das BremHLR hauptsächlich in der Fachberatung für Bremer Projekte am HLRN von der Antragstellung bis zur Begleitung rechenintensiver Projekte während der gesamten Projektlaufzeit.

Eine wesentliche Aufgabe im Berichtsjahr war die weitere Unterstützung der Bremer Nutzer des HLRN bei der effizienten Nutzung des HLRN Hochleistungsrechnersystems. Eine wichtige Aufgabe der Fachberater des BremHLR war hierbei die Unterstützung der Nutzer bei der Portierung ihrer Modelle auf das neue Rechnersystem HLRN-IV.

Am 5.1.2020 wurde die zweite Ausbaustufe des HLRN-IV in Berlin für alle Nutzer geöffnet. Am 25.11.2020 wurde dann auch die zweite Ausbaustufe des HLRN-IV in Göttingen für alle Nutzer geöffnet. Da dieses System kompatibel mit der zweiten Ausbaustufe in Berlin ist, sollten die bereits portierten Modelle auch in Göttingen lauffähig sein.

2.2 Weitere Aktivitäten des BremHLR

Im Veranstaltungsjahr 2020 wurde vom BremHLR der *14. Workshop zur Einführung in die parallele Programmierung mit MPI und OpenMP* organisiert und durchgeführt. Mit 21 Teilnehmern war dieser Workshop wieder sehr gut besucht.

Der Workshop wurde in der Zeit vom 17. bis zum 21. Februar 2020 an der Universität Bremen abgehalten. Als Referent konnte wie bereits bei bisherigen Workshops Dr. Hinnerk Stüben vom Regionalen Rechenzentrum der Universität Hamburg gewonnen werden, der den Workshop gemeinsam mit dem BremHLR-Fachberater Dr. Lars Nerger leitete.

Der sehr gute Zuspruch und der große Erfolg der Veranstaltungen zeigt deutlich den dringenden Bedarf zur Ausbildung im Hoch- und Höchstleistungsrechnen und gibt Anlass dazu solche Workshops auch weiterhin als regelmäßige Ausbildungs- und Schulungs-Maßnahme anzubieten.

Neben dem Workshop zur Einführung in die parallele Programmierung beteiligten sich Fachberater des BremHLR an Fachberaterworkshops des HLRN-Kompetenznetzwerks die im Jahr 2020 online stattgefunden haben. Bei diesen Workshops wurden unterschiedliche Themen des HLRN-Betriebs und der Nutzerbetreuung besprochen. Eine Übersicht über die Veranstaltungen ist in Abschnitt 4 zu finden.

3 Statistische Angaben zu den Bremer Höchstleistungsprojekten

Auch im Jahr 2020 wurde der HLRN intensiv durch Bremer Projekte genutzt. Im Zeitraum vom Januar bis September wurde auf den HLRN Systemen ein prozentualer Anteil von 6,3 % an der gesamten Rechenleistung des HLRN erreicht. Dieses liegt deutlich über dem investiven Anteil von etwa 3,5% des Landes Bremen am HLRN. Über die gesamte Laufzeit seit Einrichtung des HLRN-Verbunds wurde durch Bremer Projekte ein Anteil von 8,3% der verfügbaren Rechenzeit abgenommen.

Das erste Quartal 2020 war eine sichtbare Übergangsphase für die Nutzer. Am 5.1.2020 wurde die zweite Ausbaustufe des HLRN-IV in Berlin für alle Nutzer geöffnet, nachdem im Oktober 2019 schon das alte Rechnersystem HLRN-III abgeschaltet wurde. Entsprechend war das erste Quartal von Portierungsarbeiten und Tests geprägt, so dass hier wenger NPL abgenommen wurden. Nach dem ersten Quartal stieg die Bremer Nutzung deutlich an. Insgesamt wurden im Jahr 2019 etwas 8.400.000 NPL[1] durch Bremer Projekte am HLRN abgenommen. Dieses ist die größte bisher am HLRN abgenommene Rechenkapazität.

Abbildung 3.1 zeigt die quartalsweise Nutzung des HLRN durch die Bremer Projekte. Während der Umbauphase von HLRN-III auf HLRN-IV wurden die NPL teilweise nur unvollständig erfasst.

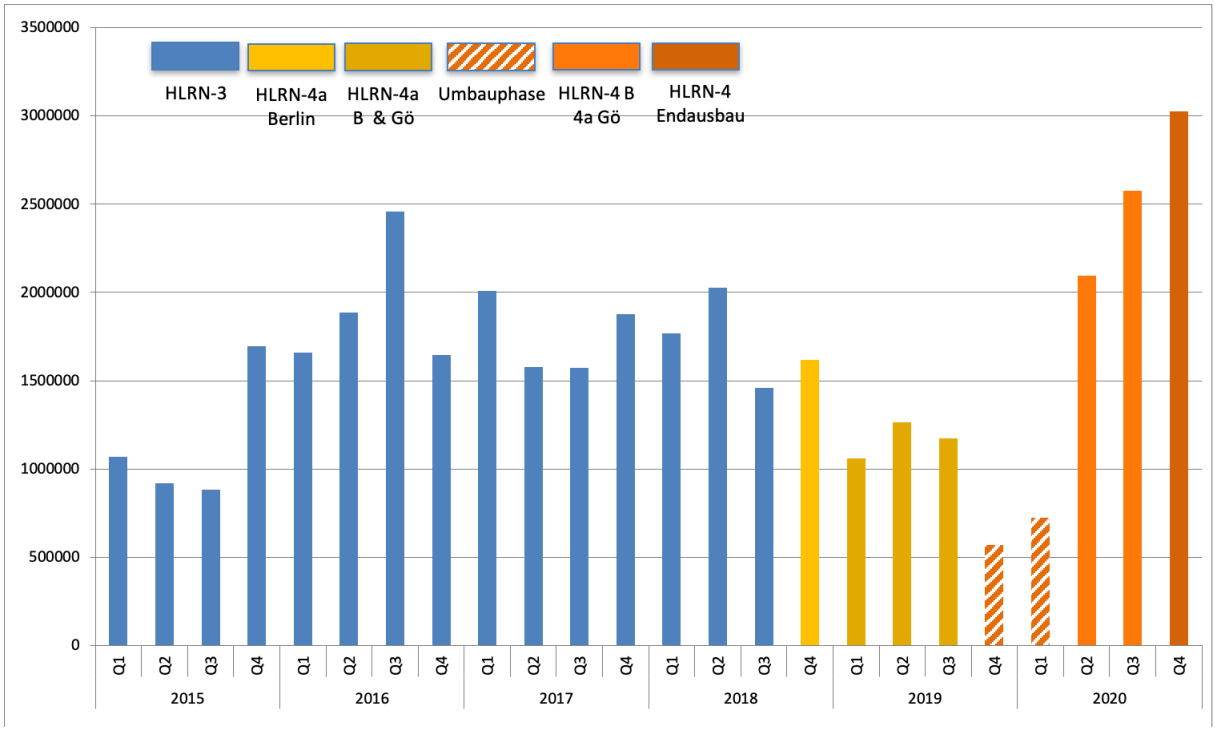

Abbildung 3.1: Quartalsweise Rechenzeitnutzung der Bremer HLRN-Großprojekte seit Januar 2015 auf den HLRN-III und HLRN-IV Systemen in der HLRN-Leistungseinheit NPL. Die Farben zeigen die Verfügbarkeit der unterschiedlichen Ausbaustufen des HLRN-Systems. Im vierten Quartal 2019 war der Betrieb durch die Umbaumaßnahmen beeinträchtigt und weitgehend nur das HLRN-IV System in Göttingen verfügbar. Im ersten Quartal 2020 waren die Nutzer vielfach mit Portierungsarbeiten befasst.

[1]Norddeutsche Parallelrechner-Leistungseinheit: Auf dem Göttinger HLRN-IV System Stufe 1 entspricht die Nutzung eines Knotens über eine Stunde 6 NPL. Auf den Systemen der Ausbaustufe 2 entspricht die Nutzung eines Knotens über eine Stunde 14 NPL.

Eine Übersicht zu allen vom BremHLR betreuten Projekten geben die Tabellen 3.1 und 3.2. Im Jahr 2020 wurden vom BremHLR 50 Projekte am HLRN betreut. 18 neue Projekte mit teilweise sehr großem Rechenzeitbedarf wurden im Jahr 2020 beantragt und vom Wissenschaftlichen Ausschuss des HLRN bewilligt. 15 Projekte wurden im Berichtsjahr beendet.

4 Veranstaltungen mit Beteiligung des BremHLR

14. BremHLR-Workshop *Einführung in die Programmierung mit MPI und OpenMP*

Veranstalter: BremHLR

Datum: 17. – 21. Februar 2020

Ort: Universität Bremen

Beschreibung: In dem Workshop wurden die Grundlagen der parallelen Programmierung vermittelt. Der Schwerpunkt lag auf den Programmiermodellen MPI und OpenMP. Praktische Übungen bildeten einen wesentlichen Teil des Workshops.

Referenten: Dr. Hinnerk Stüben (Regionales Rechenzentrum der Universität Hamburg) und Dr. Lars Nerger (BremHLR).

Teilnehmerzahl: 21

Teilnehmende Institutionen: AWI, Uni Bremen, Hochschule Bremerhaven, Universität Potsdam, Technische Universität Brandenburg, Universität Lübeck

37. HLRN-Fachberater-Workshop

Veranstalter: GWDG

Datum: 4. Juni 2020

Ort: Online

Teilnehmerzahl: 21

Teilnehmende Institutionen: BremHLR (AWI, ZARM), GWDG/Uni Göttingen, IOW, TU Braunschweig, Uni Hamburg, Uni Kiel, Uni Oldenburg, Uni Rostock, ZIB, Senatorin für Wissenschaft und Häfen Bremen

38. HLRN-Fachberater-Workshop

Veranstalter: GWDG

Datum: 20. November 2020

Ort: online

Teilnehmerzahl: 21

Teilnehmende Institutionen: BremHLR (AWI, ZARM), GWDG/Uni Göttingen, IOW, TU Braunschweig, Uni Hamburg, Uni Kiel, Uni Oldenburg, Uni Rostock, ZIB

Tabelle 3.1: Übersicht neu begonnener Bremer HPC-Projekte, die innerhalb des Berichtszeitraums vom BremHLR betreut wurden. Status: E = Erstantrag, X = Projektende im Jahr 2020; kNPL: Kontingent in tausend NPL im Jahr 2020

Kennung	Projektleiter	Institut	Laufzeit	kNPL	Status
hbb00001	Prof. Dr. L. Colombi Ciacchi	UB/BCCMS	III/20 – II/21	154	E
hbc00045	Prof. Dr. T Stauch	UB/Chemie	II/20 – I/21	75	E
hbc00046	Dr. M. Delle Piane	UB/BCCMS	II/20 – I/21	210	E
hbc00047	Dr. S. Köppen	UB/BCCMS	II/20 – I/21	90	E
hbc00048	Dr. M. Michaelis	UB/BCCMS	III/20 – II/21	140	E
hbi00043	Dr. Yan Jin	UB/ZARM	I/20 – IV/20	120	EX
hbi00045	Prof. Dr. C. Büskens	UB/ZeTeM	III/20 – II/21	70	E
hbi00046	Dr. M. Castillo	UB/ZARM	III/20 – II/21	100	E
hbi00048	Dr. Yan Jin	UB/ZARM	III/20 – II/21	90	E
hbi00049	Prof. Dr. U. Fritsching	UB/IWT	IV/20 – III/21	49	E
hbk00079	Prof. Dr. B. Rost	AWI & UB	II/20 – I/21	510	E
hbk00080	Prof. Dr. M. Schulz	UB/MARUM	III/20 – II/21	462	E
hbk00082	Dr. K. Purkiani	UB/MARUM	III/20 – II/21	20	E
hbp00054	Dr. M. Lorke	UB/Physik	II/20 – I/21	84	E
hbp00058	Prof. Dr. U. Kleinekathöfer	Jacobs U	II/20 – I/21	206	E
hbp00067	Prof. Dr. T. Frauenheim	UB/BCCMS	IV/20 – III/21	80	E
hbp00068	Prof. Dr. U. Kleinekathöfer	Jacobs U	IV/20 – III/21	150	E
hbp00069	Prof. Dr. T. Wehlling	UB/Physik	II/20 – I/21	400	E

Tabelle 3.2: Übersicht der Bremer HPC-Projekte, die innerhalb des Berichtszeitraums vom BremHLR betreut wurden. Status: F = Fortsetzung, X = Projektende im Jahr 2020; kNPL: Kontingent in tausend NPL im Jahr 2020

Kennung	Projektleiter	Institut	Laufzeit	kNPL	Status
hbc00027	Prof. Dr. P. Deak	UB/BCCMS	I/18 – I/20	35	FX
hbc00029	Dr. L. Moskaleva	UB/Chemie	I/18 – IV/20	296	F
hbc00030	Dr. M. Fischer	UB/Geo	II/18 – II/21	152	F
hbc00034	Dr. M. Delle Piane	UB/BCCMS	I/19 – II/20	30	FX
hbc00039	Dr. M. Mushed	UB/Chemie	II/19 – I/20	13	FX
hbi00033	Prof. Dr. M. Avila	UB/ZARM	I/17 – II/21	156	F
hbi00036	Prof. Dr. U. Fritsching	UB/FB4	II/17 – I/21	101	F
hbi00037	Prof. Dr. U. Fritsching	UB/FB4	II/17 – I/21	160	F
hbi00038	Dr. Y. Jin	UB/ZARM	I/19 – II/20	30	FX
hbi00041	Dr. D. Feldmann	UB/ZARM	III/19 – III/20	237	FX
hbi00042	Prof. Dr. A. Baars	HS Bremen	IV/19 – III/21	400	F
hbk00032	Prof. Dr. T. Jung	AWI & UB	II/12 – II/21	341	F
hbk00034	Prof. Dr. T.Kanzow	AWI & UB	III/13 – III/21	1350	F
hbk00038	Prof. Dr. T. Kanzow	AWI & UB	III/14 – II/21	1200	F
hbk00057	Dr. A. Rozanov	UB/IUP	I/17 – II/20	116	FX
hbk00059	Prof. Dr. M. Schulz	UB/MARUM	III/17 – III/21	365	F
hbk00062	Dr. A. Rozanov	UB/IUP	IV/17 – III/21	480	F
hbk00064	Prof. Dr. T. Jung	AWI & UB	I/18 – III/21	544	F
hbk00071	Prof. Dr. M. Schulz	UB/MARUM	I/19 – IV/21	200	F
hbk00072	Prof. Dr. D. Wolf-Gladrow	AWI & UB	I/19 – IV/20	372	FX
hbk00075	Prof. Dr. D. Wolf-Gladrow	AWI & UB	IV/19 – IV/21	950	F
hbk00076	Prof. Dr. M. Schulz	UB/MARUM	II/19 – II/20	185	FX
hbk00077	Dr. K. Purkiani	UB/MARUM	II/19 – III/20	25	FX
hbp00029	Dr. M. Lorke	UB/Physik	IV/15 – III/20	2	FX
hbp00041	Prof. Dr. C. Lämmerzahl, Prof. Dr. S. Rosswog	UB/ZARM	I/17 – I/21	170	F
hbp00047	Prof. Dr. T. Wehling	UB/Physik	I/19 – IV/20	85	FX
hbp00048	Dr. M. Lorke	UB/Physik	IV/19 – IV/20	111	FX
hbp00049	Prof. Dr. T. Wehling	UB/Physik	IV/19 – III/20	105	FX
hbp00050	Prof. Dr. T. Wehling	UB/Physik	IV/19 – III/20	66	FX
nak00001	Dr. H. Gößling	AWI	II/19 – II/21	201	F

5 Informationen zur Infrastruktur: Endausbau des HLRN-IV Systems zum Ende des Jahres 2020

Am 5.1.2020 wurde das HLRN-IV System in Berlin für alle Nutzer geöffnet. Der Aufbau der zweiten Ausbaustufe des HLRN-IV Systems in Göttingen hat sich aufgrund der Covid-19 Pandemie verzögert. Letztendlich konnte es in der zweiten Jahreshälfte 2020 installiert werden und wurde am 25.11.2020 für alle Nutzer zugänglich gemacht. Damit ist der Ausbau der HLRN-IV Systeme vollständig.

Die HLRN-IV Systeme wurden von der Firma Atos geliefert. Die Systeme sind wie folgt konfiguriert:

Göttingen:

Phase 1:
- 432 Dual-Socket Knoten mit einer standard Speicheraustattung von 192 GB
- 16 Dual-Socket Knoten mit einer großen Speicherausstattung von 768 GB
- Jeder Knoten ist ausgestattet mit
  - 2 Intel XEON Skylake Gold (6148) mit 2,4 GHz Taktung und jeweils 20 Prozessorkernen
  - 480 GB Solid-State Disk

Phase 2:
- 956 Dual-Socket Knoten mit einer standard Speicheraustattung von 384 GB
- 32 Dual-Socket Knoten mit einer großen Speicherausstattung von 768 GB
- 2 Dual-Socket Knoten mit einer sehr großen Speicherausstattung von 1,5 TB
- Jeder Knoten ist ausgestattet mit
  - 2 Intel XEON Cascade Lake Platinum (9242) mit 2,3 GHz Taktung und jeweils 48 Prozessorkernen
  - 1 Intel Omni-Path Netzwerkadapter

Netzwerk und Filesysteme werden von beiden Rechnersystemen gemeinsam genutzt:
- Netzwerk: Intel Omni-Path in Fat Tree Topologie
- 8,1 PB paralleles Lustre Dateisystem (“WORK” zur Speicherung von Simulationsdaten) über Omni-Path Netzwerk
- 340 TB Heimat-Dateisystem

Berlin:

- 1236 Dual-Socket Knoten mit einer standard Speicheraustattung von 384 GB
- 16 Dual-Socket Knoten mit einer großen Speicherausstattung von 768 GB
- 2 Dual-Socket Knoten mit einer sehr großen Speicherausstattung von 1,5 TB
- Jeder Knoten ist ausgestattet mit
  - 2 Intel XEON Cascade Lake Platinum (9242) mit 2,3 GHz Taktung und jeweils 48 Prozessorkernen
- Netzwerk: Intel Omni-Path mit 14 TB/s Bisektions-Bandbreite
- 8,1 PB paralleles Lustre Dateisystem (“WORK” zur Speicherung von Simulationsdaten) über Omni-Path Netzwerk
- 340 TB Heimat-Dateisystem

Das Göttinger System wurde nach Emmy Nöther „Emmy” benannt und das Berliner System nach Lise Meitner „Lise“. Im November 2020 wurde das Berliner System auf der Top500 Liste der weltweit schnellsten Supercomputer auf Platz 55, und das Göttinger System auf Platz 47 eingestuft. In Deutschland stehen die beiden Systeme auf den Plätzen 5 und 7.

6 Projektberichte[2]

6.1 *hbb00001:* Exploring the conformational phase space of N-linked glycans using enhanced MD and sketch-map analysis

HLRNProject ID:	hbb00001
Run time:	III/2020 – II/2021
Project Leader:	Dr. Lucio Colombi Ciacchi
ProjectScientists:	Isabell L. Grothaus, Massimo Delle Piane
Affiliation:	University Bremen

Overview

The covalent attachment of glycans to the polypeptide chain of proteins is a form of post-translational modification that occurs for over 50% of mammalian proteins. Over the years, different biological functions have been assigned to glycosylations like involvement in folding and stability of proteins, as target structures for lectins and antibodies, illustrating their importance for proteins' structure and functions. The study of glycans itself is extremely important, as they serve similarly to proteins as keys to a lock, where one glycan represents several keys due to its many conformations. Dealing with glycan structures, one is facing the problem of a high dimensional space that is required to describe the conformations explored by the sugar trees. This is due to their diversity depending on composition, linkage type and branching, giving rise to such flexible behaviours. Unfortunately, structural motives like α-helices and β-sheets for proteins are not applicable to glycans, rather classical description using torsion angles or spherical coordinates have been used. As a consequence thereof, describing conformer populations of one single glycan tree (Figure 1) unambiguously dependent on many torsion angles (multidimensional) and cumbersome to describe in a 2-dimensional manner.

Therefore, the aim of this project is to push forward the ability to visualize glycan conformers of high dimensional space in a low dimensional representation. This is thought to be achieved by applying dimensionality-reduction algoriths, which transforms data of a high-dimensional space (e. g. many torsion angles) into a 2D map (low- dimensional space). This map comprises points where each point corresponds to one conformation that was recorded during a molecular dynamics run. Conformations are clustered by the algorithm depending on their similarities.

To achieve a sufficient sampling of all relevant torsion angles, enhanced molecular dynamics simulations are required. We therefore choose an approach where replica exchange with solute scaling is combined with metadynamics (RESTmetaD) for which HPC infrastructure is greatly required. The employment of this tool is thought to facilitate the study of a large number of differently sized glycans to easily map their free energy landscape and corresponding conformer population for comparison by simple 2D maps.

[2] Für den Inhalt der Projektberichte sind ausschließlich die genannten Projektleiter bzw. die Projektbearbeiter verantwortlich.

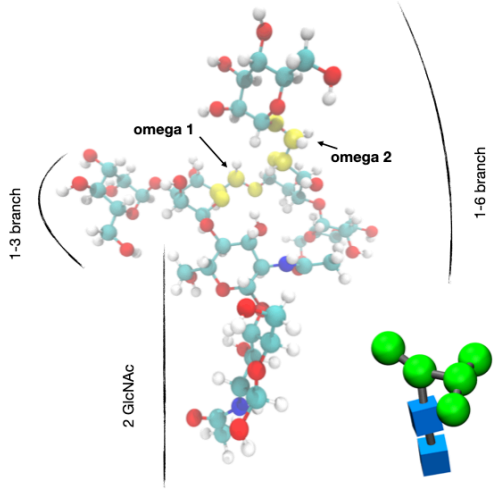

Figure 1: Atomic structure and cartoon representation of the high-mannose type N-glycan Man5, constisting of 2 N-acetyl glucosamine (GlcNac) (blue boxes) and 5 mannose (green circles) monosaccharides. Each sugar is connected via a glycosidic bond, which has a structure of carbon-oxygen-carbon (grey line between boxes or spheres). In the atomic description, important structural features like the two branches of the glycan are depicted as well as two important torsional angles called omega 1 and 2. They are known as important junctions for increased flexibility.

Results

As an overall important point in molecular dynamics (MD) simulation, it is necessary to perform sufficient long calculations of the system of interest to stay within the limits of the ergodic theorem. This means that all states the system is able to visit need to be sampled during a simulation, which is only possible within a certain amount of simulation time. There exist different methods to fulfill this goal, as they became computationally possible nowadays. The simplest one is to perform classical MD simulations in the microsecond timescale, or utilize one of the many enhanced sampling schemes, which push the system to explore different states within a shorter timescale. For a rapid and sufficient sampling of conformational phase space we employ a sampling scheme based on enhancing transitions of all relevant barriers with concurrent one-dimensional energy potentials in the framework of metadynamics. Additional degrees of freedom are enhanced by the solute scaling scheme, effictively scaling the temperature of the system and thereby overcoming energy barriers.

In order to draw comparisons of our new method with the standard classical-MD scheme we performed both methods on our modelglycan Man5 (Figure 2). For both simulation setups, glycan conformers describing the global structure of Man5 have been computed, which are constructed on the basis of a combination of all torsion angle states. For an intrasystem validation of performance, each simulation scheme was performed twice starting from a different initial glycan conformer. Ideally each method should converge to the same ensemble of states independent of the starting structure.

We are able to show with the newly employed enhanced sampling scheme that converged simulations can be obtained in a shorter time as with the classical method, because the microsecond timescale is not required for a sufficient sampling. Additionally, simulations starting from different intial states result in a more similar conformer distribution for the enhanced sampling scheme, whereas classical-MD derived conformers can differ in probability by ± 10 %. Generally, the overall conform distribution is similar for both methods, however

error bars remain large for classical-MD results as fluctuations between different minima states are slower compared to the enhanced scheme.

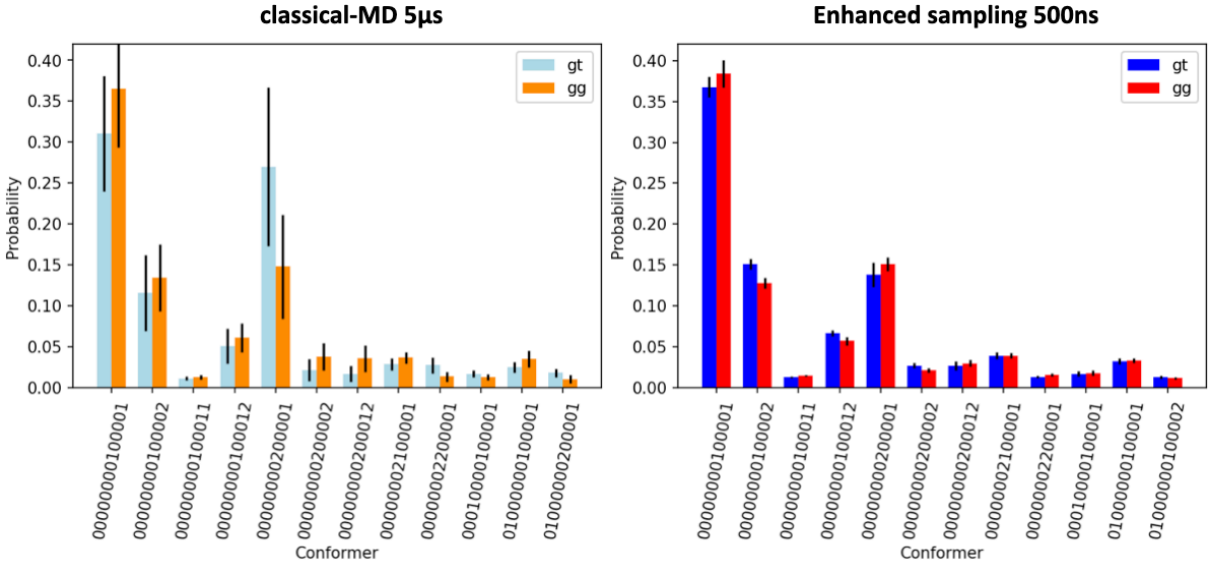

Figure 2: Comparison of global conformer distributions by classical-MD run for 5 µs and an enhanced sampling method run for 500 ns. The different conformers are plotted against their probability to be observed during the simulation time. Error bars were calculated from block averaging using ten blocks, respectively. The conformer code represents each of the 14 torsion angles in the glycan, whereas each number stands for one torsion angle and is corresponding to the free energy minima it is located in. Each method was calculated twice, starting from two different conformations (depicted as gt or gg) in order to monitor convergence.

The application of a more complex method like enhanced sampling for capturing the global free energy surface was therefore shown to be necessary in order to have a converged and reliable distribution of conformer states.

Outlook

Dimensionality reduction algorithms like sketch-map require a converged ensemble of glycan conformers in order to ensure a reliable 2D representation of the key structural features. Therefore, next steps involve the usage of our produced trajectories of the Man5 glycan to construct sketch-maps and e.g. color them by the different explored conformers described in Figure 2.

The enhanced sampling method above can be applied to other glycan systems with high biological significance. This set of different glycans can then be compared for their differing conformer distributions, originating from the addition of monosaccharides to certain places in the glycan tree.

As an application, we aim at sampling the conformation of N-glycans when attached to a model glycoprotein, to investigate the difference in adapted conformations due to interactions with the protein surface and other glycan trees.

Presentations

1. Isabell L. Grothaus, Role of N-glycosylation on structure-function relations of *Trypanosoma congolense* trans-sialidase, Poster Presentation at the Society for Glycobiology – Annual Meeting , November, 2020

6.2 *hbc00029:* Understanding the catalytic performance of rare-earth oxides: Toward a knowledge-driven design of catalysts from first-principles calculations

HLRNProject ID:	hbc00029
Run time:	I/2020 – IV/2020
Project Leader:	Dr. Lyudmila Moskaleva
ProjectScientists:	Shikun Li; Yong Li
Affiliation:	Universität Bremen, Institut für Angewandte und Physikalische Chemie, Leobener Str. UFT, 28359, Bremen

Overview

La_2O_3 doped by various metal cations has been extensively used as a catalyst in various catalytic reactions[1-3]. The dopants usually make a large modification to the surface Lewis acidity/basicity of La_2O_3 and to the bonding strength of surface oxygen, which is thought to influence the reactivity of the catalysts. In this course of the project, we systematically investigated the influence of dopants on the Lewis acidity/basicity and the energy of oxygen vacancy formation, and we constructed a relationship between them via density functional theory (DFT) on a microscopic scale. There exists a linear relationship between the oxygen vacancy formation energy and the O2s2p band center of the surface oxygen atoms on the defective La_2O_3(0001) surface doped by various metals.

Results

1) *The influence of dopants on the geometries of the defective La_2O_3(0001) surface.*

To study the influence of dopants on the X-O bond lengths in the presence of an oxygen vacancy, we removed one surface O atom (O_c, see Figure 1(a)) near the doping site to form an oxygen vacancy. The formation of an oxygen vacancy forces dopants to move closer towards the two remaining surface O atoms, O_a and O_b, as well as O_g atom located in the

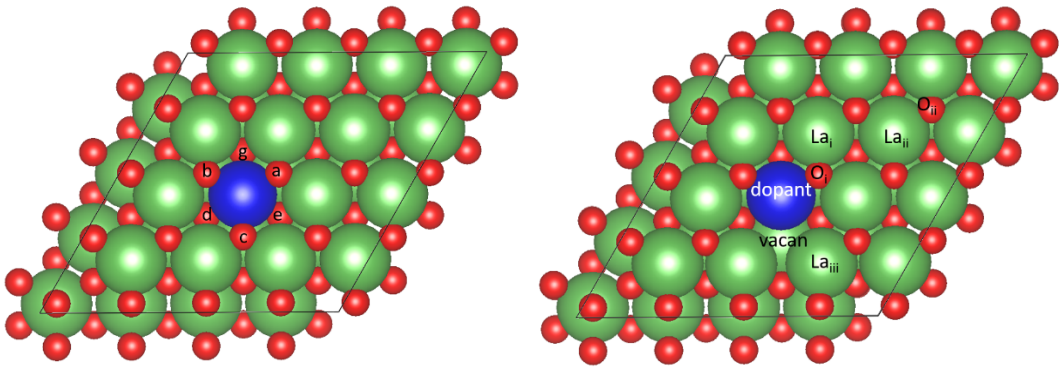

(a) (b)

Figure 1: Illustration of (a) six O sites surrounding the dopant site and (b) several surface sites considered in acidity/basicity studies: dopant, O vacancy, surface La or O sites on the La_2O_3(0001) surface. La atoms are shown in green color, O atoms in red color, and dopant atoms in blue color.

subsurface. Among the three subsurface O atoms, O_d and O_e show a larger distance to the dopant compared to X-O_g distance which shrinks along with the shift of the doping position to O_a and O_b, Figure 2. All considered dopants lead to increased X-O_e/O_d bond lengths, while the X-O_g bond length in most cases shortens with respect to the undoped defective La_2O_3(0001) surface except for Mn, Fe, Co, Ni, and Cu. Similar to the defect-free La_2O_3(0001) surface, transition-metal atoms have a larger effect on the X-O bonds than lanthanide atoms.

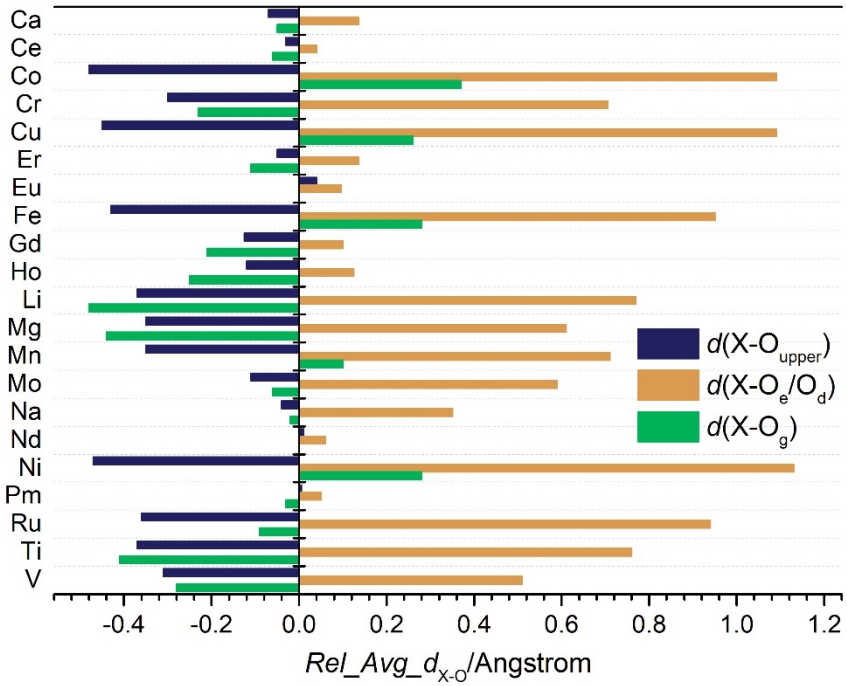

Figure 2: Relative differences in bond lengths between dopant atoms (X) and the surrounding O atoms calculated by subtracting the corresponding bond lengths on the undoped defective La_2O_3(0001) surface from those on doped defective La_2O_3(0001) surfaces. O_{upper} denotes three surface O atoms near the dopant site. X-O_{upper} and X-O_e/O_d denote the average bond lengths between the dopant atom and the three surface O atoms or two subsurface O atoms.

2) *The influence of dopants on the O2s2p band center of the defective La_2O_3(0001) surface.*

To investigate the influence of an oxygen vacancy on the Lewis basicity of the surface O atoms, we analysed the density of states of doped defective La_2O_3(0001) surfaces, specifically, the position of the O2s2p band centers of $O_{surface}$ (calculated as the average band center of all surface O atoms), O_i and O_{ii} atoms located near the dopant and far from the dopant, respectively. As seen from Figure 3, with the formation of an oxygen vacancy, the O2s2p band centers of $O_{surface}$, O_i and O_{ii} on the defective La_2O_3(0001) surface shift down in energy compared to the defect-free La_2O_3(0001) surface owing to the two extra electrons resulting from the formation of an oxygen vacancy. Different from the defect-free La_2O_3(0001) surface, the surface O2s2p band centers on the defective La_2O_3(0001) surface doped by Li or Na are heavily affected by the dopants. Mg, V, Mn, Cu, Co and Ni dopants also lead to a larger change in the O2s2p band center in the presence of an oxygen vacancy. The presence of an oxygen vacancy reduces the net ionic charges of the dopants. The magnetic moments do not change for the defective surfaces after doping most of lanthanide atoms (Ce, Er, Eu, Gd, Ho), alkali earth metals (Ca, Mg), and Mn, Ru, Ti.

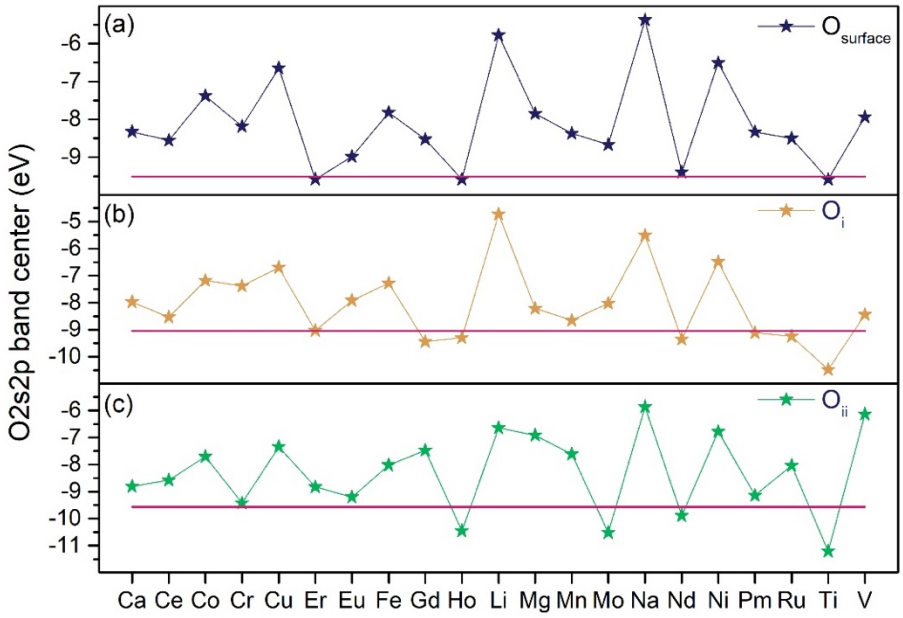

Figure 3: The O2s2p band centers of (a) the surface O atoms, and the single O atom located at (b) O_i site and (c) O_{ii} site on the defective doped $La_2O_3(0001)$ surface for different doping elements. The horizontal lines denote O2s2p band centers of the corresponding O atoms on the undoped defective $La_2O_3(0001)$ surface.

The O2s2p band centers of O_i, O_{ii} and $O_{surface}$ atoms are similarly affected by the dopants on the defective $La_2O_3(0001)$ surfaces. At the same time, the O2s2p band center of O_i in most cases slightly shifts up with respect to O_{ii} and $O_{surface}$ because of the two extra electrons resulting from the formation of the O vacancy are partially located at the O atoms adjacent to the defect, indicating that O_i atoms near the defect have stonger Lewis basicity than O_{ii} atoms far from the defect. In comparison to the undoped surface with an oxygen vacancy (indicated by horizontal lines in Figure 3), most of the dopants shift up the O2s2p band centers of $O_{surface}$, O_i and O_{ii} atoms on the doped surfaces.

3) *The relationship between oxygen vacancy formation energy and surface Lewis basicity.*

Oxygen vacancies in oxides often play crucial roles in redox reactions, where oxygen vacancy formation energy is also an important descriptor measuring the reactivity. As seen from Figure 4, oxygen vacancy formation energy is as large as 6.7 eV for the undoped $La_2O_3(0001)$ surface. All of the dopants lower the oxygen vacancy formation energy to various degree by activating the surface oxygen atoms, of which alkali metals (Li, Na) even turn the removal of the surface oxygen from an endothermic process to an exothermic process. Although still endothermic, the oxygen vacancy formation energy shows a dramatic decrease for alkali earth metals (~3 eV) and most of the transition metals (3-4 eV), except for Mo (4.9 eV), Ti (6.1 eV), and V (5.3 eV). All of the lanthanides have only little effect on the oxygen vacancy formation energy, perhaps resulting from their very similar ionic radii and therefore little change of the surface geometries upon doping and also due to similar chemical properties of threevalent lanthanides.

In view of an expected relationship between the oxygen vacancy formation energy and the surface Lewis basicity, we tried to build a relationship between the position of O2s2p band center and the oxygen vacancy formation energy. Whereas our calculations indicate that there is no clear relationship between the oxygen vacancy formation energy and O2s2p band centers of O_{surf}, O_i or O_{ii} site on the defect-free $La_2O_3(0001)$ surface, O2s2p band center of the surface oxygen atoms on the defective $La_2O_3(0001)$ surface shows a linear relationship to the oxygen vacancy formation energy as indicated in Figure 5.

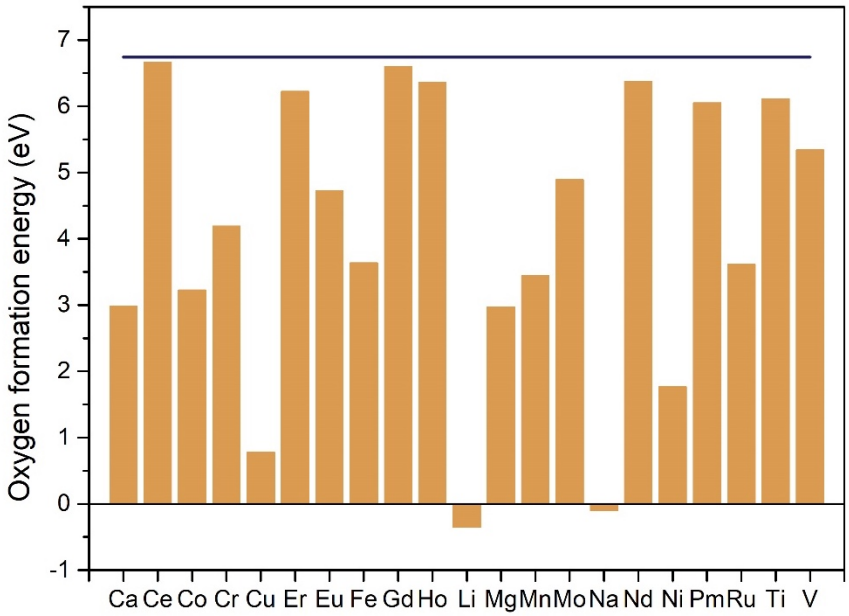

Figure 4: Oxygen vacancy formation energy of the doped $La_2O_3(0001)$ surface for various doping elements. The horizontal line represents the oxygen vacancy formation energy of the undoped $La_2O_3(0001)$ surface.

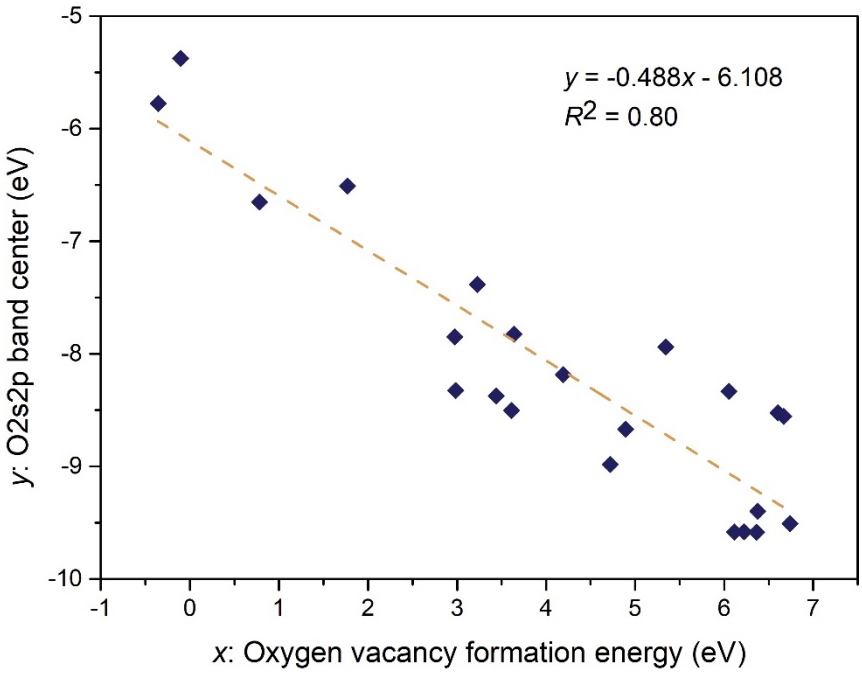

Figure 5: Linear fit between the oxygen vacancy formation energy (x) and the O2s2p band center (y) of the defective doped $La_2O_3(0001)$ surface for various doping elements.

Outlook

We have studied the relationship between the acidity-basicity and oxygen vacancy formation of the defect-free and defective $La_2O_3(0001)$ surface doped by various metal cations. In the next phase of the project, we will select the $CeO_2(111)$ surface as a model surface to investigate the acidity-basicity function of a reducible oxide surface. We doped this surface

with several alkali, alkali-earth, transition metals and lanthanide atoms to study the influence of dopants on the acidity-basicity and surface adsorption properties.

Publications

1. Shikun Li, Yong Li, Marcus Bäumer, Lyudmila Moskaleva. Assessment of PBE+ U and HSE06 methods and determination of optimal parameter U for the structural and energetic properties of rare earth oxides. The Journal of Chemical Physics 2020, 153, 164710.

References

[1] Wang, Z.-Q.; Wang, D.; Gong, X.-Q. ACS Catal. 2020, 10, 586.
[2] Wang, S.; Li, S.; Dixon, D. A. Catal. Sci. Technol. 2020, 10, 2602.
[3] Podkolzin, S. G.; Stangland, E. E.; Jones, M. E.; Peringer, E.; Lercher, J. A. J. Am. Chem. Soc. 2007, 129, 2569.

6.3 *hbc00030:* Dynamics of fluoride anions in all-silica and silico-germanate zeolites

HLRNProject ID:	hbc00030
Run time:	II/2018 – II/2021
Project Leader:	Dr. Michael Fischer
ProjectScientists:	Dr. Michael Fischer, Linus Freymann *(student assistent)*
Affiliation:	Crystallography Group, Faculty of Geosciences, University of Bremen, Klagenfurter Straße 2-4, 28359 Bremen

Overview

In this project, *ab-initio* molecular dynamics calculations are used to study the dynamic behavior of fluoride anions confined to small cages in zeolite structures. One part of the work done in the past year addressed the local environment and dynamics of fluoride anions in double four-ring cages having different compositions. Another part dealt with all-silica zeolites having different topologies, where fluoride anions are incorporated in trigonal-bipyramidal $[SiO_4F]^-$ units. Particular emphasis was put on the investigation of dynamic disorder, which occurs only in some of the studied zeolites.

Scientific background

Zeolites are a class of inorganic porous materials with important applications in ion exchange, gas and liquid separation, and catalysis.[1] Zeolite structures consist of a three-dimensional framework of tetrahedrally coordinated atoms connected by oxygen atoms. A rich variety of zeolite structures has been reported: To date, more than 250 distinct framework types have been recognized by the International Zeolite Association, which assigns three-letter framework type codes like “AST” or “MFI” to each framework. Prototypical zeolites, such as zeolite minerals, possess a negatively charged aluminosilicate framework whose charge is balanced by extra-framework cations. However, the development of sophisticated synthesis routes has led to the discovery of zeolite-like materials having a neutral framework, among them all-silica zeolites (composition SiO_2), germanates (GeO_2), silicogermanates ($Si_xGe_{1-x}O_2$), aluminophosphates ($AlPO_4$), and gallophosphates ($GaPO_4$).

The synthesis in the presence of fluoride anions ("fluoride route") is a particularly successful strategy to obtain neutral-framework zeotypes with very open frameworks and low defect concentrations. Various zeolites and zeotypes with unprecedented framework topologies can be synthesized via this route.[2,3] In the as-synthesized zeolites, the fluoride anions occupy well-defined positions in the crystal structure, balancing the charge of the cationic organic structure directing agents (OSDAs) that are used to promote the formation of a particular framework. Broadly, two different fluoride environments can be distinguished in this context: In zeolites having double four-ring (*d4r*) cages, the fluoride anions occupy the centre of this cage (Fig. 1). In structures without *d4r* units, fluoride anions also tend to occupy small cages. However, rather than being located at the cage centre, they are covalently bonded to a single silicon atom, forming trigonal-bipyramidal $[SiO_4F]^-$ units. Frequently, the fluoride anions are disordered over two or more positions (Fig. 2).

In this project, the dynamics of fluoride anions confined to small cages in zeolite structures are studied using density functional theory (DFT) calculations and DFT-based *ab-initio* molecular dynamics (AIMD) simulations, which cover a timescale of several picoseconds. These investigations are carried out in the context of the project “*Beyond tetrahedral coordination in*

zeolite-type materials - A computational approach" (project no. 389577027, Fi1800/5-1), funded by the Deutsche Forschungsgemeinschaft (DFG - German Research Foundation) since May 2018.

Results

1) AST-type systems

The AST framework is a prototypical zeolite with *d4r* building units.[4] During the first period of this project, the local environment and dynamic behavior of fluoride anions in AST-type silicogermanates was investigated using a combination of structure optimizations and AIMD calculations.[5] In subsequent work, the investigation focused on AST zeotypes having SiO_2, GeO_2, $AlPO_4$, and $GaPO_4$ compositions.[P1] In addition to studying different framework compositions, the influence of the OSDA on the dynamic behavior was investigated by comparing two different organic cations, tetramethyl-ammonium (TMA), which does not form any localized bonds to the framework atoms, and quinuclidinium (QNU), which can act as a hydrogen bond donor. In order to analyze the impact of temperature on the dynamic behavior, AIMD simulations were performed for three temperatures (−123 °C, 25 °C, 300 °C).

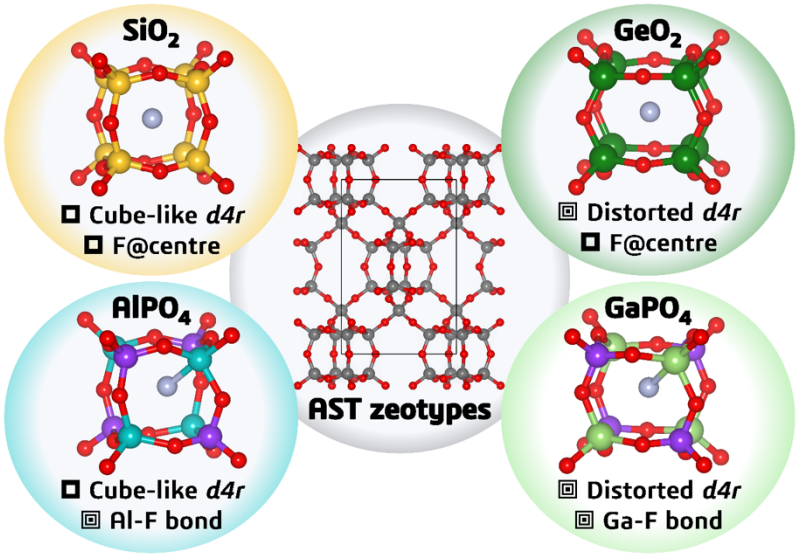

Fig. 1: Influence of framework composition on the local environment of fluoride in AST zeotypes.

Some key findings from this study are visualized in Fig. 1 (designed as "Table of Contents" figure for publication [P1]). When looking at the average structures from the AIMD simulations, the four AST zeotypes differ in the local structure of the *d4r* cages: In SiO_2- and GeO_2-AST, the fluoride anions reside at the centre of the cage, whereas an off-centre displacement with formation of Al−F/Ga−F bonds is observed in $AlPO_4$- and $GaPO_4$-AST. Moreover, a "pyritohedron-like" distortion of the *d4r* cages occurs in GeO_2- and $GaPO_4$-AST, but the cages retain their cube-like shape in the other two zeotypes. The variation of the OSDA has a more prominent effect on those systems where localized bonds are formed between the fluoride anions and framework atoms: In systems containing TMA cations, the off-centre displacements occur without any preferred orientation. In contrast, inclusion of the QNU OSDA leads to an ordered displacement pattern, because the hydrogen bonds between the QNU −NH group and framework oxygen atoms cause a perturbation in the environment of the nearest Al/Ga atoms, rendering them more susceptible to the formation of Al−F/Ga−F bonds. The ordering is almost perfect at −123 °C, but becomes less pronounced at room temperature and above, because the increased thermal motion of the QNU OSDAs weakens the hydrogen bonds. Nevertheless,

the OSDA-induced ordering of the anions is an interesting phenomenon that, if realized experimentally at ambient conditions, could be a pathway to tune application-relevant properties, *e.g.*, with regard to the dielectric behavior. Finally, it should be noted that most of the distortions of the local environments observed in the AIMD average structures were not present in DFT-optimized starting structures (*i.e.*, in the absence of temperature effects). This highlights the importance of including thermal motion in the simulations in order to allow a structure to leave the initial local minimum.

2) All-silica zeolites with different topologies

In this part of the project, the equilibrium position of fluoride anions and their dynamic behavior was studied for five different all-silica zeolites having CHA, IFR, NON, STF, and STT topologies. For all these systems, experimental structure determinations of the as-synthesized forms (including OSDA molecules and fluoride anions) have been reported previously (see [6] for an overview), and NMR-spectroscopic investigations of the fluoride dynamics have been published for all except CHA.[7,8] A DFT-based prediction of the energetically preferred fluoride positions delivered excellent agreement with the experimentally determined locations for all zeolites except STF, where the experimental site was second-lowest in energy. In the most complex system, STT, the fluoride anions are disordered over three non-equivalent sites in the experimental structure. According to the DFT calculations, these three sites are energetically very close together, whereas other positions in the cage are significantly less stable (Fig. 2). Altogether, the results show that the DFT calculations reliably reproduce the equilibrium positions of fluoride. An evaluation of the energetic ordering of sites revealed that the energetically preferred site(s) are determined by a complex interplay of factors, precluding the development of simple crystal-chemical rules that could enable a prediction of the most likely sites without calculations.

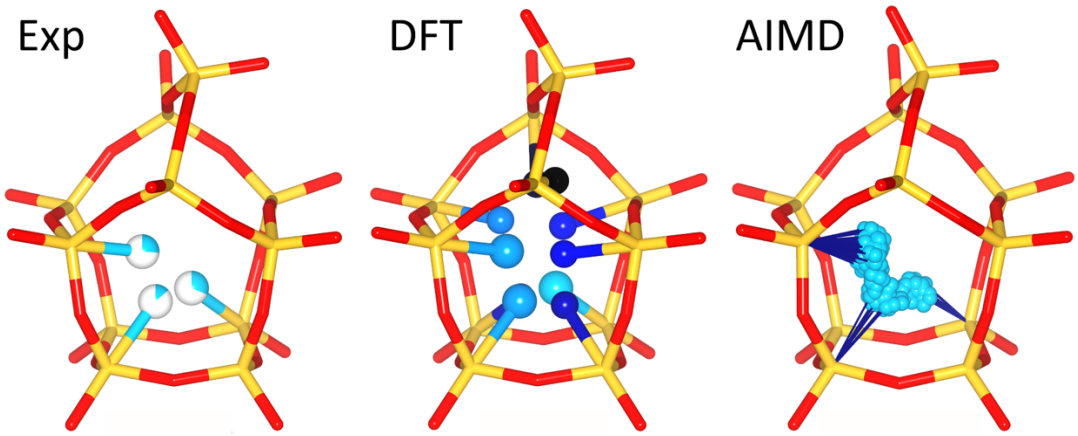

Fig. 2: Visualization of the fluoride-containing cage in the STT-type zeolite SSZ-23. **Left:** Fluoride positions from the experimental crystal structure.[9] **Middle:** Summary of DFT results, with fluoride locations colored according to their total energy (cyan/light blue = energetically favorable; dark blue = unfavorable). **Right:** Representative trajectory of a single fluoride anion during an AIMD simulation.

AIMD simulations were performed for 25 °C, 100 °C, and 200 °C, and the trajectories of the fluoride anions were analyzed to determine the occurrence of a “hopping” of fluoride anions between different Si atoms, *i.e.*, dynamic disorder. For room temperature, such events were found for IFR and STT, but not for the other three zeolites, in perfect agreement with experiment.[7,8] The right panel of Fig. 2 shows an individual trajectory of a fluoride anion in STT, which, incidentally, visits all three experimental positions during the simulation. At higher temperatures, dynamic disorder also occurs in CHA and STF, but not in NON. In addition to reproducing experimental findings, the AIMD simulations also allow to explain the marked

differences in the dynamic behavior among the different zeolites, showing that the local environment, especially the distance from the fluoride anions to “secondary” Si atoms, determines the likelihood of dynamic events. On the other hand, long-range interactions with the OSDA molecules play only a minor role. Such detailed insights into the dynamic behavior of complex host-guest systems are not only of fundamental interest, but they might also aid the development of improved synthesis routes of all-silica/high-silica zeolites.[P2]

3) Ongoing work

The zeolite ITQ-13 (ITH topology) is a particularly interesting system, as two different fluoride environments, F-containing *d4r* cages and $[SiO_4F]^-$ units, coexist in the crystal structure.[10] It can be synthesized in all-silica form and as silicogermanate with Si/Ge ratios up to about 3. Using an alkaline treatment, the fluoride anions can be removed from the $[SiO_4F]^-$ units in all ITQ-13 systems, but removal from the *d4r* cages is possible only for the Ge-containing forms.[11] Further computational work aims to elucidate the unique behavior of this system, studying three different aspects: First, DFT structure optimizations are carried out to predict the energetically favored Ge arrangements at different Si/Ge ratios. Second, DFT optimizations of partially defluorinated models will be used to study the thermodynamics of fluoride removal. Third, AIMD simulations will be performed to compare the dynamics of the fluoride anions in different environments and as a function of Si/Ge ratio.

Project-related publications (including preprint)

P1 M. Fischer, L. Freymann, *Local Distortions in a Prototypical Zeolite Framework Containing Double Four-Ring Cages: The Role of Framework Composition and Organic Guests*, ChemPhysChem *22, 40–54, (2021)*

P2 M. Fischer, *Fluoride Anions in All-Silica Zeolites: Studying Preferred Fluoride Sites and Dynamic Disorder with Density Functional Theory Calculations*, ChemRxiv preprint (2021), https://doi.org/10.26434/chemrxiv.13607645.v1

Project-related presentations

P3 M. Fischer, L. Freymann, *Random vs. cooperative distortions in a prototypical zeolite framework containing double four-ring cages – The role of framework composition and organic guests*, virtual poster presentation at the RSC Faraday Discussion “Cooperative phenomena in framework materials”, October 2020

References

[1] A. F. Masters, T. Maschmeyer, Microporous Mesoporous Mater. *142, 423–438 (2011)*
[2] M. A. Camblor, L. A. Villaescusa, M.-J. Díaz-Cabañas, Top. Catal. *9, 59–76 (1999)*
[3] P. Caullet, J. Paillaud, A. Simon-Masseron et al., Comptes Rendus Chim. *8, 245–266 (2005)*
[4] Y. Wang, J. Song, H. Gies, Solid State Sci. *5, 1421–1433 (2003)*
[5] M. Fischer, J. Phys. Chem. C *123, 1852–1865 (2019)*
[6] D. S. Wragg, R. E. Morris, A. W. Burton, Chem. Mater. *20, 1561–1570 (2008)*
[7] H. Koller, A. Wölker, L. A. Villaescusa et al., J. Am. Chem. Soc. *121, 3368–3376 (1999)*
[8] L. A. Villaescusa, I. Bull, P. S. Wheatley et al., J. Mater. Chem. *13, 1978–1982 (2003)*
[9] M. A. Camblor, M.-J. Díaz-Cabañas, J. Perez-Pariente et al., Angew. Chem. Int. Ed. *37, 2122–2126 (1998)*
[10] A. Corma, M. Puche, F. Rey, et al., Angew. Chem. Int. Ed. *42, 1156–1159 (2003)*
[11] X. Liu, U. Ravon, A. Tuel, Chem. Mater. *23, 5052–5057 (2011)*

6.4 *hbc00046:* Towards an atomistic picture of phage display: the case of TiO_2 binding peptides

HLRNProject ID:	hbc00046
Run time:	II/2020 – I/2021
Project Leader:	Dr. Massimo Delle Piane
ProjectScientists:	Dr. Monika Michaelis
Affiliation:	Bremen Centre for Computational Materials Science (BCCMS) and Hybrid Materials Interfaces (HMI) group, Faculty of Production Engineering, University of Bremen

Overview

The identification of the primary structure (amino acid sequence) of a peptide which possesses the property to bind selectively and/or specifically to a substrate of interest is referred to as genetically engineered polypeptides for inorganics (GEPI). Within this framework, combinatorial biological protocols like for instance phage display (PD), are applied to identify peptide sequences to allow for faster, rational design. Additionally, these display techniques enable the identification of the genotype of the peptide that binds to the targeted material without requiring a detailed knowledge of the system. For this purpose, randomized peptide libraries with up to 10^9 variations of sequences encoding peptides of fixed lengths are inserted into the capsid genome of the phage. An unrivaled property of these viruses is the direct relation of its genotype and its phenotype as, for example, chimeric peptides are directly expressed on the surface of the coat protein pIII *via* a linking sequence displayed at one end of the bacteriophage (cf. Figure 1a). Another outstanding property of the bacteriophages is their ability to infect bacteria and replicate within them, which leads to their quick reproduction.

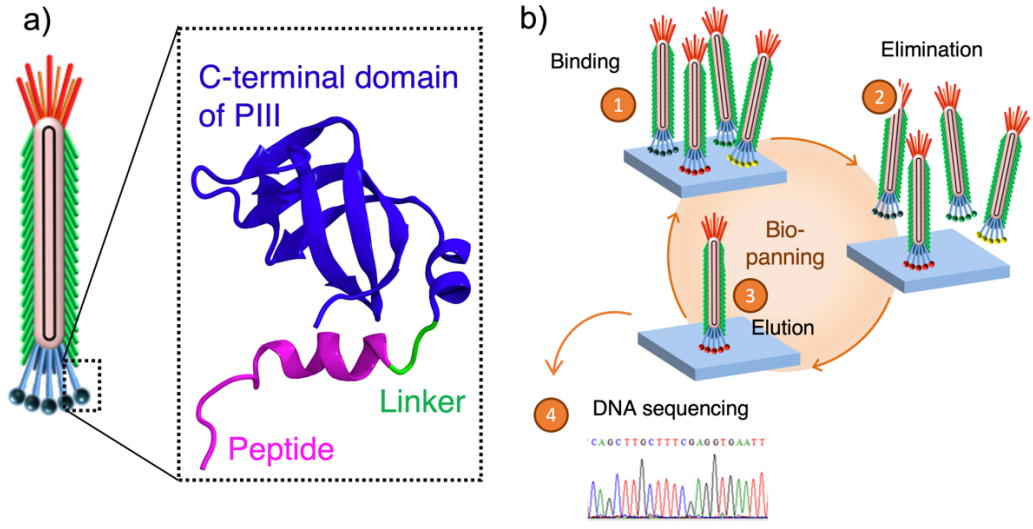

Figure 1: Overview of Phage display. a) Phage M13 in schematic representation with a zoom in revealing the atomistic setup and the subunits. b) Process of biopanning in Phage display on the material of interest.

The affinity selection is performed by a process known as biopanning (Figure 1.b). Briefly, the phage library and substrate are brought into contact and incubated in an appropriate solvent allowing the phages displaying the chimeric peptides to bind to the substrate. After the incubation time, unbound or weakly bound bacteriophages are removed by a washing step with a suitable detergent-containing solution. The phages that are still bound to the target material after this step, and therefore have a potential high binding affinity, are eluted. The obtained phages with the desired peptide sequences are replicated by infection of *Escherichia coli*. Gene sequencing of individual phage clones is performed to identify the peptides that can specifically and strongly bind to the target material.

Since the adaptation of phage display for the identification of specifically binding peptides to materials, a huge variety of sequences for different materials could be identified. The limited understanding of how to exploit the relationship between peptide sequences identified during phage display and their corresponding materials-binding affinity as well as their specificity of interaction is so far a significant obstacle towards reliable peptide-based strategies for the generation and organization/activation of (nanostructured) inorganic materials.

In this project, we focus on TiO_2 (Titania), which is an attractive material used in medical and environmental applications based on its optical, adsorbent, and catalytic properties as well as its use in biomedical implant materials. We chose two 12mer peptides for our investigation, which were originally identified via Phage display against 100 nm titanium nanoparticles. It was revealed that although these peptides have very similar binding affinities towards Titania, their binding shows profoundly different modes of surface interaction.

A fundamental understanding of the atomistic aspects of peptide-materials recognition during phage display in comparison to peptide binding in their intended application is absolutely necessary to advance peptide-based generation and organization of nanostructured inorganic materials. Therefore, the general question we aim at answering during the project is: How does the attachment to a phage, as happens in widespread phage display binding assays, influence the conformation and bio-material interaction behavior of titania binding peptides?

Results

As a first step we investigated the conformational ensemble of the selected titania binding peptides, to use as a reference to identify the perturbation induced by the phage linkage. The sequences of the two selected peptides, obtained via phage display assay, are: QPYLFATDSLIK (Ti-1) and GHTHYHAVRTQT (Ti-2). Based on quartz-crystal microbalance with dissipation (QCM-D) preliminary studies, we focused also on the two 6-mer halves of each peptide. We generated starting conformations based on the known sequences, using *de novo* secondary structure prediction tools. The REMD method was used to identify molecular equilibrium structures of the peptide strands. 16 replicas of each strand with initial random configuration were simulated at temperatures between 300 and 800K to ensure sampling of the entire conformational space. The simulations were carried out using the CHARMM force field. REMD was run for 10 ns /sample (total of 160 ns) and the temperatures exchanged every 0.2 ps. Statistical analysis was performed using the MMTSB toolbox, with a k-means clustering algorithm. Representative final ensemble structures were chosen from the lowest temperature replica (300 K). The higher temperatures were used for fast conformational search and overcoming kinetic trapping in the REMD scheme. The center of the most populated cluster, meaning the structure with minimum RMSD, was exported for analysis. The secondary structure of each structure is determined using the STRIDE toolset and VMD.

After the equilibration, the individual structures were arranged in a circle with diameter 3 nm, representing a phage display. The structures were then equilibrated for 50ns in explicit solvent with ions present and the final structure was determined. A second set of computational experiments was performed where the peptides are equilibrated in explicit solvent with ions as part of a larger protein structure. The peptides were built in random conformation onto that

structure (1TOL.pdb). Exposed amino acids were identified (parts of the sequence that were “sticking out”) that could potentially interact with an abiotic surface.

Estimating the free energy of adsorption of materials-binding peptides is fundamental to quantifying their interactions across bio/inorganic interfaces. Among experimental methods that can be used to estimate this quantity, QCM-D has been already performed in our group on the selected peptides. As a second step in this project, we decided to couple the experiment with the accurate calculation of the free energy of adsorption by means of Replica Exchange with Solute Tempering augmented with metadynamics (RESTmetaD) simulations, performed on the interaction of the peptides with a model amorphous titania surface in pure water. However, both during this project and during the parallel investigation of the adsorption of peptides on a zinc oxide (ZnO) surface, we have encountered some issues in this approach, hindering convergence and the quality of the computed free energies of adsorption. This was due to a deficient sampling of the area in proximity to the surface. Indeed, metaD has been shown to very poorly converge in the case of molecules interacting with material surfaces with high solvent affinity, due to the inherent difficulty of displacing solvent molecules within the strongly adsorbed solvent layer. In our case distinct solvent rearrangements induced by the surface created entropic barriers to the adsorption process. We would like to note that this is not necessarily due to a high free-energy barrier along the free energy profile, but to the narrowness of the adsorption pathway that can lead to successful displacement of the chemisorbed water layer by the amino acids. After several trials and methods’ benchmarking, we found that convergence and agreement with experiment can only be achieved by explicitly biasing the surface/solvent interactions, in a novel extension to the standard RESTmetaD approach. Figure 2 reports a comparison between three methods for the adsorption of an amino acid on the oxide surface, to demonstrate this point. We are currently employing this method to extract binding free energies of out titania binding peptides.

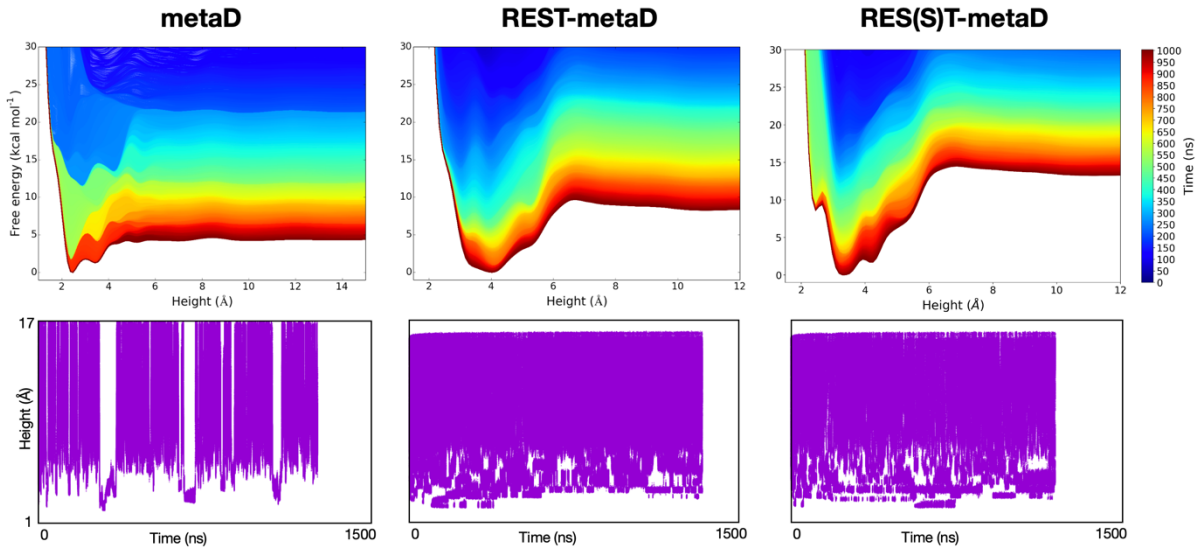

Figure 2: Comparison in performance between different enhanced sampling methods for the adsorption of histidine on the oxide surface. metaD: standard metadynamics with CV set as the height of the amino acid's center of mass with respect to the surface. REST-metaD: metadynamics augmented with Replica Exchange with Solute Tempering (solute = amino acid). RES(S)T-metaD: metadynamics augmented with Replica Exchange with Solute and Surface Tempering. Top: evolution of the free energy profiles profiles during the simulations, according to the color scale on the right. The zero of the free energies is set at the minimum value. Bottom: value of the CV along the simulations.

Outlook

The next step will be to compare the interaction of the peptides with titania as free in solution as opposed to linked to a phage, understanding how the additional structural constraint influences the way these biomolecules approach and interact with the inorganic material. We will therefore investigate the interaction of the “minimal phage” system with our titania surface. We plan to perform only a qualitative investigation of the interaction by simulating the phage approach to the material surface via slow steered molecular dynamics simulations, followed by long standard MD simulations to investigate the equilibrium ensemble of the system at the surface interface.

We believe that the obtained results, although obtained for titania binders, will be of general interest within the larger (bio)material community, adding caveats to the extrapolation of results from phage display assays and providing a better atomistic understanding of the biomolecular recognition of inorganic material surfaces.

6.5 *hbc00048:* Antimicrobial peptides: structure-activity relationships and antimicrobial mechanisms

HLRNProject ID:	hbc00048
Run time:	III/2020 – II/2021
Project Leader:	Dr. Monika Michaelis
ProjectScientists:	Dr. Massimo Delle Piane, Prof. Lucio Colombi Ciacchi
Affiliation:	Bremen Centre for Computational Materials Science (BCCMS) and Hybrid Materials Interfaces (HMI) group, Faculty of Production Engineering, University of Bremen

Overview

Infections are a major concern in global healthcare, especially from bacteria that form biofilms. Their presence can for instance lead to the establishment of chronic wounds, which cause persistent inflammation and damage and can ultimately result in death. In particular, multidrug-resistant bacteria, that are difficult or even impossible to treat, have evolved increasingly into a global health threat, with special emphasis on strains that belong to the so-called ESKAPE panel. According to the WHO priority list, future development strategies should therefore focus on antibiotics and their alternatives that are active against 'critical-priority' bacteria, especially multidrug-resistant and Gram-negative bacteria. It was recently shown that antibiotic resistant bacteria have a high propensity towards a collateral sensitivity against so-called Antimicrobial Peptides (AMPs). AMPs are short-chain, cationic peptides that evolved as a host-defense mechanism and are conserved in all kingdoms of life. AMPs are excellent candidates for the functionalization of biomaterials and medical devices. However, despite their advantages, few AMPs have been advanced to date for clinical use and/or passed clinical trials.

Understanding the mechanisms behind AMP antimicrobial action is crucial for their application. A complex interplay of physicochemical and structural parameters mediates the antimicrobial performance of such peptides. It was previously shown that antimicrobial activity is strongly correlated to peptide conformation (structure activity relationship) or, more precisely, to their induced amphipathic conformation upon membrane interaction. A promising candidate for computer-assisted AMP design, is the synthetic oligopeptide SAAP-148. Developed from human peptide LL-37, SAAP-148 shows enhanced antimicrobial and antibiofilm activity under physiological conditions. However, its structure and the precise mechanism of action are unknown.

Within this project we want to understand the atomistic details of the conformational ensemble of SAAP-148 in solution and upon interaction with the membrane. Based on these results we want to identify potential interaction mechanisms. We focus on the application of enhanced sampling methods to overcome the timescale problems described in previous approaches. The general question we aim at answering during the proposed project is: How do the conformational ensemble and the membrane-induced conformational changes influence the antimicrobial action of an antimicrobial peptide?

Results

In a first step we used *de novo* secondary structure prediction (Pep-Fold3) to provide an initial "educated guess" about the intrinsic propensities to form either well-defined or unordered secondary structures for both LL-37 and SAAP-148. With this structure prediction we obtained

a first impression on the variability within the conformational ensemble. As expected, structure prediction resulted in a high degree of helicity for both peptides.

Based on these structure predictions we chose the alpha-beta collective variable to thoroughly explore the peptides' conformational space in solution, using Replica Exchange with Solute Tempering (REST) simulations coupled with Metadynamics (RESTMetaD). Figure 1 reports the free energy landscapes for LL-37 and SAAP-148 in solution, plotted based on the alpha-beta collective variable. At variance from secondary structure predictions, the free energy profiles do not show a global minimum close to 100% helicity, but a more variable conformational landscape is found, with global minima around 50%. Indeed, these peptides are expected to gain helicity only when in contact with the bacterial membrane

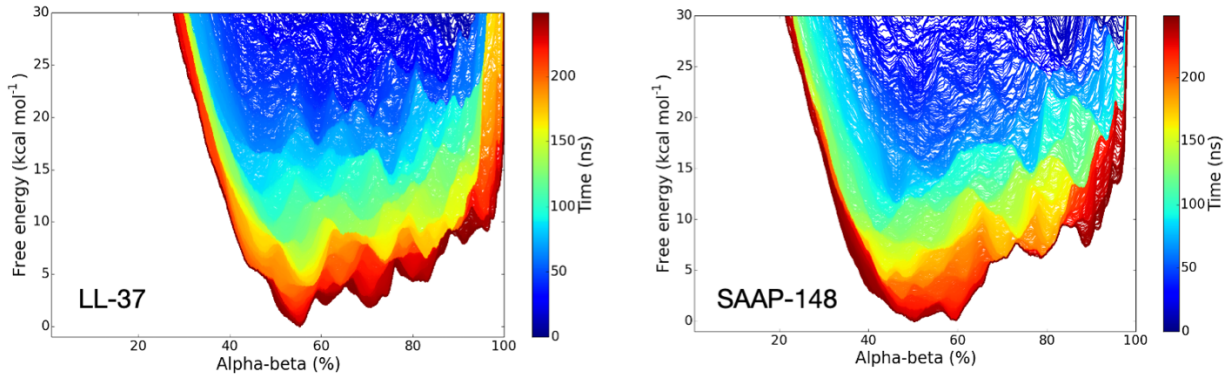

Figure 1: Free energy profiles for LL-37 and SAAP-148 in solution, plotted based on the alpha-beta collective variable. The evolution of the profiles during the REST-MetaD simulations is reported, according to the color scalse on the right. The zero of the free energies is set at the minimum value.

The construction of accurate atomistic models for bacterial membranes is an important part of our project. The cell envelope of Gram-negative bacteria consists of two separated membranes. The outer membrane is asymmetric, and the outer leaflet is composed of lipopolysaccaride (LPS), while the inner leaflet contains a mixture of zwitterionic and anionic phospholipids. This asymmetry is important to rationalize the first membrane/peptide interactions and was taken into account. The inner membrane contains a symmetric arrangement of phospholipids including zwitterionic (phosphatidyl-ethanolamine) and anionic (cardiolipin and phosphatidylglycerol) phospholipids (similar to the membrane of Gram-positive bacteria). The parameter set CHARMM36 was used to reproduce the realistic lipid properties as closely as possible.

For the outer membrane of *Pseudomonas Aeruginosa,* the upper leaflet consists of the penta-acyl Lipid A domain of *P. aeruginosa* LPS which contains β (1-6)-linked D-glucosamine disaccharides decorated with two negatively charged phosphates at 1 and 4' position and five symmetrically distributed fatty acids. The inner leaflet has combinations of head and tail groups with 60% PE, 30% PG and 10% PC with 59% DP and 41% DO. We focused on symmetric acyl chains with the same levels of acyl chains in both leaflets. The system was built with the CHARMM-GUI Membrane Builder, which enables us to include all relevant components. 150 mM NaCl with Ca ions were added to balance the charge of the sugar coating. We have confirmed the correct description of the physicochemical properties of the membranes, in particular the lipid density per surface area, the lateral diffusion coefficient of individual molecules within the membrane and the overall membrane stability in long MD runs at at 37°C within the NPT ensemble (Figure 2).

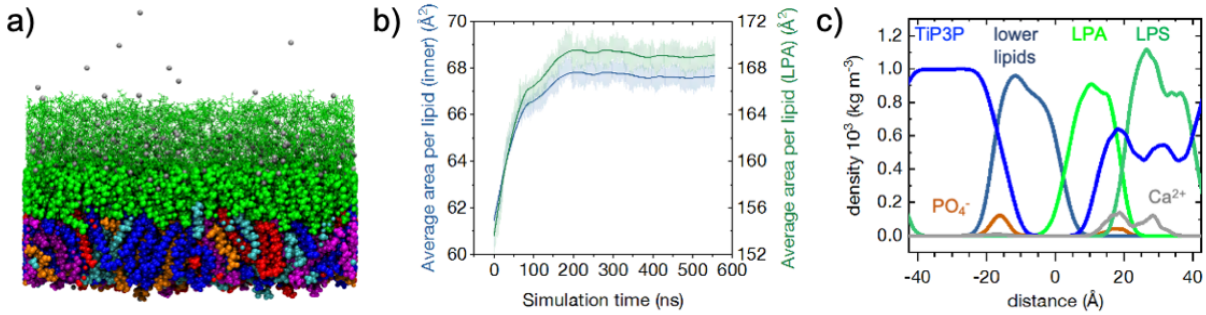

Figure 2: a) representative snapshot of the equilibrated membrane, b) area per lipid of inner lipids and LPA and c) mass density profiles of selected functional groups across the membrane (averaged from the last 100ns).

Outlook

In the next step of the project, we are currently identifying the preferential binding configuration of SAAP-148 and LL-37 on the membrane. This step is the most computationally demanding, due to the combination of system size, necessity of multiple replicas and expected slow convergence of the profiles. From the simulations, we will be able to compute an accurate estimation of the free energy of adsorption and we will determine the predicted dominant structures of the peptides in the adsorbed states.

Finally, we want to provide insight into the mechanisms of antimicrobial activity using either state-of-the-art, unbiased and long MD simulation with increased temperature or steered MD simulations of the peptide across the membrane.

We believe that the obtained results, although obtained for a selected peptide and an exemplary outer and inner membrane composition of a gram-negative bacteria, will be of general interest within the larger microbiological and (bio)material community, adding caveats to the extrapolation of results from experimental assays and providing a better atomistic understanding of the antimicrobial mechanisms of AMPs.

6.6 *hbi00033:* Flow transitions and regimes in core-annular pipe flow

HLRNProject ID:	hbi00033
Run time:	I/2016 – III/2021
Project Leader:	Prof. Dr. Marc Avila
Project Scientists:	C. Plana, Dr. B. Song
Affiliation:	Center of Applied Space Technology and Microgravity (ZARM) Universität Bremen

Overview

Core-annular pipe flow (CAF) has applications in transporting highly viscous fluids, such as crude oil in pipelines, as well as in microuidic flows. However, the perfect core-annular flow is in general linearly unstable and can exhibit multiple flow configurations, such as bamboo waves, slug flow, bubble flow, and oil in water dispersion, as a function of the operating conditions. The core annular flow has been investigated widely, mainly in experiments, and some rather crude phase-diagram was given in terms of dimensional parameters, such as the nominal water flow rate and oil flow rate. For generality, the phase-diagram in terms of non-dimensional control parameters (e.g., Reynolds number) is highly desired for applications to different experimental setups and flow conditions, and for in-depth theoretical investigation on the bifurcation leading to different flow patterns. This project aims to probe the phase-diagram of Core-annular pipe flow using direct numerical simulation (DNS) of the Navier-Stokes equations together with the Cahn-Hilliard equation that allows to naturally capture the interface in the binary fluid system.

Results

During 2020 we continued the study of the evolution of the initial core-annular flow at low and moderate Re using a mixture of kerosene and water, which presents a moderate viscosity and density ratios ($\hat{\rho} = 0.79, \hat{\mu} = 1.6$). We found that the results of the linear stability analysis underestimate the required pipe length to reach the final state. In the case with Re = 3000, the pipe length predicted by the most unstable mode in the linear stability analysis ($L = \pi$) led to an unphysical stratified flow with no preferential direction, as seen in Figure 1. This regime showed a relatively large volume flow ratio between the phases, meaning a hold-up ratio larger than 1.

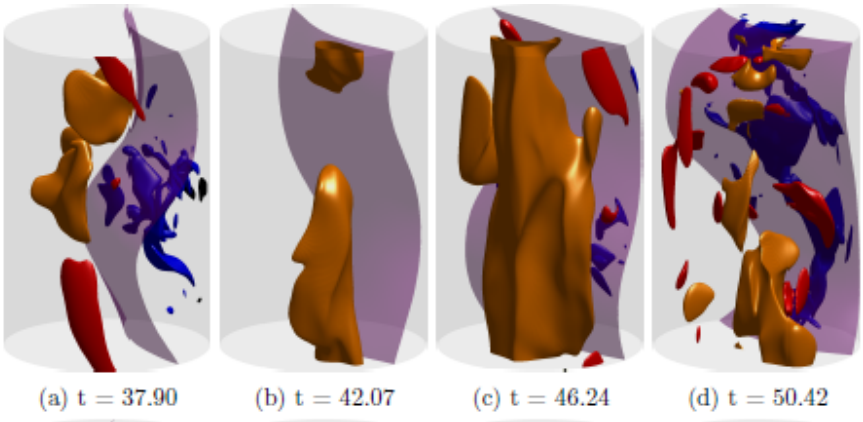

Figure 1: Saturated state of the initial CAF with Re = 3000 in a pipe with length $L = \pi$. Purple: Interface. Brown: Axial velocity. Red: Oil turbulent kinetic energy. Blue: Water turbulent kinetic energy. $E^{r\theta} = 0.0012$

On the other hand, increasing in the pipe length ($L = 4\pi$) allowed the system to relax to a more physical state in the form of slug flow, as seen in Figure 2, which has been observed in experiments with similar flow conditions [1]. In this configuration, both phases presented the same volume flow, leading to a hold-up ratio of unity. In this state, the flow showed a consistently lower intensity of turbulent kinetic energy (estimated with the cross-section kinetic energy,$E^{r\theta}$), and concentrated close to the interface.

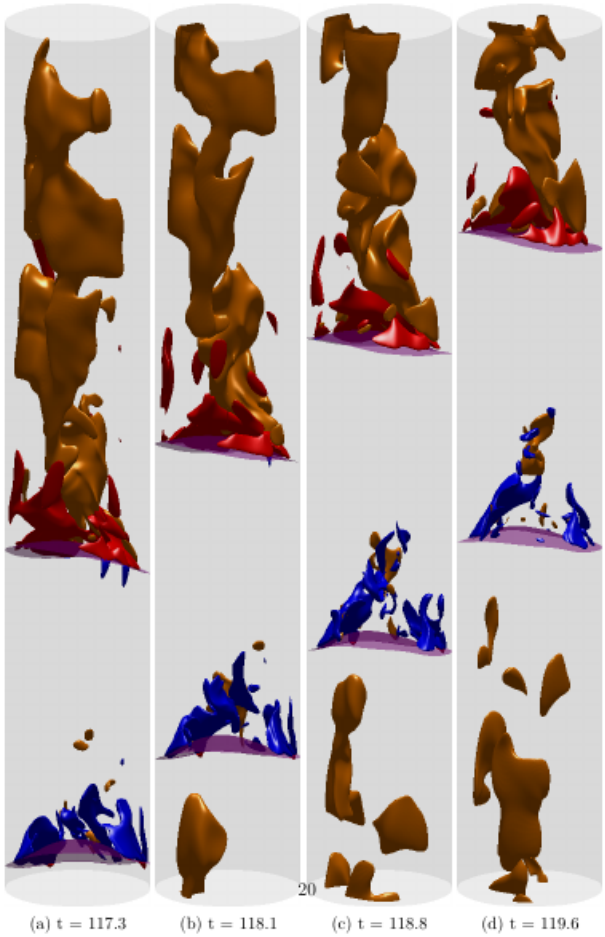

Figure 2: Saturated state with Re = 3000 in a pipe with length $L = 4\pi$. Purple: Interface. Brown: Axial velocity. Red: Oil turbulent kinetic energy. Blue: Water turbulent kinetic energy. $E^{r\theta} = 0.004$

Additionally, we continued the expansion of our hybrid multiphase pipe flow code. We added the possibility to work with pipes of variable inclination, ranging from a pipe incliniation angle of $\theta_p = 0$ (horizontal pipes) to $\theta_p = 90°$ (vertical pipes). We validated the new feature against the analytical solution of stratified flow in horizontal and inclined pipes reported in [2] with a good agreement between the the analytical and numerical solutions, as seen in figure 3.

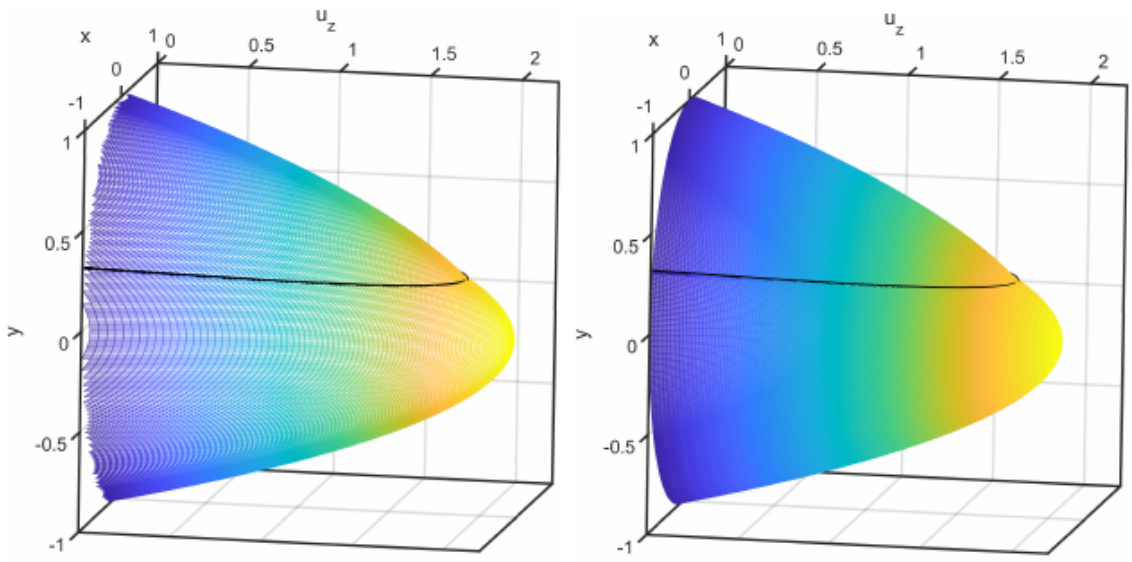

Figure 3: Validation of the horizontal pipe calculations against the stratified flow solution from [2]. Black line: fluid interface. Re = 2268. Same fluid properties (oil and kerosene) and volume ratio as the case with the vertical pipe

Outlook

We are currently finishing a paper reporting our results with the flow transitions and low Re and the influence of the pipe length on the final state. We also plan to continue our simulations at higher Re until the saturate state is reached.

Presentations

1. C. Plana, B. Song, M. Avila, APD DFD 2020, Online, November 22-24, 2020

Literature

1. S. Ghosh, G. Das, P.K. *Das. Inception and Termination of the Core-Annular Flow Pattern for Oil-Water Downflow Through a Vertical Pipe*. AIChE Journal 58 (2012). 2020-029

2. D.V. Maklakov, I.R. Kayumov, R.R. Kamaletdinov. *Stratified laminar flows in a circular pipe: new analytical solutions in terms of elementary functions.* Applied Mathematical Modelling 59 (2018) 147-163

6.7 *hbi00036:* Fluiddynamische Untersuchung der Stressbeanspruchungen proteinstabilisierter o/w-Phasengrenzflächen beim Premix-Membranemulgieren

HLRN-Projektkennung:	hbi00036
Laufzeit:	III/2020 – II/2021
Projektleiter:	Prof. Dr.-Ing. Udo Fritsching
Projektbearbeiter:	A. Kyrloglou, P. Giefer
Institut / Einrichtung:	Fachgebiet Mechanische Verfahrenstechnik Universität Bremen

Überblick

In der Verfahrens- und Prozesstechnik finden Dispersionen, also flüssig / flüssig Systeme eine breite Anwendung. In der Prozessierung von Lebensmitteln sowie pharmazeutischen Anwendungen spielen Emulsionen eine entscheidene Rolle. Das Premix-Membranemulgieren ist ein Verfahren, bei dem grobdisperse Voremulsionen mittels Dispergierung durch eine poröse Membran in eine Feinemulsion bzw. Dispersion überführt werden. Ein Schlüsselparameter der Emulsionsqualität ist die Tropfengrößenverteilung, die maßgeblich durch das Stress-Verweilzeitverhalten beeinflusst wird. Bei der Einbindung von schersensitiven Medien, in diesem Fall Proteinen, ist die genaue Charakterisierung von besonderer Relevanz und bedarf wissenschaftlicher Klärung. Daraus können mechanistische Schädigungsmodelle abgeleitet werden.

Um einen genauen Einblick in das Aufbruchphänomen zu bekommen, konzentriert sich das Forschungsvorhaben auf die Beschreibung der mehrphasigen Strömung in porösen und idealisierten Strukturen. Um die Scher- und Dehnkräfte an den Phasengrenzflächen analysieren zu können, wurde ein Modell entwickelt und in die Open Source Software OpenFOAM implementiert. Da die im Prozess eingebundenen Proteine an den Phasengrenzen adsorbieren ist dies von besonderem Interesse. Ziel des Projektes ist es, die Kriterien für die Tropfendeformation und den Tropfenaufbruch anhand dieser Belastungen zu quantifizieren. Darüber hinaus werden die Ergebnisse dieses Projektes für ein weiteres Projekt (Molekulardynamische Untersuchung der Stressbeanspruchung auf Proteine an der Phasengrenzfläche beim Premix-Membranemulgieren, hbi00037) herangezogen. Die Projekte sind in das DFG Schwerpunktprogramm 1934 „DISPBiotech“ mit einem Förderzeitraum von 36 Monaten sowie das DFG - GRK 1860 MIMENIMA an der Universität Bremen eingebunden. Im folgenden Abschnitt werden ausgewählte Ergebnisse der bisherigen Studien aus den vorangegangenen Förderperioden des HLRN dargestellt.

Ergebnisse

In der letzten Förderperiode wurden Simulationen in idealisierten Porenstrukturen durchgeführt. Gleichzeitig wurde ein zweiphasiger viskoelastischer Solver für openFoam 7 entwickelt.

Komplexere Strömungs-Systeme wurden behandelt, indem das Scher-Stress-Verweilzeitverhalten von Tropfen in verschiedenen idealisierten Porenstrukturen untersucht wurde. Im Folgenden wird das Verweilzeitverhalten anhand einer Verengung von einer großen Kapillare in eine kleinere dargestellt (Abbildung 1). Das vorliegende dreidimensionale Gitter hat eine Zellanzahl von 1,6 Mio. Zellen mit einer mittleren Kantenlänge von 8 µm. Eine

Gitterunabhängigkeit wurde für Zellgrößen von 8 – 10 µm Kantenlänge nachgewiesen. Das System ist massenkonservativ.

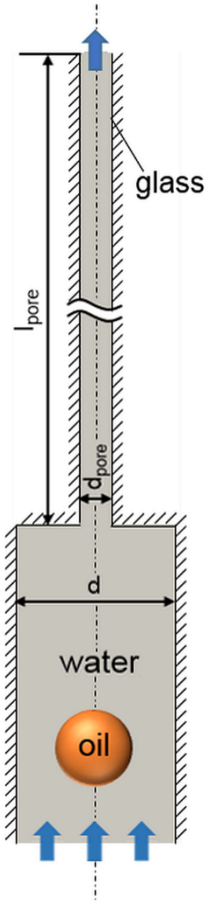

Abbildung 1: Querschnitt der vereinfachten Porenstruktur mit einer abrupten Reduktion des Kapillardurchmessers von d = 1 mm auf d_{pore} = 0,2 mm (Wollborn et al., 2019).

Tropfendispersion in Einzelporen

Parallele Aufbruchvorgänge von mehreren Tropfen und Fluidelementen unterschiedlicher Größe in Membranen machen eine mechanistische Betrachtung der Dispersionsherstellung in Membranen sehr schwierig. Um die Tropfendispersion in Membranen verstehen zu können, ist es sinvoll, den Tropfenaufbruch in Einzelporen zu analysieren.

Dazu wurden idealisierte Einzelporen betrachtet und verschiedene Parameter, wie die Benetzbarkeit der Porenoberfläche, die Viskosität der dispersen Phase, als auch die Grenzflächenspannung und Geschwindigkeit variiert.

Während der Einfluss von Viskosität und Grenzflächenspannung weitestgehend bekannt ist, ist die Abhängigkeit der Porenbenetzbarkeit auf die mechanistische Dispersion ungeklärt. Die Ergebnisse zeigen, dass die erste Wandinteraktion der dispersen Phase für den Tropfenaufbruch entscheidend ist. Mit steigender Benetzbarkeit der Wand für die disperse Phase bilden sich Instabilitäten im Eingang der Pore aus, deren Wellenlänge deutlich kleiner sind, als die auftretenden Rayleigh-Plateau Instabilitäten (siehe Abbildung 2).

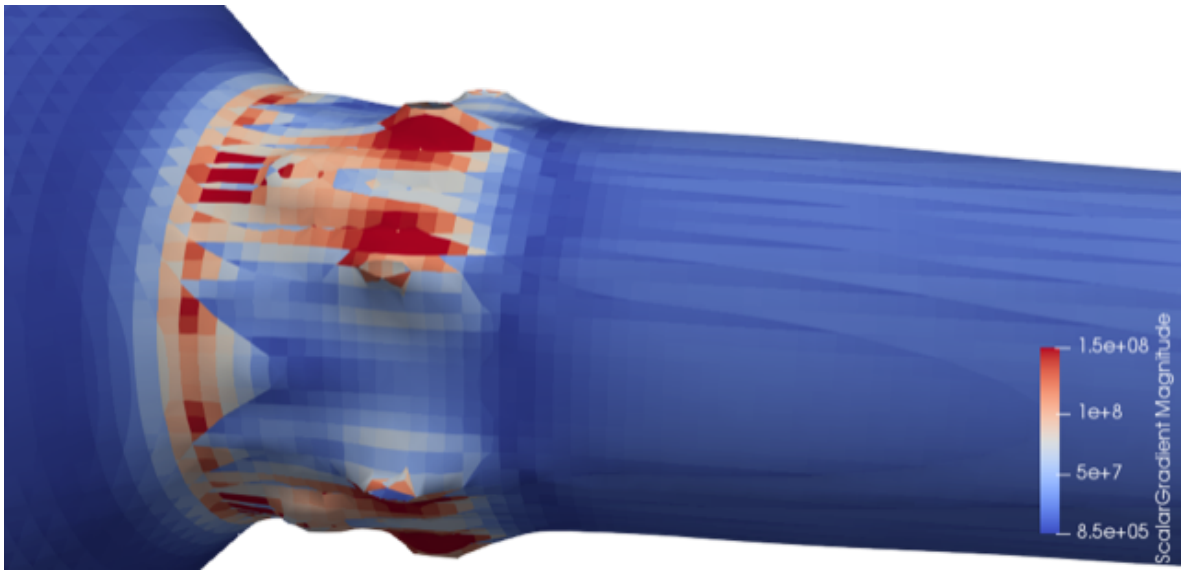

Abbildung 2: Kapillarwellen im Eintrittsbereich der Einzelpore

Diese Instabilitäten beeinflussen maßgeblich die Wellenlänge der Rayleigh-Plateau Instabilitäten, was in kürzeren Aufbruchszeiten resultiert. Dieses Verhalten lässt darauf schließen, dass sich die Kapillarwellen stromabwärts ausbreiten. Dies bestätigt sich durch den Fakt, dass die Wellenlänge der Rayleigh-Plateau Instabilitäten bei ausbleibendem Wandkontakt gleichbleiben und maßgeblich von der Oberflächenspannung abhängen. Dieses Verhalten wurde sowohl mit höherer Geschwindigkeit als auch durch Änderung der Porengeometrie gewährleistet.

Die Variation der Grenzflächenspannung zeigt, dass die Anzahl und Wellenlänge der Instabilitäten am Poreneintritt mit sinkender Oberflächenspannung steigt und eine anormale Dispersion aufweisen. Was in der Summe für einen kapillaren Aufbruchsvorgang spricht, welcher von der Oberflächenspannung und weniger von der Viskosität getrieben wird. Mit steigender Viskosität der dispersen Phase werden kapillare Wellen gedämpft.

Entwicklung des Viskolastischen Solvers

Zur Untersuchung komplexer mehrphasiger Fluide bei der Dispergierung wurde ein zweiphasiger viskoleastischer Solver in der letzten Förderperiode entwickelt. Basierend auf dem Solver viscoelasticFluidFoam von OpenFoamExt 4.1 und interFoam von OpenFoam 7, der neue viscoInterFoam-Solver wird auch die Quantifizierung und Untersuchung der Scherspannungsverteilung auf die Flüssig-Flüssig- und Flüssig-Wand-Grenzflächen unterstützen.

In Abbildung 3 ist eine qualitative Simulation des die-swell Effekts zur Darstellung des viskoelastischen Verhaltens des Solvers zu sehen. In dieser Simulation eines viskoleastischen Polymers fließt ein Strahl durch eine kleine Öffnung. Wegen der Viskoelastizität kann man eine Schwellung am Auslass und die charakteristische Links-Rechts Bewegung und den Einschluss von Luftblasen im Polymer beobachten.

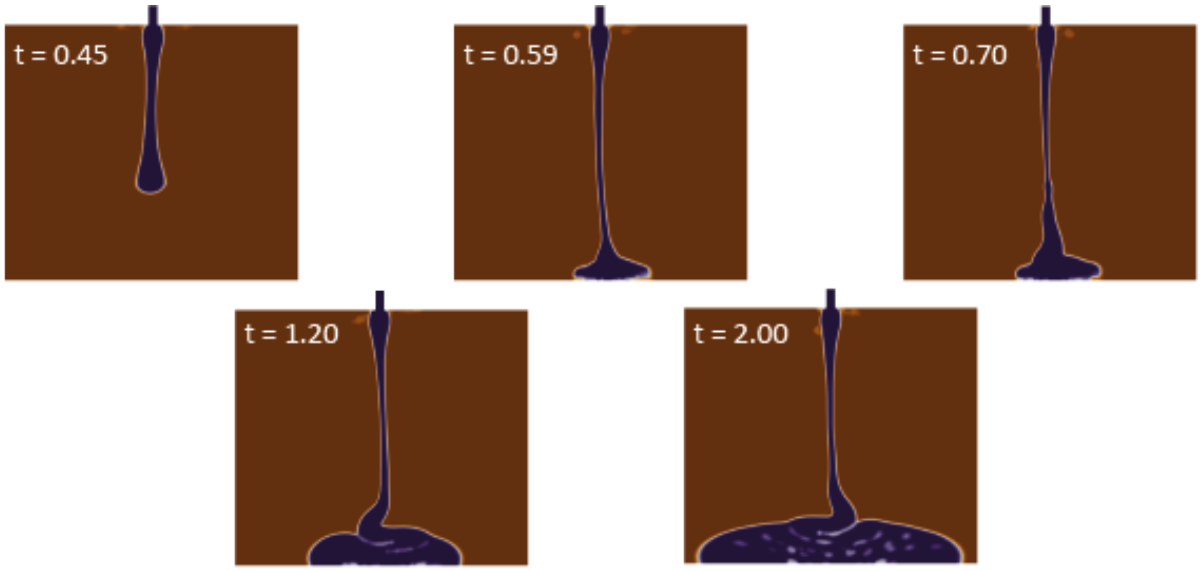

Abbildung 3: Die-Swell Simulation zur Darstellung des viskoelastischen Verhaltens des neu entwickleten viscoInterFoam-Solvers

In der Fortführung der Arbeiten folgt ein detailierter Benchmark des viskolastischen Solvers mit Simulationen, die im nächsten Jahr auf dem HLRN durchgeführt werden sollen, beispielsweise für idealisierte Einzelporen und die Deformation von Tropfen beim Durchtritt durch Membranen und Kugelschüttungen.

Ausblick

In der neuen Förderperiode werden weitere Parameter und Geometrien im Bereich der Modellstruktur untersucht. Insbesondere bei reellen, hohen Kapillarzahlen sind Effekte zu beobachten, die zu einer Dispergierung der kontinuierlichen Phasen innerhalb des Einzeltropfens führen.

Bei Emulgierexperimenten wurde der Tropfenaufbruch bereits bei geringen Kapillarzahlen beobachtet, welcher in den bisher untersuchten Modellstrukturen nicht gezeigt werden konnte. Der Aufbruch erfolgt in diesem Fall durch Verzweigungen und die Änderung der Geschwindigkeitsfelder durch wechselnde Porengrößen. Dieses Verhalten soll mit neuen Modellstrukturen abgebildet werden. Die Stressbelastung an einer Verzweigung sowie einer Pore mit einem Durchmesser entsprechend einem Vielfachen der Tropfengrößen werden untersucht. Dabei werden neben den Kapillarzahlen auch die Kontaktwinkel und Viskositätsverhältnisse variiert.

Publikationen

1. Wollborn, T., Luhede, L., & Fritsching, U. (2019). Evaluating interfacial shear and strain stress during droplet deformation in micro-pores. *Physics of Fluids,* 31(1), 012109. https://doi.org/10.1063/1.5064858

Vorträge / Poster

1. Kyrloglou A., Schulz, A.; Luhede, L.; Fritsching, U.: Numerical Investigation of Emulsification of Viscoelastic Fluids through Porous Membranes; Vortrag in CellMAT 2020, 7-9 October 2020, Germany, Web Conference

6.8 *hbi00037:* Molekulardynamische Untersuchung der Stressbeanspruchungen auf Proteine an der Phasengrenzfläche beim Premix-Membranemulgieren

HLRN-Projektkennung:	hbi00037
Laufzeit:	I/2019 – II/2021
Projektleiter:	Prof. Dr.-Ing. habil. Udo Fritsching
Projektbearbeiter:	M.Sc. Patrick Giefer
Institut / Einrichtung:	Fachgebiet Mechanische Verfahrenstechnik, Universität Bremen

Überblick

Emulgierverfahren werden im Rahmen des Downstream-Prozessierens und der Weiterverarbeitung/Formulierung zur Homogenisierung oder auch Verkapselung in biogenen Produkten eingesetzt. Beim Premix-Emulgieren wird eine grobdisperse Voremulsion mittels der Dispergierung in porösen Membranen in eine Feinemulsion bzw. -dispersion überführt. Insbesondere das Stress-Verweilzeitverhalten und die darauf erfolgende Reaktion eines protein-stabilisierten dispersen Systems bedarf einer vertieften wissenschaftlichen Klärung. Hieraus können mechanistische Schädigungsmodelle abgeleitet werden. Die im Emulgier-Prozess auftretenden mikromechanischen Belastungen auf biologische Systeme sind nicht vollständig geklärt, die Prozessumgebung ist somit noch weiter zu entwickeln im Hinblick auf die Anpassung an spezielle biologische Systeme. Um den Einfluss des Premix-Emulgierverfahrens und der dabei auftretenden Stress-Verweilzeit-Belastungen auf die agglomerierten Proteine (hier β-Lactoglobulin) im Fluid und an den Phasengrenzflächen zu untersuchen, werden numerische Untersuchungen auf molekulardynamischer Ebene an Proteinstrukturen durchgeführt. Diese Untersuchungen zeigen, inwieweit die Proteinstrukturen durch den Emulgiervorgang belastet und geschädigt werden können, beziehungsweise ob eine proteinschonendere Emulgierung mit den Membranen möglich ist.

Das Projekt ist in dem DFG geförderten Schwerpunktprogramm 1934 „DISPBiotech“ eingebunden. Der Förderungszeitraum der zweiten Förderperiode beträgt 36 Monate.

Ergebnisse

Zielsetzung des vorhergegangenen Projektzeitraumes war die Untersuchung von hochdruckgeschädigtem Protein. Dazu wurde natives Lactoglobulin in Simulationen hochdruckgeschädigt. Die Ergebnisse werden nachfolgend dargestellt.

Eine Betrachtung von hochdruckgeschädigten Proteinen erweitert das Bild der molekulardynamischen Betrachtung stresssensitiver Proteine an Grenzflächen, da ein verändertes Adsorptionsverhalten durch die Schädigung zu erwarten ist. Dazu wurden MD Simulationen unter Hochdruck durchgeführt um die Struktur des Proteins zu schädigen und nachfolgend zu analysieren. Die unter Hochdruck simulierten Monomere zeigen im Vergleich zum Protein unter Normaldruck einen geringeren Streumasseradius. Dieser vergrößert sich im Verlauf der Simulation, was auf eine strukturelle Veränderung hinweist.

Bei der Betrachtung der Solvent Accessible Surface (Abb.1) wird deutlich, dass diese Vergrößerung des Streumasseradius auf eine Freilegung von hydrophilen, als auch hydrophoben Bereichen erfolgt. Zweiteres entspricht einer Penetration von Wasser in den hydrophoben Kern des Proteins (Abb.2). Auf Sekundärebene geht dies mit einer Veränderung

der Strukturelemente einher. Konkret steigt der Anteil von alpha Helix um 5%, intramolekulare beta sheets nehmen um 9% zu und random coils nehmen um 4% ab. Zur Validierung der Ergebnisse wurde Beta Lactoglobulin im Experiment hochdruckgeschädigt und die Sekundärstruktur mittels CD und FTIR Messungen ausgewertet. Der Anstieg der Helixstruktur und der Abfall der Coilstruktur ließen sich dabei bestätigen. Die Änderung der Helixstruktur ist dabei besonders interessant, da diese durch Hochdruck stabilisiert wird.

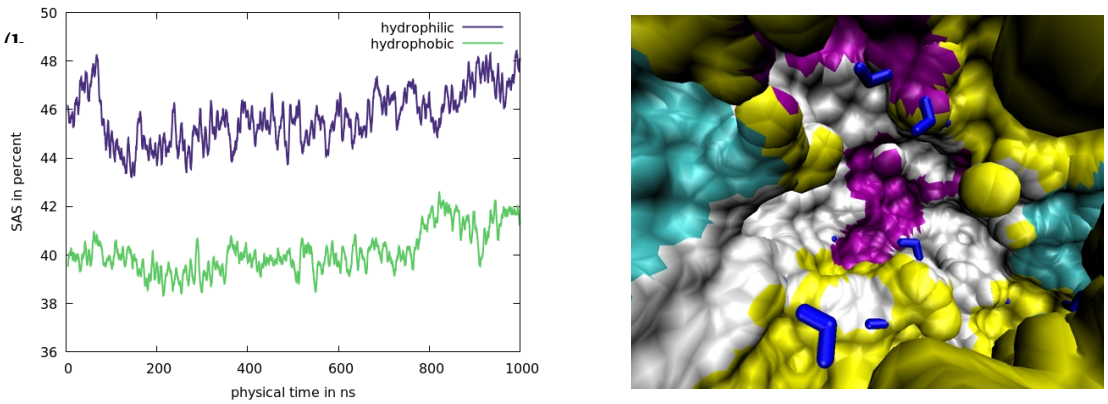

Abbildung 1: (a) Solvent Accessible Surface von hochdruckgeschädigtem Beta Lactoglobulin Monomer bei 600 MPA, Darstellung der hydrophilen und hydrophoben Bereiche, (b) Penetration von Wasser in den hydrophoben Kern des Proteins unter Hochdruck

Konträr lässt sich die Zunahme von intra beta sheets diskutieren, da diese im Experiment nicht nachgewiesen werden konnten. Im Zusammenhang mit der Öffnung des Dimer Interfaces (Abb. 2) und dem experimentell nachgewiesenen erhöhten Anteil von Dimeren lässt der Unterschied auf eine reversible Strukturänderung im Zuge der Dimerbildung vermuten. Zur Bestätigung dieser Hypothese wurden Dimere unter Hochdruck gebildet und auf Normaldruck entspannt. Die Entspannung auf Normaldruck entspricht dabei dem analytischen Vorgehen. Bei der Entspannung auf Normaldruck kann eine Abnahme der intra- und Zunahme der inter-beta sheets verzeichnet werden, was auf eine Stabilisierung der hochdruckgeschädigten Dimere über inter-beta sheets hinweist, sowie eine reversible Strukturänderung.

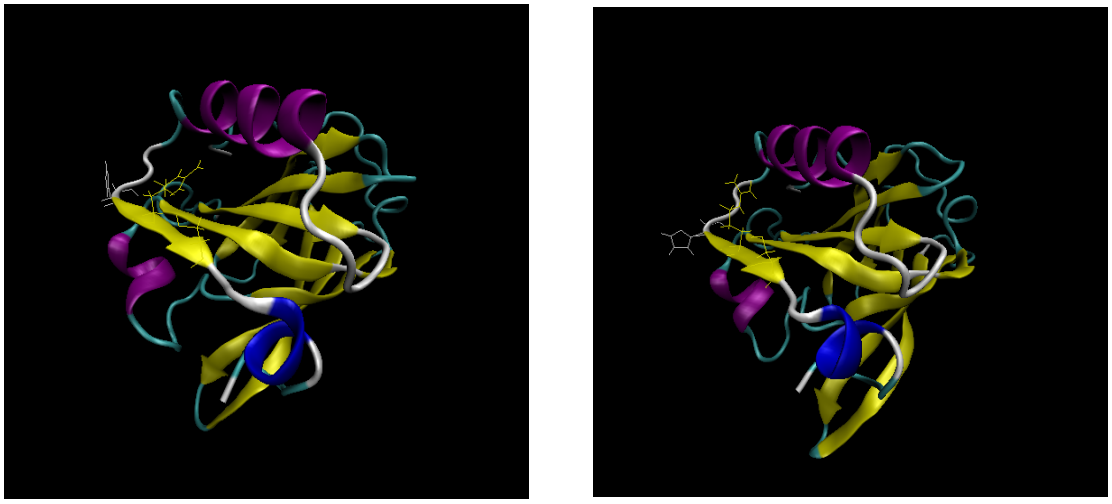

Abbildung 2: Darstellung der Öffnung von Teilen des Dimer Interfaces (Strichdarstellung) unter Hochdruck, links geschlossen und rechts geöffnet

Des Weiteren ist Abb. 3 zu entnehmen, dass die Freilegung von positiven und neutral geladenen Residuen an der Adsorptionsseite des Proteins zur erhöhten Adsorptionsaffinität führt, welche experimentell nachgewiesen werden konnte.

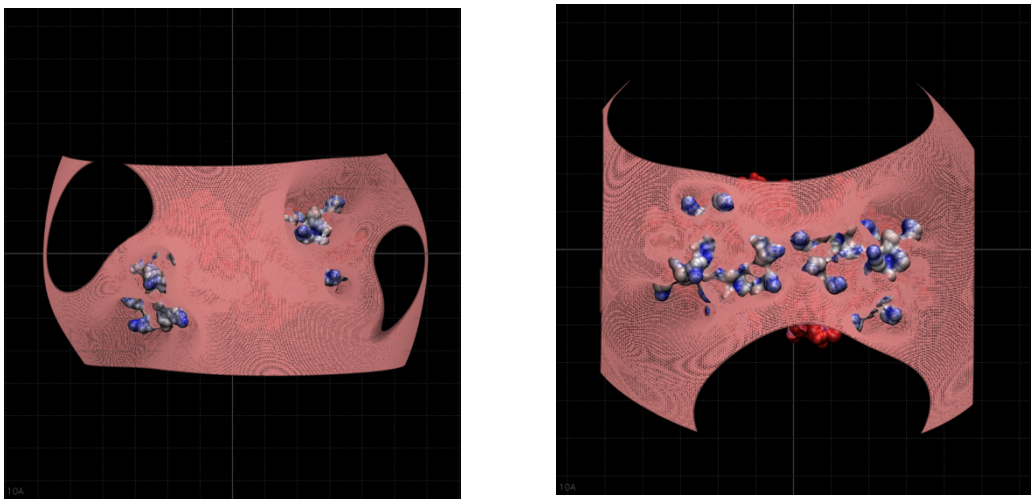

Abbildung 3: Darstellung des elektrostatischen Potentials von rot -5 eV bis blau +5 eV an der Oberfläche von beta Lactoglobuin Dimeren, Darstellung der isosurface bei -3eV, links ein ungeschädigtes Dimer und rechts ein hochdruckgeschädigtes Dimer

Die gezeigten Daten wurden in einer Veröffentlichung mit dem Titel „Structure and interfacial stabilization process of hydrostatic high pressure-treated β-lactoglobulin" (Schestkowa et al.) verschriftlicht und befinden sich derzeit im Review Prozess.

Ausblick

Um das Grenzflächenverhalten geschädigter Strukturen genauer zu charakterisieren, sind weitere Simulationen geplant, in denen die geschädigte Struktur an flüssige und feste Grenzflächen adsorbiert und geschädigt wird.

Darüber hinaus werden rekombinante β-Lactoglobulin Strukturen hinsichtlich ihrer Grenzflächenstabilisierung untersucht.

Vorträge / Poster

1. P. Giefer, Adsorption behaviour of high-pressure treated β-lactoglobulin at the oil/water-interface, Jahrestreffen der ProcessNet-Fachgruppen "Lebensmittelverfahrenstechnik, Mischvorgänge und Grenzflächenbestimmte Systeme und Prozesse", 11. März. 2021

6.9 *hbi00042:* Drag reduction by air retaining surfaces

HLRN Project ID:	hbi00042
Run time:	III/2019 – II/2020
Project Leader:	Prof. Dr. Albert Baars
Project Scientists:	Christoph Wilms
Affiliation:	Bionik-Innovations-Centrum, Hochschule Bremen

Overview

Superhydrophobic surfaces have the ability to retain air in their microstructure when submerged in water. The reduced contact area between water and solid as well as the lower viscosity of air in comparison to water can decrease viscous drag of such surfaces. Depending on Reynolds number, size, and shape of the surface structure, as well as the deformation of the water-gas interface drag reductions of 30 % and more have been reported by experiments and numerical simulations (Daniello et al. 2009, Seo et al. 2018). In this work, the drag reduction of such surfaces with one surface ratio liquid-gas interface to total surface (3/4) and different structure geometries (pillars, holes, grooves in stream- and spanwise direction), sizes ($79 < L^+ < 237$) have been investigated at Re_τ = 300 using direct numerical simulation (DNS). The results show an increase in DR with growing structure size and from grooves in spanwise direction, holes, pillars to grooves in streamwise direction. In the investigated parameter range the minimum and maximum DR amounts to 24.9 and 75.7 %, respectively.

Method

The effect of superhydrophobic surfaces is investigated in turbulent channel flow using DNS. The channel of height $2h^*$, length in streamwise $2\pi h^*$, and in spanwise direction πh^* contains fluid of constant density ρ^* and kinematic viscosity ν^*. The two walls of the channel are considered as flat. The liquid-gas interface is modelled by a slip condition and the tips of the structure with no-slip.

In the following, all lengths x_i^*, the time dependent velocity u_i^*, the averaged velocity $\langle u_i \rangle^*$, and the vorticity ω_i^* are presented in wall units.

$$x_i{}^+ = \frac{x_i^* u_\tau^*}{\nu^*} \quad ; \quad u_i{}^+ = \frac{\langle u_i \rangle^*}{u_\tau^*} \quad ; \quad \tilde{u}^+ = \frac{u_i^*}{u_\tau^*} \quad ; \quad \tilde{\omega}^+ = \frac{\omega^* h^*}{u_\tau^*}$$

The friction velocity $u_\tau^* = \sqrt{\tau_w^*/\rho^*}$ is obtained by a spatial and temporal average of the wall shear stress τ_w^*. Further dimensionless quantities are the Reynolds number, the friction Reynolds number, and the friction coefficient

$$Re = \frac{h^* u_b^*}{\nu^*} \quad ; \quad Re_\tau = \frac{h^* u_\tau^*}{\nu^*} \quad ; \quad c_f = \frac{\tau_w^*}{\frac{1}{2}\rho^* {u_b^*}^2} = 2\left(\frac{Re_\tau}{Re}\right)^2$$

with the bulk velocity u_b^*. The simulations are carried out at $Re_\tau = 300$. The drag reduction DR is calculated via the friction coefficient c_f and its reference c_{f0} (full no-slip condition)

$$DR = \frac{c_f - c_{f0}}{c_{f0}} = 1 - \left(\frac{u_{b0}^*}{u_b^*}\right)^2 .$$

The Navier Stokes equations are discretised second order in space (convective term: linear interpolation) and time (Crank-Nicolson) and solved numerically by OpenFOAM v6. The flow is upholded by a volume related force in streamwise direction. Cyclic boundary conditions are applied in stream- and spanwise direction. The number of grid cells amounts to 620 x 260 x 310. The grid spacing is in stream- and spanwise direction equal to $\Delta x^+ = \Delta z^+ = 3.04$, in wall

normal direction at the wall $\Delta {y_w}^+ = 0.37$ and in the channel centre $\Delta {y_c}^+ = 2.87$. The maximum Courant number is smaller one.

Results

The influence of geometry and size on drag reduction is shown in Figure 1. The reduction increases from grooves in spanwise direction, followed by holes, pillars and grooves in streamwise direction as well as with rising structure size. Generally, these findings are similar to the data reported by Seo et al. 2018. Deviations to literature can be explained by the different ratio of interface area (Seo et al. 2018: 8/9; own data: 3/4). With increasing structure size, the drag reduction tends towards that ratio. DR of grooves in streamwise direction slightly exceeds 3/4, which may be explained by local relaminarisation, as observed by Jung et al. 2016.

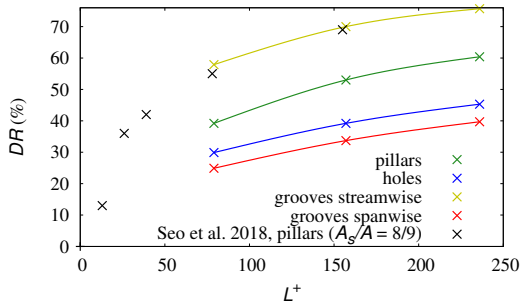

Figure 1: Drag reduction DR plotted over structure size L^+ for different structure geometries with a surface ratio of $A_s/A = 3/4$ in comparison to data of Seo et al. 2018.

To analyse this behaviour, the averaged velocity profiles for different structure geometries and sizes are depicted in Figure 2. Ablatively, all profiles show a similar progression, which seem to follow the universal law of the wall.

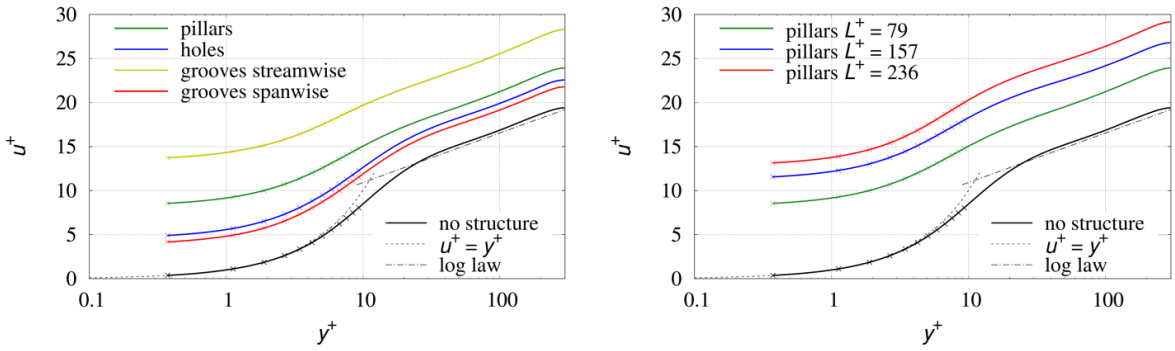

Figure 2: Averaged velocity u^+ plotted versus wall normal distance y^+ for different structure geometries at L^+= 79 (left) and structure sizes L^+ in case of pillars (right).

In comparison to the reference (full no-slip condition), differences for the cases with inhomogeneous boundary condition can be observed:

- upward shift of the of whole curves towards higher velocities
- expansion of the logarithmic domain towards the wall
- downwards shift of the logarithmic domain.

The first point can be described by the slip velocity ${u_S}^+$ and the latter by the shift velocity Δu^+ which also leads to an expansion of the logarithmic domain. Seo and Mani 2016 extended the logarithmic law by these two terms

$$u^+ = \frac{1}{\kappa} \ln y^+ + C^+ + {u_S}^+ - \Delta u^+.$$

The progressions of both quantities are displayed in Figure 3 for different structure geometries over size. Qualitatively, the curves of the slip velocity correspond to those of the DR. This is comprehensible because the bulk velocity increases with slip velocity and the drag reduction grows with bulk velocity. The shift velocity Δu^+ rises from grooves in spanwise direction and holes via pillars to grooves in streamwise direction, similar to the slip velocity. From this, one could conclude that there is a certain correlation between Δu^+ and the slip velocity. On the other hand, the progressions behave differently with structure size. An increase of Δu^+ leads to a reduction of bulk velocity and of drag reduction. In all cases and for one parameter constellation the values of Δu^+ are more than a factor two smaller in comparison to the slip velocity. This indicates, that the slip velocity dominates the drag reduction.

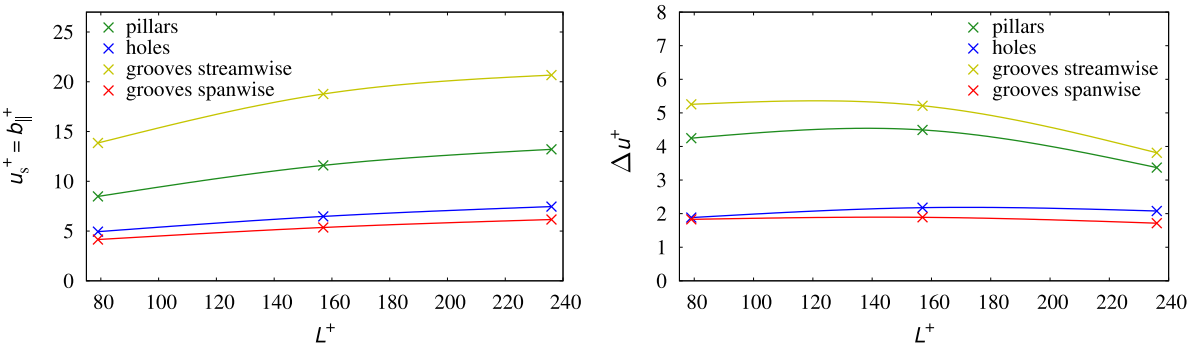

Figure 3: Slip velocity u_s^+ and shift velocity Δu^+ plotted versus structure size L^+ in wall units.

The effect of the surface structure on the slip velocity can be observed by the instantaneous velocity fields at the wall ($y^+ = 0$), see Figure 4. The main flow direction is from left to right. One can easily recognize the no-slip ($u^+ = 0$) and the slip ($|u^+| \geq 0$) areas. The slip velocity and drag reduction rise with increasing length of continuous slip areas in the mentioned direction. This gets apparent for the extreme cases of grooves in streamwise and spanwise direction. In the latter case fluid near the wall is accelerated and decelerated periodically.

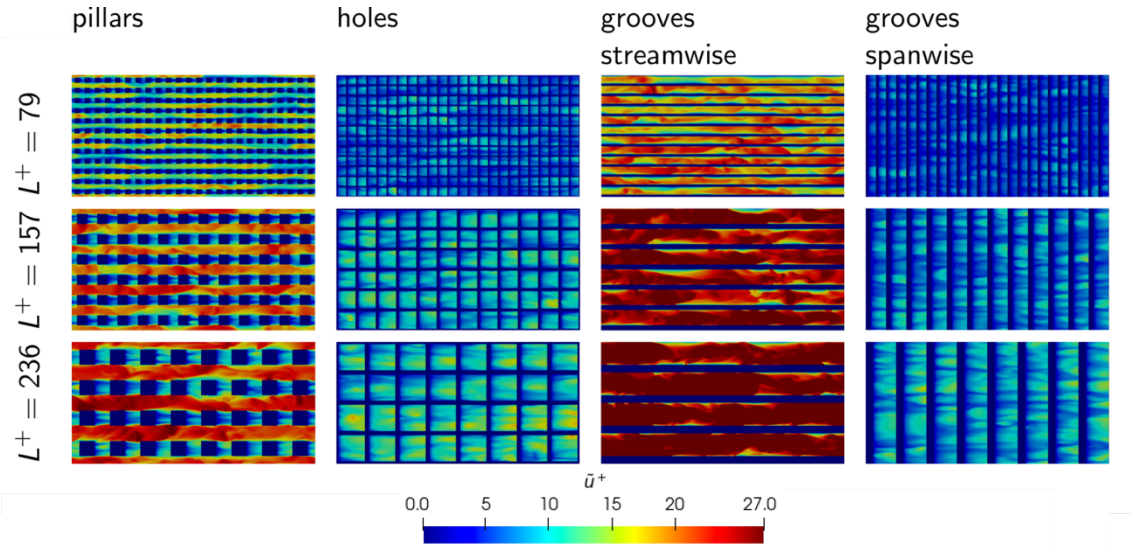

Figure 4: Instantaneous velocity field $\tilde{u}^+$ on the wall ($y^+ = 0$) for the investigated structure geometries and sizes L^+. The main flow direction is from left to right.

In Figure 5, the instantaneous flow topology near the wall is visualised by the Q-criterion, viewed from a wall normal perspective. The vortical structures exhibit a predominant orientation in streamwise direction. Generally, this is known from literature for wall bounded turbulent flows with (Jelly et al. 2014, Im and Lee 2017) and without (Jelly et al. 2014) surface

modifications. Bigger structure sizes and especially grooves in streamwise direction reveal a higher concentration of vortical structures above the no-slip areas, which can be explained by higher velocity gradients which contribute to turbulence production. A similar manner holds for pillars. Grooves in spanwise direction and holes do not allow a clear distinction between those areas presumable due to the periodically changes of the boundary condition.

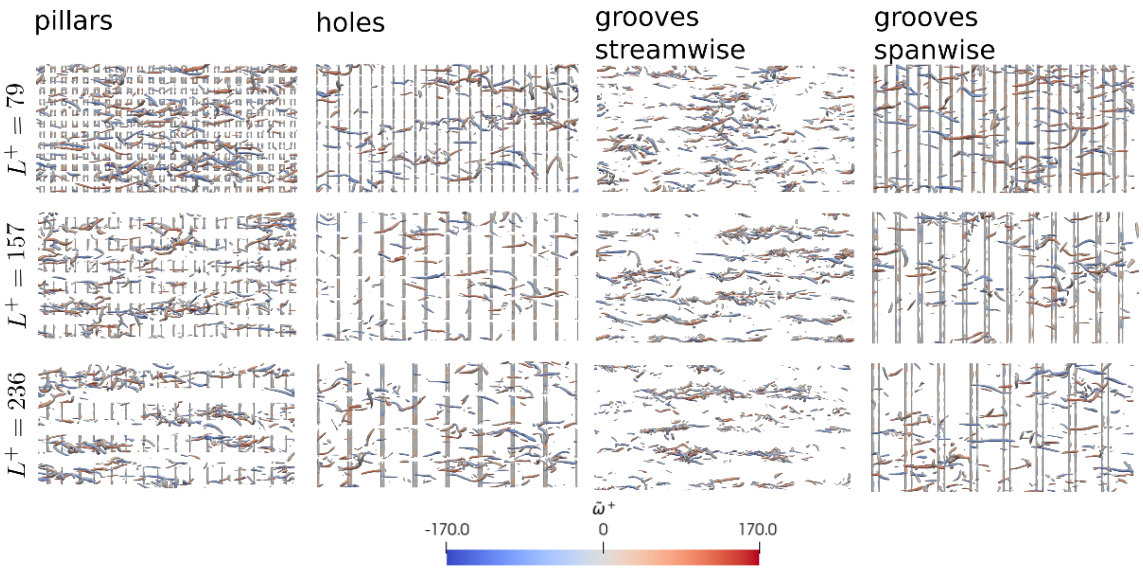

Figure 5: Visualised instantaneous flow topology by isosurfaces of the Q-criterion for all investigated structure geometries and sizes L^+. The isosurfaces are coloured by the vorticity component in main flow direction, which runs from left to right.

Outlook

Currently, simulations are conducted with Nek5000, a higher-order spectral element code. Here, a higher spatial resolution and higher order discretisation of the Navier-Stokes equations are applied to smaller structure sizes.

References

1. Daniello, R. J., Waterhouse, N. E. and Rothstein, J. P. (2009). “Drag reduction in turbulent flows over superhydrophobic surfaces”. Physics of Fluids 21(8): 085103.
2. Im, H. J. and J. H. Lee (2017). “Comparison of superhydrophobic drag reduction between turbulent pipe and channel flows.” Physics of Fluids 29(9): 095101.
3. Jelly, T.O., S. Y. Jung and T. A. Zaki (2014). “Turbulence and skin friction modification in channel flow with streamwise-aligned superhydrophobic surface texture.” Physics of Fluids 26(9): 095102.
4. Jung, T., H. Choia and J. Kim (2016). “Effects of the air layer of an idealized superhydrophobic surface on the slip length and skin-friction drag.” Journal of Fluid Mechanics 790: R1.
5. Seo, J., R. García-Mayoral and A. Mani (2018). “Turbulent flows over superhydrophobic surfaces: Flow-induced capillary waves, and robustness of air-water interfaces.” Journal of Fluid Mechanics 835: 45-85.
6. Seo, J. and A. Mani (2016). “On the scaling of the slip velocity in turbulent flows over superhydrophobic surfaces.” Physics of Fluids 28: 025110.

The AIRCOAT project has received funding from the European Union’s Horizon 2020 research and innovation programme under grant agreement N° 764553.

6.10 *hbi00043:* Direct Numerical Simulation and Modeling of Turbulent Convection in Porous Media

HLRN Project ID:	hbi00043 (former hbi00038)
Run time:	I/2020 – IV/2020
Project Leader:	Dr. Yan Jin
Project Scientists:	Stefan Gasow
Affiliation:	Center of Applied Space Technology and Microgravity (ZARM), University Bremen

Overview

A porous medium is a material containing a porous matrix and pores. The porous matrix is usually solid while the pores are filled with a fluid (liquid or gas). A wide range of materials falls to porous media under this definition, e.g. fractured rocks, wood, sand or body tissue. Porous media like materials have been widely used in heat and mass transfer applications since their high surface area to volume ratio may significantly enhance heat and mass transfer.

Design and optimization of these engineering applications require accurate simulation of convection in porous media. Porous medium convection was traditionally calculated by solving the macroscopic equations. However, the physics of it is still not clear. Significant simplifications and strong assumptions have been made in these macroscopic equations. For example, the turbulent momentum and thermal dispersion terms were often neglected. In addition, there are still contradictory views on whether there is macroscopic turbulence in porous media.

As a result, numerical simulation results sometimes have considerable model errors. More efforts are required to develop more accurate macroscopic models. The main purpose of the proposed project is to better understand the physics of porous medium convection. Microscopic direct numerical simulation (MIC-DNS) methods, in which the detailed flows within the porous elements will be considered, will be used in the study. Particular attentions will be paid to natural convection problems due to their significance in emerging industries like the long-term storage of CO_2 in deep saline aquifers. Through our understanding of physics, a more accurate macroscopic model for calculating porous medium convection should be developed. The developed model will be validated with our DNS results.

Results

In our previous HLRN project hbi00038, we simulated the 2-dimensional transient natural convection for a mass transfer problem in a porous media in the high Rayleigh-Darcy regime with a MIC-DNS method to analyse the physics of turbulent natural convection in porous media. In this HLRN project hbi00043 we used the results of hbi00038 and carried out more MIC-DNS studies to develop an improved macroscopic model for natural convection in porous media.

Natural convection in porous media is a fundamental process for the long-term storage of CO_2 in deep saline aquifers. Typically, details of mass transfer in porous media are inferred from the numerical solution of the volume-averaged Darcy-Oberbeck-Boussinesq (DOB) equations, even though these equations do not account for the microscopic properties of a porous medium. According to the DOB equations, natural convection in a porous medium is uniquely determined by the Rayleigh number. However, in contrast with experiments, DOB simulations

yield a linear scaling of the Sherwood number with the Rayleigh number (Ra) for high values of Ra (Ra>>1,300). Here, we perform Direct Numerical Simulations (DNS), fully resolving the flow field within the pores, see Fig. 1 for the porous matrices used in our DNS.

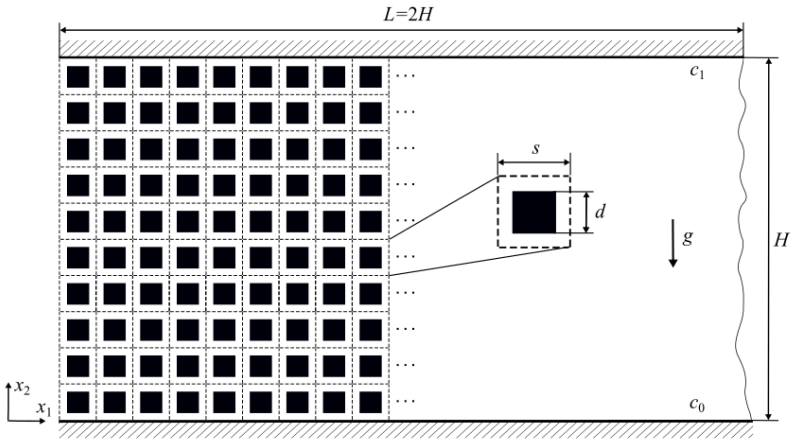

Figure 1: The 2-dimensional generic porous matrix for simulating natural convection (mass transfer) in a porous medium. A constant species concentration difference at the top and bottom walls, periodic boundary conditions in the horizontal direction and adiabatic obstacles are utilized.

Our MIC-DNS results show that, besides the macroscopic length scale which is the distance between the bounding walls, the pore-scale geometry has also significant effects on natural convection in porous media, which is not accounted for by the DOB equations.

Based on our physical findings, we have developed a new macroscopic model for natural convection in porous media, which is taking also the pore scale into account. Whereby a paper ("A macroscopic two-length-scale model for natural convection in porous media driven by a species-concentration gradient") has been already submitted for publication to a journal.

Further MIC-DNS studies have been carried out to validate the new assumptions of our model, whereby the physics of natural convection in porous media can be well modelled by our new proposed macroscopic model. Which can be for example seen in Fig. 2, where the local Reynolds number (Re_K) of the MIC-DNS results is compared to the results of the new macroscopic model. It can be seen that the flow structures predicted by the macroscopic model accurately fits the flow structures of the MIC-DNS results.

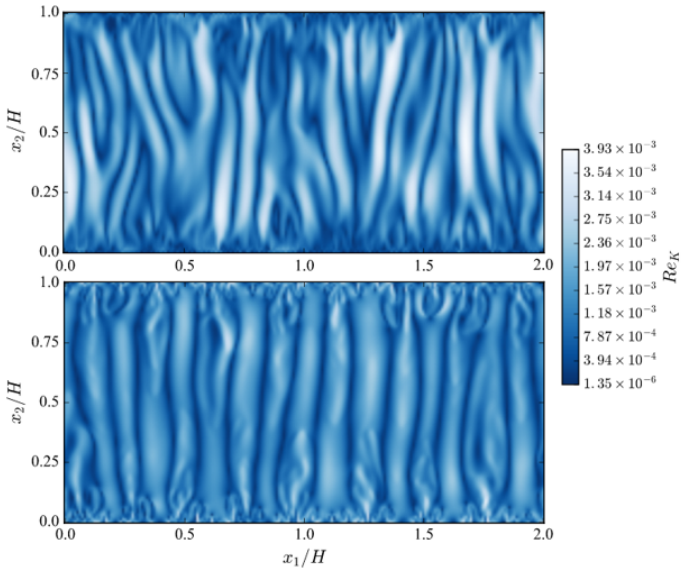

Figure 2: Instantaneous volume averaged Reynolds number Re_K, H/s=100, s/d=1.5, (ϕ=0.56), Ra=20000, and Sc=250. Upper: MIC-DNS results, lower: macroscopic model results.

The results of our model are validated extensively by comparison with the DNS as well as the DOB results. The comparison shows that the new macroscopic model predicts a much more accurate Sherwood number, than the DOB simulation. Which can be seen in Fig. 3.

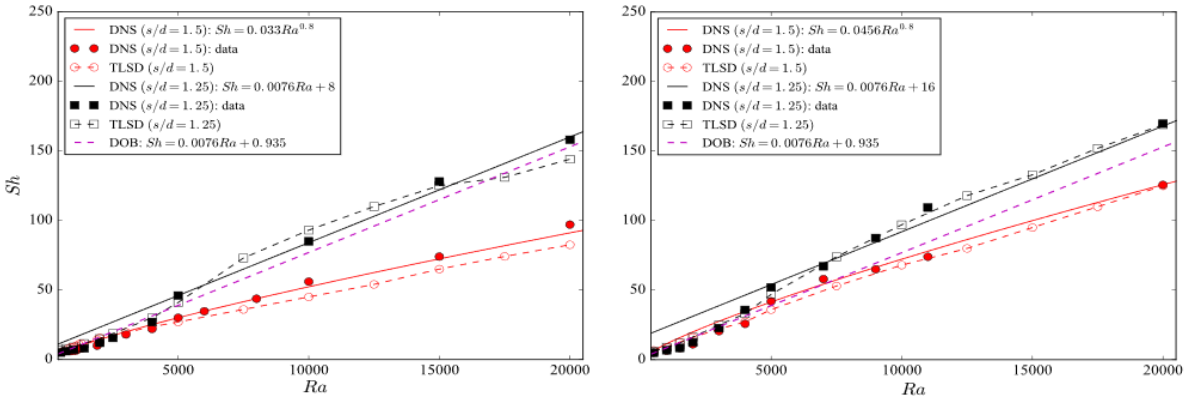

Figure 3: Sherwood number versus the Rayleigh number with Ra in the range 500-20000 and H/s=20 for left: Sc=1, right: Sc=250.

As it can be seen in Fig. 3, the new model results show that the Sh=f(Ra) scaling changes from a linear scaling to a non-linear scaling as the porosity increases (the s/d ratio increases from 1.25 to 1.5). If the Rayleigh number is fixed, the Sherwood number increases with the increase of the Schmidt number and the decrease of the porosity. These trends agree with the previously described MIC-DNS results, while they cannot be captured by the DOB simulations. Hence the current macroscopic model is preferable due to its small model error and simplicity.

Outlook

We are currently investigating the ultra high Rayleigh Darcy Regime (Ra>20000) and trying as well to extand our macroscopic model to be applicable for conjugate heat transfer.

Publications

1. S. Gasow, Z. Lin, H. C. Zhang, A.V. Kuznetsov, M. Avila, Y. Jin, *Effects of pore scale on the macroscopic properties of natural convection in porous media*, Journal of Fluid Mechanics, 891, A25-1-22 (2020)

6.11 *hbi00045:* Multifunktionale äußere Steuerfläche

HLRN-Projektkennung:	hbi00045
Laufzeit:	III/2020 – II/2021
Projektleiter:	Prof. Dr. Christof Büskens
Projektbearbeiter:	M. Sc. Matthias Otten
Institut / Einrichtung:	Zentrum für Technomathematik, Universität Bremen

Überblick

Um die Potentiale neuer Technologien für einen noch sichereren, umweltfreundlicheren und wirtschaftlicheren Luftverkehr zu identifizieren, deren Einführung zu beschleunigen und um technologische Risiken zu reduzieren, sind die Entwurfs-, Entwicklungs-, Test-, Herstellungs- und Produktionsprozesse zukünftig weitaus stärker zu virtualisieren. Die beispielhafte Anwendung der multifunktionalen Steuerfläche eines Flugzeugs ist als Bremer „Know-How“ hervorragend geeignet, um existierende industrielle Konzepte mit den Fähigkeiten der Großforschung zu Aerodynamik, Lasten und Struktur sowie Systemen mit Ideen zum virtuellen Testen und zur Berücksichtigung von Fertigungs- und Montageaspekten zu verbinden und in einem Simulationsprozess zu demonstrieren. Dies geschieht im Startprojekt des Virtual Product House (VPH), eines Integrationsplateaus des Deutschen Zentrums für Luft- und Raumfahrt, zusammen mit industriellen Partnern und anderen Forschungseinrichtungen. Die Hochauftriebsaerodynamik ist ein wichtiger Aspekt des VPH und es ist essentiell, die auftretenden physikalischen Phänomene basierend auf hochaufgelösten Rechengittern durch die Anwendung der drei-dimensionalen Reynolds-gemittelten Navier-Stokes (RANS) Gleichungen zu erfassen. Nur dadurch kann eine genaue Vorhersage der Leistungsfähigkeit des Flugzeugs im Start- und Landefall gewährleistet oder auch ein Flugversuch digital abgebildet werden. Für die Bestimmung der aerodynamischen Flugeigenschaften und Lasten wird der vom DLR entwickelte TAU-Code verwendet und vom Zentrum für Technomathematik auf dem HLRN eingerichtet. Ferner wird zur Bereitstellung der Lastenberechnung im Gesamtprozess eine Schnittstelle zur Hochauftriebsaerodynamik aufgebaut. Die berechneten Kennwerte sind für den Gesamtentwurf besonders relevant, denn je genauer die Vorhersage der am realen Flugzeug auftretenden Lasten ist, desto kleiner sind die Unsicherheiten der davon abgeleiteten Auslegungsprozesse. Die Minimierung dieser Unsicherheiten ist essentiell für die spätere Bewertung des Gesamtentwurfs und kann über den Erfolg und die weitere Umsetzung eines Flugzeugentwurfs entscheiden.

Beschleunigte Entwicklungszyklen und Minimierung der Unsicherheiten im Entwurf können neuen Technologien, unter Berücksichtigung der hohen Ansprüche an die Sicherheit in der Luftfahrt, schneller zur Integration verhelfen. Dieses Ziel wird aber nur dann erreicht, wenn die im Projekt gewonnen Daten den Anforderungen der Behörden entsprechen und das Vorgehen eng mit der Industrie abgestimmt ist.

Ergebnisse

Zielsetzung in den Quartalen Q3 und Q4 2020 war es, die Lasten für die aktuellen Konfigurationen der Steuerfläche zur Verifikation des Prozesses und der Bestimmung von Unsicherheiten zu berechnen. Hierbei mussten für jede Prozess-Iteration mindestens drei Manöver beziehungsweise drei Lastfälle berechnet werden: die Reiseflugkonfiguration bei einem -1G und einem +2.5G Manöver sowie eine Hochauftriebskonfiguration bei einem 2G-Abfangmanöver.

Dazu wurde die kompressible drei-dimensionale RANS-Gleichung mit einem Finite-Volumen Ansatz [1] für bis zu 120 Millionen Gitterpunkte gelöst. Das größte Rechengitter wird für die Hochauftriebskonfiguration wegen der höheren geometrischen Komplexität benötigt. Zur Steigerung der Effizienz wurden ein lokales Zeitschrittverfahren und Mehrgitterverfahren verwendet.

Nur Dank der Bereitstellung von Rechenkapazität durch den HLRN konnten die aerodynamischen Simulationen zertifizierungsrelevanter Lastfälle auf repräsentativen Rechengittern durchgeführt werden.

Abbildung 1 zeigt dazu ein exemplarisches Ergebnis für die Hochauftriebskonfiguration während des Landeanflugs.

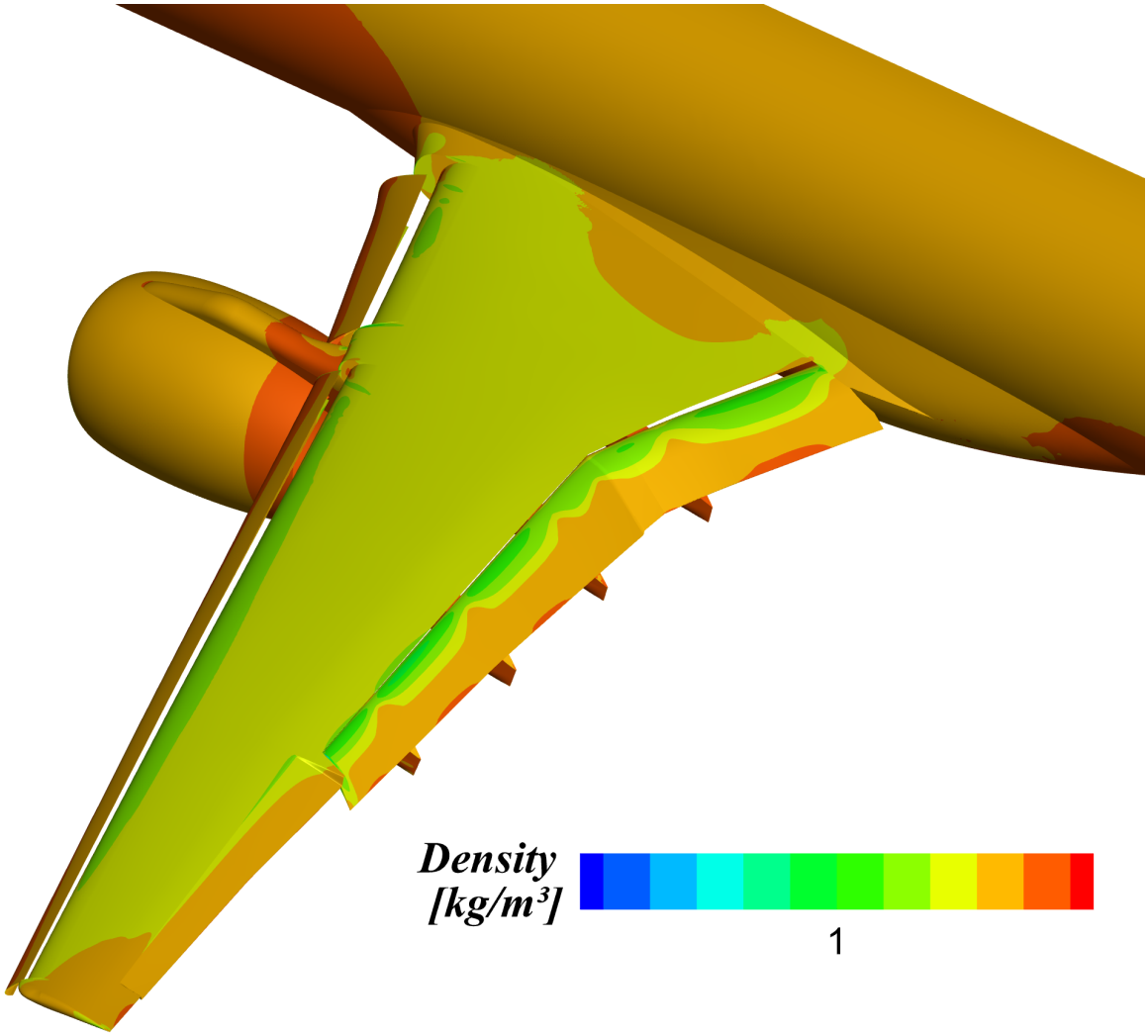

Abbildung 1: Aerodynamische Lasten in der Hochauftriebskonfiguration während eines Landeanflugs

Ausblick

Durch den Entwurf einer neuen Hochauftriebskonfiguration soll die Flexibilität des gesamten Prozesses demonstriert werden. Hierfür sind neben den genannten Lastfällen Rechnungen zum Nachweis der Flugeigenschaften notwendig. Folglich müssen alle relevanten Hochauftriebskonfigurationen für Start und Landung bis zum Strömungsabriss simuliert werden. Nur so ist eine aussagekräftige und vollständige Bewertung der Start- und

Landeleistung mit Hilfe von hoch-genauen Methoden möglich als essentieller Bestandteil des Gesamtflugzeugentwurfs.

Ferner sollen parallel zu diesen Arbeiten weitere Berechnungen der bestehenden Konfiguration zur Berücksichtigung von Unsicherheiten in den Referenzbedingungen, wie beispielsweise Flughöhe oder Geschwindigkeit, durchgeführt werden.

Quellen

[1] Schwamborn, D., Gerhold, T., Heinrich, R.: The DLR TAU-Code: Recent Applications in Research and Industry, ECCOMAS CFD (2006).

6.12 *hbi00046:* Investigations of Defects and Luminescent Origins in Zinc Sulfide and Doped Zinc Sulfide Materials utilizing Optimized Hybrid Functionals

HLRN Project ID:	hbi00046
Run time:	III/2020 – II/2021
Project Leader:	Dr. Martin Castillo, Dr. Quoc Duy Ho
Project Scientists:	Dr. Martin Castillo, Dr. Quoc Duy Ho
Affiliation:	University of Bremen, Center of Applied Space Technology and Microgravity (ZARM)

Overview

Screens and displays consume tremendous amounts of power. Global trends to significantly consume less power and increase battery life have led to the reinvestigation of electroluminescent materials for usage in screens and displays. The work herein aims at improving the energy efficiency of electroluminescent zinc sulfide (ZnS) doped materials that were synthesized in microgravity. The state of the art in ZnS materials has not been furthered in the past 30 years and there is much potential in improving electroluminescent properties of these materials with advanced processing techniques and numerical analysis.

These new advanced zinc sulfide doped materials are synthesized with a new process involving a rapid exothermic process involving high energy and nonlinearity coupled with a high cooling rate to produce materials formed outside of normal equilibrium boundaries (under patent). The elimination of gravity during this process allows capillary forces to dominate mixing of the reactants, which results in a superior and enhanced homogeneity in the produced materials. ZnS and ZnS doped materials are synthesized at the Center of Applied Space Technology and Microgravity (Zentrum für angewandte Raumfahrttechnologie und Mikrogravitation, ZARM) drop tower. Utilizing this process with ZnS doped with Cu, Mn, Er, or Pr leads to electroluminescence (EL). Furthermore, a plasmon enhancement will be applied to this material to yield an even greater improvement in the efficiency of electroluminescence.

This HLRN project aims at understanding and improving the energy efficiency of these synthesized electroluminescent zinc sulfide (ZnS) doped materials. Unfortunately, characterization of these synthesized materials alone is insufficient for the identification of specific defects and in the explanation of electroluminescent origins in semiconductor materials. It is necessary to perform theoretical analysis parallel with the characterization of the synthesized materials in order to identify intrinsic and extrinsic defects. The operation of semiconductors-based devices is related to defects, which control electronic and optical behaviors. The commonly used approximation, density functional theory (DFT) with local density approximation (LDA) or generalized gradient approximation (GGA) exchange, often fail completely in describing defects in wide band gap semiconductors. In recent years, screened hybrid functionals (like HSE06) have emerged as a useful alternative. This project will deal with the refinement, extension and application of the HSE-type functionals for defects in the sphalerite and wurtzite structures of ZnS. We will study charge transition levels, hyperfine interaction, and luminescent origins in ZnS with the goal of explaining origins and improving electroluminescent ZnS-based devices thus making this a highly energy efficient material.

Current Results

The 100 kNPL allocated for this project was extremely useful to begin calculations and was highly appreciated. With this amount of calculation time, we have optimized the HSE-parameters for the sphalerite phase of ZnS. This result is shown in Figure 1 where the entire band structure for the sphalerite structure of ZnS is calculated from the optimized hybrid functional. The calculated band gap at the gamma point is 3.49 eV and the measured band gap from Fang et al. ranged from 3.68 - 3.70 eV [1]. This result agrees very well to the GW results [2] as well as the total energy from a Zn defect vacancy resulting in a linear function of the fractional occupation numbers.

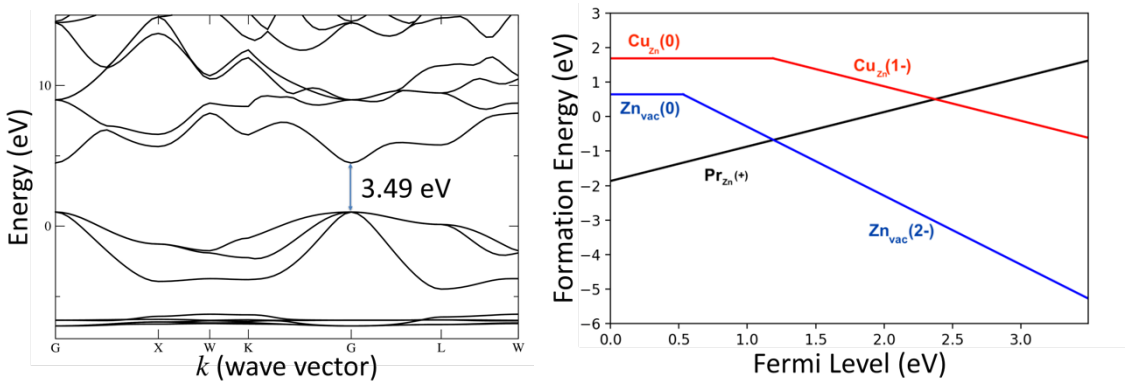

Figure 1: The calculated band structure from the optimized the HSE-parameters for the sphalerite phase of ZnS is shown in (a). The graph of the formation energy of Cu and Pr doped into a Zn vacancy in the Sphalerite phase of ZnS is shown in (b).

After obtaining the optimized hybrid functional, we have used this to study Cu and Pr atoms substituted at Zn sites (Cu_{Zn}, Pr_{Zn}). We have also evaluated Zn vacancies (Zn_{vac}) in ZnS. The formation energies of Cu-, Pr-doped, and Zn vacancies are shown as in Figure 1b.). Pr_{Zn} is a shallow donor thus it contributes to the electronic carrier concentration of ZnS as shown in Figure 1b. The other defects Cu_{Zn} and Zn_{Vac} are deep acceptors. Thus, they are not effective p-type defects as they act as electron trap centers in ZnS.

Outlook

HSE-type functionals for ZnS semiconductors.

Technology development in these areas requires knowledge of formation and properties of defects that can drastically change the performance of devices. Electronic structure calculations based on density functional theory (DFT) play a very important role in the understanding material structure and defects. Unfortunately, the standard local density (LDA) and semi-local generalized gradient approximation of the electron self-interaction involved with the approximations of DFT is a general problem. Notably, the energy minimization for defects leads to incorrect geometry and to false occupation of the defect levels. Unfortunately a combined approach with geometry relaxation with a GGA functional and a single-point approaching with HSE or GW will not yield the correct results. First principle total energy calculations beyond the standard DFT approximations will yield appropriate results but are very calculation intensive [3]. Due to these reasons, semi-empirical hybrid functionals are currently used in semiconductors. The hybrid functional HSE06 (0.25,0.20) are generally used in semiconductor calculations and yields the best results of band gap for many semiconductors. However, the value chosen in HSE06 works well only with a medium-size gap (and medium screening). With a few exceptions, it does not work well in ionic insulators (week screening) and metals (strong screening) [4,5]. The screening parameter (μ) plays a very important role in the success of HSE-type functionals [4,6]. However, when the standard

HSE06 underestimates the band gap, only α is often tuned and the role of the screening parameter is neglected. In doing so, the issue of the localization of defect states are not usually considered. Even though, there have been several theoretical calculations of ZnS [7,8], HSE is used without checking the gKT fulfillment that can lead to incorrect charge state levels and localization of defects. It is necessary to develop optimal parameters for each phase of ZnS as we have performed in this body of work.

For the determination of the appropriate gKT, we will check the vertical charge transition level of a sulfur (S) vacancy between the neutral and +1 charge state. The process for this is to first relax the atomic position of the neutral S vacancy with HSE(0.3,0.2) and a +1 charge state will then be calculated with this fixed geometry from the 0 charge state. Then we must compare the occupied Kohn-Sham (KS) level of the highest occupied molecular orbital (HOMO) for the 0 charge state defect with the lowest unoccupied molecular orbital (LUMO) KS level of the +1 charge state. Then we must finally determine the total energy after the charge correction which is the difference between 0 and +1 charge state with the same geometry. The exact functional will give the same value for HOMO, LUMO, and the total energy difference. The gKT fulfillment will be shown by total energy as a linear function of occupation numbers and total energies will be calculated with different charge state (0.00, +0.25, +0.50, +0.75, +1.00). Again, we have found the optimized parameters for sphalerite phase of ZnS and the optimization wurtzite ZnS has begun.

After obtaining the optimized parameters, the equilibrium geometry of the primitive unit cells will be determined. We will then relax the atomic position with at least 5 different constant volume. After this, the Murnaghan equation of state will be used to fit energies. The band structure will be calculated at equilibrium geometry with 6x6x6 and 4x4x4 Monkhorst-Pack sets for both of sphalerite and wurtzite, respectively.

Like other researchers in the field of defect calculations, we use the supercell model for all defect calculations. We will then apply the same size of supercell, 64 atoms for sphalerite and 128 atoms for wurtzite, which are equal or larger than the supercells were used in the previous research [6,7]. The next symmetric multiplication, one would use 216 atoms for sphalerite and 300 atoms for wurtzite. It should be noted that we would use 216 atoms, as this is unnecessary and would drastically lead to over usage of computational time for hybrid functional calculations. The case of the Coulomb interaction between charged defects cannot be neglected at any realistic supercell size. Therefore, the artificial interaction of charge defects should be considered by applying a charge correction method. In our calculations, we use the scheme of Freysoldt et al. [9] to compensate the spurious periodic Coulomb interaction of charged defects.

We have begun this work with the optimization of the HSE-type Hybrid Functional for sphalerite ZnS. We ran defects calculations with the obtained optimized hybrid functional, implemented in the VASP package. We have performed the calculations of copper substitutions at the zinc site in sphalerite phase and sulfide vacancy in the wurtzite phase. From these calculations we found that a full self-consistent field (SCF) cycle takes around ~40 steps, a defect geometry optimization usually reaches the convergence conditions after ~50 SCF. This is again a demonstration that this methodology can be performed without over consuming wasteful amounts of computational time and highly important in this new body of work.

Identification of defects in ZnS for determination the electrical activity

Copper, aluminum, and chlorine are often observed in ZnS as dopants and/or unintentional impurities [10-12]. Recently in theoretical research, a number of reports about intrinsic and extrinsic defects have been published, but information about the defects in ZnS are still very limited or missing. For example, the origin of luminescence of Cu-doped sample at around 2.76 eV is often assigned to Cu at Zn site [13,14]. However, other studies show that an intrinsic defect or a complex one can be the source of that radiation [10,15]. That has shown the

complication of a luminescent origin identification procedure. To identify a source of luminescence, a stable defect should be identified at a specific Fermi-level. Generally in semiconductor materials, multiple defects (intrinsic extrinsic and complex) can be present at the fermi-level. Therefore many possible defects should be studied to find out the origin of luminescence. The procedure has been shown in a previous report of Quoc Duy Ho et al. [14]. In the first part of this procedure, Zn, S vacancies, Zn_{vac} + S_{vac} complex vacancy, Zn, S interstitial, Zn at S site, and S at Zn site will be studied. In the next step, we will consider extrinsic defects such as Mn, Pr (for wurtzite), Er, Eu, Al, Fe, Cl, O, C, H, as well as the complex of defects. In each case, the equilibrium geometry of defect must be found in all possible charge states. The relative charge transition levels of defect will be calculated and compared to the experimental results.

Identification paramagnetic resonance (EPR) centers

The identification of paramagnetic resonance (EPR) centers is very important in our project as the calculated results can be compared directly with the experimental results. This method has been previously demonstrated by the author for β-Ga2O3 [17,18]. The hyperfine interaction is very sensitive to the localization of a defect and the defect distance to neighboring atoms. The calculated results from an optimized HSE for β-Ga2O3 has shown very good agreement to experimental results [17,18]. The hyperfine tensor that describes the interactions between a nuclear spin and the electronic spin distribution consists of the isotropic Fermi-contact and anisotropic dipolar term. The Fermi-contact requires calculating the spin density at the nuclear sites that carry a nuclear spin. This interaction occurs on an electron that is inside the nucleus, where electrons in the s orbital exhibit this kind of interaction. After a paramagnetic defect state has been relaxed, the hyperfine tensor will be calculated with the electron spin density from the previous calculation.

Presentations

M. Castillo, D. Ho, 2diZplays Project Update, DLR FuW Symposium 2020, Bonn, Germany, 04.03.2020.

M. Castillo, D. Ho, Investigations of Advanced Electroluminescence Materials Synthesized in Microgravity, University of Bremen MAPEX SpaceMat 2020, online conference, 08.31.20-09.02.20.

M. Castillo, D. Ho, Investigations of Electroluminescence of Zinc Sulfide and Doped Zinc Sulfide Materials Synthesized in Microgravity, COSPAR, G0.2 Drop Tower Days, online conference, 30.01.21.

References

[1] X. Fang, T. Zhai, U. K. Gautam, L. Li, L. Wu, Y. Bando, D. Golberg Progress in Materials Science 56 175–287 (2011)
[2] P. Rinke, A. Qteish, J. Neugebauer, C. Freysoldt, and M. Scheffler, New Journal of Physics 7, 126 (2005).
[3] P. Liu, M. Kaltak, J. Klimeš, and G. Kresse, Physical Review B 94, 165109 (2016).
[4] M. Marsman, J. Paier, A. Stroppa, and G. Kresse, Journal of Physics: Condensed Matter 20, 064201 (2008).
[5] J. Paier, M. Marsman, K. Hummer, G. Kresse, I. C. Gerber, and J. G. Ángyán, The Journal of Chemical Physics 124, 154709 (2006).
[6] F. Fuchs, J. Furthmüller, F. Bechstedt, M. Shishkin, and G. Kresse, Physical Review B 76, 115109 (2007).
[7] K. Hoang, C. Latouche, and S. Jobic, Computational Materials Science 163, 63 (2019).
[8] J. B. Varley and V. Lordi, Applied Physics Letters 103, 102103 (2013).

[9] C. Freysoldt, J. Neugebauer, and C. G. Van deWalle, Phys. Rev. Lett. 102, 016402 (2009).
[10] C. Corrado, Y. Jiang, F. Oba, M. Kozina, F. Bridges, and J. Z. Zhang, The Journal of Physical Chemistry A 113, 3830 (2009).
[11] S. Sambasivam, B. Sathyaseelan, D. Raja Reddy, B. K. Reddy, and C. K. Jayasankar, Spectrochimica Acta Part A: Molecular and Biomolecular Spectroscopy 71, 1503 (2008).
[12] A. A. Bol, J. Ferwerda, J. A. Bergwerff, and A. Meijerink, Journal of Luminescence 99, 325 (2002).
[13] S. Ummartyotin, N. Bunnak, J. Juntaro, M. Sain, and H. Manuspiya, Solid State Sciences 14, 299 (2012).
[14] S. J. Xu, S. J. Chua, B. Liu, L. M. Gan, C. H. Chew, and G. Q. Xu, Applied Physics Letters 73, 478 (1998).
[15] J. Dong, X. Zeng, W. Xia, X. Zhang, M. Zhou, and C. Wang, RSC Advances 7, 20874 (2017).
[16] Q. D. Ho, T. Frauenheim, and P. Deák, Physical Review B 97, 115163 (2018).
[17] N. T. Son, Q. D. Ho, K. Goto, H. Abe, T. Ohshima, B. Monemar, Y. Kumagai, T. Frauenheim, and P. Deák, Applied Physics Letters 117, 032101 (2020).
[18] Q. D. Ho, T. Frauenheim, and P. Deák, Journal of Applied Physics 124, 145702 (2018).

6.13 *hbi00048:* Parameter Extension Simulation (PES) and Large Scale Motion Simulation (LSMS) of turbulent flows

HLRN Project ID:	hbi00048
Run time:	III/2020 - II/2021
Project Leader:	Dr. Yan Jin
Project Scientists:	Dr. Yan Jin
Affiliation:	Center of Applied Space Technology and Microgravity (ZARM), University of Bremen

Overview

Turbulent flows are fluid motions that are characterized by transient and almost chaotic changes in pressure and flow velocity. They are usually accompanied by three-dimensional and transient velocities, a large range of time and length scales, and nonlinear pressure gradients. Turbulent flows are often observed in everyday surroundings and are prevalent in industry processes. Many intensive studies have been performed over the last century to predict turbulent flows. However, turbulence is a highly complex process, and the physics of turbulence remains incompletely understood. For this reason, the prediction of turbulent flows is extremely difficult.

The most often used set of computational fluid dynamics (CFD) approaches for solving turbulent flows include direct numerical simulation (DNS), Reynolds-averaged Navier–Stokes equation simulation (RANS), large-eddy simulation (LES), scale-adaptive simulation (SAS), and detached-eddy simulation (DES).

DNS is the most accurate CFD approach, but it is rarely employed in industrial applications due to its high computational costs, especially for high-Reynolds-number problems. RANS is often used to solve turbulent flows in industry due to its low computational costs and reasonably accurate results. Despite the popularity of these RANS methods, the assumptions used in RANS may lead to considerable model errors and uncertainties in the results. LES is more accurate than RANS, but it is still too expensive for many engineering problems with a high Reynolds number. Other turbulence models blend LES and RANS; among these are SAS and DES. Because the deficiencies of LES and RANS also apply to these approaches, they likewise require further improvement and validation.

The purpose of this project is to develop a new method for simulating turbulent flows. The proposed method should be more accurate than RANS and less expensive than LES. For this purpose, I proposed two methods for simulating turbulent flows. They are Parameter Extension Simulation (PES) and Large Scale Motion Simulation (LSMS). The PES is the solution of the turbulent flows with the help of a reference solution. LSMS is the resolution of the large scale motions of the turbulent flows, it acts as the reference solution for PES. To further improve the efficiency of PES and LSMS, the following fundamental questions should be answered:

Q1: How to determine the reference weighting coefficient for PES?
Q2: How does the reference solution for PES approach the DNS solution as the weighting coefficient is reduced to zero asymptotically?
Q3: Whether capturing the large scale motions is the necessary and sufficient condition for accurate simulation of turbulent flows with High Reynolds numbers?

To answer these fundamental questions, different types of turbulent flows are simulated, they are about flows in a smooth wall channel, in a rough wall channel, and in a compressor cascade. The PES results are compared with the experimental and DNS data.

Results

Smooth-wall channel flows

The first test case is about turbulent flows in a smooth wall channel. Figure 1 shows the PES and LES results for the friction coefficient f with different values for Reynolds number. The model results are compared with the DNS results. The PES solution has the highest accuracy among all the solutions under consideration, particularly for high Reynolds numbers. The Smagorinsky and k-equation-transport model solutions have the lowest accuracy at high Reynolds numbers.

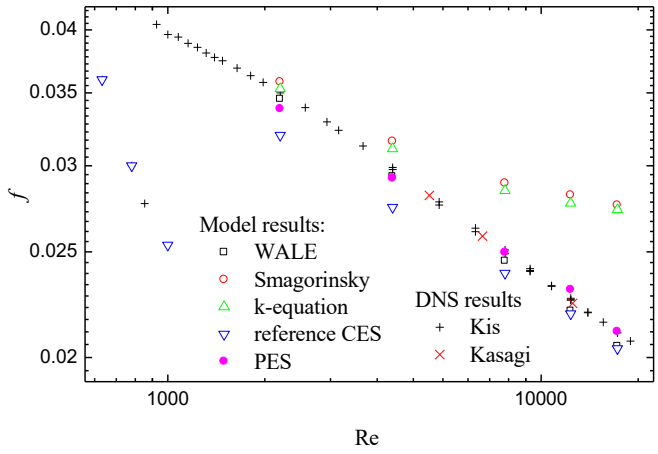

Figure 1: Friction coefficient f versus Reynolds number Re. The model results are compared with the DNS results given by Kis and by Kasagi.

Rough-wall channel flows

The geometry for this test case is a channel with two rough walls. The rough walls are made of two dimensional square-shaped riblets of size d which are distance d from each other in the streamwise direction. The turbulent structures obtained from the PES and DNS results are compared in Fig. 2.

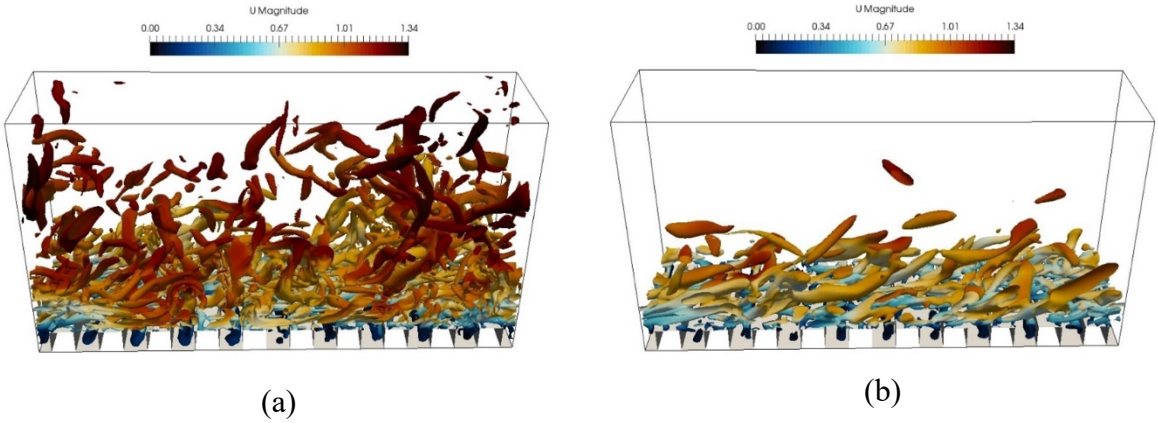

Figure 2: Snapshots of the instantaneous vortical structures in a box ($2H \times 1.05H \times 0.5H$, 1/4 flow domain); iso-surfaces $Q(H^2/u_m^2) = 5$, Re=11200. (a) DNS results; (b) Reference soluton for PES.

Figure 3 shows the PES, RANS, LES, and DNS results for the friction coefficient f. It can be seen that the PES solution is much more accurate than the RANS solutions. The PES solution is also more accurate the LES solutions when the same mesh resolution is used.

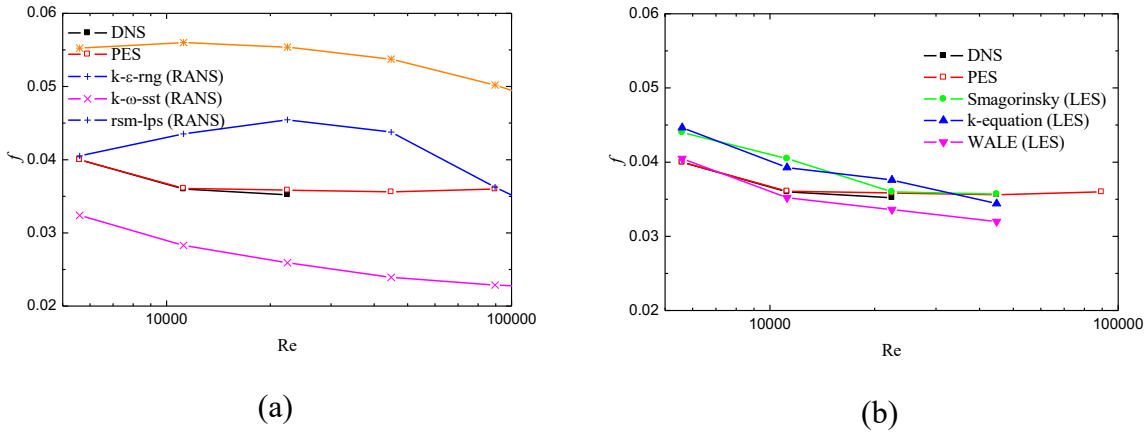

Figure 3: Friction coefficient f versus Reynolds number Re. (a) Comparison between the PES and RANS results; (b) comparison between the PES and LES results.

Compressor cascade flows

In the third test case, the turbulent flow in a compressor cascade was calculated. The computational domain is a passage of the cascade made of airfoils NACA0065-009. A periodic boundary condition in the pitchwise direction is used to account for the effects of the neighboring airfoils. The flows have the Reynolds number 3.82×10^5, determined by the chord length c and the free stream velocity u_∞. Figure 4 shows the vortical structures identified by the iso-surfaces of Qc^2/u_∞^2=1.4, which are calculated from the reference solution of PES. The iso-surfaces are colored to indicate the velocity magnitude. The flow structures are well captured by the PES solution.

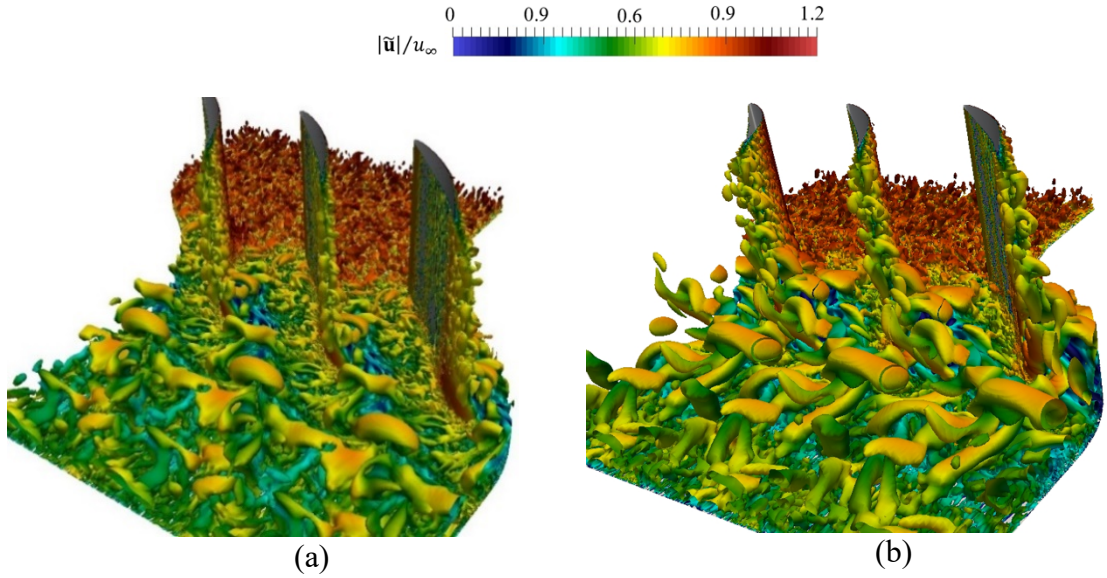

Figure 4: Turbulent structures Identified by Qc^2/u_∞^2=1.4, reference CES results. (a) $\alpha = 4^\circ$, (b) $\alpha = 7^\circ$.

Outlook

The proposed PES method has been used to simulate three types of turbulent flows: smooth-wall channel flows, rough-wall channel flows, and compressor blade cascade flows. The PES results are intensively compared with the RANS, LES, DNS, and experimental results. The comparison shows that the PES is more accurate than RANS. When the same mesh resolution is used, the PES results are also more accurate than the LES results. Calculation of more test cases is still needed to better understand the physics of the PES and further improve its efficiency.

Publications

1. Y Jin, Parameter extension simulation of turbulent flows, Phys. Fluids, 31, 125102 (2019).
2. Y Jin, Parameter extension simulation of turbulent flows in a compressor cascade with a high Reynolds number, Proceedings of ASME Turbo Expo 2020: Turbomachinery Technical Conference and Exposition, GT2020, GT2020-14809 (2020).

Presentations

3. Y Jin, Controlled eddy simulation of wall bounded flows at large Reynolds numbers, 17th European Turbulence Conference (ETC-17), Torino, 2019.

6.14 *hbk00032:* Improving physics and efficiency of AWI-CM multi-resolution climate model

HLRNProject ID:	hbk00032
Run time:	III/2020 – II/2021
Project Leader:	Prof. Dr. Thomas Jung
Project Scientists:	Dmitry Sidorenko [2], Dirk Barbi, Sergey Danilov, Helge Gößling, Ozgur Gurses, Sven Harig, Jan Hegewald, Nikolay Koldunov, Thomas Rackow, Natalja Rakowsky, Patrick Scholz, Dmitry Sein, Tido Semmler, Qiang Wang, Claudia Wekerle
Affiliation:	[1] also at University of Bremen [2] Alfred-Wegener-Institute for Polar and Marine Research, Bremerhaven

Summary

In the ocean, the Atlantic Meridional Overturning Circulation (AMOC) is one of the most important characteristics of an ocean model run. Commonly it is computed as a streamfunction of zonally averaged flow along constant depth levels (z framework). However, motion in the deep ocean follows isopycnals and the AMOC computed along constant density surfaces (density framework) is more revealing. We use both frameworks to interpret the differences in AMOC related to the change in resolution. The z and density frameworks do not lead to the same interpretation and show different variability. We demonstrate the high value of the density framework and conclude that it should be used routinely in standard analyses, including forthcoming intercomparison projects.

FESOM v.2.0

FESOM 2.0 builds on FESOM1.4 (Wang et al., 2014) but differs by its dynamical core. FESOM 2.0 exploits the finite volume approach with the cell centered placement of horizontal velocities (quasi-B-grid). This speeds up the dynamical core of FESOM by a factor of 3 compared to the finite element implementation in version 1.4. For vertical discretization the new version exploits the Arbitrary Lagrangian Eulerian Method. This allows users to switch between different discretizations which already include linear/non-linear free-surface, Z star, partial cell etc. The model inherits the framework and sea ice model from the previous version, which minimizes the efforts needed from a user to switch from one version to the other. In this project we analyzed the response of z~AMOC and σ~AMOC to the change in horizontal resolution in two global simulations with FESOM 2.0. For this FESOM 2.0 was used in a standard configuration (Scholz et al. 2019) to conduct runs on two different meshes using CORE-II interannual atmospheric forcing (1948–2008). Two meshes differ in horizontal resolution shown in Fig. 1.

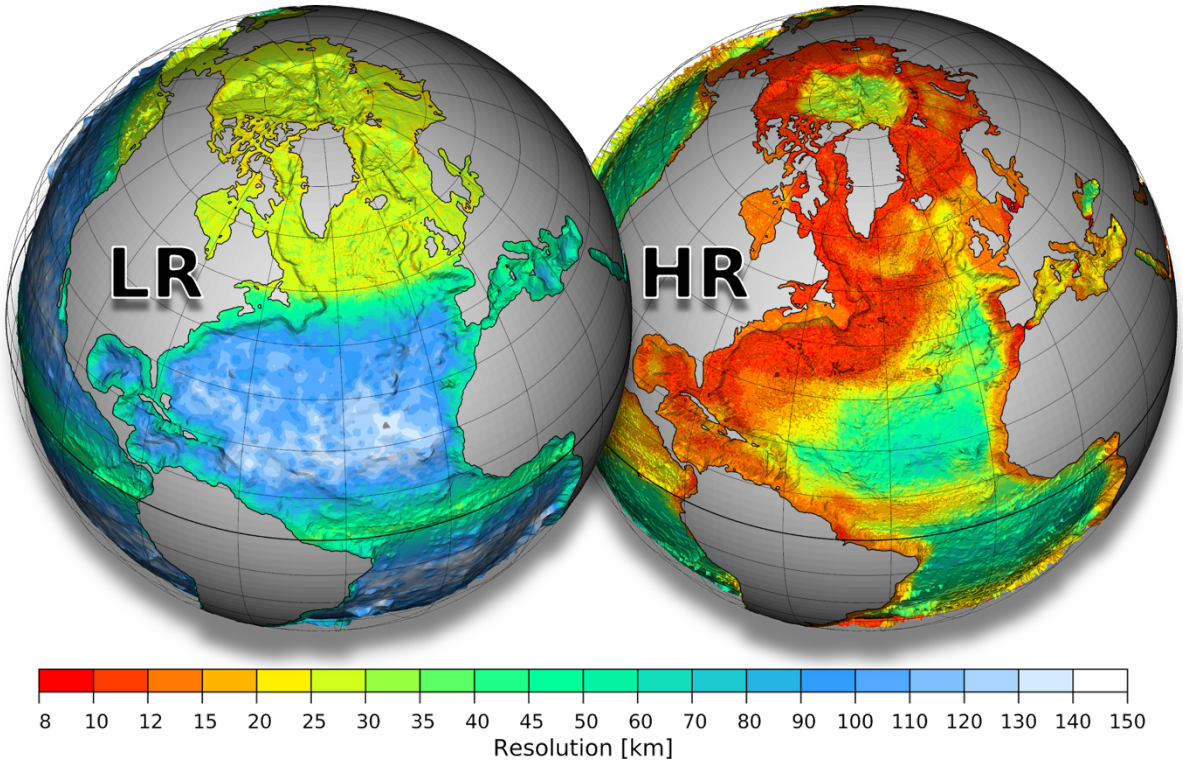

Figure 1: Resolution (in km) of the LR and HR ocean meshes. The number of surface vertices is 126,858 in LR and 1,306,775 in HR (taken from *Sidorenko et al. 2020*).

AMOC and vertical coordinate

The mid-depth cell of AMOC in z coordinates (Fig. 2, top panels) is centered around 1000 m depth in both setups. In LR it contains a recirculation at ~40°N which is absent in HR. The maximum of z~AMOC at 40°N is ~15 Sv in LR and is larger than in HR which reaches only ~12 Sv at this latitude. Such model behavior agrees with that described by Katsman et al. (2018) who found a weakening of simulated z~AMOC from ~18 Sv to ~13 Sv when changing the resolution from 1° to 1/4°. Interestingly, because of the absence of the recirculation in HR, the strength of the mid-depth cell there does not decrease towards the South and is by ~2Sv higher in the southern part of the North Atlantic than in LR.

Simulated AMOCs in σ2 representation are shown in Fig. 2 (bottom panels). There, the mid-depth cells are localized at σ2=~36.62 in both runs. In contrast to the z representation, both runs show recirculations which are, however, shifted further north (as compared to z~AMOC in LR) and are found at ~55°N where intense watermass transformations take place. This confirms the generally known fact that the AMOC in density coordinate maps the transformation between different density classes into a zonally-mean picture and is more directly connected to the physics of governing processes (see e.g. Johnson et al. 2019). Also, the values of the northern maximums become higher than those in z representation and, interestingly, do not differ between runs reaching ~16Sv at ~55°N. Similar to the z formulation, however, σ~AMOC in HR shows a continuous increase (but of smaller amplitude) of the mid-depth cell towards the south of 30°N while a slight decrease is found in LR there.

More results from this project have been published in Sidorenko et al. 2020.

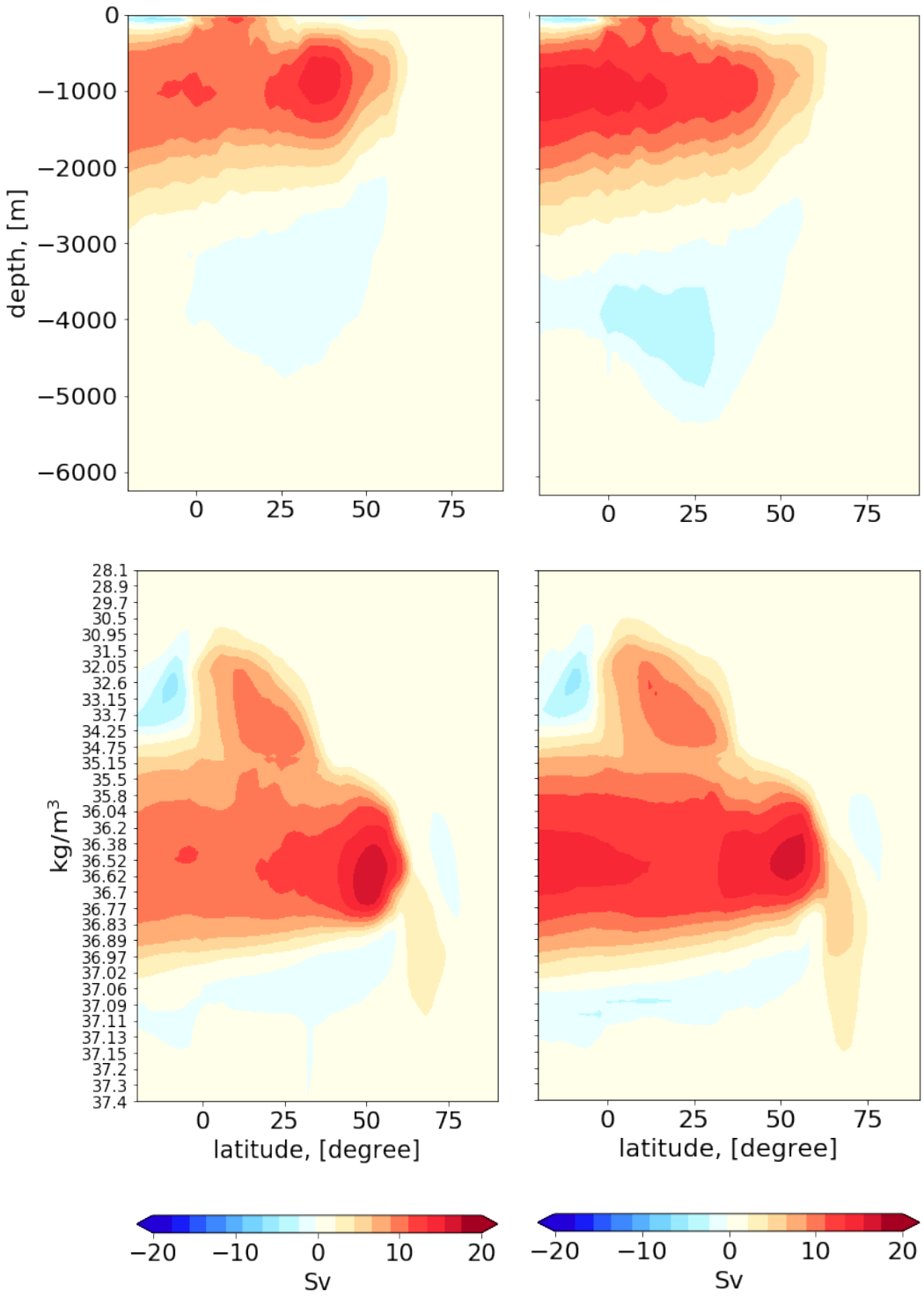

Figure 2: Upper panel: z~AMOC in LR (left) and HR (right) model runs. Lower panel: same as the upper panels but for σ~AMOC (taken from *Sidorenko et al. 2020*).

References

Johnson, H. L., Cessi, P., Marshall, D. P., Schloesser, F., & Spall, M. A. (2019). Recent contributions of theory to our understanding of the Atlantic Meridional Overturning Circulation. Journal of Geophysical Research: Oceans, 124, 5376–5399, doi:10.1029/2019JC015330

Katsman, C. A., Drijfhout, S. S., Dijkstra, H. A., & Spall, M. A. (2018). Sinking of dense North Atlantic waters in a global ocean model: Location and controls. Journal of Geophysical Research: Oceans, 123. doi:10.1029/ 2017JC013329

Scholz, P., Sidorenko, D., Gurses, O., Danilov, S., Koldunov, N., Wang, Q., ... & Jung, T. (2019). Assessment of the Finite-volumE Sea ice-Ocean Model (FESOM2. 0)–Part 1: Description of selected key model elements and comparison to its predecessor version. Geoscientific Model Development, 12(11). doi:10.5194/gmd-12-4875-2019

Sidorenko, D.*,* Danilov, S., Fofonova, V., Cabos, W., Koldunov, N., Scholz, P., et al. (2020). AMOC, watermass transformations and their responses to changing resolution in the Finite-volumE Sea ice–Ocean Model. Journal of Advances in Modeling Earth Systems, 12, e2020MS002317. Accepted Author Manuscript. doi.org/10.1029/2020MS002317

Wang, Q., Danilov, S., Sidorenko, D.*,* Timmermann, R., Wekerle, C., Wang, X., Jung, T., and Schröter, J., 2014: The Finite Element Sea Ice-Ocean Model (FESOM) v.1.4: formulation of an ocean general circulation model, Geosci. Model Dev., 7, 663–693, doi:10.5194/gmd-7-663-2014

6.15 *hbk00034:* Ice sheet – ice shelf – ocean interaction in the marginal seas of the Southern Ocean

HLRNProject ID:	hbk00034
Run time:	III/2013 – III/2021
Project Leader:	Prof. Torsten Kanzow[1, 2]
Project Scientists:	Verena Haid[2], Yoshihiro Nakayama[2], Frank Schnaase[1], Lukrecia Stulic[2], Ralph Timmermann[2]
Affiliation:	[1] University of Bremen [2] Alfred Wegener Institute, Helmholtz Centre for Polar and Marine Research

Overview

The melting of glaciers and ice sheets contributes to changes in the global sea level. As the largest ice sheet, the Antarctic Ice Sheet is prone to have a strong global impact. Most of the Antarctic Ice Sheet drains into floating ice shelves, which buttress the ice flow from the grounded areas. Ice shelf basal melting has been shown to be a crucial component in the southern hemisphere's ice mass budget and its variability.

For a study of the mechanisms of ice-ocean interaction and the potential of substantial changes in ice-shelf basal mass loss in a warmer climate, we use the global Finite Element Sea ice–ice shelf–Ocean Model FESOM (Timmermann et al., 2012) on an unstructured grid with high resolution in the Antarctic marginal seas. Simulations are performed with prescribed cavity geometries and with a dynamic ice-shelf component as part of a coupled ocean–ice shelf–ice sheet model. Next to the implications for the Antarctic ice sheet mass budget (which is relevant to global sea level), we are interested in the effects on Southern Ocean hydrography and possible tippings points in the Antarctic climate system.

Results

Coupling of FESOM and high-resolution PISM works efficiently. The FESOM-PISM coupled model projection suggests a thinning of FRIS by about 15% (spatial average) between 2060 and 2160. The thinning is strongest near the grounding lines of Support Force and Foundation ice streams (Fig. 1). These results are currently being prepared for publication.

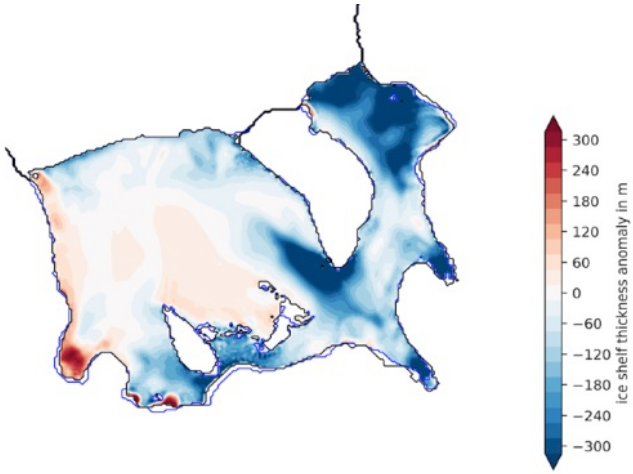

Figure 1: FRIS thickness anomaly for 2160 relative to the year 2000 and the evolution of cavity geometry between these two years in the coupled FESOM-PISM model run with HadCM3-A1B atmospheric forcing. The coloured area represents the modelled ice shelf extent.

Our work in the Horizon 2020 project Tipping Points in Antarctic Climate Components (TiPACCs) aims to investigate the Southern Ocean / Antarctic Ice Sheet system and its tipping points. Currently (including the work done in 2020), our focus is on the mechanisms potentially causing a rapid transition from 'cold' to 'warm' conditions in the ice shelf cavities (Timmermann and Hellmer, 2013; Hellmer et al., 2017). This regime shift within the ocean results in a strong increase of basal melt rates of the ice shelf, which in turn by freshening the water stabilizes the 'warm' conditions and hinders an easy reversal. Additionaly, it leads to a destabilization of the Antarctic Ice Sheet by thinning the ice shelves and weakening their buttressing effect.

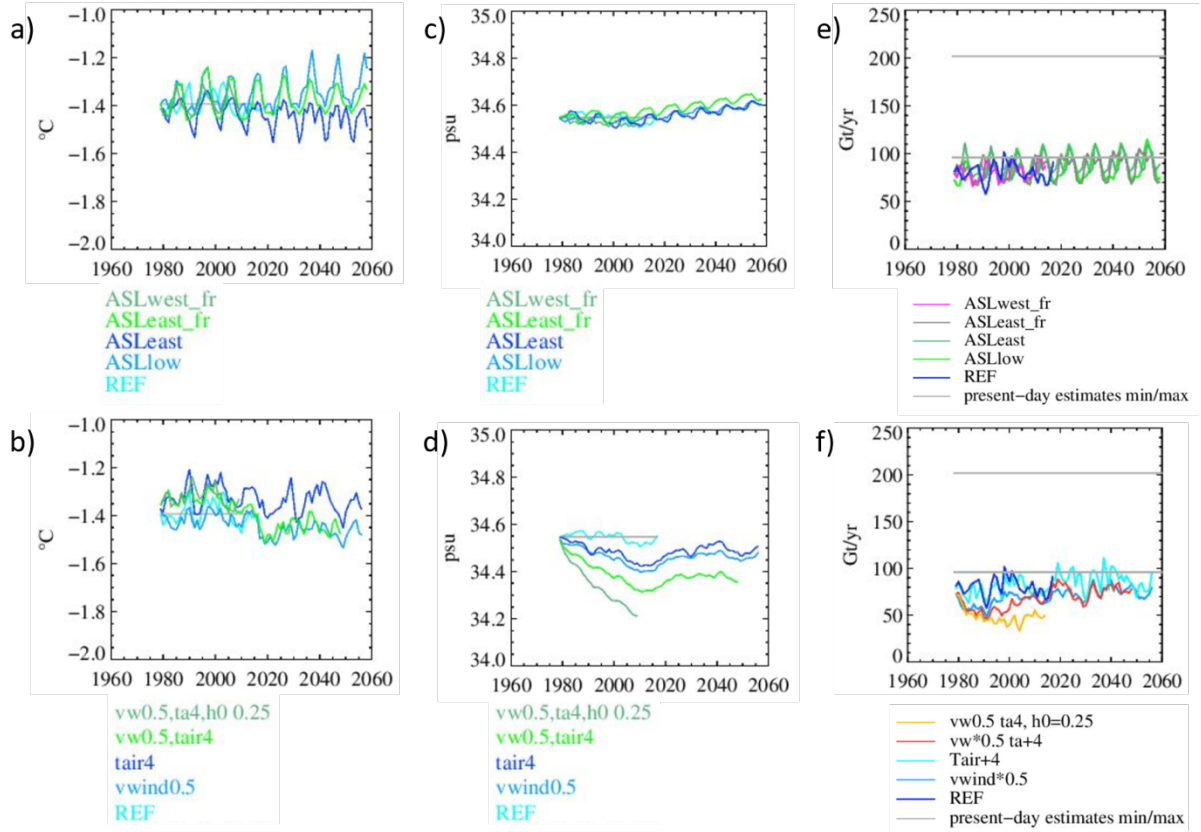

Figure 2: (a, b) Potential temperature and (c, d) salinity on the Weddell Sea continental shelf, and (e, f) melt rates under the Filchner-Ronne Ice Shelf. The individual experiments with perturbations of the atmospheric forcing: REF – Reference run (unperturbed ERA Interim forcing); ASLlow – repetition of the ten years with lowest central pressure for the Amundsen Sea Low (ASL); ASLeast – repetition of 10 years with ASL center located furthest east; ASLeast_fr – repetition of 10 years with ASL center located furthest east during April-September; ASLwest_fr – repetition of 10 years with ASL center located furthest west during April-September; vwind0.5 – meridional wind decreased by factor 0.5 south of 70°S; tair4 – air temperature increased by 4 °C south of 70°S; vw0.5,tair4 – meridional wind decreased by factor 0.5 and air temperature increased by 4 °C south of 70°S; vw0.5,tair4,h0 0.25 – meridional wind decreased by factor 0.5 and air temperature increased by 4 °C south of 70°S, the ice model's lead-closing parameter was reduced to 0.25 (compared to 0.5 in all other runs).

We investigate under which conditions such a 'tipping' will occur for different ice shelf cavities, with a focus on the Filchner-Ronne and the Ross cavity. A suite of sensitivity experiments with various perturbations of the atmospheric forcing was conducted.

Results from these experiments indicate that the location of and the pressure in the centre of the Amundsen Sea Low (ASL) have only limited influence on the salinity of the Weddell Sea and Ross Sea continental shelves compared to variables such as meridional wind and air temperature (Figure 2a-d). Specifically, a combination of increased air temperatures and reduced meridional wind has a strong impact on the salinity (Figure 2d) as it very effectively

suppresses sea-ice production at the ice-shelf front. As expected, perturbations in precipitation and thermal radiative heat flux proved to be of minor influence (not shown).

The freshening on the continental shelf alone, however, proves not to be sufficient to allow for warm water to cross the continental shelf and enter the cavity and thus trigger a tipping point for FRIS melt rates. Instead of a substantial increase in melt rates, these experiments rather show a tendency towards lower melt rates (Figure 2f). According to Daae et al. (2020), it is expected, however, that a reduced shelf salinity in combination with a lifted thermocline at the continental shelf break may allow warm water to penetrate into the ice shelf cavity. Work on this project is continued in 2021.

References

Daae, K., T. Hattermann, E. Darelius, R. D. Mueller, K. A. Naughten, R. Timmermann and H. H. Hellmer (2020): Necessary conditions for warm inflow toward the Filchner Ice Shelf, Weddell Sea, Geophysical Research Letters, 47, e2020GL089237.

Timmermann, R., Q. Wang, and H.H. Hellmer (2012): Ice shelf basal melting in a global finite-element sea ice–ice shelf–ocean model, Annals of Glaciology, 53(60), 303-314, doi:10.3189/2012AoG60A156.

Timmermann, R. and H.H. Hellmer (2013): Southern Ocean warming and increased ice shelf basal melting in the twenty-first and twenty-second centuries based on coupled ice-ocean finite-element modelling. Ocean Dyn. 63, 1011–1026.

Timmermann, R. and Goeller, S. (2017): Response to Filchner–Ronne Ice Shelf cavity warming in a coupled ocean–ice sheet model – Part 1: The ocean perspective, Ocean Sci., 13, 765-776, https://doi.org/10.5194/os-13-765-2017.

6.16 *hbk00038:* Interaction between marine terminating glaciers and the ocean circulation in Northeast Greenland

HLRN Project ID:	hbk00038
Run time:	IV/2020 – III/2021
Project Leader:	Prof. Dr. Torsten Kanzow
Project Scientists:	Dr. Claudia Wekerle, Dr. Qiang Wang and Dr. Ralph Timmermann
Affiliation:	Alfred Wegener Institute

Overview

Future projections of climate warming around Greenland indicate particularly large melting rates on the east coast of Greenland, between Fram Strait and Denmark Strait (Lique et al. 2015). In Northeast Greenland, the Zachariæ Isstrøm (ZI) lost its entire floating ice tongue between 2012 and 2014, and warming of Atlantic Water that flows underneath the cavity has been suggested to be the main driver for the collapse of the ice tongue (Mouginot et al. 2015). Both ZI and the 79 North Glacier (79NG) drain the Northeast Greenland Ice Stream, which comprises around 15% of the Greenland ice sheet. Oceanic observations of the glacier dynamics are limited to the glacier front, and cover only a short time period of a few years (e.g. Schaffer et al 2020). Thus, high resolution model integrations will help to better understand the long-term variability of the glacier system and reveal possible driving mechanisms.

In this project, we carry out high-resolution ocean-sea ice simulations which explicitly resolve the cavities of the 79NG and ZI. Some of the important scientific questions that we are investigating with our simulations are listed below:

- Which processes are responsible for the heat transport into the cavity of the 79NG?
- What is its variability from seasonal to decadal time scales?
- What determines the thickness of the Atlantic Water layer on the East Greenland continental shelf?

Methods

To study the interaction of the Northeast Greenland marine-terminating glaciers with the ocean circulation on the Northeast Greenland continental shelf, we set up a FESOM configuration which includes the ice shelf cavities of the 79NG and ZI. The global unstructured mesh has a resolution of 700 m in the vicinity of the glaciers, 2.5 km on the Northeast Greenland continental shelf, and 4.5 km in the Nordic Seas and Arctic Ocean. In the vertical, we use 90 unevenly spaced z-levels. Ice shelf draft and ocean bathymetry needed to generate the 3D-mesh was taken from RTopo-2 (Schaffer et al. 2016), which has been updated with new bathymetric data along the Northeast Greenland coast. We apply realistic Greenland runoff data from Mankoff et al. (2019, 2020), which comprises solid ice discharge and liquid runoff from glaciated and non-glaciated Greenland land. The simulation is being carried out at the moment for the time period 1980-2019 with JRA-55 atmospheric forcing, and results from the first 4 years are shown here.

Preliminary results

Circulation on the Northeast Greenland continental shelf

Warm Atlantic Intermediate Water (AIW) has to pass through the trough system of the Northeast Greenland continental shelf to reach the glacier fronts. Schaffer et al. (2017) showed, based on observations from 1979-2016, that the AIW mainly reaches the 79NG via the southern trough, i.e., the Norske Trough. Mooring measurements in the central Norske Trough from 2014-2016 revealed a ~10-km-wide bottom-intensified jet carrying the warm AIW towards the glaciers (Münchow et al. 2020). Consistent with these observations, the simulated velocity field in the AIW layer reveals an anticyclonic circulation on the shelf, with flow towards the glaciers in the southern Norske Trough and flow towards the shelf break in the northern Westwind Trough (Fig. 1a). The bottom-intensified jet observed by Münchow et al. (2020) is also well represented in the model (Figure not shown). We are currently investigating the processes that bring the warm AIW from the deep basin onto the shelf.

Circulation in the cavity of the 79NG

The recent study by Schaffer et al. (2020) showed that bathymetry in front of the 79NG plays an important role for the circulation inside the cavity. Their observations based on mooring measurements at the glacier front indicate that a year-round bottom-intensified inflow of warm AIW into the cavity is constrained by a sill. However, so far not much is known about the circulation in the cavity itself. Consistent with Schaffer et al. (2020), our FESOM simulation shows a strong inflow of warm AIW into the cavity across the sill located at around 19.5°W/79.5°N (Fig. 1b). The simulated inflowing jet is bottom-intensified, and reaches on average velocities of more than 35 cm/s. For comparison, the mooring measurements revealed values between 30 and 60 cm/s. The AIW circulates cyclonically around the cavity, with high velocities on its southern side.

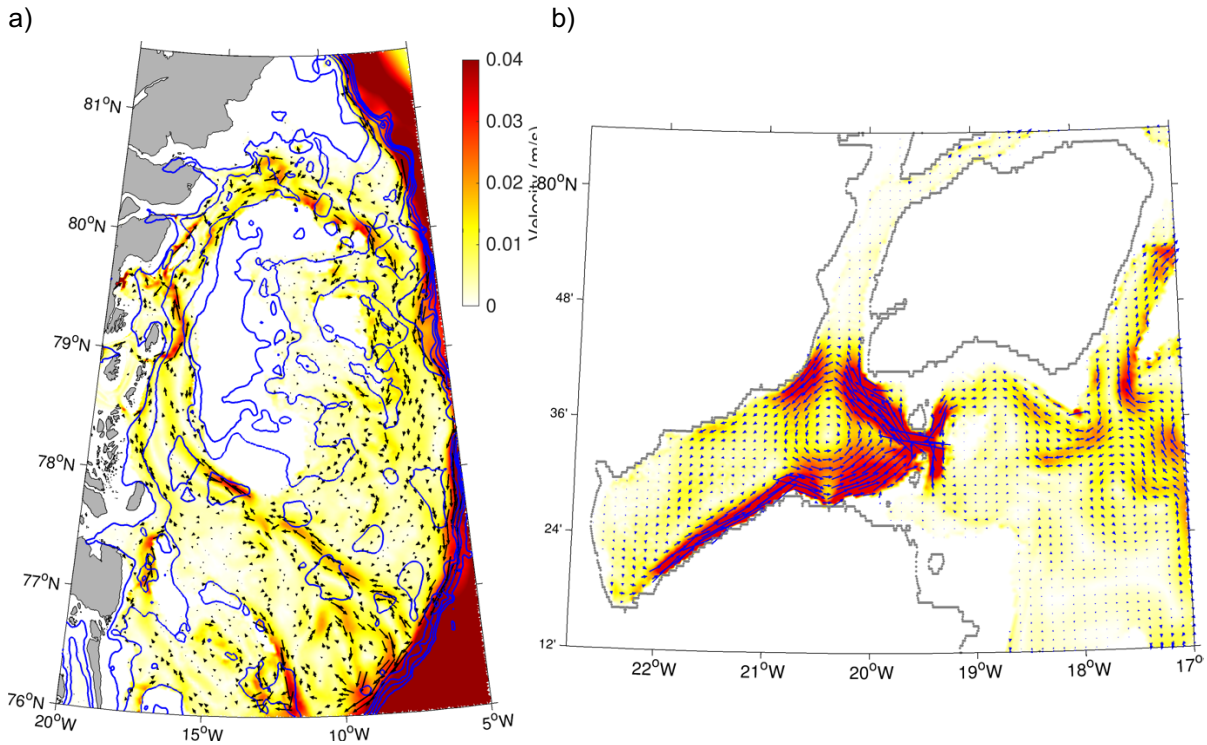

Figure 1: Simulated circulation on the Northeast Greenland continental shelf (a) and in the region of the 79NG (b) in the Atlantic Intermediate Water layer, defined as waters with temperature above 0°C, averaged over the time period 1980-1983.

Basal melt rates underneath the cavities

A map of basal melt rates underneath the 79NG and time series of melt rates for both the 79NG and the ZI are shown in **Fig. 2**. Largest basal melt rates in the 79NG cavity occur close to the grounding line, consistent with observations from satellite imagery (Wilson et a. 2017). The simulated total volumetric basal melt rate of the 79NG averaged over the years 1980-1983 amounts to 12.3 km^3/year, which compares well with the estimate of 11.9 km^3/year from Wilson et al. (2017).

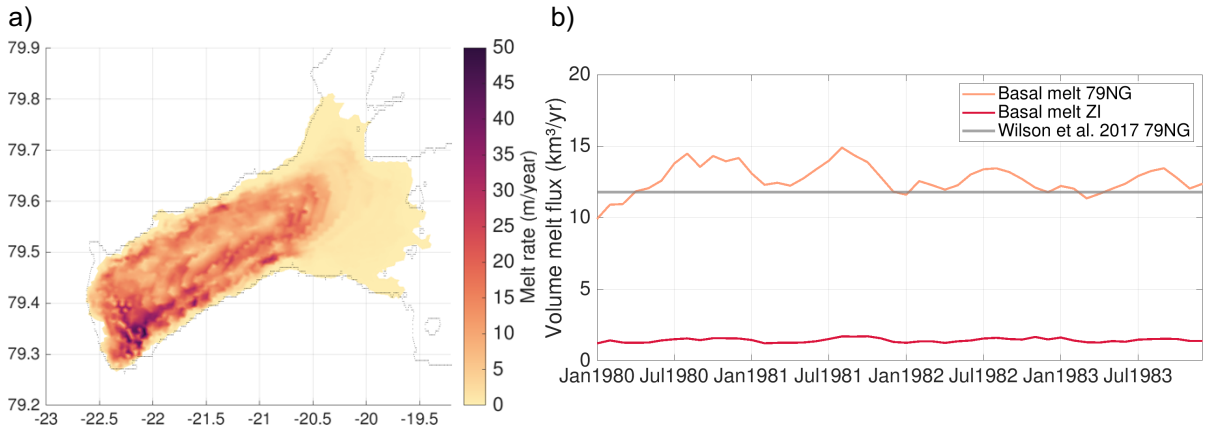

Figure 2: a) Simulated basal melt rate in m/year in the 79NG cavity, averaged over the years 1981-1983. b) Time series of integrated basal melt rate in km^3/year of ice shelves 79NG and ZI. The grey line shows the observational estimate for the 79NG by Wilson et al. (2017).

Outlook

The Atlantic Water transport through the Nordic Seas increased in recent years (Beszczynska-Möller et al. 2012). We plan to perform dedicated sensitivity experiments to quantify the effect of increased Atlantic Water transport on the ocean dynamics of the Northeast Greenland continental shelf and eventually on the marine terminating glaciers of Northeast Greenland.

Furthermore, we plan to couple our FESOM configuration with the ice sheet model ISSM (Larour et al. 2012). ISSM is a parallel, state-of-the art ice sheet model based on the finite element method, and allows for high spatial resolution. The overall goal is to set up a coupled model system which will be used to investigate the interaction between the Greenland ice sheet and ice shelves and the ocean-sea ice dynamics.

Presentations

Wekerle, C. et al., The future of the 79°N-Glacier, Groce-2 seminar, February 11, 2021.

Publications

Hoffmann, Z., von Appen, W.-J. and C. Wekerle, Seasonal and Mesoscale Variability of the Two Atlantic Water Recirculation Pathways in Fram Strait, under review, JGR Oceans.

References

Beszczynska-Möller, A., E. Fahrbach, U. Schauer, and E. Hansen (2012), Variability in Atlantic water temperature and transport at the entrance to the Arctic Ocean, 1997-2010, ICES J. Mar. Sci., 69, 852-863.

Larour, E., Seroussi, H., Morlighem, M., and Rignot, E. (2012), Continental scale, high order, high spatial resolution, ice sheet modeling using the Ice Sheet System Model (ISSM), J. Geophys. Res., 117, F01022.

Lique, C., H. L. Johnson, Y. Plancherel, and R. Flanders (2015), Ocean change around Greenland under a warming climate, Clim. Dyn., 45, 1235-1252.

Mankoff, K. D., Solgaard, A., Colgan, W., Ahlstrøm, A. P., Khan, S. A., and Fausto, R. S. (2019), Greenland Ice Sheet solid ice discharge from 1986 through March 2020, Earth Syst. Sci. Data, 12, 1367–1383.

Mankoff, K. D., Ahlstrøm, A. P., Colgan, W., Fausto, R. S., Fettweis, X., Kondo, K., Langley, K., Noël, B., Sugiyama, S., and van As, D. (2020), Greenland liquid water runoff from 1979 through 2017, Earth Syst. Sci. Data.

Mouginot, J., E. Rignot, B. Scheuchl, I. Fenty, A. Khazendar, M. Morlighem, A. Buzzi, and J. Paden (2015), Fast retreat of Zachariae Isstrom, northeast Greenland, Science.

Münchow, A., J. Schaffer, and T. Kanzow (2020), Ocean Circulation Connecting Fram Strait to Glaciers off Northeast Greenland: Mean Flows, Topographic Rossby Waves, and Their Forcing. J. Phys. Oceanogr., 50, 509–530.

Schaffer, J., R. Timmermann, J. E. Arndt, S. S. Kristensen, C. Mayer, M. Morlighem, and D. Steinhage (2016), A global high-resolution data set of ice sheet topography, cavity geometry and ocean bathymetry, Earth System Science Data.

Schaffer, J., W.-J. von Appen, P. A. Dodd, C. Hofstede, C. Mayer, L. de Steur, and T. Kanzow (2017), Warm water pathways toward Nioghalvfjerdsfjorden Glacier, Northeast Greenland, J. Geophys. Res. Oceans, 122 (5), 4004-4020.

Schaffer, J., T. Kanzow, W. J. von Appen, L. von Albedyll, J. E. Arndt, and D. H. Roberts (2020), Bathymetry constrains ocean heat supply to Greenland’s largest glacier tongue, Nat. Geosci., 13, 227-231.

Wilson, N., Straneo, F., and Heimbach, P.: Satellite-derived submarine melt rates and mass balance (2011–2015) for Greenland's largest remaining ice tongues (2017), The Cryosphere, 11, 2773–2782.

6.17 *hbk00057:* Persistent ozone depletion in the tropical stratosphere: identifying possible reasons

HLRN Project ID:	hbk00057
Run time:	I/2017 – II/2020
Project Leader:	Dr. Alexei Rozanov
Project Scientists:	Dr. Evgenia Galytska
Affiliation:	Institute of Environmental Physics, University of Bremen

Overview

Playing a key role in the radiative budget of the Earth's atmosphere stratospheric ozone also protects the biosphere from the harmful UV radiation and is closely related to stratospheric circulation and meteorology. After the anthropogenic emission of the ozone depleting species has been ruled out by Montreal Protocol and its amendments the severe ozone decline discovered in early eighties of the last century began to slow down and even some indications of the ozone recovery have been inferred from observations (Newchurch et al., 2003, WMO, 2007, 2011, Yang et al., 2006). During the last decade the vertical distribution of stratospheric ozone trends has been moved into the focus (Eckert et al., 2014, Gebhardt et al., 2014, Kyrola et al., 2013). Analyzing the vertically resolved time series of ozone in the tropics during the first decade of the XXI century all authors agree in their conclusions that a strong ozone recovery was seen in the middle to lower stratosphere (below about 30 km) while a significant ozone depletion was observed at altitudes of about 35 km. Being vertically integrated these opposite trends result in a slightly positive change which is consistent with the signatures of a recovery seen in the observations of the ozone total column.

In this study we focused at the investigation of vertical distributions of NO_2 and BrO retrieved from limb measurements from the SCIAMACHY (SCanning Imaging Absorption spectroMeter for Atmospheric CHartograohY) instrument (Bovensmann et al., 1999) onboard the ESA Envisat satellite. The main objective of this study was to assess if the behavior of NO_2 is consistent with the findings of Nedoluha et al. (2015) with respect to the NO_y family and if halogen species might have a significant contribution to the ozone depletion mechanisms in this latitude/altitude region. The investigation includes modeling studies using the Chemical Transport Model (CTM) TOMCAT (Chipperfield et al., 2006) to evaluate if the observed behavior of the species can be reproduced by the model and if the observed trends in the tropical stratospheric ozone can be explained by the observed trends in both NO_2 and BrO. A consideration of BrO is believed to be important as on the one hand it is an ozone depleting species and on the other hand it reacts with nitrogen species to form inactive reservoir species.

Results

While the anticorrelated linear changes of ozone and NO_2 inferred in the framework of this study are consistent with those reported by Nedoluha et al. (2015), the linear changes in the age of air showed no indication for a slowdown in the upwelling speed as suggested by Nedoluha et al. (2015) to explain the observed positive trends of NO_2. However, when analyzing the age of air resolved by seasons, it was found that the circulation speeds up during the boreal winter while slowing down during the boreal autumn. These trends, however, cancel out when considering the whole year. With the increasing circulation speed, the amount of N_2O, which is a precursor of NO_2, increases resulting in the increase of NO_2 and the decrease of ozone (and vice versa). As the amount of N_2O is controlled by both the transport from the

troposphere and photochemical destruction its variations are not canceled out when considering the whole year.

Figure 1 shows the linear changes of ozone, NO_2 and age of air for December-January-February (DJF) and September-October-November (SON) seasons from TOMCAT model. It is seen that the accelerating upwelling during the boreal autumn causes a strong increase in the NO_2 amount and the decrease in the ozone. For DJF season the opposite behavior is observed. Thus it was concluded that the observed trends are caused by the seasonal variations in the change of the circulation speed.

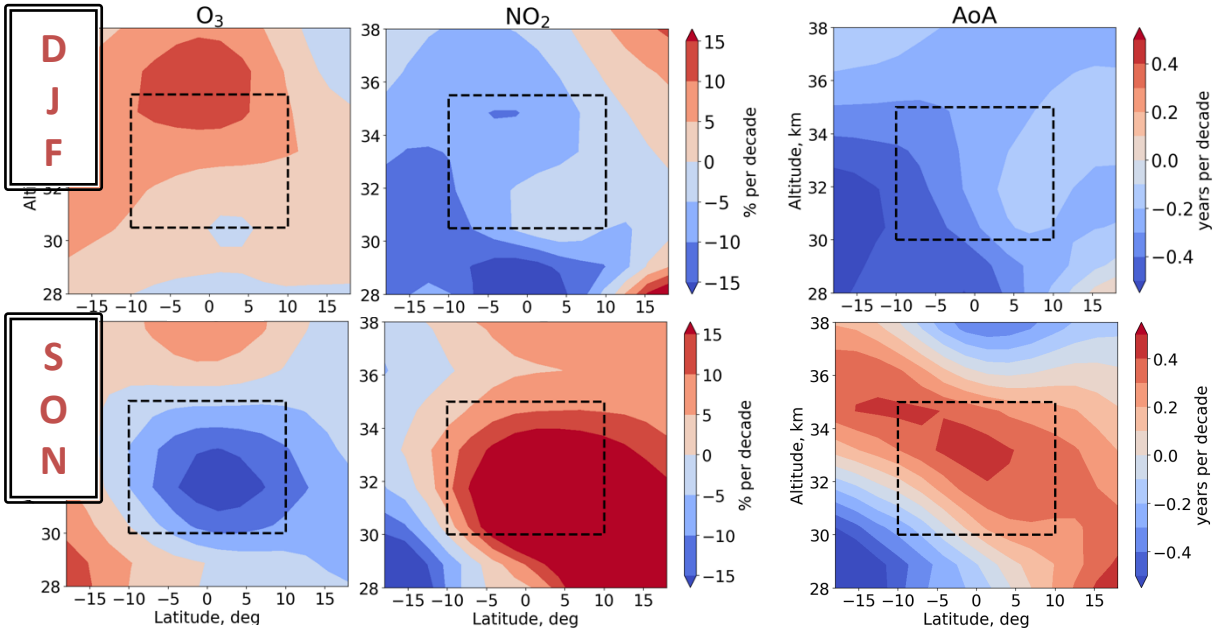

Figure 2: Linear changes of ozone, NO_2 and age of air for December-January-February (DJF) and September-October-November (SON) seasons from TOMCAT model.

A comparison of BrO profiles retrieved from the SCIAMACHY limb observations (V4.4) and from TOMCAT model simulations is shown in Fig. 2. A good agreement between both datasets is seen up to 24 km in the tropics and northern mid-latitudes and up to 27 km in the southern mid-latitudes. Above, the results start to deviate with SCIAMACHY data showing less BrO with increasing altitude. This behavior is believed to be related to a decrease in the sensitivity of SCIAMACHY measurements towards 30 km altitude. Figure 3 shows a comparison of BrO time series at different altitudes and latitudes obtained from SCIAMACHY data and TOMCAT model simulations. At 20 km, a good agreement in the seasonality of both data sets is seen with SCIAMACHY showing stronger seasonal oscillations in the northern mid-latitudes. With increasing altitude SCIAMACHY shows smaller amplitude of BrO variations than TOMCAT in tropics and southern mid-latitudes while in the northern mid-latitudes a good agreement is seen.

The linear changes in the stratospheric BrO obtained from SCIAMACHY observations and simulations with TOMCAT for the period 2005 – 2011 are shown in Figure 4. In general, both data sets show a decreasing amount of BrO in the stratosphere (above 20 km for SCIAMACHY) with the linear change values ranging from 0 to -15%. This behavior confirms the expected decrease in bromine compounds as a result of the Montreal Protocol and its amendments. The positive values below 20 km seen in the SCIAMACHY data are believed to be caused by a low sensitivity of BrO observations in the tropical UTLS range, which is related to an extremely low amount of BrO in this region (see Fig. 2). Looking, however, in the altitudinal and latitudinal distribution of the BrO linear changes, one sees a quite different behavior of the observational and modeled data. While SCIAMACHY shows increasing negative linear changes with increasing altitude there is no clear dependence on the altitude

in the model data. The latter, however, show stronger changes in the northern hemisphere, while the linear changes from SCIAMACHY are rather symmetric in the south-north direction. The reasons for the observed discrepancies are still under investigation. This, however, is beyond the HLRN project, as no further data processing is needed.

The main knowledge gain from the last phase of this project is that the BrO linear changes resulting from the SCIAMACHY measurements were found to be strongly affected by the order of the polynomial used in the retrieval and much less sensitive to other retrieval parameters. This might be an indication of an influence of the instrument degradation on the resulting linear changes. In this respect V4.4 of the retrieval, which uses a cubic polynomial, is believed to be most reliable.

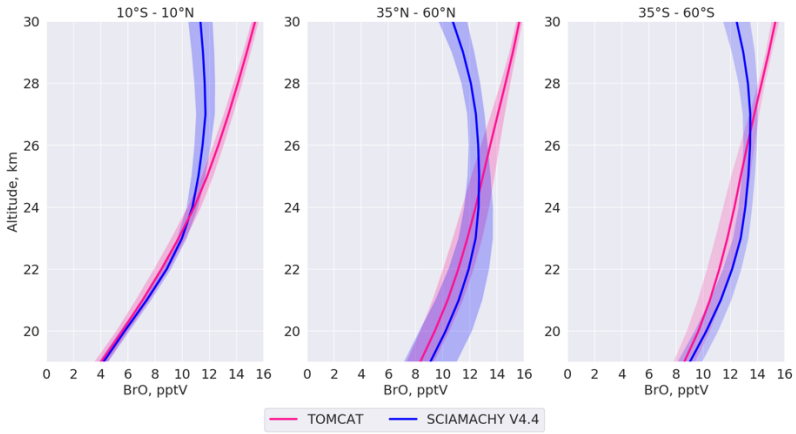

Figure 3: Vertical distributions of BrO obtained from SCIAMACHY limb observations and TOMCAT model simulations.

Figure 4: BrO volume mixing ratio (pptV) at different altitudes and latitudes from SCIAMACHY limb observations and TOMCAT model simulations.

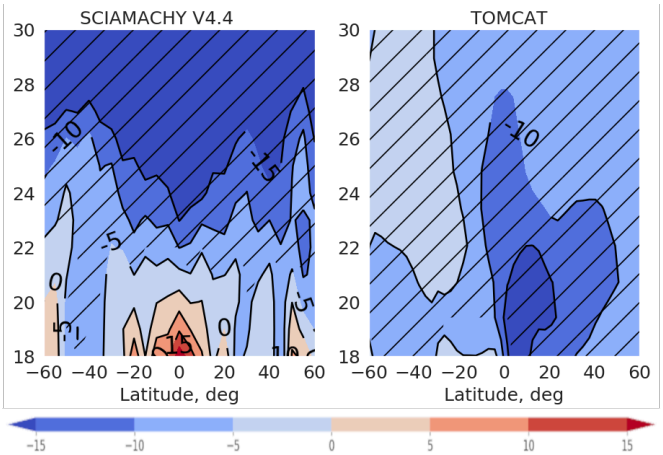

Figure 5. Linear changes in the stratospheric BrO from SCIAMACHY limb observations and TOMCAT model simulations.

Outlook

The project has been completed in the second quarter 2020. Investigations about the reasons for the discrepancies in BrO linear changes obtained from the SCIAMACHY observations and TOMCAL model data are still ongoing. All required data is, however, processed, and there is no need for any additional computation time at HLRN.

PhD Thesis

1. Galytska, E., Spatio-temporal variations of observed and modelled stratospheric trace gases, Universität Bremen, http://nbn-resolving.de/urn:nbn:de:gbv:46-00107599-10, 2019

Publications

1. Galytska, E., Rozanov, A., Chipperfield, M. P., Dhomse, S. S., Weber, M., Arosio, C., Feng, W., and Burrows, J. P.: Dynamically controlled ozone decline in thetropical mid-stratosphere observed by SCIAMACHY, Atmos. Chem. Phys., 19,767-783, https://doi.org/10.5194/acp-19-767-2019, 2019.

Presentations

1. Galytska, E., Rozanov, A., Chipperfield, M. P., Dhomse, S. S., Weber, M., Noël, S., Bourassa, A., Degenstein, D., Damadeo, R., Burrows, J. P.: Validation of SCIAMACHY limb NO2 scientific data V4.0, its changes in the stratosphere and their impact on O3 chemistry in the tropical region. 10th International Limb Workshop, Greifswald, Germany, 4-7 June 2019.
2. Galytska, E., Rozanov A., Chipperfield M. P., Arosio C., Dhomse S. S., and Burrows J. P.: Ozone decline in the tropical mid-stratosphere observed by SCIA-MACHY and its relation to the stratospheric dynamics. IUP/AWI Block Seminar, 04.02.2019, Bremen, Germany.
3. Galytska, E., Arosio C., Rozanov A., Chipperfield M. P., Dhomse S. S., Sofieva V.,and Burrows, J. P.: Seasonal variability in transport in the tropical mid-stratosphereand its impact on ozone and key trace gases. European Geosciences Union General Assembly 2019, 7-12.04.2019, Vienna, Austria.

References

1. Eckert, E., von Clarmann, T., Kiefer, M., Stiller, G. P., Lossow, S., Glatthor, N., Degenstein, D. A., Froidevaux, L., Godin-Beekmann, S., Leblanc, T., McDermid, S., Pastel, M., Steinbrecht, W., Swart, D. P. J., Walker, K. A., and Bernath, P. F.: Drift-corrected trends

and periodic variations in MIPAS IMK/IAA ozone measurements, Atmos. Chem. Phys., 14, 2571-2589, 2014.

2. Gebhardt, C., Rozanov, A., Hommel, R., Weber, M., Bovensmann, H., Burrows, J. P., Degenstein, D., Froidevaux, L., and Thompson, A. M.: Stratospheric ozone trends and variability as seen by SCIAMACHY from 2002 to 2012, Atmos. Chem. Phys., 14, 831-846, doi:10.5194/acp-14-831-2014, 2014.
3. Galytska, E., Rozanov, A., Chipperfield, M. P., Dhomse, Sandip. S., Weber, M., Arosio, C., Feng, W., and Burrows, J. P.: Dynamically controlled ozone decline in the tropical mid-stratosphere observed by SCIAMACHY, Atmos. Chem. Phys., 19, 767-783, https://doi.org/10.5194/acp-19-767-2019, 2019.
4. Kyrölä, E., Laine, M., So_eva, V., Tamminen, J., Paivarinta, S.-M., Tukiainen, S., Zawodny, J., and Thomason, L.: Combined SAGE II-GOMOS ozone profile data set for 1984-2011 and trend analysis of the vertical distribution of ozone, Atmos. Chem. Phys., 13, 10645-10658, doi:10.5194/acp-13-10645-2013, 2013.
5. Nedoluha, G. E., D. E. Siskind, A. Lambert, and C. Boone, The decrease in mid-stratospheric tropical ozone since 1991, Atmos. Chem. Phys., 15, 4215-4224, doi:10.5194/acp-15-4215-2015, 2015.
6. Newchurch, M. J., Yang, E.-S., Cunnold, D. M., Reinsel, G. C., Zawodny, J. M., and Russell III, J. M.: Evidence for slowdown in stratospheric ozone loss: First stage of ozone recovery, J. Geophys. Res., 108, 4507, doi:10.1029/2003JD003471, 2003.
7. WMO: Scientific Assessment of Ozone Depletion: 2006, Global Ozone Research and Monitoring Project Report 50, World Meteorological Organization, Geneva, www.wmo.int/pages/prog/arep/gaw/ozone2006/ozoneasstreport.html, 2007.
8. WMO: Scientific Assessment of Ozone Depletion: 2010, Global Ozone Research and Monitoring Project Report 52, World Meteorological Organization, Geneva, www.unep.ch/ozone/AssessmentPanels/SAP/ScientificAssessment2010/00-SAP-2010-Assement-report.pdf, 2011.
9. Yang, E.-S., Cunnold, D. M., Salawitch, R. J., McCormick, M. P., Russell III, J. M., Zawodny, J. M., Oltmans, S., and Newchurch, M. J.: Attribution of recovery in lower-stratospheric ozone, J. Geophys. Res., 111, D17309, doi:10.1029/2005JD006371, 2006.

6.18 *hbk00059:* Joint state-parameter estimation for the Last Glacial Maximum with CESM1.2

HLRN Project ID:	hbk00059
Run time:	II/2017 – III/2021
Project Leader:	Prof. Dr. Michael Schulz
Project Scientist:	Dr. Tamás Kovács
Affiliation:	Fachbereich Geowissenschaften, MARUM--Zentrum für Marine Umweltwissenschaften, Universität Bremen

Overview

The PALMOD project seeks to understand climate system dynamics and variability during the last glacial cycle. Specific topics are: i) to identify and quantify the relative contributions of the fundamental processes which determined the Earth's climate trajectory and variability during the last glacial cycle, ii) to simulate with comprehensive Earth System Models (ESMs) the climate from the peak of the last interglacial (the Eemian warm period) up to the present, including the changes in the spectrum of variability, and iii) to assess possible future climate trajectories beyond this century during the next millennia with sophisticated ESMs tested in such a way.

Relevant to this computing project proposal, an expected major outcome of PALMOD is to obtain a comprehensive data synthesis of paleoclimatic conditions during the last glacial cycle, associated with explicit estimates of uncertainty. This involves combining in the best possible ways the outcome of long-term climate model simulations with the latest generation of multi paleo proxy data (planktic foraminifera, diatoms, dinoflagellates, radiolaria, geochemical proxies such as Mg/Ca in planktic foraminifera shells, etc.). In the current phase, our main focus is on the direct forward modeling of stable water isotopes, combined with a comprehensive analysis of reconstructed and simulated isotope distribution. For this, we are using a global and comprehensive Earth system model: the Community Earth System Model version 1.2, in its isotope-enabled configuration (Brady et al. 2019). This version can provide stronger constraints regarding model-data comparison than simulations of only the basic physical variables without the explicit simulation of isotopes.

Results

Since the previous period we have moved our simulations to HLRN-IV phase 2 in Berlin, and have conducted further performance tests with different processor layouts for the model components. In comparison with the performance at HLRN-IV phase 1 in Göttingen, we have been able to increase the model speed more than three times while also reducing the computing cost by 25%.

Due to changes in our working group, the project was interrupted in August 2019. After it was continued in February 2020, we identified the reason for the previously experienced lack of convergence of oceanic water isotopes in our preindustrial simulation: although the coupling of ^{18}O and HDO between model components was correct, the adjustment of their surface fluxes in the ocean component contained an error that caused the surface to receive only a fraction of the fluxes it should have. Restarting our previous preindustrial simulation now there is a convergence in oceanic water isotopic composition, and the simulated water isotopologues are stable in other components too.

The main features of the simulated spatial variations of water isotopes in precipitation are associated with spatial characteristics of precipitation and evaporation (Fig. 1a), and are in good agreement with observations. In general, there are high delta values in the subtropics, where evaporation dominates. In contrast, the polar regions are characterized by low delta values, corresponding to these regions being a terminus for the atmospheric water cycle with much more precipitation than evaporation. It is also notable that there are lower delta values over land, and higher values over sea, a feature that is also present in observations. The relationship between $\delta^{18}O$ and δD of precipitation (Fig. 1b) is captured remarkably well in iCESM. Their simulated values show a good correlation, and both the slope and the intercept of the global meteoric water line representing their relationship are close to values derived from observations that vary around 8 and 10, respectively.

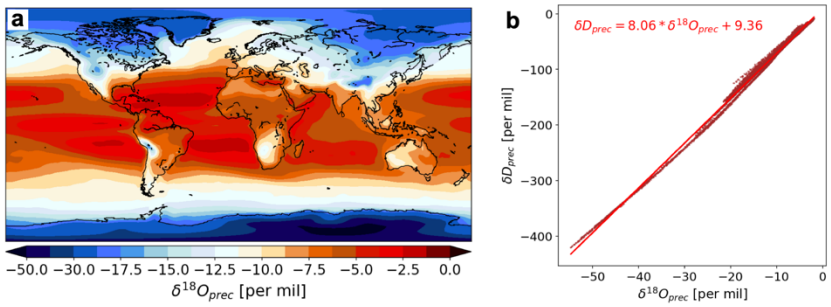

Figure 1: Water isotopes in precipitation from our preindustrial iCESM1.2 simulation: (a) map of precipitation $\delta^{18}O$ and (b) the relationship between precipitation $\delta^{18}O$ and δD.

The climatology of $\delta^{18}O$ in the ocean is shown on Fig. 2 that presents the vertical sections of the zonally averaged seawater $\delta^{18}O$ in the Atlantic and in the Pacific Sector. In our simulations (Fig. 2a-b) the surface waters are more enriched in the subtropics, and are depleted at high latitudes in both sectors. This relects that the stronger evaporation in the subtropics removes more of the lighter $\delta^{16}O$ there. This ^{16}O-enriched moisture is transported to high latitudes where it precipitaties, decreasing the delta values in the surface ocean. Except for at high latitudes, the surface and shallow waters in the Atlantic Ocean are much more enriched than in the Pacific Ocean, due to the net atmospheric moisture transport from the Atlantic to the Pacific basin.

In the subsurface, major water masses are identifiable by their isotopic composition. The signature of North Atlantic Deep Water is apparent in the Atlantic with $\delta^{18}O$ values around 0.2-0.3 per mil, and so are the Antarctic Intermediate Water and Antarctic Bottom Water in the south with slightly negative values.

We compare our simulation to a state estimate of Breitkreuz et al. (2018), shown in Fig. 2c-d. Compared to their reconstruction, our preindustrial simulation with iCESM1.2 shows a slight depleted bias in low/mid latitude surface waters. We can also see that the simulated values are somewhat too high for the deep ocean. For example, the $\delta^{18}O$ value of Antarctic Bottom Water in the Atlantic sector is just below zero in our simulation, in comparison with the much more depleted -0.3 per mil in the reconstruction. Nevertheless, our simulation captures relatively well the isotopic composition of major water masses not only in the surface, but also in subsurface waters. This is important, because seawater $\delta^{18}O$ has important applications in paleoclimatology, due to its strong relationship with salinity and temperature.

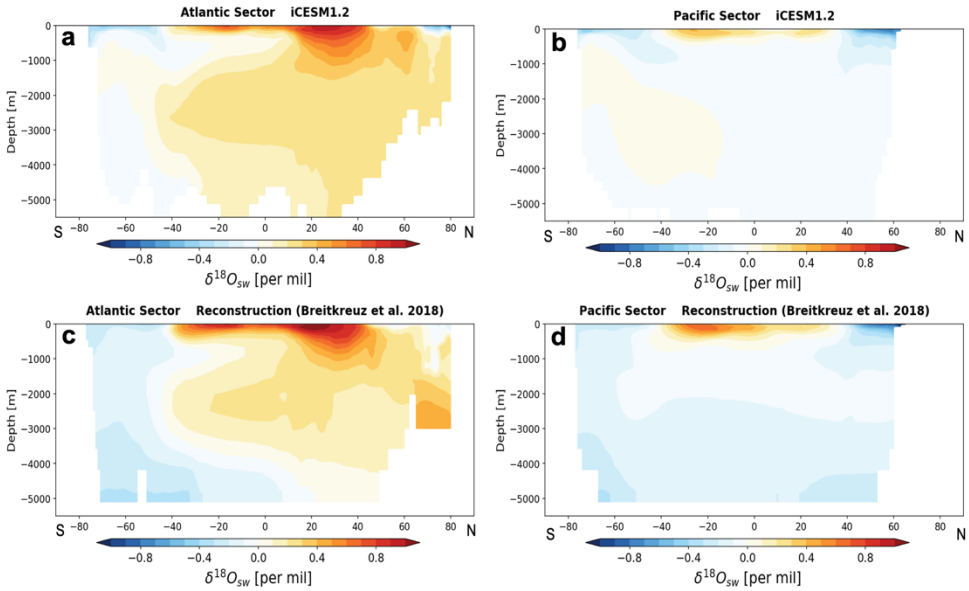

Figure 2: Vertical sections of the zonally averaged seawater $\delta^{18}O$ in the Atlantic Sector and in the Pacific Sector from (a,b) our preindustrial iCESM1.2 simulation, and from (c,d) the reconstruction of Breitkreuz et al. (2018).

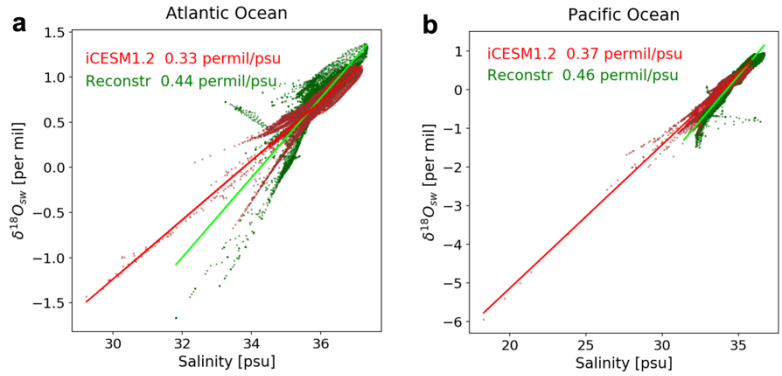

Figure 3: Scatter plots of ocean surface salinity and $\delta^{18}O$ in the (a) Altantic Ocean and in the (b) Pacific Ocean from our preindustrial iCESM1.2 simulation in red, and from the reconstruction of Breitkreuz et al. (2018) in red. The lines show the linear regression to data points, with their slope indicated in the plots.

The connection between surface salinity and $\delta^{18}O$ in the Altantic and in the Pacific Ocean is presented on scatter plots (Fig. 3). Data points from our iCESM1.2 simualtion are shown in red, and the reconstruction of Breitkreuz et al. (2018) are in green. The regression lines are also plotted along with the values for their slopes. According to this comparison, our simluation captures the robust relationship between the two variables in both oceans, although with a slighly shallower slope than what the reconstruction suggests. As seawater $\delta^{18}O$ is often used as a proxy for salinity, this indicates the potential of iCESM1.2 simulations for our planned paleoclimate experiments.

Outlook

Our planned experiments comprise transient simulations of different periods of the last glacial cycle, branching from a simulation that has reached equilibrium under climate forcings of a specific time-slice at the Last Glacial Maximum (LGM, 19-23 kyr BP). Within the coming year,

this computing project will focus on the effect of glacial meltwater forcing and its role in climate variability. For the first time, transient simulations of the Marine Isotope Stage 3 characterized by abrupt climate changes (Heinrich events), and the last deglaciation will be performed with a fully coupled model with a full carbon cycle, as well as carbon and oxygen isotopes.

The model results will be compared to the deglacial proxy-data synthesis prepared by the previous project phase. Furthermore, the integration of a proxy-system model and model-data comparison metrics in data assimilation algorithms for CESM will be evaluated, building on Kurahashi-Nakamura et al. (2017) and García-Pintado et al. (2018).

References

1. Brady, E., Stevenson, S., Bailey, D., Liu, Z., Noone, D., Nusbaumer, J., Otto-Bliesner, B. L., Tabor, C., Tomas, R., Wong, T., Zhang, J., Zhu, J, *The connected isotopic water cycle in the Community Earth System Model version 1*. Journal of Advances in Modeling Earth Systems, *11, 2547–2566 (2019).*
2. Breitkreuz, C., Paul, A., Kurahashi-Nakamura, T., Losch, M., and Schulz, M., *A dynamical reconstruction of the global monthly-mean oxygen isotopic composition of seawater*, J. Geophys. Res.-Oceans, *123, 7206–7219 (2018).*
3. J. García-Pintado, A. Paul, *Evaluation of iterative Kalman smoother schemes for multi-decadal past climate analysis with comprehensive Earth system models*, Geoscientific Model Development, *11, 5051-5084 (2018).*
4. Kurahashi-Nakamura, T., A. Paul, M. Losch, *Dynamical reconstruction of the global ocean state during the Last Glacial Maximum* Paleoceanography, *32, 326–350 (2017)*.

6.19 *hbk00062:* Retrieval of stratospheric ozone profiles from OMPS observations in limb geometry and long term trends

HLRN Project ID:	hbk00062
Run time:	IV/2017 – III/2021
Project Leader:	Dr. Alexei Rozanov
Project Scientists:	Dr. Carlo Arosio, Dr. Alexei Rozanov
Affiliation:	Institute of Environmental Physics, University of Bremen

Overview

A stratospheric ozone recovery is expected during the 21st century according to model studies (Eyring et al. 2010), as a consequence of the decreasing emission of chlorine-containing ozone depleting substances (ODSs) and the increasing concentration of CO_2 in the troposphere. ODSs are namely involved in catalytic cycles, which contribute to ozone destruction, while the increasing CO_2 concentration leads to a cooling of the stratosphere, which reduces the efficiency of some temperature-dependent ozone depleting reactions.

To monitor the status of the ozone layer and the onset of its recovery, satellite measurements are an important tool, as they provide observations with high temporal and spatial resolution. In particular, measurements in limb geometry, as performed by SCIAMACHY (SCanning Imaging Absorption spectroMeter for Atmospheric Chartography) and OMPS-LP (Ozone Mapping and Profiler Suite – Limb Profiler), enable the study of ozone profiles with a vertical resolution of about 3 km. However, single satellite missions are generally too short to assess long-term ozone changes and the merging of several time series is therefore required.

Several studies addressed the analysis of stratospheric ozone trends over the last decades, for example Harris et al. (2015), Sofieva et al. (2017) and Steinbrecht et al. (2017). The authors considered zonally averaged data and found a large variability between data sets. They detected positive trends in the upper stratosphere, particularly at mid-latitudes, a hint of the ozone recovery. In the lower stratosphere, where a decrease in ozone concentration is expected due to the speed-up of the tropical upwelling, results are still affected by a large uncertainty and the observation of negative trends still disputed (Ball et al. 2017).

In this framework, the main activities within this project are related to the retrieval of ozone profiles from OMPS-LP satellite observations, starting from the beginning of 2012 till present. The radiative transfer model and spectroscopic data bases are the same used for the retrieval of SCIAMACHY ozone profiles. The retrieval approach is also similar, in order to minimize systematic biases between the two time series. Once OMPS-LP ozone profiles are retrieved and validated, the second goal is the merging with the SCIAMACHY time series, to study altitude, latitude and longitude resolved ozone changes over the last 15 years. Improvements in the retrieval of ozone profiles have been implemented throughout the project and still ongoing, with a particular interest over the last year to the lower stratosphere in the tropics and to polar regions.

Results

1) Retrieval of ozone profiles

A new complete retrieval of the OMPS-LP time series (from February 2012 to December 2020) has been performed during the last months. The focus has been on two atmospheric regions:

the lower stratosphere, where the reduced sensitivity of limb observations and the low concentration of ozone make the retrieval more challenging, and the polar regions.

The sensitivity of the ozone retrieval in the lower stratosphere to several parameters, such as aerosol extinction, albedo, used spectral range and threshold for the cloud filter, was first investigated, with the aim of improving the quality of the profiles, particularly in the tropical lower stratosphere – upper troposphere.

We implemented the changes in the retrieval settings and to check the consistency of the produced data set, we validated the ozone profiles using ozonesonde measurements, particularly valuable in the lower stratosphere up to 30 km. The high vertically-resolved observations from sondes had first to be convolved with the averaging kernels of the retrieval, to be comparable with lower resolution satellite observations. Fig. 1 shows the results of the comparison in terms of averaged profiles in the tropics (panel a) and as relative differences between OMPS-LP and sonde ozone profiles, averaged over the 2012-2019 period. The improvement w.r.t. the previous version is shown in panel (b); a good agreement has been found on average down to 12 km, although a systematic positive discrepancy of about 10 % is visible at about 16-18 km.

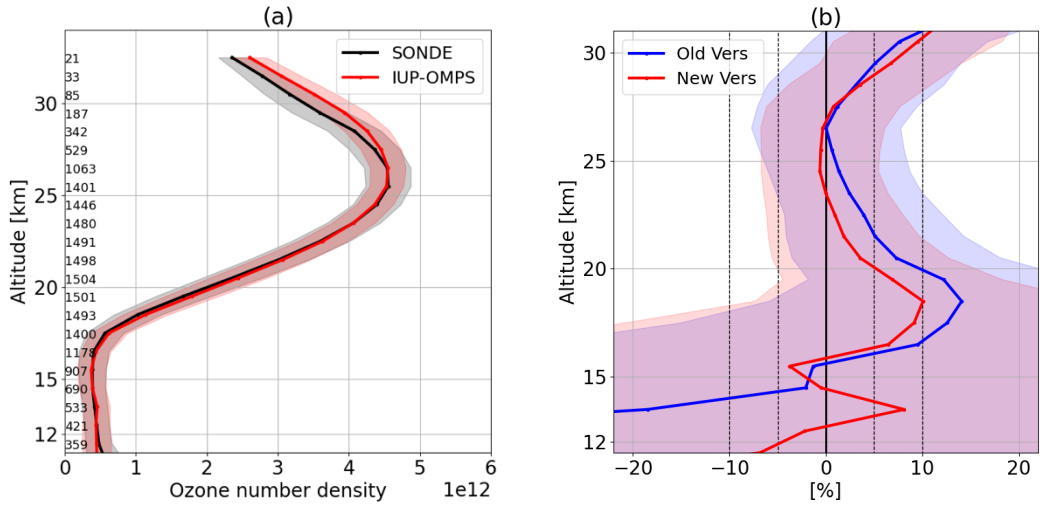

Figure 1: In panel (a), ozone profiles in the tropics [25°S, 25°N], averaged over the period 2012-2019, from OMPS retrievals and ozonesonde measurements. In panel (b), relative differences between OMPS and ozonesonde profiles for the old retrieval version and the current one (tropics, 2012-2019).

A second retrieval development over the last year is related to the polar regions. During local summer the extensive presence of polar mesospheric clouds (PMCs) perturbs the UV radiance used in the retrieval. These clouds are located at about 80 km but affect the ozone retrieval down to 40 km. First, a retrieval of PMCs was implemented, then this information was used in the ozone retrieval to take into consideration the presence of additional scatterers in the mesosphere. The processing of all measurements affected by the presence of PMCs has been performed over the 2012-2020 period and a validation of the results was done using MLS (Microwave Limb Sounder) satellite observations as a reference, which are not affected by these clouds (due to the used spectral range). The results of this validation are shown in Fig. 2 in terms of relative difference w.r.t. MLS. In panel (a), only profiles in the presence of PMCs are considered and the comparison with the standard retrieval version in blue shows that the mean relative difference in the northern polar region at 50 km decreases from ~40 % down to ~5 %, when PMCs are taken into account. In panel (b), all profiles are considered and the relative difference w.r.t. MLS is shown as a function of altitude and latitude. A very good agreement within ±5 % was found in most of the bins, with larger positive discrepancies in the southern hemisphere at about 30 km and in the tropics below 20 km.

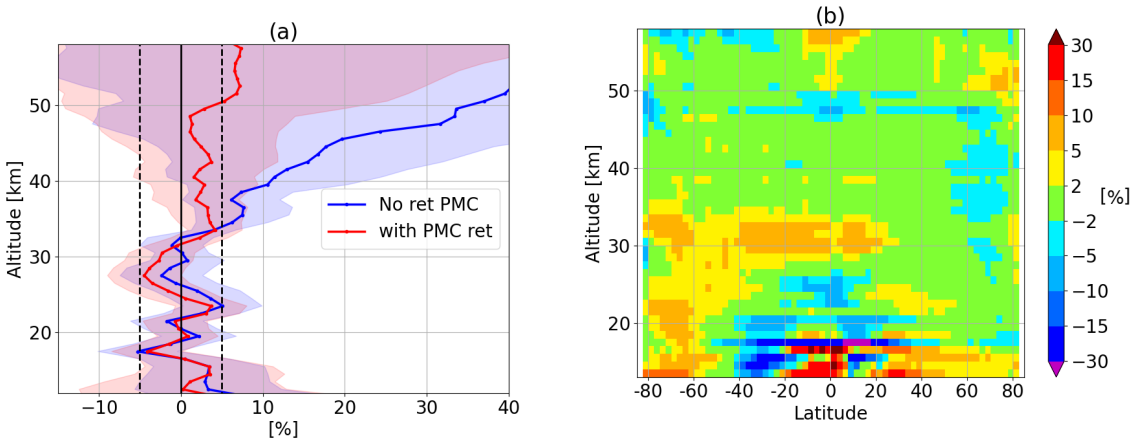

Figure 2: In panel (a), relative differences between OMPS and MLS observations, at northern polar latitude [60°N, 90°N] averaged over 2012-2019, before and after accounting for the presence of PMCs. In panel (b), relative difference between OMPS and MLS observations as a function of altitude and latitude, averaged over 2016.

2) Merging and long term trends

The merging with SCIAMACHY time series was performed using MLS satellite observations as a transfer function. SCIAMACHY and OMPS missions have an overlap of only 2 months, not sufficient to remove the bias between the two. By merging the two data sets, we obtained an ozone time series starting from 2003, vertically resolved every 3.3 km. Spatially, we binned the profiles every 5° latitude and 20° longitude, enabling the study of longitudinally resolved structures and changes in the ozone distribution. Details of the merging procedure can be found in Arosio et al. (2019).

A multi-linear regression model, accounting for several phenomena which affect the ozone distribution, like the Quasi Biennial Oscillation, the Solar activity and El Nino, was applied. Results are reported in Fig. 2: on the left panel zonally averaged trends over the 2003-2018 period are shown. Statistically significant trends correspond to non-dashed areas and were mainly found at mid-latitudes in the middle and upper stratosphere, with the highest values in the northern hemisphere. In the lower tropical stratosphere, we detected negative but not significant trends. In the right panel, the longitudinally resolved structure is displayed at 41 km, where a lage variability was found: positive values over the Canadian sector and small non-significant values over Siberia. The assessment of the stability and reliability of these longitudinal structures is still ongoing, exploiting a possible synergy with a chemistry transport model.

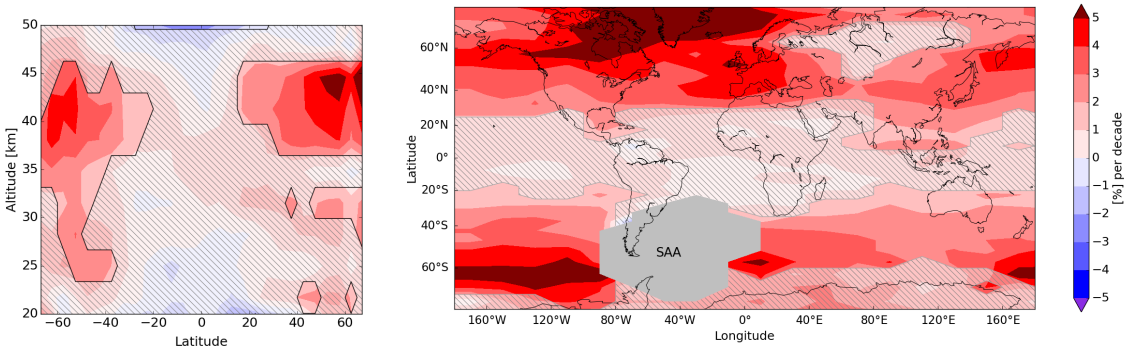

Figure 2: Long-term ozone changes over the 2003-2019 period: in the left panel the zonally averaged trends, in the right panel longitudinally resolved results at the altitude of 41 km. Shaded areas indicate non-significant trends.

In the tropical middle stratosphere over the last 15 years, a fluctuation of the trend has been found, from negative values until 2011 to positive values from 2011. The causes behind this change are still under investigations. Galytska et al. (2019) studied the long-terms changes over SCIAMACHY period and related the positive trend around 35 km in the tropics to dynamical changes: the vertical transport was found to speed up during winter months, causing a change in the residence time of NO_2, which in turns affects ozone concentration in this region.

Outlook

Further validation of the results is planned, with a particular interest in a longitudinally-resolved comparison with ozonesondes.

A comparison with a chemistry transport model is planned to help understanding the changes in ozone distribution over the last 15 years and assess the reliability of the longitude-resolved features that we found in our merged data set. This activity is part of a Living Planet Fellowship started in November 2020.

Publications

1. Arosio, C., et al. “Retrieval of ozone profiles from OMPS limb scattering observations.” Atmospheric Measurement Techniques, 11.4 (2018): 2135-2149.
2. Arosio, C., et al. “Merging of ozone profiles from SCIAMACHY, OMPS and SAGE II observations to study stratospheric ozone changes”, Atmospheric Measurement Techniques, 12.4, (2019): 2423-2444.
3. Arosio, C. “Retrieval of ozone profiles from OMPS-LP observations and merging with SCIAMACHY and SAGE II time series to study long-term changes.”, PhD dissertation, (July 2019).
4. Weber, M., et al. “The unusual stratospheric Arctic winter 2019/20: Chemical ozone loss from satellite observations and TOMCAT chemical transport model.“, Earth and Space Science Open Archive ESSOAr, (2020).

References

Ball, W. T., et al. "Continuous decline in lower stratospheric ozone offsets ozone layer recovery." *Atmospheric Chemistry and Physics* (2017).

Eyring, V., et al. "Multi-model assessment of stratospheric ozone return dates and ozone recovery in CCMVal-2 models." *Atmospheric Chemistry and Physics* 10.19 (2010): 9451-9472.

Galytska, E., et al. "Dynamically controlled ozone decline in the tropical mid-stratosphere observed by SCIAMACHY." *Atmospheric Chemistry and Physics* 19.2 (2019): 767-783.

Harris, N. R. P., et al. "Past changes in the vertical distribution of ozone–Part 3: Analysis and interpretation of trends." *Atmospheric Chemistry and Physics* 15.17 (2015): 9965-9982.

Sofieva, V. F., et al. "Merged SAGE II, Ozone_cci and OMPS ozone profile dataset and evaluation of ozone trends in the stratosphere." *Atmospheric Chemistry and Physics* 17.20 (2017): 12533-12552.

Steinbrecht, Wolfgang, et al. "An update on ozone profile trends for the period 2000 to 2016." *Atmospheric chemistry and physics* 17.17 (2017): 10675-10690.

6.20 *hbk00064:* Coupled ensemble data assimilation for Earth system models

HLRNProject ID:	hbk00064
Run time:	I/2019 – III/2021
Project Leader:	Prof. Dr. Thomas Jung[1,2]
ProjectScientists:	Dr. Qi Tang[2], Dr. Lars Nerger[2]
Affiliation:	[1]also at University of Bremen [2]Alfred-Wegener-Institute for Polar and Marine Research, Bremerhaven

Overview

Earth system models simulate different compartments like the ocean, atmosphere, or land surface. Data assimilation for Earth system modeling is challenging due to the complexity of different compartments within the model. In this project, we explore the role of data assimilation into an Earth system model which contains different compartments like the ocean and the atmosphere. Numerical experiments are carried out using the AWI climate model AWI-CM (Sidorenko et al., 2015) and the parallel data assimilation framework PDAF (http://pdaf.awi.de, Nerger et al., 2005, Nerger and Hiller, 2013). Within AWI-CM, the ocean model FESOM and the atmospheric model ECHAM are coupled through the coupler software OASIS3-MCT.

In the first step the system allows assimilating global satellite sea surface temperature (SST) and temperature and salinity profiles into the ocean state such that the atmospheric state is only influenced through the model dynamics, which is the so-called 'weakly coupled DA'. During the lst year, the system was extended for 'strongly coupled DA'. In this variant, the ocean observations can directly influence the state of the atmosphere by utilizing ensemble-estimated cross-covariances between the ocean and the atmosphere. The satellite SST observations used in this study are the Copernicus Level-3 product, which are available daily covering almost the complete globe (80 ^{o}N - 80 ^{o}S) with a resolution of 0.1 degrees. Data gaps exist due to clouds. The temperature and salinity profiles are from the EN4 data set from the UK MetOffice. They can reach down to 5000m and the average number of profiles is about 1000 per day. The sea surface height, velocity, temperature and salinity are updated daily using an ensemble Kalman filter (EnKF) for period of the year 2016. The ensemble size is set to 46. For FESOM, the resolution is varying between 160 km in the open ocean and about 30 km in the equatorial region and parts of the Arctic Ocean. For ECHAM a resolution of T63 with 47 layers is used. The initial ensemble was generated from an EOF decomposition of a 1-year model run for the same year 2016. For the one-year assimilation run, 12,144 processor cores were used with fully parallelized codes for 5.5 hours on HLRN.

Results

Four different simulation scenarios were carried out for different types of observations:
1) A free run scenario without data assimilation, denoted as 'Free_run';
2) A scenario where only the SST data were assimilated, denoted as 'DA_SST';
3) A scenario where only the profile data were assimilated, denoted as 'DA_proTS';
4) A scenario where both the SST and profile data were assimilated, denoted as 'DA_all'.

We analyze whether data assimilation can improve the prediction of ocean as well as the atmosphere states in a coupled ocean-atmosphere model by assimilating only the ocean observations. The root mean square error (RMSE) is calculated for the SST, and subsurface temperature and salinity over all the observation points and the whole simulation period to

evaluate the data assimilation experiments. An overview of the RMSE for different simulation scenarios is given in Figure 1.

1) Assimilation impact on the ocean temperature and salinity

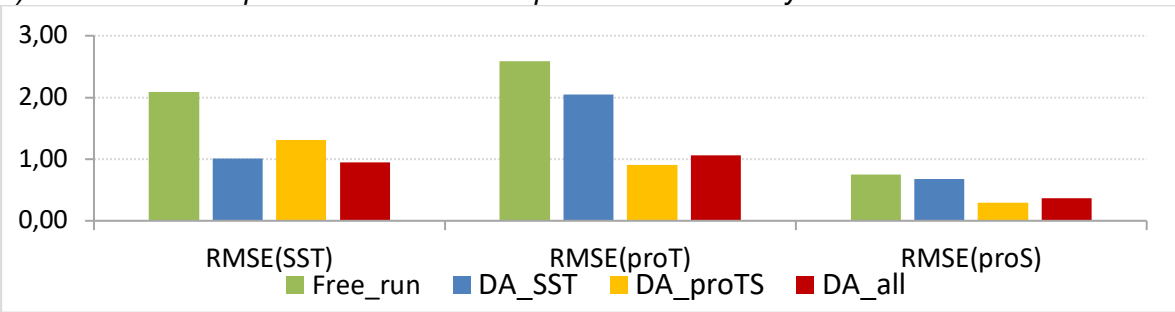

Figure 1: RMSE of SST, subsurface temperature and salinity for different simulation scenarios for the whole one-year simulation period.

When assimilating SST in DA_SST, the deviation between the modeled SST and the assimilated SST data is reduced globally by 50% compared to the free run. If only the subsurface temperature and salinity are assimilated (DA_proTS), the reduction of the RMSE of SST is still 35%. This indicates that the limited subsurface temperature information can also improve the SST, utilizing the highly vertical correlations in the mixed layer. The RMSE of the subsurface temperature is reduced by 18% by assimilating only the surface temperature (DA_SST), which again shows that the temperature at deeper layers is highly related to the surface temperature.

Figure 2 shows the SST difference between the model simulation and the observations at the end of the assimilation period on 31st Dec 2016. It is strongly decreased when assimilating either the surface or the subsurface temperature or both of them. The global average of the absolute SST difference is only 0.44 °C for scenario DA_SST compared to 1.54 °C for the free run. The subsurface deviation is also reduced by all the assimilation runs, which is not shown here. The reduction can be up to 65% by scenario DA_proTS, and 30% by scenario DA_SST.

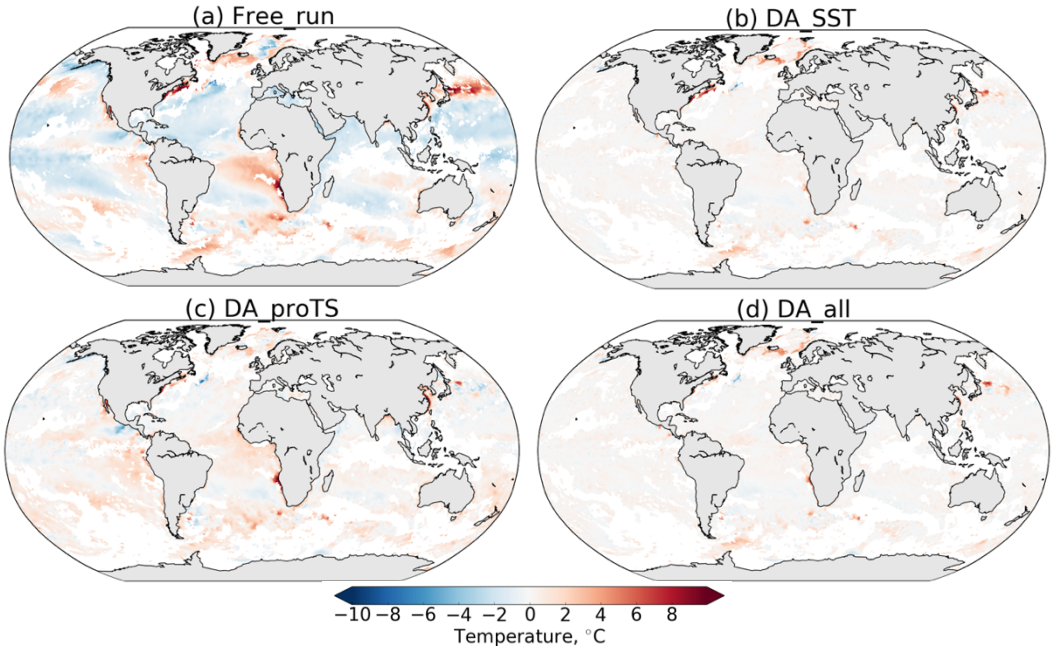

Figure 2: Difference of sea surface temperature between the model simulation and the observations on December 31st, 2016 for different simulation scenarios: a) Free_run, b) DA_SST, c) DA_proTS and d) DA_all.

Assimilating the profile observations in scenario DA_proTS leads to a 51% reduction in the RMSE of the subsurface salinity compared to the free run. If only SST is assimilated (DA_SST), the error in the salinity is reduced by 7%. This is quite limited compared to the other scenarios. As expected, scenario DA_all gives the lowest errors for the salinity prediction with an RSME reduction of subsurface salinity of up to 59%.

2) Assimilation impact on the atmosphere temperature and wind velocity

We evaluate the impact of the DA into the ocean on the atmosphere by comparing the atmospheric variables from the model prediction with daily fields from the ERA-Interim atmospheric reanalysis provided by ECMWF (Berrisford et al., 2011) for temperature at 2m above surface, surface pressure, zonal and meridional wind velocity at 10m above surface.

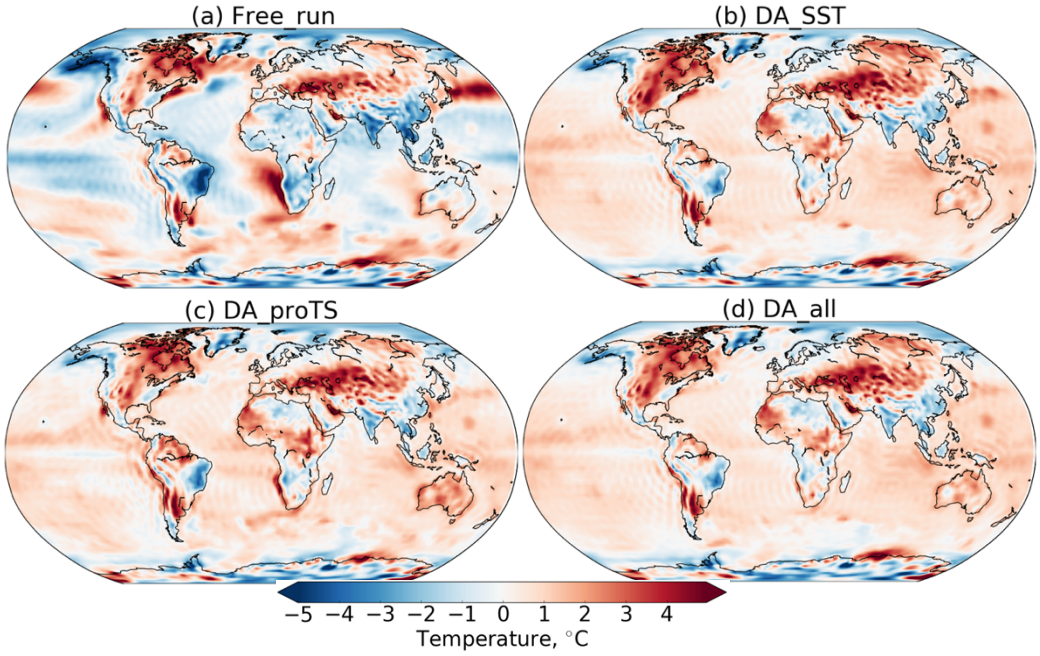

Fig. 3: Annual mean difference of temperature at 2m above surface for different simulation scenarios: (a) the free run, (b) DA_SST, (c) DA_proTS and (d) DA_all.

Figure 3 shows the mean difference for the months March to December of temperature at 2m above surface between the model simulation and the ERA-Interim reanalysis data for the different simulation scenarios. In general, the three assimilation runs show a smaller difference than the free run in essentially all oceans. When assimilating only profile data in DA_proTS, the predicted 2-m temperature is also closer to ERA-Interim than the free run yielding a similar spatial pattern to assimilating only SST or both the SST and profile data. While the amplitude of the difference is generally smaller and more homogeneous for the assimilation scenarios compared to the free run, a positive bias is visible everywhere over the oceans except in the Arctic Ocean and parts of the Southern Ocean. While the free run has a bias of -0.15 °C, the assimilation leads to this positive bias of 0.32 °C for DA_SST, 0.26 °C for DA_proTS, and 0.28 °C for DA_all. Thus, the assimilation of DA_SST has the largest effect.

As SST is at the interface of the ocean and the atmosphere, an improved prediction of SST is expected to lead to a better prediction of the temperature in the atmosphere. However, the effect is only direct for the air temperature above the ocean. Over the continents the changes in the 2-m temperature are less evident than over the ocean. In particular the strong negative bias over South America is reduced by the assimilation. Likewise, the negative bias over India and South-East Asia is reduced. On the other hand the positive bias extending from the eastern Mediterranean to Siberia is increased.

Over land, the 10-m meridional and zonal wind velocities in the free run and the three data assimilation runs are rather similar (figures now shown in this report). The assimilation does not give rise to significant influence on the velocities there.

Outlook

The results discussed above represent the weakly coupled data assimilation, which is limited to assimilating only ocean observations. They are published by Tang et al. (2020). Further the implementation aspect in PDAF is published in Nerger et al. (202). The experiments using strongly coupled assimilation have been completed. They are currently being analized and prepared for publication.

Publications

Tang, Q., Mu, L., Sidorenko, D., Goessling, H., Semmler, T., Nerger, L. (2020) Improving the ocean and atmosphere in a coupled ocean-atmosphere model by assimilating satellite sea surface temperature and subsurface profile data. Q. J. Royal Metorol. Soc., 146, 4014-4029 doi:10.1002/qj.3885

Nerger, L., Tang, Q., Mu, L. (2020). Efficient ensemble data assimilation for coupled models with the Parallel Data Assimilation Framework: Example of AWI-CM. Geoscientific Model Development, 13, 4305–4321, doi:10.5194/gmd-13-4305-2020

References

Berrisford, P., et al. (2011). The ERA-Interim archive, version 2.0.

Nerger, L., and W. Hiller (2013), Software for ensemble-based data assimilation systems – Implementation strategies and scalability, Computers & Geosciences, 55, 110-118.

Nerger, L., W. Hiller, and J. Schröter (2005), PDAF-the parallel data assimilation framework: experiences with Kalman filtering, in Use Of High Performance Computing In Meteorology, edited, pp. 63-83, World Scientific.

Sidorenko, D., et al. (2015), Towards multi-resolution global climate modeling with ECHAM6–FESOM. Part I: model formulation and mean climate, Climate Dynamics, 44(3), 757-780.

6.21 *hbk00071:* Development of an Earth system model coupled with a sediment diagenesis model toward long-term paleoclimate simulations

HLRNProject ID:	hbk00071
Run time:	I/2020 – IV/2020
Project Leader:	Prof. Dr. Michael Schulz
Project Scientists:	Dr. Takasumi Kurahashi-Nakamura
Affiliation:	Fachbereich Geowissenschaften, MARUM – Zentrum für Marine Umweltwissenschaften, Universität Bremen

Overview

The CO_2 concentration in the atmosphere (hereafter, CO_2 level) has been increasing so that it has reached a level that is unprecedented for at least the last 800,000 years. Our life in the future can suffer from the increase in the CO_2-level in many respects. To reliably project the CO_2 level in the future, it is essential to understand the mechanisms for CO_2-level changes and to have comprehensive Earth System Models (ESMs) including the latest knowledge and skills.

The last glacial cycle in the last 100 kyrs is considered to be one of the most qualified research targets offering many test cases with large variations in the CO_2 level. Thus far, comprehensive models are unable to quantitatively reproduce the CO_2-level history in the 100 kyrs. This project will tackle that issue by focusing on the marine carbon cycle because it is widely considered that the ocean would have played a key role in the variations of the CO_2 level.

In the last two phases of this project, we carried out an interactive coupling of the Community Earth System Model version 1.2 (CESM1.2) and Model of Early Diagenesis in the Upper Sediment of Adjustable complexity (MEDUSA) and found that the MEDUSA-coupled CESM outperformed the uncoupled CESM in reproducing the observation-based global distribution of sediment properties through modern-based simulations. The coupling also contribute to the better modelling of exchange of biogeochemical matter between the bottom seawater and ocean-floor sediments, which would lead to the improvement of model representation of seawater chemistry. Moreover, the sediment model will act as a “bridge” between the ocean model and paleoceanographic data providing an important fingerprint for the paleo-carbon cycle.

Following them, we proceeded to a series of time-slice simulations aiming at the Last Glacial Maximum (LGM, 19–23 kyr BP) and constrained the physical ocean state by paleoceanographic evidence. To simulate the carbon cycle including marine carbon isotopes in the LGM and to initialize simulations for the subsequent time period (Termination I), it was required to adequately reconcile the modelled tracer distributions for the LGM with the corresponding observation-based reconstructions.

Results

For the purpose, we conducted a sensitivity study consisting of several LGM time-slice runs with different ocean circulation fields to see the dependency of the biogeochemical ocean state on its physical state. Considering the model would have potential uncertainties of freshwater budget on the sea surface around large ice sheets during the glacial period, we

focused on changing the freshwater budget to alter buoyancy flux especially in high-latitude regions that would have a large influence on the deep convection of seawater.

Following several test runs, we managed to obtain three LGM simulations having different global ocean states: 1. an LGM run without any artificial freshwater addition or subtraction that has a stronger and deeper AMOC than in our standard PI run (LGMorg), 2. an alternative run with positive (i.e. additional) freshwater flux onto the high-latitude North Atlantic, which led to a weaker and shallower AMOC (LGMws), and 3. another LGM run with negative freshwater flux for the high-latitude North Atlantic, and for the Weddell Sea and the Ross sea as well, which has a stronger but shallower AMOC (LGMss).

We subsequently conducted biogeochemical simulations corresponding to each of the three physical ocean states. Thereby, we were able to evaluate those three characteristic ocean states from various perspectives. For this particular purpose, aiming at a better comparison with observation-based data, the CESM output was downscaled to a 1deg x 1deg horizontal grid to drive MEDUSA, so that MEDUSA can be forced by more accurate water-depths that would enhance the carbonate chemistry in the model. As a result, we obtained a better model--data agreement for a modern case than in the preceding study (Kurahashi-Nakamura et al., 2020) in some small-scale regions.

Model--data comparisons in terms of the difference between LGM and PI in biogeochemical-tracer distributions along an Atlantic section evidently distinguish the ocean state with a deeper AMOC from those with shallower AMOC (Figs. 1 and 2). The noticeable negative anomaly of $d^{13}C_{dic}$ in the deep ocean (deeper than ~2500 m) found in the observation-based reconstruction by Oppo et al. (2018) was reproduced only in the model oceans with a shallower AMOC (LGMss and LGMws), which suggest that an ocean state having a shallower AMOC (and a shoaled northern-source deep water) would be much preferable.

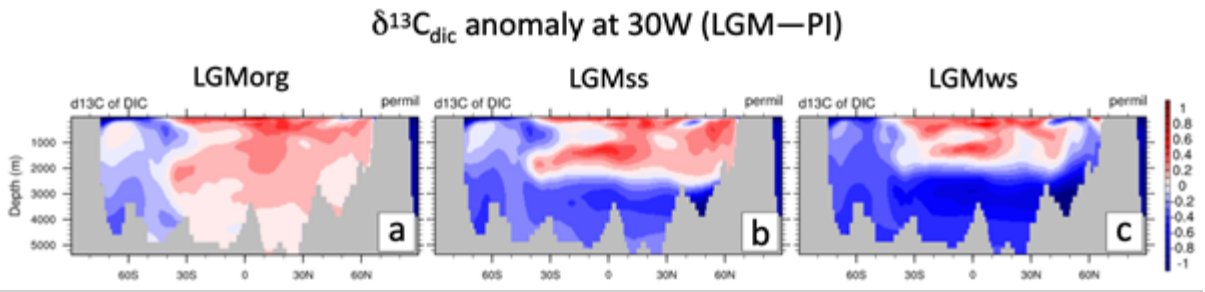

Figure 1: Simulated distribution of d13Cdic along an Atlantic meridional section. The differences between each of the LGM runs and the PI run are shown: (a) LGMorg, (b) LGMss, and (c) LGMws.

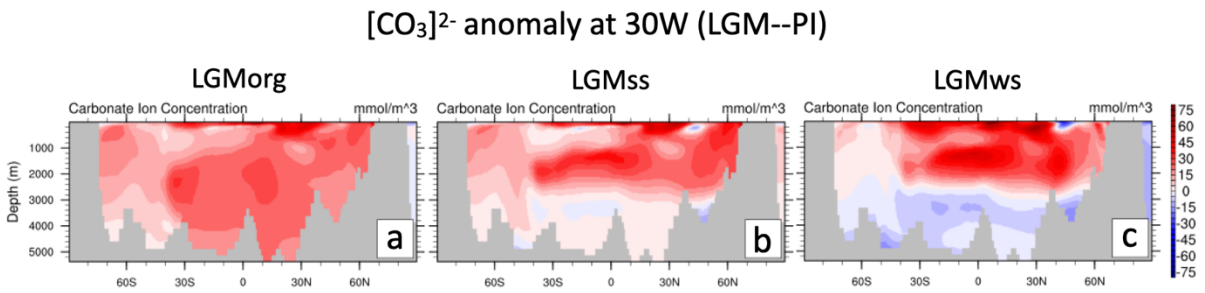

Figure 2: Simulated distribution of the carbonate ion concentration along an Atlantic meridional section. The differences between each of the LGM runs and the PI run are shown: (a) LGMorg, (b) LGMss, and (c) LGMws.

The anomalies of the carbonate ion concentration strongly supported the fact. Moreover, the carbonate-ion anomalies might even prefer the weaker-and-shallower AMOC case (LGMws) based on the concurrence with the observation-based reconstruction by Yu et al. (2020) that shows lower carbonate-ion concentrations by 30-40 mmol/m^3 in the deep Atlantic (deeper then ~3000 m) for the LGM.

On the other hand, the simulated global fields of the $CaCO_3$ weight-fraction in the upper sediment were more elusive to interpret (Fig. 3). A key observational fact is that the weight fraction for the LGM is lower in the Atlantic and higher in the Pacific than the modern counterparts (Catubig et al., 1998), and all of the three LGM simulations satisfy the requirement in spite of the much diverse global ocean states. Further detailed analyses will be made to understand the processes to control the weight-fraction distributions.

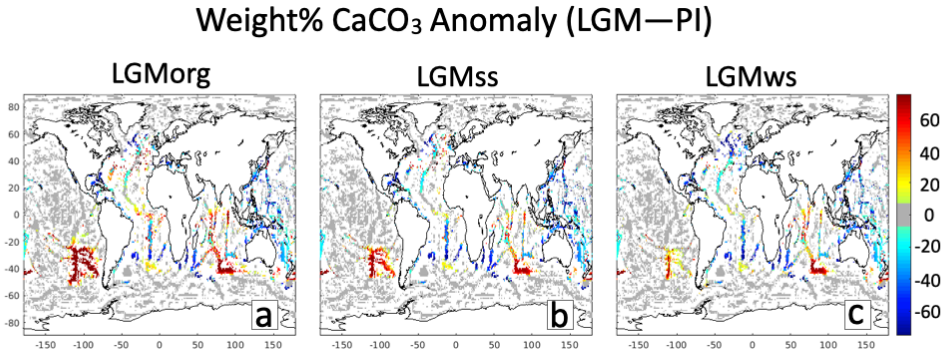

Figure 3: Simulated weight percentage of calcite in the upper sediment. The differences between each of the LGM runs and the PI run are shown: (a) LGMorg, (b) LGMss, and (c) LGMws. Note that the regions where the 1deg x 1deg bathymetry is out of the POP2 depth domain are excluded.

In summary, we managed to reconcile a modelled ocean state for the LGM with important observation-based constraints by taking into account the uncertainties of the freshwater budget at the ocean surfaces in high latitudes. In other words, we have obtained a common model configuration (e.g. fundamental model parameters) that provides appropriate model performance both for the PI and LGM, and are ready for the next simulations in the coming phase.

Outlook

In the coming phase of the project, we will extend the current framework to the time evolution of the global climate during the transition from the glacial to the interglacial climate state (Termination I), and during another characteristic time period in the last glacial cycle that shows remarkable millennial-scale climate variability (Marine Isotope Stage 3; MIS3).

It is known that the millennial-scale climate variability during the Pleistocene was most pronounced during intermediate glacial conditions like MIS3 (approx. 60–25 ka BP), rather than during interglacial and fully glaciated climates like LGM. Although the mechanisms of the climate variations during MIS3 are still unclear, it has been suggested that the variations were closely related to the change in the strength of the AMOC that was possibly caused by fresh-water input into the North Atlantic. On the other hand, a significant increase in the CO_2 level during some of the colder “stadial” periods in MIS3 is observed in Antarctic ice core records, suggesting presumable interactions between the physical ocean states and the marine carbon cycle. The response of the marine carbon cycle including the upper-sediment properties to the climate changes at millennial timescales and under a glacial background climate state is unclear because previous modelling studies were mostly limited to the physical systems and did not detail the biogeochemical aspects during MIS3.

Those work will provide other test cases to investigate the responses and roles of the carbon cycle in the ocean--sediment system in paleo climate variations.

Publications

1. T. Kurahashi-Nakamura, A. Paul, G. Munhoven, U. Merkel, and M. Schulz, *Coupling of a sediment diagenesis model (MEDUSA) and an Earth system model (CESM1.2): a contribution toward enhanced marine biogeochemical modelling and long-term climate simulations*, Geosci. Model Dev., 13, 825–840, https://doi.org/10.5194/gmd-13-825-2020 (2020)

References

1. Catubig, N. R., et al.: *Global deep-sea burial rate of calcium carbonate during the Last Glacial Maximum*, Paleoceanography, 13(3), 298-310, doi:10.1029/98PA00609, 1998.
2. Oppo, D.W., et al.: *Data Constraints on Glacial Atlantic Water Mass Geometry and Properties,* Paleoceanography and Paleoclimatology, 33: 1013-1034. doi:10.1029/2018PA003408, 2018.
3. Yu, J., et al.: *Last glacial atmospheric CO_2 decline due to widespread Pacific deep-water expansion,* Nat. Geosci. 13, 628–633, https://doi.org/10.1038/s41561-020-0610-5, 2020.

6.22 *hbk00072:* Interannual variability of air-sea CO2 exchange: high-resolution ocean biogeochemical simulations

HLRNProject ID:	hbk00072
Run time:	I/2019 – IV/2020
Project Leader:	Dr. Dieter Wolf-Gladrow[1]
ProjectScientists:	Dr. Judith Hauck[2], Dr. Özgür Gürses
Affiliation:	Alfred Wegener Institute, Helmholtz Centre for Polar and Marine Research, [1]principal investigator, also at the University of Bremen, [2]project administrator

Overview

Carbon dioxide (CO2) emissions from fossil fuels and land-use change amounted to 11.7 PgC yr^{-1} in 2019 (Friedlingstein et al., 20120) and force anthropogenic climate change. Ocean and land sinks provide an extremely valuable service to humankind by each drawing down about 25% of anthropogenic CO2 emissions (Le Quéré et al., 2018a), thereby slowing the rate of anthropogenic climate change. On time-scales longer than a century the ocean will be the main repository for anthropogenic CO2 emissions (Archer et al., 1997) and the Southern Ocean is the main conduit by which this CO2 enters the ocean (Khatiwala et al., 2009).

In the Global Carbon Budget 2018 (Le Quéré et al., 2018a), a model evaluation metric was introduced that illustrates the mismatch between modelled and observed surface ocean pCO2. It illustrates the amplitude of interannual variability that the models and the pCO2-based flux products (Rödenbeck et al., 2014; Landschützer et al., 2014, surface ocean CO2 Atlas, SOCAT) produce. One important outcome of this evaluation is that models and data-products disagree on interannual to decadal variability that is seen in the pCO2-based flux products, especially in the temperate and high-latitudes (polewards of 30° N/S). The 'true' magnitude of variability, however, remains unknown as also various data-products result in different amplitudes of variability (e.g., DeVries et al., 2017).

In this project, we use FESOM (Finite Element Sea Ice-Ocean Model v. 1.4, Wang et al. 2014) coupled to REcoM2 (Regulated Ecosystem Model 2, Geider et al., 1996, 1998). Our main objective is to quantify the differences between low and high ocean resolution to test the hypothesis that variability of ocean circulation and air-sea CO2 exchange will change in a higher resolution set-up.

Methods

We compare simulations performed with FESOM1.4-REcoM2 on two unstructured meshes having non-uniform resolution distributions (Fig. 1). The first mesh is a relatively coarse resolution mesh containing almost 0.13 M surface nodes (CORE). Most parts of the global ocean have a nominal resolution of 1° except north of 50° N, where resolution is increased to ca. 25 km, and in the equatorial belt, where resolution is increased to 1/3°.

The design of the second mesh uses a metric called resolution density function (RDF). RDF is produced based on the information from the pattern of sea surface height (SSH) variance from satellite altimetry (AVISO). In areas of high variability such as western boundary currents or along the coastlines, RDF is further increased to provide higher resolution up to 10 km (see Sein et al. 2016, for details).

We performed a high-resolution ocean model spin-up run with JRA55 forcing. The spin-up span one full cycle from 1958 – 2017, and a second cycle 1958-1980 using the HR. We initialized our model from an existing simulation driven by CORE-II forcing (Large and Yeager (2009)). We branched of our simulations with coupled physics and biogeochemistry at the end of 1980 and run two simulations from 1981 to 2019 using the HR mesh 1) with constant atmospheric CO2 concentration and climatological forcing to quantify a potential model drift (simulation B) and 2) with an increasing atmospheric CO2 concentration and interannual varying atmospheric forcing (simulation A). The initial biogeochemical model fields for the year 1980 are taken from a simulation on the CORE mesh and are interpolated to the HR mesh. This approach of interpolating biogeochemical fields to a higher resolution grid is also applied in other modelling groups to produce high-resolution ocean biogeochemical model simulations (e.g. Terhaar et al., 2018) due to computational costs of running expensive biogeochemical models in high resolution. Both simulations have been completed, recently.

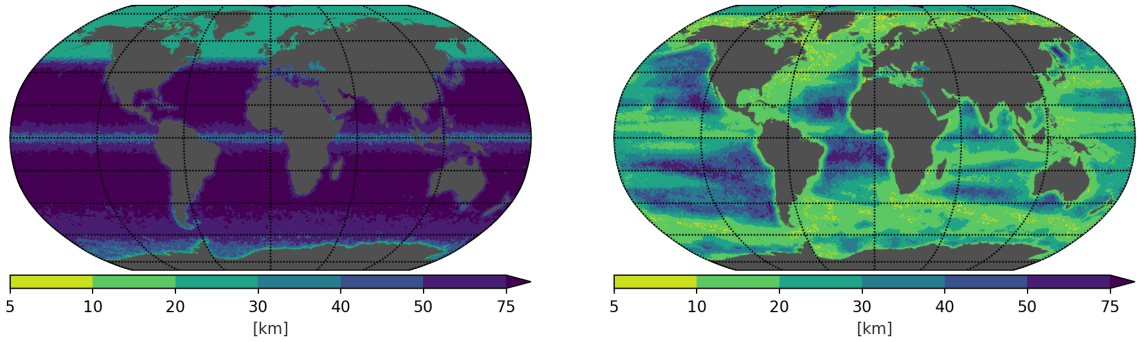

Figure 1: Mesh resolution of the model grids used in this study. CORE (left) and HR (right) that is produced to meet sea surface height in addition to Rossby radius of deformation, respectively. Number of surface nodes: CORE = ~0.13 M, HR = ~1.3 M.

Preliminary Results

We observe differences in regional CO2 flux time-series in the control simulation between the two meshes. This might be partly related to initialisation of the biogeochemical fields in 1980. Large-scale remain the spatial patterns of the CO2 flux same, but on a smaller scale differences occur, e.g. there is more variation of the CO2 flux along longitude in the Southern Ocean. These differences will be analyzed with respect to topographic features, circulation, etc. Preliminary analyses suggest that resolution has a modest impact on the integrated CO2 fluxes and their variability, especially in the high-latitudes.

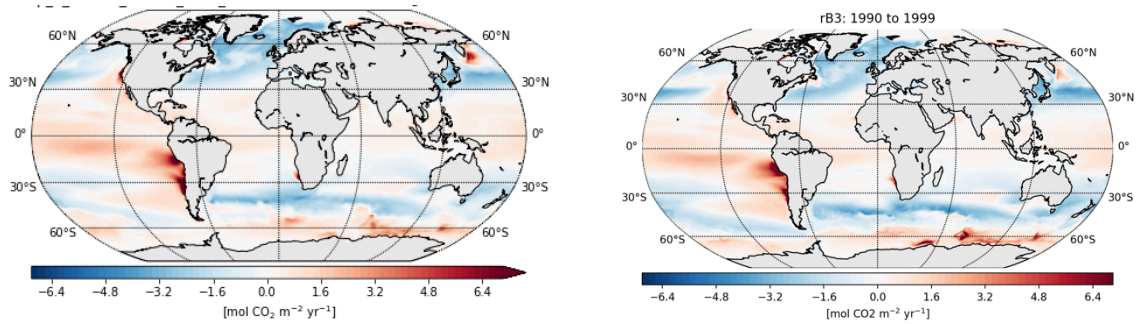

Figure 2: Simulated spatial distribution of sea-air CO_2 flux (left panel:CORE mesh, right panel:HR mesh) in the simulation B (control simulation) averaged over the time period 1990-1999. Negative values means fluxes are into the ocean.

References

Archer, D., H. Kheshgi, and E. Maier-Reimer (1997), Multiple timescales for neutralization of fossil fuel CO2, Geophysical Research Letters, 24, 405–408, doi:10.1029/97GL00168.

DeVries, T., M. Holzer, and F. Primeau (2017), Recent increase in oceanic carbon uptake driven by weaker upper-ocean overturning, Nature, 542(7640), 215, doi:10.1038/nature21068.

Geider, R. J., MacIntyre, H. L., and Kana, T. M.: A dynamic model of photoadaptation in phytoplankton, Limnol. Oceanogr., 41, 1–15, 1996.

Geider, R. J., MacIntyre, H. L., and Kana, T. M.: A dynamic regulatory model of phytoplanktonic acclimation to light, nu- trients, and temperature, Limnol. Oceanogr., 43, 679–694, doi:10.4319/lo.1998.43.4.0679, 1998.

Khatiwala, S., F. Primeau, and T. Hall (2009), Reconstruction of the history of anthropogenic CO2 concentrations in the ocean, Nature, 462, 346–349, doi:10.1038/nature08526.

Landschützer, P., N. Gruber, D. C. E. Bakker, and U. Schuster (2014), Recent variability of the global ocean carbon sink, Global Biogeochemical Cycles, 28(9), 927–949, doi:10.1002/2014GB004853.

Large, W. G., and S. G. Yeager (2009), The global climatology of an interannually varying air–sea flux data set, Climate Dynamics, 33(2), 341–364, doi:10.1007/s00382-008-0441-3.

Le Quéré, C., R. M. Andrew, P. Friedlingstein, S. Sitch, J. Hauck, J. Pongratz, P. A. Pickers, J. I. Korsbakken, G. P. Peters, J. G. Canadell, A. Arneth, V. K. Arora, L. Barbero, A. Bastos, L. Bopp, F. Chevallier, L. P. Chini, P. Ciais, S. C. Doney, T. Gkritzalis, D. S. Goll, I. Harris, V. Haverd, F. M. Hoffman, M. Hoppema, R. A. Houghton, G. Hurtt, T. Ilyina, A. K. Jain, T. Johannessen, C. D. Jones, E. Kato, R. F. Keeling, K. K. Goldewijk, P. Landschützer, N. Lefèvre, S. Lienert, Z. Liu, D. Lombardozzi, N. Metzl, D. R. Munro, J. E. M. S. Nabel, S. Nakaoka, C. Neill, A. Olsen, T. Ono, P. Patra, A. Peregon, W. Peters, P. Peylin, B. Pfeil, D. Pierrot, B. Poulter, G. Rehder, L. Resplandy, E. Robertson, M. Rocher, C. Ro ̈denbeck, U. Schuster, J. Schwinger, R. Séférian, I. Skjelvan, T. Steinhoff, A. Sutton, P. P. Tans, H. Tian, B. Tilbrook, F. N. Tubiello, I. T. van der Laan-Luijkx, G. R. van der Werf, N. Viovy, A. P. Walker, A. J. Wiltshire, R. Wright, S. Zaehle, and B. Zheng (2018a), Global carbon budget 2018, Earth System Science Data, 10(4), 2141–2194, doi:10.5194/essd-10-2141- 2018.

Rödenbeck, C., D. C. E. Bakker, N. Metzl, A. Olsen, C. Sabine, N. Cassar, F. Reum, R. F. Keeling, and M. Heimann (2014), Interannual sea-air CO2 flux variability from an observation-driven ocean mixed-layer scheme, Biogeosciences, 11(17), 4599–4613, doi:10.5194/bg-11-4599-2014.

Sein, D. V., S. Danilov, A. Biastoch, J. V. Durgadoo, D. Sidorenko, S. Harig, and Q. Wang (2016), Designing variable ocean model resolution based on the observed ocean variability, Journal of Advances in Modeling Earth Systems, 8(2), 904–916, doi:10.1002/2016MS000650.

Terhaar, J., J. C. Orr, M. Gehlen, C. Eth ́e, and L. Bopp (2018), Model constraints on the anthropogenic carbon budget of the Arctic Ocean, Biogeosciences Discussions, 2018, 1–36, doi:10.5194/bg-2018-283.

Wang, Q., Danilov, S., Sidorenko, D., Timmermann, R., Wekerle, C., Wang, X., Jung, T., and Schröter, J.: The Finite Element Sea Ice–Ocean Model (FESOM) v.1.4: formulation of an ocean general circulation model, Geosci. Model Dev., 7, 663–693, doi:10.5194/gmd-7-663-2014, 2014.

Publications and Presentations

Biogeochemical simulations have just finished, no publications yet.

6.23 *hbk00075:* Assessing the effect of environmental and biological conditions on Antarctic krill large-scale connectivity facilitated by ocean currents

HLRN-Projektkennung:	hbk00075
Laufzeit:	IV/2019 – IV/2021
Projektleiter:	Prof. Dr. Dieter Wolf-Gladrow[1]
Projektbearbeiter.	Dr. Judith Hauck[2], Dr. Bettina Fach, Dr. Ralph Timmermann
Institut / Einrichtung:	Alfred-Wegener-Institut, Helmholtz Zentrum für Polar- und Meeresforschung [1] principal investigator, also at the University of Bremen, [2] project administrator

Overview

In this project we use a global version of the Finite Element Sea Ice-Ocean Model (FESOM) coupled with the Regulated Ecosystem Model 2 (REcoM2) to investigate the possible connectivity of Antarctic krill (*Euphausia superba*) throughout the Southern Ocean via ocean currents with special focus on the Lazarev Sea. The aim is to find populations supplying input to the Lazarev Sea krill population, and investigate how environmental and biological parameters such as temperature and food availability influence the survival of krill during such a long-distance transport. Transport and connectivity of Antarctic krill between regions spatially far apart have been demonstrated for the western Antarctic Peninsula and South Georgia regions (Hofmann et al., 2002; Fach and Klinck, 2006; Fach et al, 2006). Separate, observational studies in the Lazarev Sea concluded that this region does not support a single self-maintaining population, but represents a complex transition zone of stocks with different origins. Krill found in the Lazarev Sea may possibly originate in the Scotia Sea and the Cosmonaut Sea. It is this hypothesis that this project is going to investigate.

In this project special emphasis is laid on an adequate representation of eddy-resolving current dynamics in the greater Lazarev Sea area (between 20°W to 40°E), specifically the continental shelf and the upwelling regions, through a higher resolution grid in this region. Lagrangian particle simulations with an individual based model (IBM) of krill utilize the FESOM-REcoM2 model output in form of environmental conditions (temperature, salinity and currents) as well as biological conditions (phytoplankton and zooplankton distribution and abundance) and elucidate how environmental and biological factors impact population dynamics of Antarctic krill during transport.

Aim

The aim of this study is to quantify the connectivity of Antarctic krill living in different regions in the Southern Ocean large distances apart and how both environmental (temperature, currents) and also biological factors (food concentration) can impact this connectivity. To achieve this, we 1) investigate the impact of the horizontal model resolution on the representation of filaments, fronts and eddies, 2) find out from which regions krill populations can supply input to the Lazarev Sea krill population, and 3) investigate how environment and biological parameters influence the survival of krill during such a long-distance transport.

Results

In the first project phase, the resolution of the BOLD mesh (also called HR grid in Sein et al., 2016) used with FESOM was increased in an area between 20°W to 40°E, the larger Lazarev Sea region, so that it becomes eddy resolving (Figure 6). We named this the LAZAREV grid. This is of importance in the context of this study, as eddies are important features for krill retention and accumulation of food such as phytoplankton and copepods. In the vertical dimension z-coordinates are used. The current model setup has a total of 47 levels with resolution of 10 m in the top 100 m.

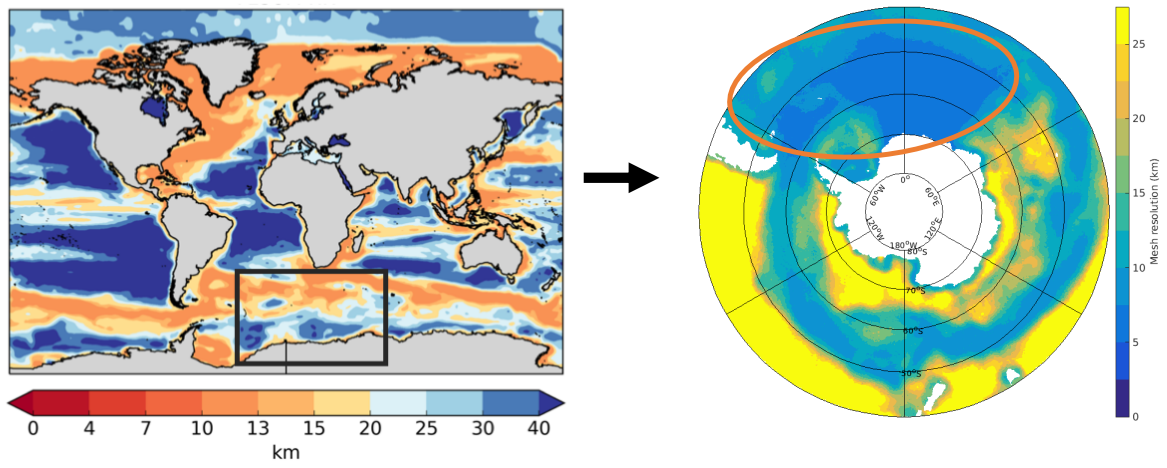

Figure 6: Global resolution of the BOLD mesh to be used in this project (reproduced from (https://fesom.de/models/meshessetups/). The grid has a finer resolution in regions where observed eddy variability is high. The resolution is about 10 km in places of high variability, including the western boundary currents and ACC and it is smoothly coarsened to the background resolution of 60 km in areas with relatively weak variability. For details see Sein et al. (2016). The black box marks the greater Lazarev Sea area for which a higher resolution mesh was implemented. On the right the high resolution LAZAREV mesh developed in this study.

Further, it has been accomplished to parameterize sea ice algae biomass, an important input parameter to the Antarctic krill IBM, from FESOM shortwave radiation and sea-ice thickness and distribution output. The highest values of sea ice algae are calculated for austral summer of 2010, particularly from September to December. Less algae are present from January to March, because sea ice algae are mostly abundant at times when sea ice cover is present and enough radiation can pass through the sea ice for algae to grow. From April to July the lack of radiation does not allow for algal growth.

As a first step test runs with FESOM-1.4-REcoM2 on the CORE und BOLD-grids were undertaken to establish methods. Currently tuning of the FESOM-REcoM2 model on the locally high-resolution LAZAREV grid is underway. This includes test runs concerning time stepping and viscosity.

The model is validated against observations using the following data sets: The World Ocean Atlas 2013 data sets for the validation of temperature (Locarnini et al., 2013), salinity (Zweng et al., 2013) and nutrient distributions (Garcia et al., 2014); estimates of volume transport through Drake Passage (Donohue et al, 2016); sea ice extent from satellite data available from the National Snow and Ice Data Center (NSIDC); sea surface height data from satellite data (AVISO), satellite data on chlorophyll concentration and its seasonal cycle available from The ESA (European Space Agency) Ocean Colour Climate Change Initiative (OC-CCI) version 3.1 (http://www.esa-oceancolour-cci.org); data from the Surface Ocean CO_2 Atlas (SOCAT)

(https://www.socat.info/) on the annual mean und seasonal cycle of pCO2; available data on sea–air CO2 flux (Landschützer et al., 2014; Rödenbeck et al., 2013; 2014).

Outlook

Tuning of the updated FESOM-REcoM2 model with 25-year tuning experiments is under way. After tuning of the model, the reference simulation will be run: this entails a long-term spin-up of the coupled model from 1958 to 2000 (FESOM stand alone) to assure sufficient dynamical adjustment of the model followed by a reference run with FESOM-REcoM2 for the time frame 2000-2010. The biogeochemical model fields for the year 2000 from the simulation on the BOLD mesh will be interpolated to the LAZAREV mesh and be used as initial fields. This is done in an effort to minimize computational costs of running the expensive biogeochemical model in this high resolution and has been previously applied (Terhaar et al., 2018).

References:

Donohue, K. A., K. L. Tracey, D. R. Watts, M. P. Chidichimo, and T. K. Chereskin (2016), Mean Antarctic Circumpolar Current transport measured in Drake Passage, Geophys. Res. Lett., 43, 11,760–11,767, doi:10.1002/2016GL070319.

Everson, I., Miller D.G.M., 1994. Krill mesoscale distribution and abundance: results and implications of research during the BIOMASS programme. In: El-Sayed, S.Z. (Ed.), Southern Ocean Ecology, the BIOMASS perspective. Cambridge University Press, Cambridge, pp. 129-143.

Fach, B.A. and Klinck, J.M. (2006) “Transport of Antarctic krill (Euphausia superba) across the Scotia Sea. Part I: Circulation and particle tracking simulations.” Deep-Sea Research I 53 (6), 987-1010. https://doi.org/10.1016/j.dsr.2006.03.006

Fach, B. A., Hofmann, E. E., & Murphy, E. J. (2002). Modeling studies of antarctic krill Euphausia superba survival during transport across the Scotia Sea. Marine Ecology Progress Series, 231, 187203. https://doi.org/10.3354/meps231187

Fach, B. A., Hofmann, E. E., & Murphy, E. J. (2006). Transport of Antarctic krill (Euphausia superba) across the Scotia Sea. Part II: Krill growth and survival. Deep-Sea Research Part I: Oceanographic Research Papers, 53(6), https://doi.org/10.1016/j.dsr.2006.03.007

Garcia, H. E., R. A. Locarnini, T. P. Boyer, J. I. Antonov, O.K. Baranova, M.M. Zweng, J.R. Reagan, D.R. Johnson, 2014. World Ocean Atlas 2013, Volume 4: Dissolved Inorganic Nutrients (phosphate, nitrate, silicate). S. Levitus, Ed., A. Mishonov Technical Ed.; NOAA Atlas NESDIS 76, 25 pp.

Hofmann, E.E., Klinck, J.M., Locarnini, R.A., Fach, B., Murphy, E., 1998. Krill transport in the Scotia Sea and environs. Antarctic Science 10 (4), 406–415.

Landschützer, P., Gruber, N., Bakker, D. C. E., and Schuster, U.: Recent variability of the global ocean carbon sink, Global Biogeochem. Cy., 28, 927–949, https://doi.org/10.1002/2014GB004853, 2014.

Locarnini, R. A., A. V. Mishonov, J. I. Antonov, T. P. Boyer, H. E. Garcia, O. K. Baranova, M. M. Zweng, C. R. Paver, J. R. Reagan, D. R. Johnson, M. Hamilton, and D. Seidov, 2013. World Ocean Atlas 2013, Volume 1: Temperature. S. Levitus, Ed., A. Mishonov Technical Ed.; NOAA Atlas NESDIS 73, 40 pp.

Rödenbeck, C., Keeling, R. F., Bakker, D. C. E., Metzl, N., Olsen, A., Sabine, C., and Heimann, M. (2013) Global surface-ocean pCO2 and sea–air CO2 flux variability from an observation-driven ocean mixed-layer scheme, Ocean Sci., 9, 193–216, https://doi.org/10.5194/os-9-193-2013.

Rödenbeck, C., Bakker, D. C. E., Metzl, N., Olsen, A., Sabine, C., Cassar, N., Reum, F., Keeling, R. F., and Heimann, M (2014) Interannual sea–air CO2 flux variability from an observation- driven ocean mixed-layer scheme, Biogeosciences, 11, 4599– 4613, https://doi.org/10.5194/bg-11-4599-2014.

Sein, D.V., Danilov , S., Biastoch, A., Durgadoo, J.V., Sidorenko, D., Harig, S., Wang, Q. (2016) Designing variable ocean model resolution based on the observed ocean variability. Journal of Advances in Modeling Earth Systems 8 (2): 904-916. doi: 10.1002/2016MS000650

Siegel V (2012) Krill stocks in high latitudes of the Antarctic Lazarev Sea: seasonal and interannual variation in distribution, abundance and demography. Polar Biol 35:1151–1177 DOI 10.1007/s00300-012-1162-y

Terhaar, J., J. C. Orr, M. Gehlen, C. Eth´e, and L. Bopp (2018), Model constraints on the anthropogenic carbon budget of the Arctic Ocean, Biogeosciences Discussions, 2018, 1–36, doi:10.5194/bg-2018-283.

Zweng, M.M, J.R. Reagan, J.I. Antonov, R.A. Locarnini, A.V. Mishonov, T.P. Boyer, H.E. Garcia, O.K. Baranova, D.R. Johnson, D.Seidov, M.M. Biddle, 2013. World Ocean Atlas 2013, Volume 2: Salinity. S. Levitus, Ed., A. Mishonov Technical Ed.; NOAA Atlas NESDIS 74, 39 pp.

Publications and Presentations

No presentation of results yet.

6.24 *hbk00076:* Simulation der letzten glazialen Termination mit einem gekoppelten Klima-Eisschild-Modell

HLRN-Projektkennung:	hbk00076
Laufzeit:	II/2019 – I/2020
Projektleiter:	Prof. Michael Schulz
Projektbearbeiter.	Dr. Matthias Prange
Institut / Einrichtung:	MARUM – Zentrum für Marine Umweltwissenschaften, Universität Bremen

Überblick

Die letzte eiszeitliche Termination (21.000-11.000 Jahre vor heute) stellt eine Schlüsselperiode für unser Verständnis von globalen Klimaveränderungen dar. Diese Phase ist das paläoklimatologisch bestdokumentierte Beispiel für eine massive Reorganisation des Erd- und Klimasystems, bei der große Eismassen vom amerikanischen und eurasischen Kontinent, aber auch von der Antarktis, abschmolzen und sich der globale Meeresspiegel infolgedessen um rund 120 m hob. Globale Temperaturen stiegen im Jahresmittel um mehrere Grad Celsius und der atmosphärische Kohlendioxid-Gehalt nahm um fast 100 ppmv zu. Dieser Übergang vom letzten glazialen Maximum (LGM) in die jetzige Zwischeneiszeit (Interglazial) geschah jedoch nicht gleichmäßig, sondern war vielmehr durch mehrere abrupte Teilübergänge gekennzeichnet. Dabei wurde die extreme Kaltphase in nördlichen Breiten des Heinrich-Stadials 1 (ca. 18.000-14.700 Jahre vor heute) von der wärmeren Periode des Bölling-Alleröd-Interstadials (ca. 14.700-12.800 Jahre vor heute) abgelöst, bevor es mit dem Jüngeren-Dryas-Stadial (12.800-11.700 vor heute) vorübergehend wieder kälter wurde. Schmelzwassereinträge von den sich zurückziehenden Eisschilden in den Ozean und deren Effekt auf die Tiefenwasserbildung und Tiefenzirkulation werden für diese Klimaschwankungen mitverantwortlich gemacht. Gleichwohl ist das genaue zeitliche Zusammenspiel zwischen Eiszerfall und Änderungen der Ozeanzirkulation noch immer unverstanden.

Bislang wurden Simulationen der Termination mit ungekoppelten Eisschildmodellen (angetrieben durch vorgeschriebene Klimatologien und statistischen Modellen der Atmosphäre), Eisschildmodellen gekoppelt mit einfachen Energiebilanzmodellen der Atmosphäre oder Erdsystemmodellen mittlerer Komplexität durchgeführt. Wichtige Wechselwirkungsprozesse zwischen Ozean und Eisschilden, aber auch zwischen Eisschilden und Atmosphärenzirkulation konnten somit nicht simuliert werden. Zur Untersuchung der relevanten Prozesse, die zum Zerfall der eiszeitlichen Eisschilde führen und dem resultierenden Einfluss auf das Klimasystem (z.B. mögliches Auslösen von Stadialen), verwenden wir in diesem Projekt daher das komplexe Klimamodell (allgemeines Zirkulationsmodell) CESM, gekoppelt an ein dynamisch-thermodynamische Eisschildmodell. Die Untersuchung der Termination mit gekoppelten Eisschilden erfordert zwangsläufig lange transiente Simulationen (im Gegensatz zu kostengünstigeren Zeitscheiben-Klima-Experimenten, die von Gleichgewichtszuständen ausgehen und bei denen die Randbedingungen konstant bleiben). Zur Einsparung von Rechenzeit verwenden wir für die Spin-up- und Tuning-Phase zunächst eine asynchrone Koppelungstechnik zwischen Klima- und Eisschildmodell. Hierbei kann das im Vergleich zum Eismodell wesentlich rechenzeitaufwändigere Klimamodell beschleunigt gerechnet werden.

Das Projekt ist Teil des Arbeitspaketes WG1 der BMBF-finanzierten nationalen Klimamodellierungsinitiative „PalMod – From the Last Interglacial to the Anthropocene“. Das übergeordnete Ziel dieses Arbeitspakets ist die Simulation der letzten Termination mit Hilfe

gekoppelter Klima-Eisschild-Modelle angetrieben durch kontinuierliche Änderungen in Treibhausgaskonzentrationen und Erdorbitalparametern. In einer späteren Projektphase soll das mit Hilfe von Paläo-Proxydaten validierte gekoppelte Modell dann in die Zukunft gerechnet werden, um verlässlichere Aussagen über die zukünftige Entwicklung der Eisschilde und des globalen Meeresspiegels machen zu können.

Das verwendete Klimamodell CESM1.2 wird mit einer horizontalen Auflösung von 2° für das Atmosphären-/Landmodellgitter betrieben, während das Ozean-/Meereisgitter eine räumlich variable Gitterweite von ca. 1° in zonaler und bis zu 0,3° in meridionaler Richtung besitzt. Die vertikale Darstellung des Atmosphärenmodells umfasst 30 Schichten, der Ozean wird mit 60 Niveaus in der Vertikalen diskretisiert. Das Eisschild-Modell SICOPOLIS wird mit einer Auflösung von 20 km integriert.

Ergebnisse

Erste transiente Klima-Eisschild-Simulationen der letzten Deglaziation wurden zur Untersuchung der Sensitivität des gekoppelten Systems bzgl. bestimmter Modellparameter oder Störungen durchgeführt. Dabei hat sich gezeigt, dass die Simulation des Rückgangs des antarktischen Eisschildes eine besondere Schwierigkeit darstellt. Einerseits sind Eis-Ozean-Wechselwirkungen und basales Schmelzen von großer Bedeutung für die Deglaziation und stellen eine besondere Herausforderung für die Modellsimulation dar, andererseits ist auch der glaziale Anfangszustand für die Simulation der Deglaziation ein entscheidender Faktor. Dieser war in ersten Simulationen insbesondere durch ein zu geringes Eisvolumen gekennzeichnet. Zur Verbesserung der Simulation wurde daher eine neue Parameterisierung für basales Schmelzen ins Eismodell implementiert sowie eine neue Spin-Up-Prozedur zur Eisschildinitialisierung entwickelt und angewandt.

Schmelzraten unter dem Schelfeis hängen vom thermischen Antrieb ab, der aus der Differenz zwischen der Ozeantemperatur und dem Gefrierpunkt des Meerwassers (abhängig von Salzgehalt und Tiefe) errechnet wird. Wir konnten in das Eisschildmodell eine neue Parameterisierung zur dynamischen Berechnung basaler Schmelzraten unterhalb des Schelfeises implementieren, welche in unserer bereits erfolgreich durchgeführten Kontrollsimulation die heutigen beobachteten Muster und Raten sehr gut reproduziert und für die großräumige Eisschildmodellierung von höchster Relevanz ist. Die Parameterisierung ist trotz ihrer Güte rechnerisch relativ einfach und somit für lange Simulationen sehr gut geeignet.

Abbildung 1 zeigt den antarktischen Eisschild des LGM in unserer neuen voll gekoppelten Klima-Eisschild-Simulation. In der neuen Simulation rückt der Eisschild in hervorragender Übereinstimmung mit Rekonstruktionen bis zur kontinentalen Schelfkante vor. Teile der Ostantarktis haben eine bis zu 300 m geringere Höhe als heute, was sich auf geringere Niederschlagsraten im LGM zurückführen lässt. Trotz der teilweise geringen Höhe ist das glaziale Eisvolumen aufgrund der horizontalen Ausdehnung signifikant größer als das heutige und resultiert in ein zusätzliches Absinken des globalen eiszeitlichen Meeresspiegels von ca. 9 m. Die erfolgreiche Simulation des antarktischen Eisschildes im LGM mit einem voll gekoppelten, komplexen Klima-Eisschild-Modell ist unseres Wissens bislang einzigartig.

In einer weiteren Phase des Projekts ist geplant, den erfolgreich simulierten Eisschild des LGM zur Initialisierung weiterer, zunehmend realistischerer Deglaziationsexperimente zu verwenden.

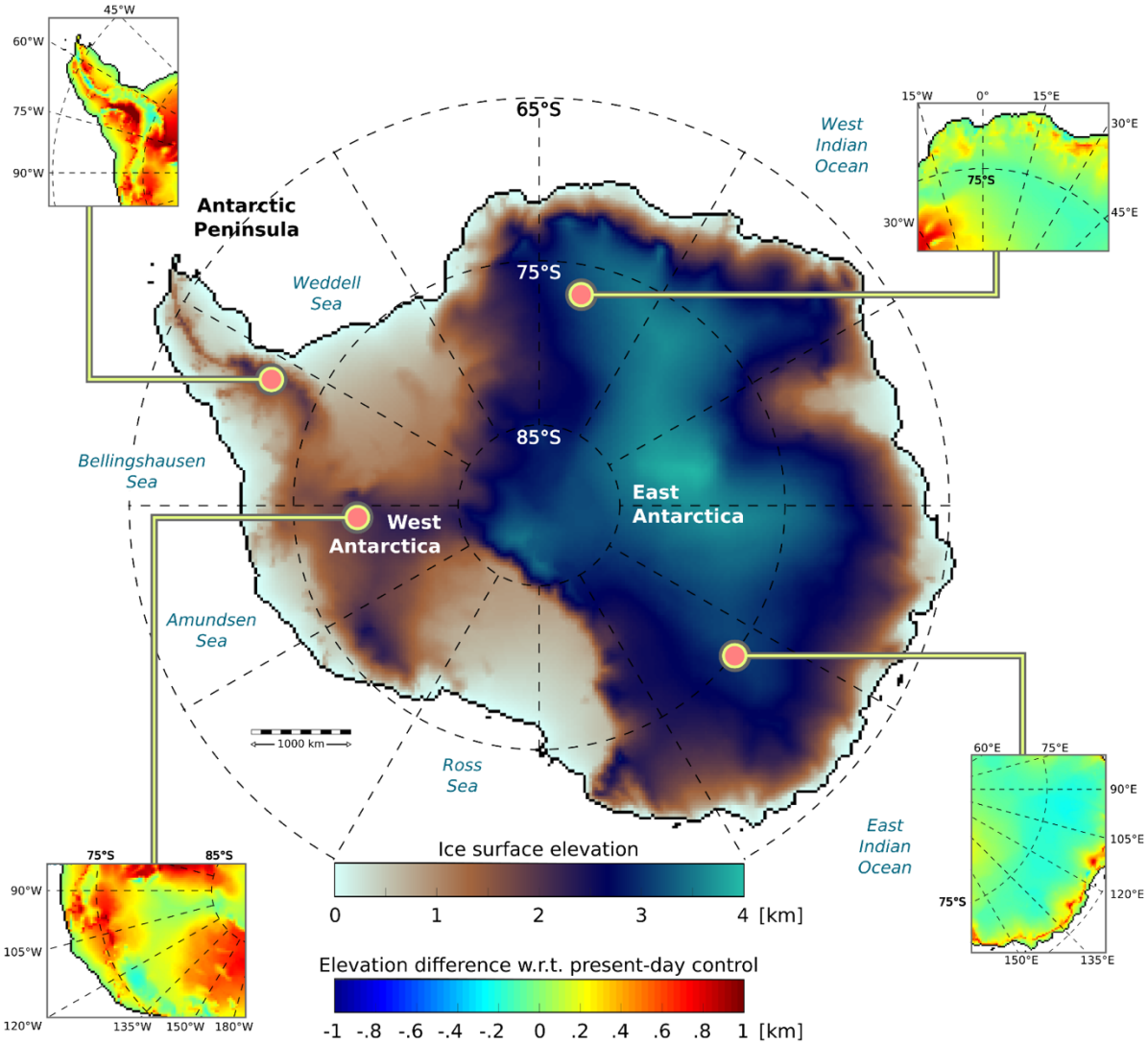

Abbildung 1: Antarktischer Eisschild im LGM (hier 23.000 Jahre vor heute) aus neuer voll gekoppelter Klima-Eisschild-Simulation.

6.25 *hbk00079:* Tipping points in Antarctic Bottom Water formation and Southern Ocean carbon sequestration

HLRNProject ID:	hbk00079
Run time:	II/2020 – I/2021
Project Leader:	Prof. Dr. Björn Rost[1]
ProjectScientists:	Dr. Cara Nissen[2], Dr. Judith Hauck, Dr. Mario Hoppema, Dr. Ralph Timmermann
Affiliation:	Alfred Wegener Institute, Helmholtz Centre for Polar and Marine Research
	[1]principal investigator, also at the University of Bremen, [2]project administrator

Overview

The Southern Ocean plays an essential role in oceanic carbon uptake, carbon sequestration, global ocean circulation, and hence global climate, but the ability of this ocean basin to draw down atmospheric CO_2 has varied in the past and is projected to be altered in the future due to on-going climate change (Hauck et al., 2015). In general, ocean circulation largely controls the oceanic uptake of CO_2 and the transfer of carbon to greater depths in the Southern Ocean. On the one hand, the upwelling of deep water masses brings naturally carbon-rich waters to the surface layers, where the carbon can be released to the atmosphere (Fig. 1a). On the other hand, large amounts of carbon are locked away from the atmosphere by the sinking of water masses to the ocean floor at high-latitudes, i.e., the formation of Antarctic Bottom Water. In this context, the Antarctic Bottom Water formation regions have been suggested to dominantly set global atmospheric CO_2 levels (Marinov et al., 2006), as these can sequester carbon on time scales of centuries to millenia. Amongst all Antarctic Bottom Water formation regions, the Weddell Sea has been suggested to be the most important one (Orsi et al., 1999), making any change in Antarctic Bottom Water formation in this area especially critical for global carbon cycling and climate.

The formation of Antarctic Bottom Water is a result of an increase in the density of surface waters (Orsi et al. 1999), due to air-ocean and ice-ocean interactions, i.e., due to a cooling from the overlying atmosphere and due to the increase in salinity as a result of ice formation, respectively (Fig. 1a). Similarly, this suggests that any addition of freshwater to the Southern Ocean, which leads to a decrease in water density, directly impacts the formation rates of Antarctic Bottom Water and subsequently Southern Ocean carbon transfer to depth.

In fact, as a consequence of the recent warming, the mass loss of Antarctic ice sheets has accelerated over the last decades (Rignot et al., 2019), discharging additional freshwater into the coastal areas of the Southern Ocean. While especially the melt rates of ice shelves in West Antarctica have accelerated, those in East Antarctica, including the Weddell Sea, have done so to a much lesser extent (Rignot et al., 2019). However, modeling experiments have demonstrated the possibility of accelerating melt rates of ice shelves in the Weddell Sea in the upcoming centuries as well (Timmermann & Hellmer 2013), with a possible complete shutdown of Antarctic Bottom Water formation within a few decades (Lago & England 2019). Yet, the possible response of Antarctic Bottom Water formation rates and Southern Ocean carbon cycling to the expected future changes in freshwater discharge remain surrounded by large uncertainties or largely unquantified altogether, as these have so far been hindered by model resolution and/or missing model complexity, e.g., by not accounting for changing freshwater discharge from ice shelves and associated feedbacks in their simulations.

In this project, our goal is to quantify changes in Antarctic Bottom Water formation and carbon sequestration over the 21st century by performing model experiments with FESOM-REcoM2 (Timmermann et al., 2012; Schourup-Kristensen et al., 2018). The setup used here resolves ice shelf cavities and has a higher grid resolution in the Weddell Sea, allowing for a realistic representation of processes inducing Antarctic Bottom Water formation in this area.

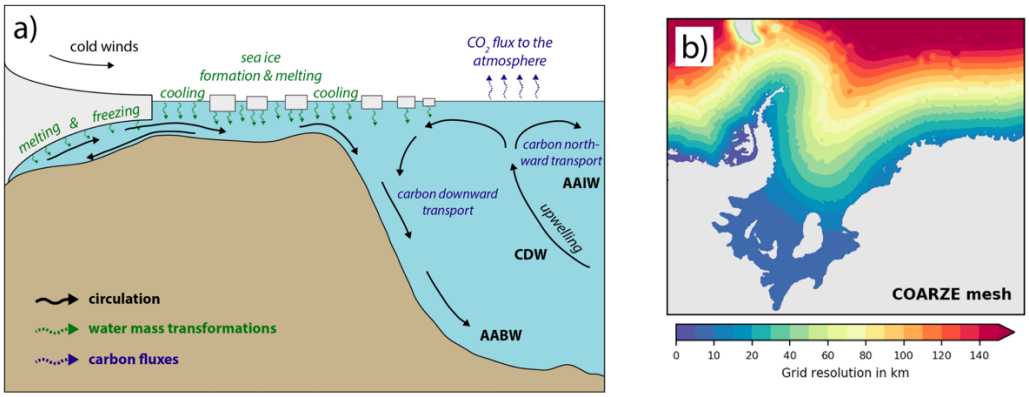

Figure 1: a) Sketch illustrating the main features of high-latitude Southern Ocean circulation (black arrows), the air-ocean and ice-ocean interactions involved in water mass transformations (green), and the main features of Southern Ocean carbon cycling (blue). CDW = Circumpolar Deep Water, AAIW = Antarctic Intermediate Water, and AABW = Antarctic Bottom Water and b) Horizontal grid resolution in km of the COARZE mesh in the Weddell Sea as used in this project.

Results

Over the past year, we have completed all changes to the model code which were necessary to address the knowledge gaps highlighted in the previous section. As a first step, we have updated the ice shelf component in the FESOM version of the coupled FESOM-REcoM2 setup. Subsequently, after testing different meshes, we have ultimately settled on the COARZE mesh for this project (Fig. 1b). The horizontal grid resolution in this mesh is <15 km on the southern Weddell Sea shelf, 40-80~km in the central Weddell Sea, and >100 km north of it. Due to the computational efficiency of the COARZE mesh, we are able to perform transient model simulations from 1950-2100 in the coupled FESOM-REcoM2 setup. To that aim, we use output from the AWI Climate Model (AWI-CM) as atmospheric forcing for our model experiments (CMIP6 contribution of the AWI-CM; first ensemble member for the historical period for 1950-2014 and the ssp585 scenario for the period 2015-2100; see Semmler et al., 2020). After applying all necessary code updates for the use of this forcing product in FESOM-REcoM2 simulations, we have then successfully performed a full transient simulation in the fall of 2020, using interannually varying atmospheric forcing and increasing atmospheric pCO_2 levels (referred to as simA; O'Neill et al., 2016, Meinshausen et al., 2017). In this simulation, we have used the regridded 1949-restart file from FESOM in the AWI-CM as initial conditions for the year 1950. Similarly, the biogeochemical tracers in REcoM2 were initialized with the 1949-restart file of a simulation for the on-going "Regional Carbon Cycle Assessment and Prossesses 2 (RECCAP2)" project.

As a consequence of the continuous increase in surface ocean CO_2 uptake in the Weddell Sea over the 21st century, the total DIC inventory below 2000 m increases over the course of simA. Yet, maybe surprisingly, the northward carbon transport in dense deep waters out of the Weddell Sea declines. A quantification of the contribution of vertical and lateral fluxes to the simulated change in the DIC inventory is on-going, but the decline appears to be dominated by changes in the northward volume transport of dense waters, demonstrating the dominant role of dense water formation rates for carbon sequestration. In fact, in FESOM-REcoM2, dense waters are almost exclusively formed via water mass transformations on the shelf (i.e.,

open-ocean deep convection is negligible). Using a water mass transformation framework (Abernathey et al., 2016), we find a reduction in the formation of dense waters, a direct result of a lower sea ice formation, the increased presence of modified Warm Deep Water on the shelf, and higher basal melt rates, but whether atmospheric warming or changed wind patterns drive these simulated changes remains unresolved.

Outlook

A control experiment with constant climate forcing and atmospheric pCO_2 levels is on-going, which will allow us to quantify the model drift. Building on these existing or on-going simulations, we plan a set of four additional model experiments as a next step, in order to fully disentangle the contribution of changes in the cycling of natural and anthropogenic carbon to changes in Weddell Sea carbon sequestration, as well as to disentangle the relative importance of warming and changing wind patterns in controlling water mass properties and dense water formation rates on the Weddell Sea shelf.

References

Abernathey, R. P., Cerovecki, I., Holland, P. R., Newsom, E., Mazloff, M., & Talley, L. D. (2016). Water-mass transformation by sea ice in the upper branch of the Southern Ocean overturning. *Nature Geoscience*, *9*(8), 596–601. https://doi.org/10.1038/ngeo2749

Hauck, J., Völker, C., Wolf-Gladrow, D. A., Laufkötter, C., Vogt, M., Aumont, O., Bopp, L., Buitenhuis, E. T., Doney, S. C., Dunne, J., Gruber, N., Hashioka, T., John, J., Quéré, C. Le, Lima, I. D., Nakano, H., Séférian, R., & Totterdell, I. (2015). On the Southern Ocean CO 2 uptake and the role of the biological carbon pump in the 21st century. *Global Biogeochemical Cycles*, *29*(9), 1451–1470. https://doi.org/10.1002/2015GB005140

Lago, V., & England, M. H. (2019). Projected Slowdown of Antarctic Bottom Water Formation in Response to Amplified Meltwater Contributions. *Journal of Climate*, *32*(19), 6319–6335. https://doi.org/10.1175/JCLI-D-18-0622.1

Marinov, I., Gnanadesikan, A., Toggweiler, J. R., & Sarmiento, J. L. (2006). The Southern Ocean biogeochemical divide. *Nature*, *441*(7096), 964–967. https://doi.org/10.1038/nature04883

Meinshausen, M., Vogel, E., Nauels, A., Lorbacher, K., Meinshausen, N., Etheridge, D. M., Fraser, P. J., Montzka, S. A., Rayner, P. J., Trudinger, C. M., Krummel, P. B., Beyerle, U., Canadell, J. G., Daniel, J. S., Enting, I. G., Law, R. M., Lunder, C. R., ODoherty, S., Prinn, R. G., … Weiss, R. (2017). Historical greenhouse gas concentrations for climate modelling (CMIP6). *Geoscientific Model Development*, *10*(5), 2057–2116. https://doi.org/10.5194/gmd-10-2057-2017

O'Neill, B. C., Tebaldi, C., van Vuuren, D. P., Eyring, V., Friedlingstein, P., Hurtt, G., Knutti, R., Kriegler, E., Lamarque, J.-F., Lowe, J., Meehl, G. A., Moss, R., Riahi, K., & Sanderson, B. M. (2016). The Scenario Model Intercomparison Project (ScenarioMIP) for CMIP6. *Geoscientific Model Development*, *9*(9), 3461–3482. https://doi.org/10.5194/gmd-9-3461-2016

Orsi, A. H., Johnson, G. C., & Bullister, J. L. (1999). Circulation, mixing, and production of Antarctic Bottom Water. *Progress in Oceanography*, *43*(1), 55–109. https://doi.org/10.1016/S0079-6611(99)00004-X

Schourup-Kristensen, V., Wekerle, C., Wolf-gladrow, D. A., & Völker, C. (2018). Progress in Oceanography Arctic Ocean biogeochemistry in the high resolution FESOM 1 . 4-REcoM2 model. *Progress in Oceanography*, *168*(August), 65–81. https://doi.org/10.1016/j.pocean.2018.09.006

Timmermann, R., Wang, Q., & Hellmer, H. H. (2012). Ice-shelf basal melting in a global finite-element sea-ice/ice-shelf/ocean model. *Annals of Glaciology*, *53*(60), 303–314. https://doi.org/10.3189/2012AoG60A156

Timmermann, R., & Hellmer, H. H. (2013). Southern Ocean warming and increased ice shelf basal melting in the twenty-first and twenty-second centuries based on coupled ice-ocean finite-element modelling. *Ocean Dynamics*, *63*(9–10), 1011–1026. https://doi.org/10.1007/s10236-013-0642-0

Rignot, E., Mouginot, J., Scheuchl, B., van den Broeke, M., van Wessem, M. J., & Morlighem, M. (2019). Four decades of Antarctic Ice Sheet mass balance from 1979–2017. *Proceedings of the National Academy of Sciences*, *116*(4), 1095–1103. https://doi.org/10.1073/pnas.1812883116

Semmler, T., Danilov, S., Gierz, P., Goessling, H. F., Hegewald, J., Hinrichs, C., Koldunov, N., Khosravi, N., Mu, L., Rackow, T., Sein, D. V., Sidorenko, D., Wang, Q., & Jung, T. (2020). Simulations for CMIP6 With the AWI Climate Model AWI-CM-1-1. *Journal of Advances in Modeling Earth Systems*, *12*(9), 1–34. https://doi.org/10.1029/2019MS002009

Publications & Presentations

Additional model experiments and the analysis of completed experiments are on-going, therefore there is no publications or presentation of the results yet.

6.26 *hbk00080:* Modelling the Greenland Ice Sheet for past interglacials and the future

HLRN Project ID:	hbk00080
Run Time:	III/2020 – II/2021
Project Leader:	Prof. M. Schulz
Project Scientists:	Dr. M. Prange, B.Crow
Affiliation:	MARUM – Center for Marine Environmental Sciences University of Bremen

Overview

One of the most serious consequences of climate change that the world will face in the near future is rising sea levels. This rise is driven in part by thermal expansion of the ocean, melting of land-based glaciers, and partial melting of the large ice sheets in Antarctica and Greenland. Studies of past climates (thousands to millions of years ago) have shown that the volume of ice sheets has varied greatly throughout Earth's history, leading to significant fluctuations in global sea level. However, the exact magnitude and rates of change for these episodes of ice melt and accumulation are poorly determined, even for the more recent geologic past. In addition, the processes controlling the dynamics of the ice sheets are not yet well understood. Our goal is therefore to simulate two interglacials (warm phases of the Quaternary) from about 125,000 years ago and 400,000 years ago (Marine Isotope Stages 5e and 11c; MIS 5e and MIS 11c, respectively) using a complex climate model together with an ice sheet model. These interglacials stand out in reconstructions of the Quarternary due to particularly high sea levels. Ice sheet modeling in this study will focus on Greenland, so our investigation of climate mechanisms will also focus on processes specific to the North Atlantic and Arctic.

For the interglacial of MIS 5e, the last interglacial (130,000-115,000 years before present), reconstructions have estimated that the global mean annual temperature was half to one degree Celsius warmer than during pre-industrial times, while summer temperature anomalies in the Arctic may have been up to five degrees Celsius higher. Reconstructions of sea level indicate values of 6-9 m above the present level. The contribution of the Greenland ice sheet is estimated to be several meters, but the uncertainty is considerable. The interglacial of MIS 11c (425,000-395,000 years before present) is characterized by its unusually long duration of about 30,000 years. Estimates of global mean temperature are subject to enormous uncertainty, but marine sediment cores indicate unusually high sea surface temperatures in the North Atlantic that were 1-2 degrees Celsius higher than today. In addition, there is evidence that the Greenland ice sheet was at times almost completely melted and sea level was 6-13 m higher than today.

Understanding the processes that led to the enormous ice loss in Greenland during MIS 5e and MIS 11c is essential for improving projections of future cryosphere and global sea level. In addition, this project aims to deepen the basic understanding of the climatic processes that modify the transport of heat and moisture and thus Greenland ablation and accumulation rates. For this purpose, the complex climate model CESM1.2 is used together with the ice sheet model PISM v1.2. The climate model is run with a horizontal resolution of 2 degrees for the atmosphere/land model grid, while the ocean/sea ice grid has a spatially variable grid size of about 1 degree in zonal and up to 0.3 degrees in meridional direction. The vertical representation of the atmosphere model includes 30 layers, and the ocean is discretized with 60 levels in the vertical. The ice sheet model PISM v1.2 is integrated with a resolution of 20 km.

The DFG-funded project is part of the German-Canadian International Research Training Group ArcTrain (GRK 1904).

Results

Because CESM is computationally expensive to run for long periods of time, we used representative shorter time integrations within the longer periods of interest (“time slices”). Time slices were selected to be representative of key points in the cycle of orbital insolation forcing experienced during each period, primarily centered around maxima and minima in the precession index and with intermediate steps taken between for even 5000-year increments between slices. Each time slice experiment uses prescribed orbital parameters and ice core-derived greenhouse gas concentrations and represents quasi-equilibrium climate conditions.
In comparing experiments, a wide array of analyses were produced, examining such variables as air and ocean temperatures, cloud cover, precipitation, fraction of precipitation occurring as snow, sea-level pressure and its patterns of variance across the North Atlantic, the meridional overturning circulation of the oceans, and many others. This enables us to assess the degree to which varying orbital and greenhouse gas forcing affects the modelled climate system and any feedbacks therein. To obtain a first overview, Figure 1 shows global maps of simulated annual mean temperature anomalies (i.e. differences to the modern pre-industrial climate) for the various MIS 11c time slices. Since melting of the ice sheet mainly takes place in summer, boreal summer temperature anomalies may provide first estimates of ablation and the evolution of the ice sheet. Figure 2 shows the summer temperatures for the different MIS 11c time slices in the North Atlantic region. Strong warming takes place from 418 to 408 ka (kiloyears before present) over and around Greenland, which turns into cold anomalies afterwards.

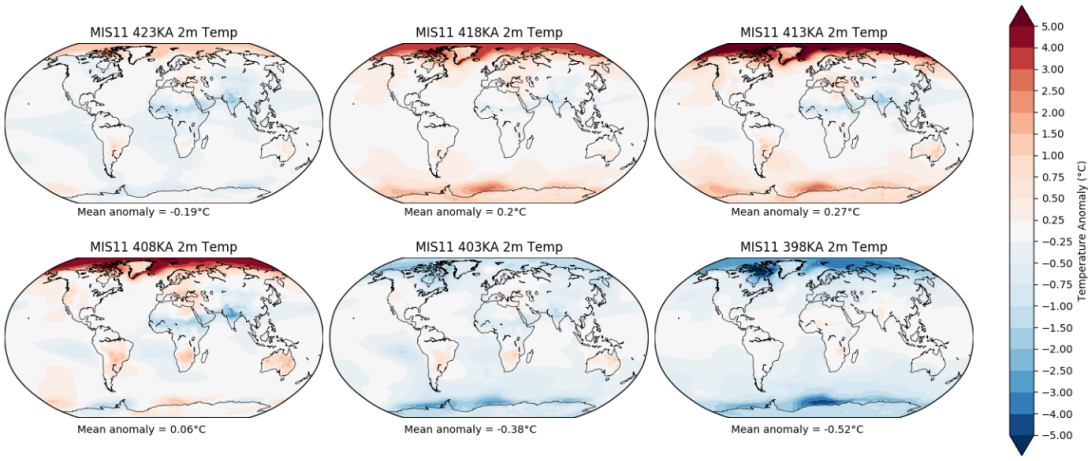

Figure 1: Annual mean surface air temperature anomalies relative to the pre-industrial control run for MIS 11c time slices from 423 to 398 ka (kiloyears before present).

A focus of our study is on dynamic aspects of the atmosphere that may have induced either a greater/lower degree or duration of warmth over and near the Greenland ice sheet that served to enhance/reduce melt during the warm interglacials. We are now in the process of analyzing the dynamic consequences of the reduced equator-to-pole surface temperature gradient evident in Figure 1 owing to a very strong warming of the Arctic during the early-to-mid phase of MIS 11c. While a weaker meridional temperature gradient may result in reduced baroclinicity and transient eddy fluxes, another hypothesis is that a weaker, more variable midlatitude jet stream could result in greater poleward eddy heat flux over the North Atlantic region, transporting greater amounts of warm, moist air over Greenland than in the preindustrial baseline period. Figure 3 shows results from our analysis of poleward transient eddy heat

transports during the summer season. The model suggests that anomalous warming of the Arctic during the early-to-mid phase of MIS 11c is associated with reduced transient eddy heat fluxes over the Greenland section, which would mitigate Greenland warming and, hence, act as a negative feedback.

Outlook

Thus far, our climate simulations have not included coupling or a dynamically evolving ice sheet. Our next step will be to examine the sensitivity of the Greenland ice sheet to the climatic changes and, in turn, the effects of a changing ice sheet on climate. In a second phase of the project, coupled climate-ice sheet simulations will be performed for the two interglacials, utilizing acceleration techniques to make longer-term integrations feasible. Combined, these experiments will provide greater insight into the climate system's sensitivity to large physical changes in the Greenland ice sheet and which atmospheric feedbacks have the greatest impact on surface mass balance. By improving understanding in these areas, we intend to provide better, more physically realistic constraints on the dynamic ice-climate evolution in future emissions scenarios, thus improving forecasts of Greenland's contribution to sea level rise.

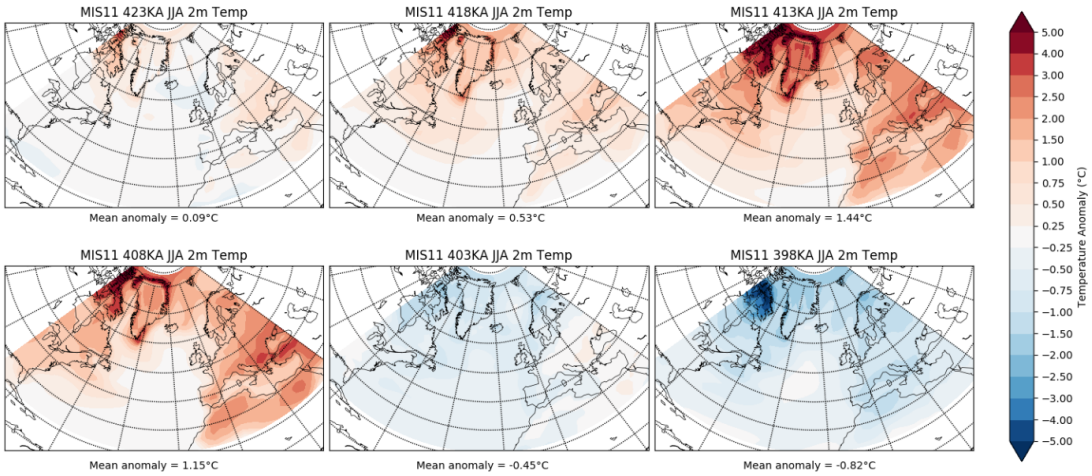

Figure 2: Summer (July-August) mean surface air temperature anomalies relative to the pre-industrial control run for MIS 11c time slices from 423 to 398 ka in the North Atlantic region.

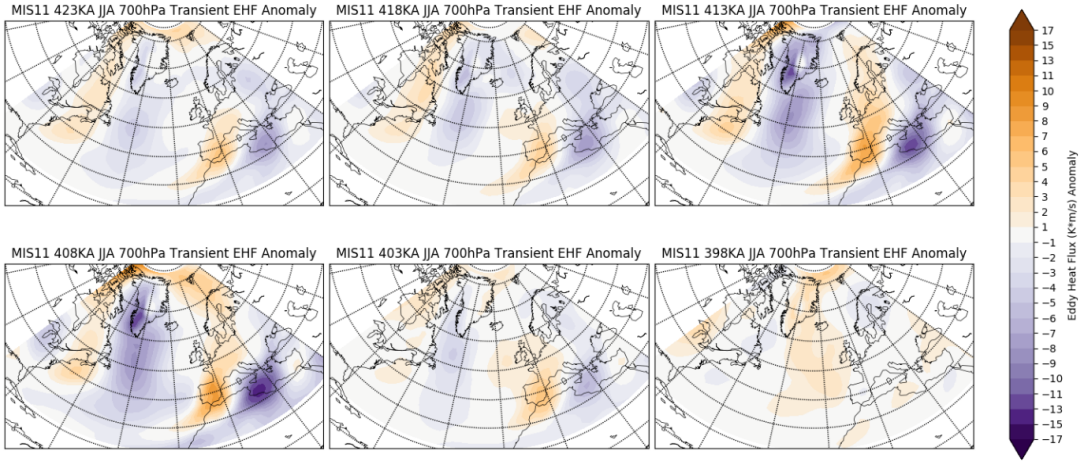

Figure 3: Summer (July-August) northward transient eddy heat flux anomalies at 700 hPa relative to the pre-industrial control run for MIS 11c time slices from 423 to 398 ka in the North Atlantic region.

6.27 *hbp00029:* Carrier dynamics and optical properties of transition metal dichalcogenides / *hbp00048:* Interplay of structural, electronic, and optical properties of transition metal dichalcogenide nanostructures

HLRN Project ID:	hbp00029
Run time:	I/2020 – IV/2020
Project Leader:	Dr. rer. nat. Michael Lorke Prof. Dr. Frank Jahnke
Project Scientists:	Dr. rer. nat. Alexander Steinhoff Dr. rer. nat. Matthias Florian Dr. rer. nat. Daniel Erben

HLRN Project ID:	hbp00048
Run time:	III/2019 – III/2020
Project Leader:	Dr. rer. nat. Christian Carmesin Dr. rer. nat. Michael Lorke Dr. rer. nat. Matthias Florian Prof. Dr. Frank Jahnke
Project Scientists:	Dr. rer. nat. Daniel Erben

Overview

Monolayers of transition metal dichalcogenide (TMD) semiconductors exhibit strong Coulomb interaction of their charge carriers that occupy a rich valley structure in reciprocal space. For a better understanding of the underlying physics and the prospects of TMD semiconductors as active materials in future optoelectronic devices like light-emitting diodes, solar cells or lasers, experimental techniques such as photoluminescence and pump-probe spectroscopy are used. These experiments involve photoexcitation of electron-hole pairs, frequently above the quasi-particle band gap,and benefit from reliable estimates of the present excited carrier density. As soon as the exciting laser pulse is intense enough, effects such as phase space filling and screening are expected to influence the absorption in a nonlinear way. Therefore, it is desirable to quantify the involved nonlinearities microscopically and calculate the resulting excitation densities for typical experimental situations. This aspect has been investigated in project hbp0029 using state-of-the-art many-body methods.

TMD semiconductors offer unique ways to manipulate excitonic phenomena on the nanoscale. Within this collection of capabilities strain engineering is pre-eminent, offering unprecedented flexibility and precision, and opening new routes to highly tailored optoelectronic materials. In project hbp0048 a state-of-the-art tight-binding and force field approach has been used to investigate the structural, electronic, and optical properties of TMD nanostructures.

Results

Optical nonlinearities in the excited carrier density of atomically thin transition metal dichalcogenides

In atomically thin semiconductors based on TMDs, photoexcitation can be used to generate high densities of electron-hole pairs. Due to optical nonlinearities, which originate from Pauli

blocking and many-body effects of the excited carriers, the generated carrier density will deviate from a linear increase in pump fluence. In publication [1], a numerical analysis of the photo-excited charge carrier dynamics as well as optical nonlinearities in absorption and excited carrier density is provided. To this end, an approach is used that combines material-realistic electronic state and interaction matrix element calculations with semiconductor Bloch equations including many-body effects. The validity range of a linear approximation for the excited carrier density vs. pump power is determined and the role and magnitude of optical nonlinearities at elevated excitation carrier densities is identified for MoS_2, $MoSe_2$, WS_2, and WSe_2 considering various excitation conditions. Results are different for pumping at or above the quasi-particle band gap. In the former case, a linear regime is found for surprisingly large excited carrier densities up to 1×10^{13} cm^{-2} for $MoSe_2$ and up to 2×10^{12} cm^{-2} for MoS_2 , WS_2, and WSe_2 due to a compensation of Pauli-blocking nonlinearities in the absorption and band-structure renormalizations. For above-gap excitation, excited carrier densities can strongly exceed the linear extrapolation values since absorption reduction due to Pauli blocking remains weak while stronger absorption regions at higher energies can be shifted onto the pump resonance due to giant band-gap shrinkage. Numerical results for MoS_2 are shown in Figure 1.

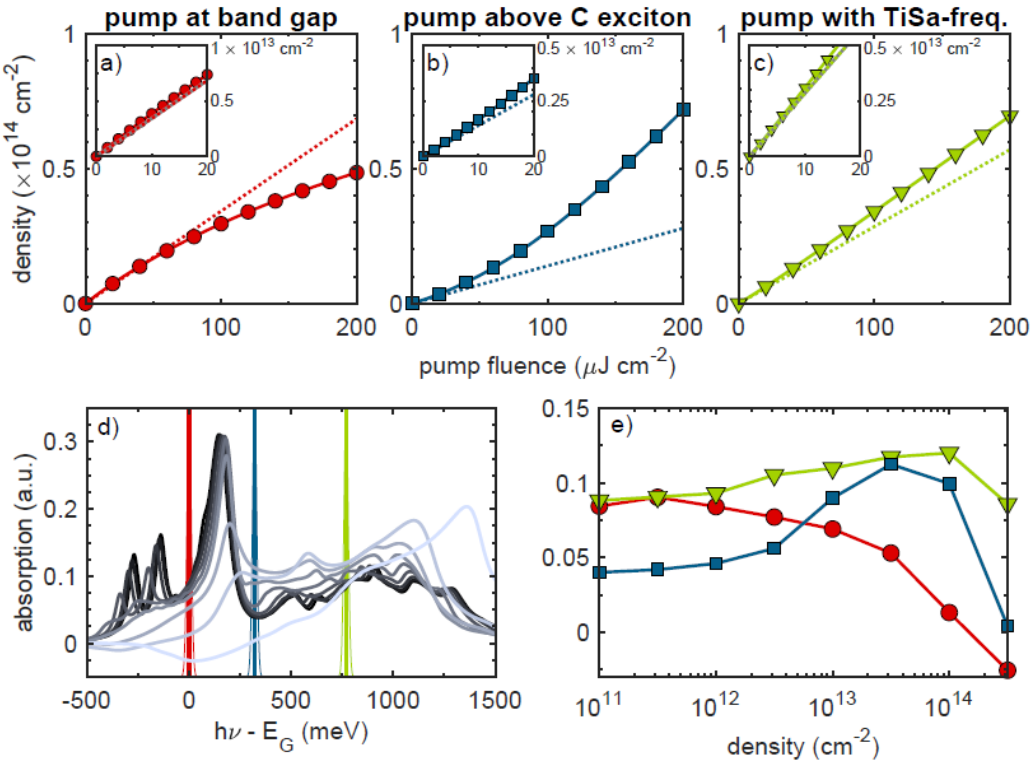

Figure 1: Optically excited charge carrier density vs. pump fluence for excitation of MoS_2 with 150 fs laser pulse tuned to the band-gap energy (a), above the C exciton (b), and well above band gap corresponding to the Ti-sapphire laser emission wavelength (c). Solid lines and symbols represent calculated carrier densities including optical nonlinearities. Dashed lines correspond to carrier densities obtained from the calculated linear absorption coefficients of the unexcited system at the respective energies. Absorption spectra of MoS_2 for a given excited carrier density in thermal equilibrium at 300 K are shown in (d) together with the energetic position and spectral width of the pump pulses corresponding to (a)-(c). The carrier density increases from zero (black line) to 3×10^{14} cm^{-2} (gray line) corresponding to the data points in (e). The nonlinear behavior of the extracted absorption coefficients vs. carrier density at the three pump energies is depicted in (e).

Imaging strain-localized excitons in nanoscale bubbles of monolayer WSe_2

In monolayer TMDs, localized strain can be used to design nanoarrays of single photon sources. Despite strong empirical correlation, the nanoscale interplay between excitons and local crystalline structure that gives rise to these quantum emitters is poorly understood.

In publication [2], room-temperature nano-optical imaging and spectroscopic analysis of excitons in nanobubbles of monolayer WSe_2 has been combined with atomistic models to study how strain induces nanoscale confinement potentials and localized exciton states. The imaging of nanobubbles in monolayers with low defect concentrations reveals localized excitons on length scales of around 10 nm at multiple sites around the periphery of individual nanobubbles, in stark contrast to predictions of continuum models of strain. These results agree with theoretical confinement potentials atomistically that are derived from the measured topographies of nanobubbles.

To gain insight into the carrier localization mechanism atomistic calculations have been performed in which the relevant part of the nanostructure is modelled using a lattice of atomic sites. For the calculations, we used the nanobubble geometry (Figure 2a) obtained from the AFM measurements and determined the corresponding relaxed positions of the individual atoms by a valence force field simulation. The results provide the strain field in the structure and confirm the existence of atomic-scale wrinkling. In a second step, the information on the displaced atomic positions was used within a tight-binding calculation to quantify how the strain field of the individual atoms within the nanobubble translates into confinement potentials and local electronic states.

The calculated confinement potentials (Figure 2c) for the nanobubble topography derived from the AFM data exhibit a doughnut pattern, with deeper potentials located on the nanobubble periphery that trace the wrinkling effect (Figure 2d) and its associated regions of large shear strain (Figure 2e). The theoretical confinement potentials correspond remarkably well with the nanoscale spatial distribution of the measured energies of the localized exciton (Figure 2b).

The results provide experimental and theoretical insights into strain-induced exciton localization on length scales commensurate with exciton size, realizing key nanoscale structure–property information on quantum emitters in monolayer WSe_2.

Outlook

Ongoing work is concerned with the nonequilibrium dynamics of correlated carriers in TMD heterostructures at various excitation densities and the corresponding exciton-exciton interaction effects. We are going to extend our research towards spatial superstructures made from different TMD layers, in particular moiré-like effects.

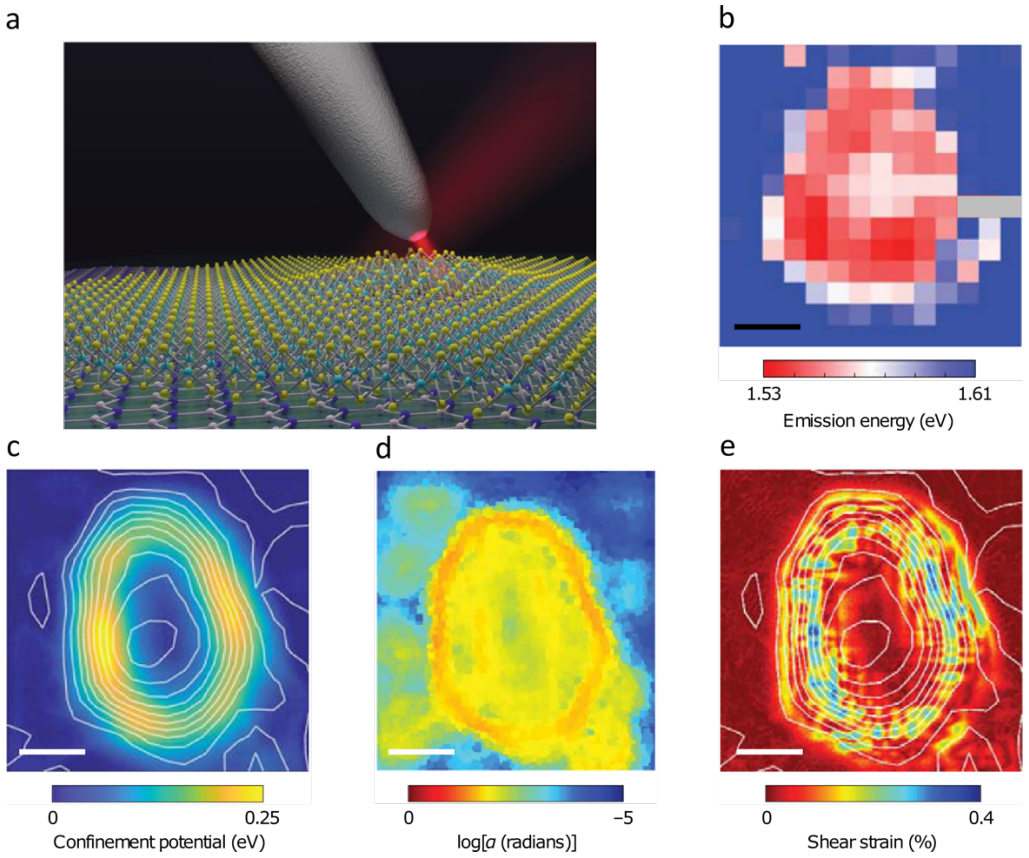

Figure 2: (**a**) Schematic of the room-temperature nanophotoluminescence imaging and spectroscopic analysis of 1L-WSe_2 on top of h-BN. (**b**) Spatial map of the LX emission energy of the nanophotoluminescence data. (**c**) Calculated carrier confinement potential for the experimentally determined nanobubble topography shown in **a**. The solid lines represent topographic contours based on the AFM measurement. (**d**), Corresponding values of the surface normal deviation, defined as the average angle, α, between normal vectors at neighbouring unit cells, obtained from relaxed atomic positions, showing wrinkling of the lattice. (**e**), Map of the shear component of the strain tensor, originating from local wrinkling of the lattice. The positive values indicate larger atomic distances leading to a local reduction of the bandgap.

Publications

1. Daniel Erben, Alexander Steinhoff, Michael Lorke, and Frank Jahnke, *Optical nonlinearities in the excited carrier density of atomically thin transition metal dichalcogenides,*arXiv:2012.07642v1 *(2020)*
2. Thomas P. Darlington, Christian Carmesin, Matthias Florian, Emanuil Yanev, Obafunso Ajayi, Jenny Ardelean, Daniel A. Rhodes, Augusto Ghiotto, Andrey Krayev, Kenji Watanabe, Takashi Taniguchi, Jeffrey W. Kysar, Abhay N. Pasupathy, James C. Hone, Frank Jahnke, Nicholas J. Borys and P. James Schuck, *Imaging strain-localized excitons in nanoscale bubbles of monolayer WSe2 at room temperature,* Nature Nanotechnology*, 15, 854-860 (2020)*

Presentations

1. M. Florian, Strain-localized exciton states in WSe2 nanostructures - comparison of microscopic theory with nano-optical imaging and spectroscopy, NOEKS15, September 14, 2020

6.28 *hbp00041:* Multi-Messenger Signals from Compact Objects

HLRNProject ID:	hbp00041
Run time:	I/2018 – II/2023
Project Leader:	Prof. Claus Lämmerzahl
ProjectScientists:	Prof. Stephan Rosswog
Affiliation:	Universität Bremen, Centre for Applied Space Technology and Microgravity, Am Fallturm, 28359 Bremen

Overview

The recent detection of a binary black hole merger has heralded the long-awaited era of gravitational wave astronomy. This watershed event confirmed a 100-year-old prediction of Einstein's General Theory of Relativity; even more importantly, it opened up a completely new channel to observe the Universe. GW astronomy allows to probe how the strongest gravitational fields warp space-time, how ultra-gravity binary stars contribute to the heaviest elements in the cosmos, how such binary systems form and, eventually, how their mergers can be used to probe of the expansion history of the Universe. All these exciting prospects, however, hinge on detecting electromagnetic counterparts of gravitational wave sources. A coincident detection of both gravitational and electromagnetic waves had been a scientific dream for decades.

This dream came true on August 17, 2017: the LIGO/Virgo detectors recorded for the first time the gravitational waves from a binary neutron star merger and subsequently telescopes around the world detected the event all across the electromagnetic spectrum (Abbott et al. 2017). This observation proved that neutron star mergers are indeed strong sources of gravitational waves, that they produce short gamma ray bursts and are a major cosmic factory for the heaviest elements as theoretically predicted (Rosswog et al. 1999, Freiburghaus et al. 1999). Moreover, the subtle tidal imprint on the gravitational wave signal constrained the behaviour of nuclear matter at high densities and the arrival time differences of gravitational waves and photons demonstrated that both propagate at the same speed with a relative precision of 10^{-15}. The combined detection also allowed for an entirely new approach to probe the expansion of the Universe. For all these reasons, this first “multi-messenger” detection of a binary neutron star merger was celebrated by *Science* Magazine as “2017 Breakthrough of the Year".

The main topic of this HLRN project is the theoretical prediction of observable signatures from encounters between compact objects.

Results

The last year has been scientifically very productive, therefore we only show a selection from the recent results. Major progress was achieved in the development of novel simulation techniques which has resulted in two new Lagrangian hydrodynamics codes: the Newtonian code MAGMA2 and the code SPHINCS_BSSN which evolves relativistic fluids in dynamically changing spacetimes.

The Lagrangian hydrodynamics code MAGMA2

We have developed a novel Lagrangian hydrodynamics code, MAGMA2 (Rosswog 2020a). MAGMA2 is a smoothed Particle Hydrodynamics code that evolves the equations of ideal hydrodynamics by means of freely moving particles. It contains a number of novel techniques that significantly increase its accuracy compared to standard approaches. These include high-order Wendland kernels, matrix-inversion techniques to calculate gradients, slope-limited

reconstruction techniques borrowed from Finite Volume methods and a novel, entropy-based method to stear dissipation (Rosswog 2020b). An example of a Kelvin-Helmholtz instability simulated with MAGMA2 is shown in Fig.1. MAGMA2 will be used in the future for long-term evolution of the ejecta from neutron star mergers.

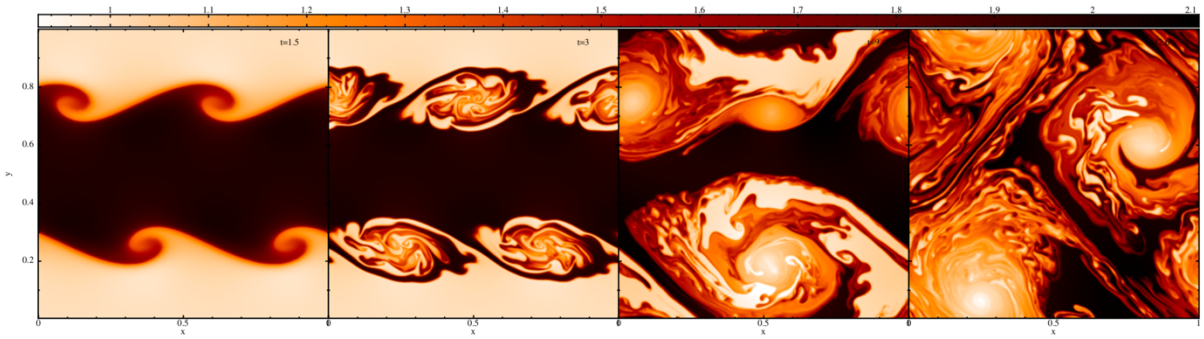

Figure 1: Simulation of a Kelvin-Helmholtz instability with our novel Lagrangian hydrodynamics code MAGMA2 (Rosswog 2020a).

SPHINCS_BSSN, a general relativistic Smooth Particle Hydrodynamics code for dynamical spacetimes

We have developed a new type of Numerical Relativity code that evolves the spacetime dynamically on a mesh and the matter by means of Lagrangian particles (Rosswog & Diener 2021). The name stands for ***S**moothed **P**article **H**ydrodynamics **I**n **C**urved **S**pacetime*, the "BSSN" in the code name stands for the method with which the spacetime is evolved (due to Baumgarte, Shapiro, Shibata, Nakamura). This is the world-wide first code that is both Lagrangian and fully general relativistic in its spacetime evolution. The major advantage of this code compared to existing Numerical Relativity codes is that is allows to very accurately track the small amounts of matter that are ejected during the merger of two neutron stars. It is these small amounts of ejecta that are responsible for the entire electromagnetic emission. SPHINCS_BSSN has passed a number test cases with excellent precision. As an example, we show in Figure 2 a relativistic neutron star that has been evolved (both hydrodynamics and spacetime) for many oscillation periods. The star remains very accurately on the initial solution that had been obtained by solving the Tolman-Oppenheimer-Volkoff equations. An example of one of our first neutron star merger simulations with SPHINCS_BSSN, performed on HLRN resources, is shown in Figure 3.

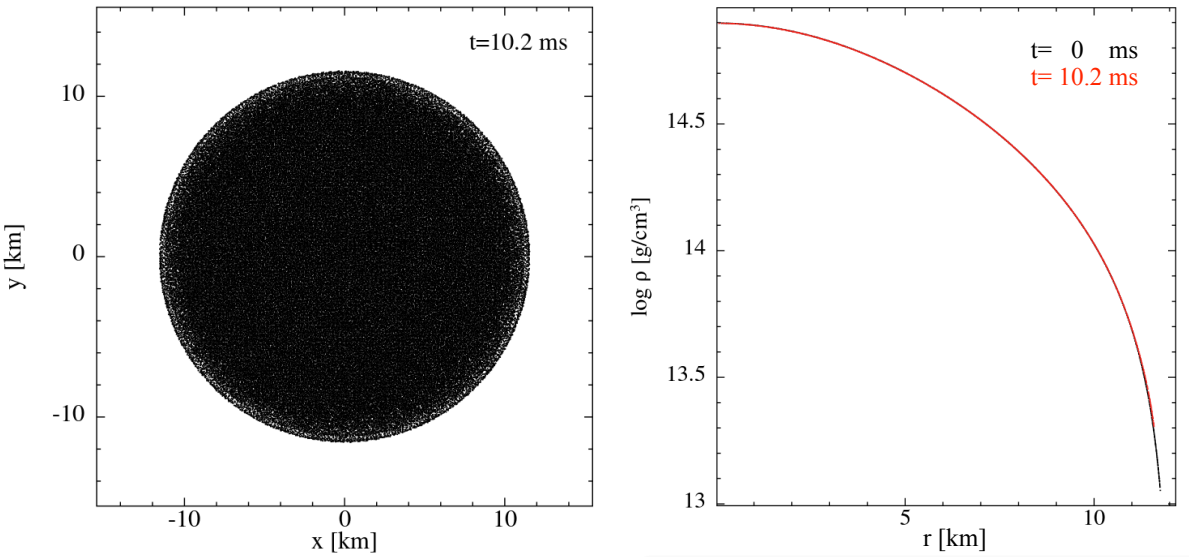

Figure 2: Simulation of a relativistic neutron star where both the fluid and the spacetime are evolved. The left panel shows the distribution of the SPH particles, the right panel shows that after many oscillation periods the evolved solution (red) is practically in perfect agreement with the initial condition (black).

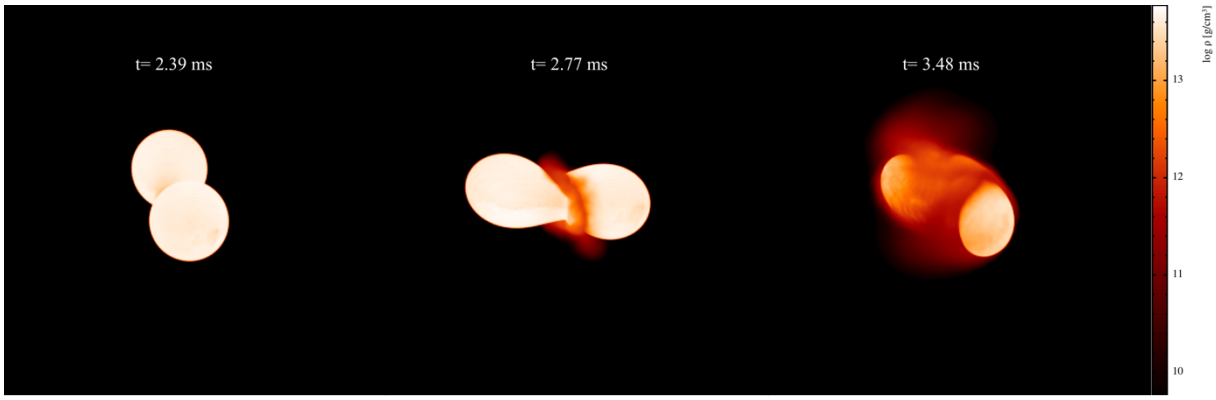

Figure 3: Simulation of two merging neutron stars (1.2 and 1.4 solar masses). Simulation performed with the newly developed general-relativistic Lagrangian hydrodynamics code SPHINCS_BSSN.

Outlook

In the year 2020 we have made major progress in developing new simulation tools, the codes MAGMA2 and SPHINCS_BSSN. These will be our major “workhorses” for future studies. We will in particular explore the ejecta from neutron star mergers, their long-term evolution, nucleosynthesis and the variety of electromagnetic signals the produce. Such studies will be crucial for the interpretation of future multi-messenger detections.

Publications

1. S. Rosswog, *The Lagrangian hydrodynamics code MAGMA2*, MNRAS 498, 4230 (2020)
2. S. Rosswog, *A simple, entropy-based dissipation trigger for SPH*, ApJ 898, 60 (2020)
3. McGuire et al., *Tidal Disruption of White Dwarfs: Theoretical Models and observational prospects*, Space Science Reviews 216, 39 (2020)

4. A. Murguia-Berthier et al., *The fate of the merger remnant in GW170817 and its imprint on the jet structure*, ApJ in press, arXiv:2007.12245 (2021)
5. K. Ackley et al., Observational constraints on the optical and near-infrared emission from the neutron star black hole candidate S190814bv, A&A 643, 48 (2020)
6. O. Korobkin et al., *Axisymmetric radiative transfer models of of kilonovae*, ApJ in press, arXiv:2004.00102 (2021)
7. L. Nativi et al., *Can jets make the radioactively powered emission from neutron star mergers bluer?*, MNRAS 500, 2, 1772 (2021)
8. S. Rosswog & P. Diener, *SPHINCS_BSSN: a general relativistic Smooth Particle Hydrodynamics code for dynamical spacetimes*, Classical and Quantum Gravity, in press, arXiv:2012.13954 (2021)
9. G. Camelio, *Axisymmetric models for neutron star merger remnants with realistic thermal and rotational profiles*, Phys. Rev. D in press, arXiv:2011.10557 (2021)
10. D. Gizzi, *Extension of the Advanced Spectral Leakage Scheme for neutron star merger simulations, submitted to* MNRAS, arXiv:2102.08882 (2021)

References

Abbott et al., ApJL 848, L12 (2017)

Rosswog et al., A&A 341, 499 (1999)

Freiburghaus, Rosswog, Thielemann, ApJ 525, L121 (1999)

6.29 *hbp00047:* Coulomb engineering of Mott insulators

HLRN Project ID:	hbp00047
Run time:	I/2019 – IV/2020
Project Leader:	Prof. Dr. Tim Wehling
Project Scientists:	Dr. Erik van Loon Niklas Witt MSc.
Affiliation:	Institut für Theoretische Physik

Overview

Electrons are charged particles and they therefore repel each other. This mutual interaction is responsible for spatio-temporal correlations between the electrons. These correlations play a crucial role in the electronic, magnetic and thermodynamic properties of certain classes of materials, leading to the appearance of interesting new phases where the electrons behave collectively. For this project, superconducting, magnetic and Mott insulating phase transitions are the most important examples. Systems with strong correlations are hard to treat theoretically, due to the breakdown of the single-particle picture. Nowadays, most knowledge is obtained from large scale numerical calculations, such as those performed at HLRN in this project.

In 2020, three scientific publications stemming from this HLRN project appeared. Below, these are discussed one by one.

Coulomb engineering of two-dimensional Mott insulators [1]

An important example of a phase transition induced by correlations is the Mott metal-insulator transition. The strong repulsion between electrons can „freeze“ their motion, turning a system that would be conducting without correlations into a Mott insulator.

Since it is the electronic Coulomb interaction that is responsible for this insulating state, any mechanism that changes the interaction strength has the potential to make Mott insulators conducting. In two-dimensional materials, a way to achieve this is shown in Figure 1. By surrounding the material with a dielectric environment, environmental screening reduces the effective Coulomb interactions. This approach is called Coulomb engineering and has previously been applied to semiconducting materials.

However, it is not directly clear how effective and realistic this mechanism is for Mott insulators, since the environmental screening has to compete with the internal screening in the monolayer. In the insulator, this internal screening is usually not very strong, but as soon as the system becomes metallic, it becomes very strong. A quantitative study of Coulomb engineering of Mott insulators therefore needs to account for the rapid change in internal screening across the metal-insulator transition.

Apart from making these systems interesting, the correlations also make it hard to calculate the electronic properties. We have used diagrammatic extensions of dynamical mean-field theory to tackle this problem. The dynamical mean-field theory is able to handle Mott materials, the diagrammatic extensions are needed to deal with the large length scales involved in the screening.

Our calculations have shown that Coulomb engineering is realistically possible for two-dimensional Mott materials. The Coulomb engineering leaves clear experimental fingerprints, especially in the spectra and the effective mass.

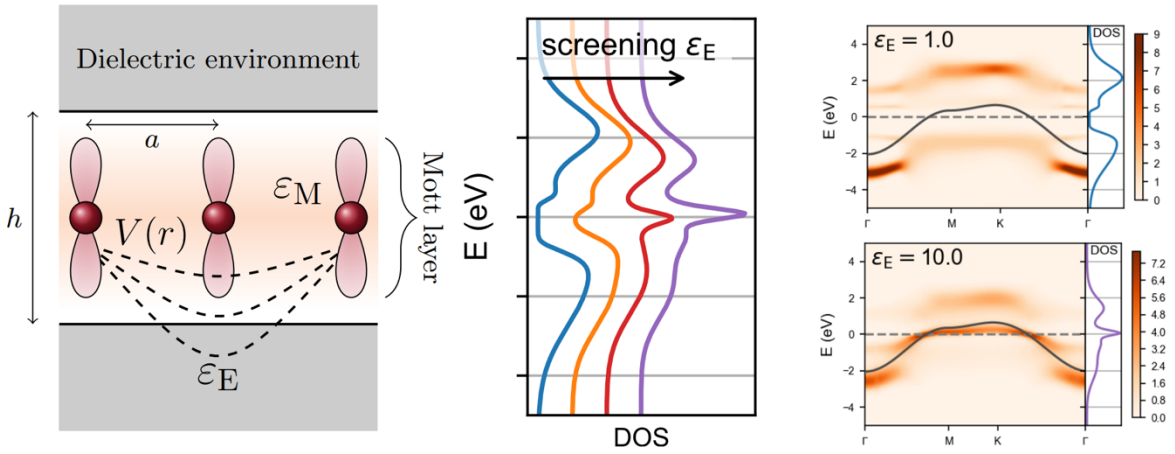

Figure 1: Coulomb engineering. By placing a monolayer correlated material in a dielectric environment (left), the environmental screening of the Coulomb interaction makes the system more metallic (middle and right).

Dual fermion for multi-orbital systems [2]

The orbital character of electronic correlations is an important component in many of the most interesting quantum materials. Computational methods and implementations must be able to take this structure into account. In this project, we have developed an open-source multi-orbital implementation of the dual fermion approach, available at https://github.com/egcpvanloon/dualfermion. This implementation is based on the TRIQS framework (Toolbox for Research on Interacting Quantum Systems, triqs.github.io), which is aimed at facilitating the development of performant codes for quantum problems, especially for high-performance, heavily parallelized applications.

The dual fermion program allows for the evaluation of the second-order dual self-energy based on input from arbitrary impurity solvers. In particular, the interface is built in way that makes it easy to switch between Exact Diagonalization (cheap) and Quantum Monte Carlo (accurate) solvers.

The initial publication about this code demonstrated the applicability to both correlated materials (here: $SrVO_3$, which has 3 orbitals) as well as cluster-based approaches to the single-orbital Hubbard model.

Sodium cobaltate [3]

This year, Niklas Witt joined the project. He started as a MSc. student and is now a PhD student in the Research Training Group Quantum Mechanical Materials Modelling who is working on efficient computational approaches to multi-orbital correlated electron systems. In particular, he has implemented the fluctuation exchange (FLEX) approximation in the intermediate representation basis. This basis allows for a compact representation of imaginary-time quantities and sparse sampling calculations. Hence, it is much more efficient than the usual Matsubara frequency grid sampling and allows the study of correlations in complex material systems at substantially lower temperatures than previously possible.

As a first application of this new code, in collaboration with researchers at the University of Tokyo, we have studied the origin of superconductivity in hydrated sodium cobaltate (Figure 2). This is a quasi-twodimensional layered material since the low-energy band structure consists of three partially-filled t_{2g} bands coming from a triangular lattice of cobalt atoms. Experimentally, a superconducting transition occurs around T=4.5 K. The origin of the superconducting pairing is still an unresolved issue. Among others, spin fluctuations have been

proposed as the mediator of this superconductivity since good nesting conditions for the e'$_g$ electrons enable strong ferromagnetic fluctuations in this system.

Previous FLEX studies only went down to T=50 K, one order of magnitude above the observed transition temperature. With the computational improvements of the intermediate representation and the computational resources at the HLRN, we were able to perform calculations at the experimentally relevant temperature scale. We did find ferromagnetic as well as strongly enhanced superconducting fluctuations in this regime. However, with the measure for the superconducting strength reaching up to 60% of the value required transition, we did not find an actual transition occurring. Our calculations were limited by eventually running into a ferromagnetic transition before superconductivity is achieved. Methods beyond FLEX will be needed to definitively resolve this question. Still, our results indicate that triplet superconductivity is plausible in this material, in particular f-wave or p-wave pairing.

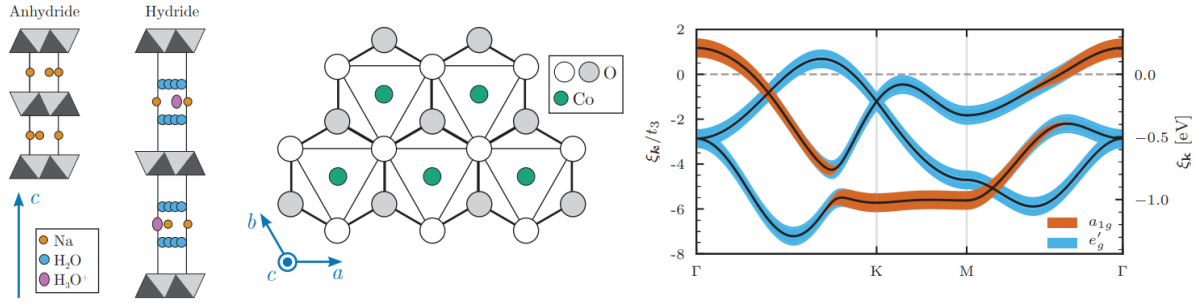

Figure 2: Hydrated sodium cobaltate. The materials consists of two-dimensional CoO layers (left), where the Co atoms form a triangular lattice (center). Three t_{2g} bands determine the low-energy band structure.

Publications

1. Erik G. C. P. van Loon, Malte Schüler, Daniel Springer, Giorgio Sangiovanni, Jan M. Tomczak, Tim O. Wehling, *Coulomb Engineering of two-dimensional Mott materials*, arXiv:2001.01735.
2. Erik G. C. P. van Loon, *Second-order dual fermion for multi-orbital systems*, J. Phys.: Condens. Matter, *33 135601 (2021).*
3. Niklas Witt, Erik G. C. P. van Loon, Takuya Nomoto, Ryotaro Arita, Tim Wehling, *An efficient fluctuation exchange approach to low-temperature spin fluctuations and superconductivity: from the Hubbard model to NaxCoO2·yH2O,* arXiv:2012.04562.
4. Niklas Witt, A multi-orbital Fluctuation Exchange Approach to Models and Materials within the Intermediate Representation Basis, MSc. Thesis, University of Bremen, July 2020.

Presentations

5. Erik van Loon, Talk at digital conference "Ultrafast dynamics of correlated electrons in solids" Nijmegen/Hamburg/Uppsala, May 8th, 2020
6. Erik van Loon, Talk at Mathematical Physics division, Lund University (digital), July 8th, 2020
7. Niklas Witt, Masterarbeitskolloquium "A multi-orbital Fluctuation Exchange Approach to Models and Materials within the Intermediate Representation Basis", July 16th, 2020

6.30 *hbp00050:* Novel exotic states in twisted bilayer materials

HLRN Project ID:	hbp00050
Run time:	IV/2019 – III/2020
Project Leader:	Prof. Dr. Tim O. Wehling
Project Scientists:	J. M. Pizarro, C. Steinke, J. Berges
Affiliation:	Institut für Theoretische Physik Bremen Center for Computational Materials Science Universität Bremen

Overview

Condensed matter quantum many-body states are often highly sensitive to stimuli such as pressure, temperature, or changes in chemical composition. Therefore, the concurrence of pronounced many-body phenomena in (quasi-) two-dimensional (2D) materials, with advances in synthesis and vertical heterostructuring, has fueled hopes for controlling electronic quantum phases on demand. These hopes are supported by experiments revealing electronic phase diagrams of several 2D systems – including Fe-based superconductors and transition metal dichalcogenides (TMDCs) - to be strongly dependent on dimensionality, thickness, and substrate. Recently, experimental observations on the so-called magic-angle twisted bilayer graphene (MA-tBLG) have demonstrated that the relative twisting between layers play an additional role to tune the many-body properties of quasi-2D materials.

MA-tBLG features low-energy flat bands around the charge neutrality point, which facilitates the emergence of strongly correlated effects [1]. The phase diagram of MA-tBLG resembled that of other high-T_c superconductors, such as the cuprates, where a strongly (and usually magnetically ordered) correlated state is suppressed by doping or pressure, and superconductivity emerges. It is believed that MA-tBLG might help to understand the elusive physics behind unconventional superconductivity. Nevertheless, MA-tBLG is not unique amongst flat band systems, and other examples appeared during the last couple of years, such as twisted double bilayer graphene, charge density wave (CDW) superlattices, twisted TMDCs, etc. Thus, it is clear that controlling many-body phenomena in van der Waals heterostructures by twisting and superlattice effects is a much broader and unexplored field.

We proposed to explore the electronic properties of Star-of-David (SoD) CDW bilayers, see Figure 1, by jointly using *ab-initio* DFT and many-body models calculations. Motivated by early 2019 experiments in 1T-$TaSe_2$ [2], we studied the strong correlated and topological effects in various bilayers of these SoD CDW materials ($TaSe_2$, TaS_2, and $NbSe_2$).

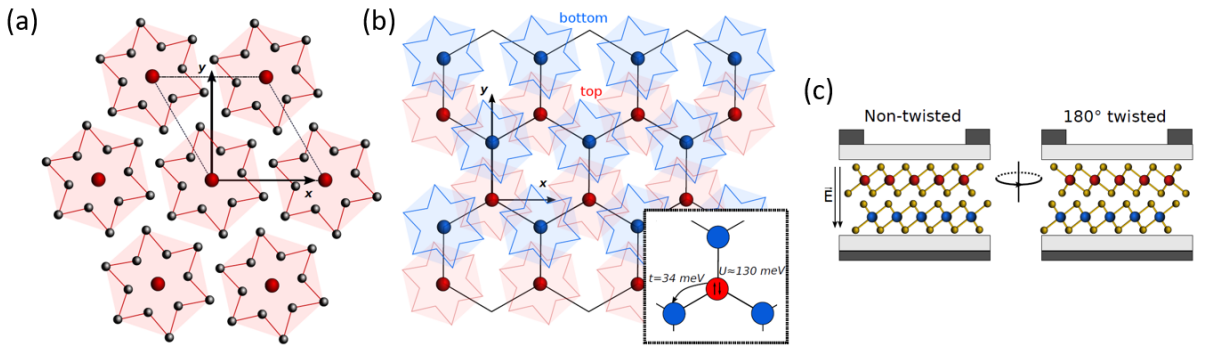

Figure 1: Crystal structures of 1T-$TaSe_2$ mono- and bilayers in the CDW phase. **(a)** Monolayer 1T-$TaSe_2$ in the SoD CDW phase. Only Ta atoms are shown. The Ta atoms are distorted into a SoD pattern, where the central Ta atoms (red) are surrounded by two rings of in total twelve Ta atoms (black). The SoDs are marked with red lines as guide to the eyes. **(b)** Top view of honeycomb stacked CDW 1T-$TaSe_2$ bilayer. Only the Ta atoms in the SoD centers are shown, with blue balls and shaded regions marking the bottom layer atoms, and red balls and shaded regions for the top layer. The inset illustrates the leading terms of the effective low-energy Hamiltonian, i.e. the nearest-neighbor hopping $t = -34\ \mathrm{meV}$ and the local interaction $U = 130\ \mathrm{meV}$. **(c)** Side view of 1T-$TaSe_2$ bilayers embedded in field effect transistor structures for the application of vertical electric fields. A non-twisted and a 180º twisted bilayer are shown with Ta atoms (red and blue) and Se atoms (yellow).

Results

We performed a systematic study of the honeycomb stacked SoD CDW bilayers. We initially calculated the electronic structure and energetics of possible stackings of the undistorted bilayers for all possible SoD CDW materials ($TaSe_2$, TaS_2, and $NbSe_2$). By doing so, we were able to elucidate that the more suitable distorted system to later study strongly correlated and topological effects is 1T-$TaSe_2$.

In the distorted phase, we calculated again the energetics of different stackings (Figure 2(a)) taking into account van der Waals corrections in the ionic relaxation within the DFT-D2 approximation, and cross-checking these calculations with a more elaborated approach, the DFT-D3. Due to its simplicity and the presence of topological Dirac fermions, we considered the honeycomb stacked bilayer. Even if this stacking is not the most energetically favorable one (At3 in Figure 2(a)), it could be accessible via current experimental techniques. Other stackings, such as the one found in the experiments [2], were also explored. We considered non- and 180º twisted honeycomb stacked bilayers. 180º twisting was considered to understand the effect of the different symmetries in the low-energy band structure and explore possible different topological states in these bilayers.

For monolayer and honeycomb stacked $TaSe_2$ bilayers, we calculated the electronic band structures as shown in Figures 2(b) and (c). We calculated such band structures with and without spin-orbit coupling (SOC) included. In the case of the monolayer 1T-$TaSe_2$, a flat band (bandwidth ≈ 14 meV) emerges around the Fermi level, and the system is known to be a Mott insulator [3]. This band adquires dispersion when a second layer is included (bandwidth in the bilayer ≈ 200 meV) with Dirac points emerging at K and K'. Thus, the effect of the out-of-plane coupling is to effectively delocalize the Mott localized electrons (in the monolayer) into topologically non-trivial Dirac fermions (in the non-twisted bilayer). In the case of the 180º bilayer, we showed that the breaking of inversion symmetry, reflected in the opening of a gap at the Fermi level, has a striking effect in the topological properties, and makes the system Z_2 topologically trivial.

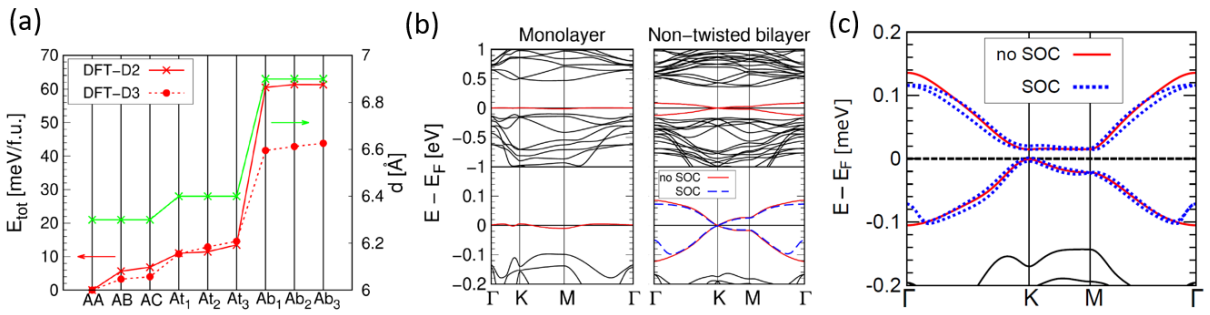

Figure 2: (a) Total stacking energies per formula unit and interlayer distances d versus stacking configurations in the CDW non-twisted bilayer 1T-$TaSe_2$ as obtained within the DFT-D2 and DFT-D3 approaches. **(b)** Band structures of CDW 1T-$TaSe_2$ monolayer (left) in comparison to honeycomb stacked non-twisted CDW 1T-$TaSe_2$ bilayer (right). Bottom panels show a zoom around the Fermi level E_F. The red and dashed blue lines mark the DFT low-energy bands without and with SOC included, respectively. From the at band near E_F in the monolayer (red solid line, bandwidth ≈ 14 meV) two dispersive bands with a bandwidth ≈ 200 meV emerge in the bilayer case. The bilayer bands exhibit Dirac points in the Brillouin zone corners, K and K'. **(c)** Band structure for 180° twisted CDW bilayer without (solid red) and with (dashed blue) SOC included. The degeneracy of the bands is lifted due to the absence of the inversion symmetry after twisting.

We fitted these band structures to a Wannier tight-binding Hamiltonian, and estimated the Hubbard interaction U from *ab-initio* calculations of the screened Coulomb interaction matrices, using constraint Random Phase Approximation (cRPA). The ratio between the Coulomb interaction and the kinetic energy of the electrons is $U/t \approx 3.8$ (Figure 1(b) inset).

With the help of other research groups in the University of Würzburg (S. Adler and G. Sangiovanni), the Goethe University Frankfurt am Main (K. Zantout, T. Mertz and R. Valentí) and the CNR-SPIN in Chieti, Italy (P. Barone), we calculated the combined effect of strong correlations and topology in the honeycomb stacked 1T-$TaSe_2$ bilayer, and summarize our results in the phase diagram of Figure 3. We demonstrated that honeycomb stacked non-twisted 1T-$TaSe_2$ bilayer is the first material realization of the so-called Kane-Mele-Hubbard model, and can open new ways to study the combined effect of correlations and topology.

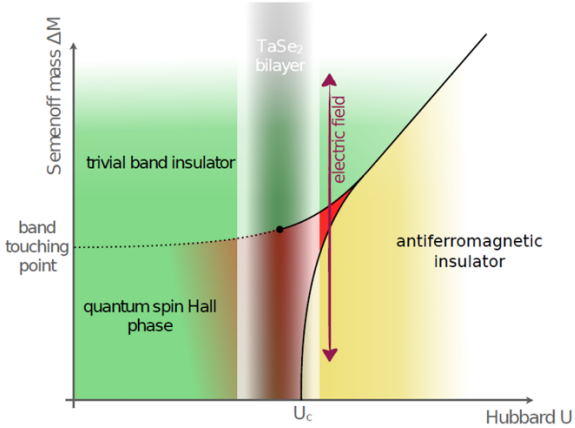

Figure 3: Schematic phase diagram of honeycomb stacked non-twisted 1T-$TaSe_2$ bilayer as a function of extrinsic Semenoff mass ΔM (external perpendicular electric field) and interaction strength U. The region accessible for non-twisted 1T-$TaSe_2$ bilayer through tuning with external electric fields is highlighted. The transition from QSH to band insulator is a continuous transition at small U (dashed line) and a first order transition at larger U (solid line). The red area in the QSH region indicates the increasing many-body character of this phase.

Three phases are found in the extrinsic Semenoff mass (or equivalently, the external perpendicular electric field) vs. Hubbard interaction phase diagram. At low Semenoff masses and Hubbard interactions, the system is a topological insulator, characterized for the appearance of a quantum spin Hall (QSH) effect. For larger masses, the system undergoes a continuous transition to a topologically trivial band insulator, while for larger interactions, there is a first order transition into an antiferromagnetically (and moderately correlated) insulator. A quantum tri-critical region exists in the moderate mass and interaction region. We demonstrated that honeycomb stacked 1T-$TaSe_2$ (non-twisted) bilayer lies in the region of this phase diagram where all the three phases coexist (including the quantum tri-critical point), and the tuning between different phases can be achieved by placing the non-twisted 1T-$TaSe_2$ bilayer in a field effect transistor experimental geometry, as shown schematically in Figure 1(c). Thus, it is possible to access and explore these three phases by simply changing an external perpendicular electric field, something that it is not achievable so far by other materials.

Outlook

By using the combined power of *ab-initio* DFT and many-body models calculations, we showed that honeycomb stacked non-twisted 1T-TaSe2 bilayers hold promises for studying the combined effect of strongly correlated physics and topological effects in quantum matter. Electrostatic doping and relative twisting of both layers will modify the phase diagram calculated in Figure 3, and other novel and exotic quantum states can appear and be easily tuned, such as superconductivity or quantum spin liquid states. We expect that experimental groups takes over our proposition and burst the research in these SoD CDW bilayers in the incoming years.

References

[1] Y. Cao et al., Nature **556**, 43 (2018).
[2] Y. Chen et al., Nature Physics **16**, 218 (2020).
[3] E. Kamil et al., J. Phys.: Condens. Matter **30**, 325601 (2018).

Publications

1. **J.M. Pizarro**, S. Adler, K. Zantout. T. Mertz, P. Barone, R. Valentí, G. Sangiovanni, and **T.O. Wehling**, *Deconfinement of Mott localized electrons into topological and spin-orbit coupled Dirac fermions,* npj Quantum Materials **5**, 79 (2020).

Presentations and posters

2. J. M. Pizarro, **Talk** at Midterm Meeting for the RTG-QM3 in Etelsen, Germany. October 2019.
3. J. M. Pizarro, **Talk** at the Progress Report for Graphene flagship FP1 in Genève, Switzerland. February 2020.
4. J. M. Pizarro, **Poster** at the online symposium Emergent Phenomena in Moiré Materials in Barcelona, Spain. July 2020.
5. J. M. Pizarro, **Talk** at online workshop CMD-GEFES 2020 in Madrid, Spain. September 2020.

6.31 *hbp00058:* Exploring the mechanistic process of vitamin B_{12} acquisition by human gut bacteria

HLRN Project ID:	hbp00058
Run time:	II/2020 – II/2021
Project Leader:	Professor Dr. Ulrich Kleinekathöfer
Project Scientists:	Dr. Kalyanashis Jana
Affiliation:	Jacobs University Bremen

Overview

Bacteria commonly obtain their essential small cofactors from their environment because of the energetically costly biosynthesis process of such cofactors. The outer membrane protein BtuB in Gram-negative bacteria takes in vitamin B_{12}, one of the essential cofactors. BtuB competes with the intrinsic factor, which transports B_{12} to the cell in the human body. It has recently been reported that an auxiliary protein, BtuG, plays a crucial role in vitamin B_{12} transport into the bacterium *B. thetaiotaomicron*. The lipoprotein BtuG directly binds vitamin B_{12} with femtomolar affinity, thereby facilitating vitamin B_{12} intake and competing with theintrinsic factor in association with the outer membrane protein BtuB. However, reports on the transport of the quite large vitamin B_{12} across membranes are scarce in the literature since investigating the transport of vitamin B_{12} is still a quite challenging issue these days.

To this end, newly resolved crystal structures of BtuBG and of B_{12} bound to the BtuG protein of *B. thetaiotaomicron* have been given the opportunity for detailed computational studies. Molecular dynamics simulations, enhanced sampling techniques, applied field simulations and the umbrella sampling approach will be employed in this investigation. In a first step, we are exploring how BtuG captures B_{12} from an arbitrary position in its proximity and which kind of interactions are responsible for the B_{12} binding to BtuG. Secondly, we extensively examine the vitamin B_{12} intake process by the BtuG surface-exposed lipoprotein in association with the BtuB outer membrane protein, i.e., BtuBG protein. An aim is to see how similar the substrate intake is to that of the nutrient intake systems SusCD and RagAB, proteins which have recently been examined by our research group as well. In the present project, we intend to examine the extent of BtuG opening as well as the closing process with B_{12} bound and without ligand, as well as the free energy associated with these processes to understand the thermodynamics of such processes. Thirdly, it is planned to explore the conformational dynamics of the B_{12}-bound-BtuBG channel and examine how the B_{12} molecule moves from the BtuG to the BtuB protein. This question is quite interesting since it is known that the binding affinity of vitamin B_{12} to BtuG is very high.

Moreover, the lipooligosaccharide plays a significant role in the dynamics of BtuB channels because of the charged oligosaccharide headgroups and the presence of many phosphate groups. Therefore, it will be interesting to explore the opening of the BtuG surface-exposed lipoprotein. It is foreseen to study the transport of the vitamin B_{12} through the BtuBG channel in a membrane consisting of lipooligosaccharides in the extracellular leaflet and phospholipids in the inner leaflet.

Furthermore, we look forward to exploring how the large large substrate vitamin B_{12} with a molecular mass of more than 600 Dalton enters the cell via this substrate-specific channel BtuBG. We will computationally mutate the substrate-binding sites of the ButG lipoprotein to achieve higher binding affinities of the substrates. To this end, we will employed unbiased

molecular dynamics simulation, enhanced sampling techniques, applied field simulations and umbrella sampling to demonstrate the above-mentioned objectives.

Results

BtuG simulations

Unbiased MD simulation of the apo-BtuG revealed a remarkable stability of the BtuG protein at 300 K while calculations of the root mean square deviation (RMSD) suggested that there are no significant structural changes after 600ns (Figure 1a). Furthermore, calculations of the root mean square fluctuations (RMSF) showed fluctuations of two loops during the simulations. These flexible loops contribute to the substrate acquisition process by the BtuG protein. To reveal the stability of the B_{12} at the active site of the BtuG protein, unbiased MD simulations with B_{12}-BtuG crystal structure have been performed. Simulations of B_{12} bound to the BtuG structure demonstrated a high stability of vitamin B_{12} at the active site cavity of the protein.

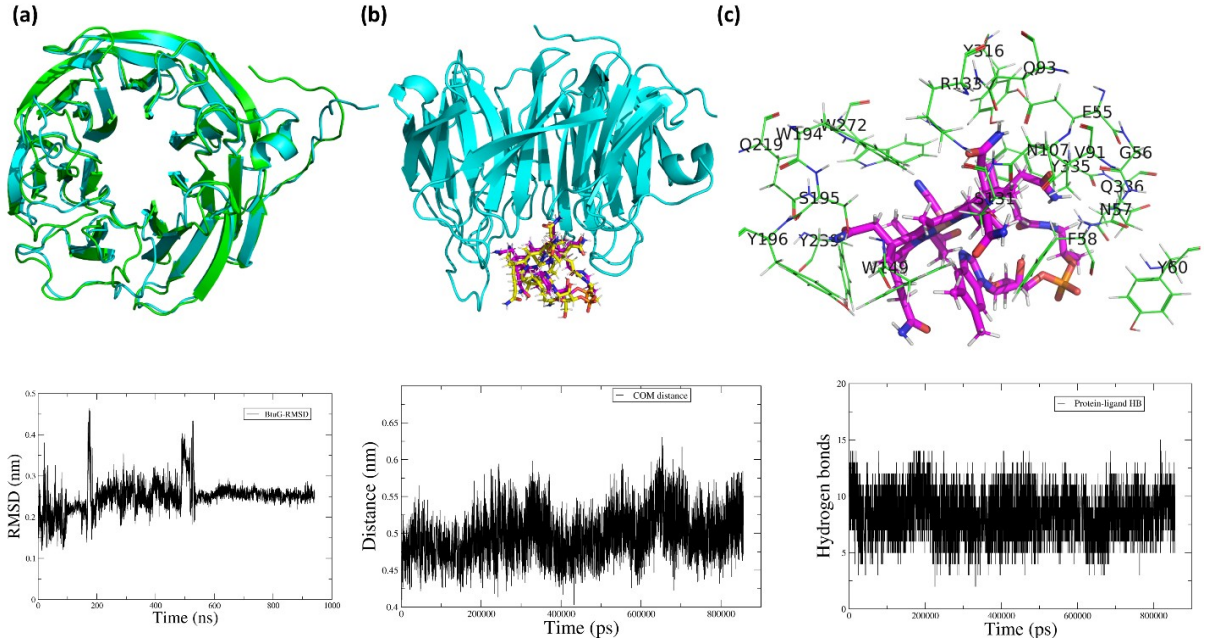

Figure 1: (a) Structural comparison of BtuG without ligand before and after an unbiased molecular dynamics simulations. The crystal structure is shown in cyan and the simulated one in green. **(b)** The same comparison but this time of the substrate vitamin B_{12} bound to BtuG. The crystal structure orientation of B_{12} is shown as a magenta stick structure and the simulated one in yellow.

Furthermore, the B_{12} affinity towards BtuG was explored considering three arbitrary ligand positions in the proximity of the protein using unbiased molecular dynamics simulations. In all three cases, the BtuG pulls vitamin B_{12} towards the active site from any of the three positions in an association-dissociation mechanism by strong electrostatic and noncovalent interactions. The unbinding of B_{12} from the active site of BtuG using the well-tempered metadynamics (WTMtD) approach corroborates the experimental dissociation constant of 10^{-14} molar.

BtuBG simulations

The BtuBG protein simulation in an POPE bilayer membrane revealed a partial opening movement of the BtuG surface protein by going away from the outer membrane protein BtuB. A partial change in the opening angle of up to 25° was observed from an initial angle of about 18° between BtuG and BtuB as shown in Figure 2. Interestingly, the molecular dynamics simulations at an elevated temperature of 400 K facilitated the opening by weakening the

respective hydrogen bonds. Moreover, well-tempered metadynamics calculations revealed that the free energy of the BtuG lid opening is about 50 kcal/mol.

To explore how the BtuG lid closes after intake of the B_{12} ligand, we performed two unbiased molecular dynamics simulations starting from configurations obtained from an SMD simulation, in which the ligand almost left the BtuBG surface. The surface-exposed lipoprotein BtuG was gradually closing the lid and a minimum angle was observed for both tsimulations. The rapid vitamin B_{12} acquisition observed during thesesimulation corroborates the experimental observation of a strong affinity of B_{12} towards the BtuG surface.

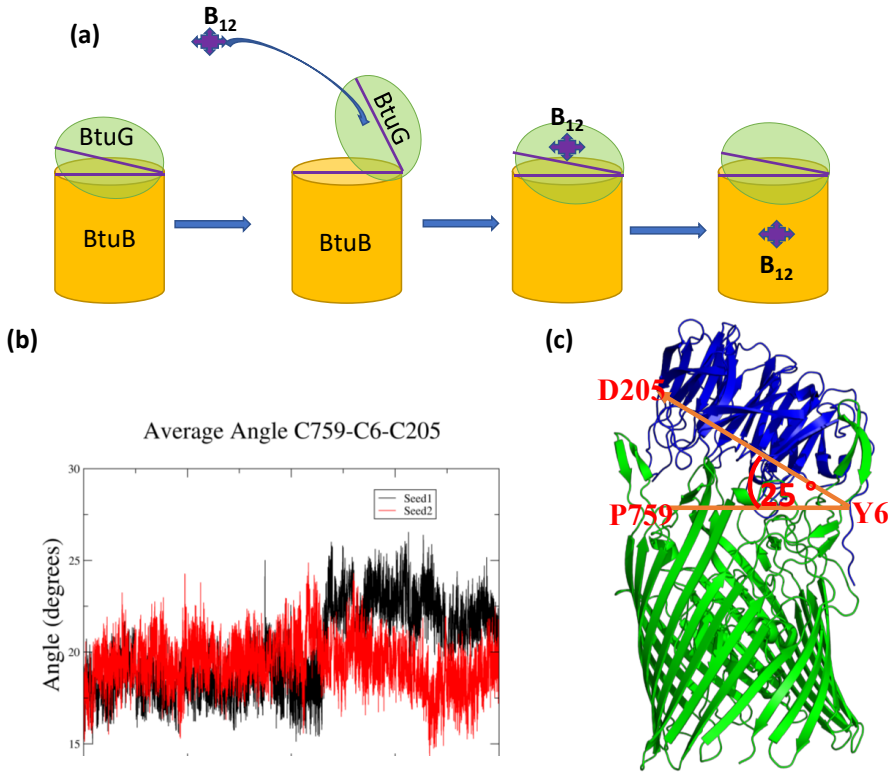

Figure 2: Conformational changes of the BtuBG protein during a 2 µs simulation. **(a)** Schematic representation of the B_{12} acquisition by lipoprotein BtuG and further translocation from the BtuG to the BtuB channel protein. **(b)** The calculated angle between BtuG and BtuB protein throughout the simulations. **(c)** Partially opened conformation of the BtuBG protein.

The B_{12}-bound BtuBG was considered to reveal the conformational dynamics of BtuBG protein and the translocation process of the substrate B_{12} from the active site cavity of BtuG to the channel protein BtuB. In the closed state of B_{12}-bound BtuBG, the protein BtuG binds the substrate B_{12} only weakly compared to the case of only studying B_{12}-BtuG due to several loop rearrangements. These conformational changes further enable the B_{12} molecules to move towards the BtuB cavity. Furthermore, the ButG lid opening process requires a higher energy in the asymmetric lipooligosaccharide-containing bilayer membrane than in the symmetric POPE bilayer system. At the same time, the free energy for the B_{12} translocation calculated using WTMtD simulations was very similar to that in case of the symmetric POPE membrane.

Outlook

In the next step, we will further mutate the substrate-binding sites of the ButG lipoprotein in the simulations to achieve a higher binding affinity of the substrates. The effect of the changes in pH on the BtuBG complex and the impact of external electric fields on the conformation of the protein will be investigated. In addition, the effect various ionic salts, e.g., KCl, NaCl, and

MgCl2 will be considered. If the allocated computer time of the project permits, additional proteins like FecA and FhuA - distant homologs of the BtuBG porin - will be investigated. Such proteins form a unique family of proteins widespread in Gram-negative bacteria, and they facilitate the substrate transport across bacterial membranes.

6.32 *hbp00068:* Enhanced sampling methods for constructing free energy surfaces of antibiotic permeation through porins

HLRN Project ID:	hbp00068
Run time:	IV/2020 – IV/2021
Project Leader:	Professor Dr. Ulrich Kleinekathöfer
Project Scientists:	Abhishek Acharya, Dr. Jigneshkumar D. Prajapati
Affiliation:	Jacobs University Bremen

Overview

Antibiotic resistance in bacterial pathogens is one of the major concerns of public health systems today. Each year, AMR causes about 670,000 cases of infections and 33,000 deaths, imposing a large economic burden of about € 1.5 billion in the EU/EEA region alone. A large body of work over the past decades have implicated several bacterial proteins in the emergence of antibiotic resistance. Among these are general diffusion channels called porins that are embedded in the outer membranes of Gram-negative bacteria and involved in the transport of essential nutrients and cofactors into the cell (Figure 1A). Particularly, OmpF and OmpC allow the passage of several antibiotics such as fluoroquinones, chloramphenicol and the β-lactam class of antibiotics. Uncovering the molecular factors and energetics underlying the transport process is of critical importance as it improves our understanding of the structural determinants of antibiotic permeation.

Studies have shown that charge distribution, hydrophobicity and size of the solute, and channel width are important determinants of effective solute permeation. Computational and electrophysiological studies have indicated that favourable, albeit transient, interactions of the antibiotic with the charged residues along the pore are essential for successful translocation. While these findings have indeed provided holistic and valuable insights into the transport mechanism, the molecular details of the permeation process for specific antibiotics have been elusive. This can be attributed to the limitations on available computational resources that precluded extensive sampling for such large systems in early studies; an accurate and quantitative description of antibiotic permeation process using simulations require a good degree of sampling and convergence in free energy estimates.

In this project, our objective is to employ biased sampling methods that provide some technical advantages over conventionally used sampling approaches, and thereby allow better sampling and reliable estimates of various system properties. Particularly, we use temperature accelerated sliced sampling (TASS) – a combination of the popularly used umbrella sampling (US) approach and temperature accelerated molecular dynamics (TAMD). Another method of interest is the recently developed WTM-eABF scheme. We study ciprofloxacin permeation through OmpF porin that poses significant challenges with conventional biasing approaches such as US and metadynamics (Figure 1B).

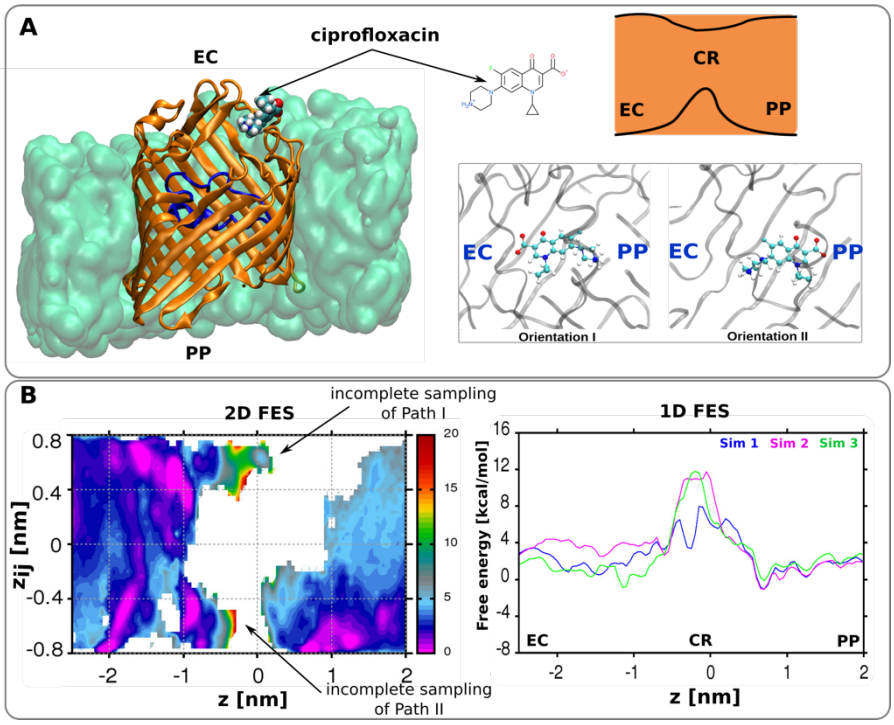

Figure 1: (A) OmpF monomer embedded in a lipid bilayer. The channel is characterised by the presence of a constriction loop (in blue) at the centre, that creates an entropically restricted region called the constriction region (CR). Ciprofloxacin passes from the extracellular (EC) to periplasmic (PP) end of the channel via the narrow CR. This restricts antibiotic rotation at the CR such that the antibiotic can attain only two possible orientations, I and II. Thus, the antibiotic has two possible permeation paths, Path I and Path II **(B)** Free energy surface (FES) from WTmetaD simulations for ciprofloxacin permeation through OmpF. Left panel: 2D free energy estimates along z (describing antibiotic translation along the channel axis) and z_{ij} (antibiotic rotation with respect to the channel axis) highlights the problem of incomplete sampling. The color bar denotes the free energy values in kcal/mol. Right panel: 1D free energy estimates along z (antibiotic translation along the channel axis) from three independent simulations. Note the differences in free energy estimates especially at the CR.

Results

In previous studies, we have shown in that aforesaid conventional sampling methods perform quite well in the studies of ion permeation through porin channels, their performance progressively deteriorates as the solute size increases. For instance, Figure 1, highlights the issues with consistent sampling of the two possible ciprofloxacin permeation paths, Path I and Path II. Figure 1B, left panel shows incomplete free energy landscape for the two paths due to inadequate sampling in these simulations. Consequently, estimates of the free energy barrier for ciprofloxacin permeation obtained from these simulations are unreliable, as highlighted by the differences in 1D free energies estimates from three independent simulations (Figure 1B, right panel).

With the TASS approach, we can now reliably sample the two permeation paths in independent simulations (Figure 2B). Notably, the 2D free energy estimates from these simulations provide a consistent picture of free energy landscape for ciprofloxacin permeation. As such, the 1D free energy estimates obtained from these simulations attain acceptable convergence (Figure 2A). Consistent sampling and convergence of independent free energy estimates are strong indicators of reliability of the results.

Outlook

While the TASS scheme enables a remarkable improvement in sampling and convergence, this does come at a high computation cost. Currently, we are also testing the WTM-eABF method on the ciprofloaxacin-OmpF system to evaluate the sampling efficiency, computational cost, and reliability of the method in obtaining converged free energy estimates from independent simulations. Based on the outcomes of this study, the most efficient and accurate method will be used in the future to investigate the permeation of antibiotics across different channels to provide detailed insights into the structure-function aspects of the permeation process.

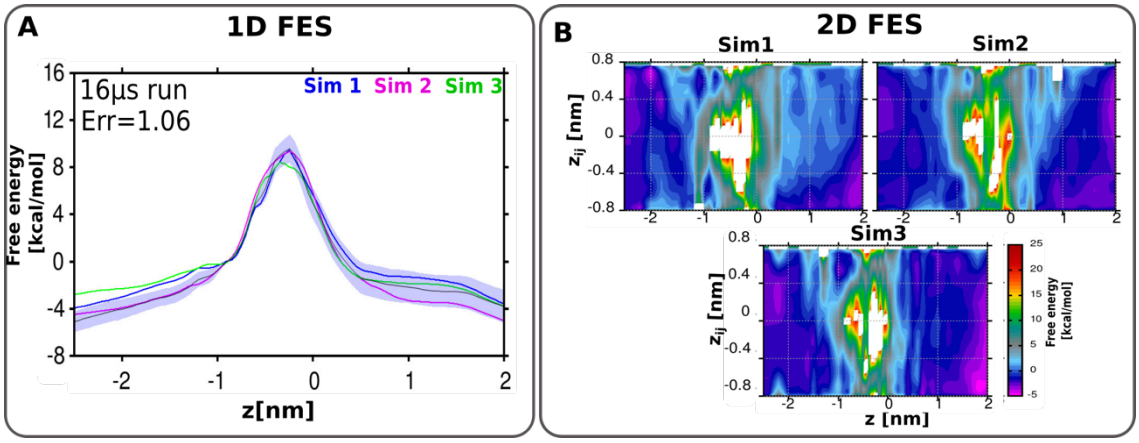

Figure 2: Free energy surface for ciprofloxacin permeation though OmpF estimated from three independent (16 µs) TASS simulations. **(A)** 1D free energy estimates along z. **(B)** 2D free energy surfaces along z and z_{ij}. The color bar denotes free energy values in kcal/mol.

6.33 *hbp00069:* Modelling correlated electron systems in presence of non-local interactions and doping

HLRN-Projektkennung:	hbp00069
Laufzeit:	IV/2020 – III/2021
Projektleiter:	Prof. Dr. Tim O. Wehling
Projektbearbeiter.	Edin Kapetanovic
Institut / Einrichtung:	Institut für Theoretische Physik, Universität Bremen

Overview

The competition of local and non-local Coulomb interactions plays an important role in the electronic structure of strongly correlated materials: Non-local interactions can effectively screen local interactions and weaken Mott Hubbard type electron correlations. They can furthermore push the electronic system into symmetry broken phases with e.g. charge order. While local and non-local Coulomb interactions naturally occur in any real material, low-energy models to describe correlated electron effects like the Hubbard model quite often neglect non local interactions completely.

In this project, we aim to study the extended Hubbard model, which includes nonlocal interactions, to bridge the gap between real materials and low-energy models. Our goal is to gain a better understanding of the inuence of non-local interactions on doped, two-dimensional systems, which is especially relevant for e.g. cuprates which display High-Tc-Superconductivity. Specifically, we want to extend a variational method, developed in our group [1,2,3], to the doped case. Our aim is to study the electronic phase diagram of the extended Hubbard model as function of interaction strengths, filling and temperature, which is to date barely understood although this model is one of the most fundamental models in correlated electron physics.

The applied variational approach allows the mapping of the extended Hubbard model to a Hubbard model with local, *effective* interactions only. As illustrated in the figure below, the old and new parameters are linked by a screening factor, which can be obtained by solving the effective model. Since a direct solution via e.g. lattice Monte Carlo leads to severe numerical problems especially in the most interesting filling regime, we employ the *Dynamical Cluster Approximation (DCA)*, an extension of DMFT, through a continuous-time Monte Carlo solver (*CT-AUX)* which is developed by the Gull group at the University of Michigan.

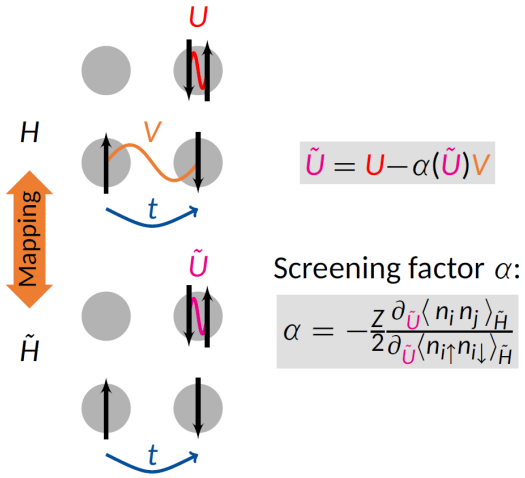

Figure 1: Mapping of the original, extended Hubbard model to the auxiliary system.

Results

We have accomplished DCA-simulations of the Hubbard model on a broad range of fillings and interaction strengths, which allows for the evaluation of the aforementioned screening factor. We specifically chose a square lattice since it is the fundamental building block of layered High-Tc-superconductors. After testing various cluster sizes up to 64 sites, we restricted ourselves to an 8-site dynamical cluster due to the numerical sign problem inherent in Quantum Monte Carlo algorithms. Even then, the accessible temperature is rather limited, but sufficient to obtain sensible data.

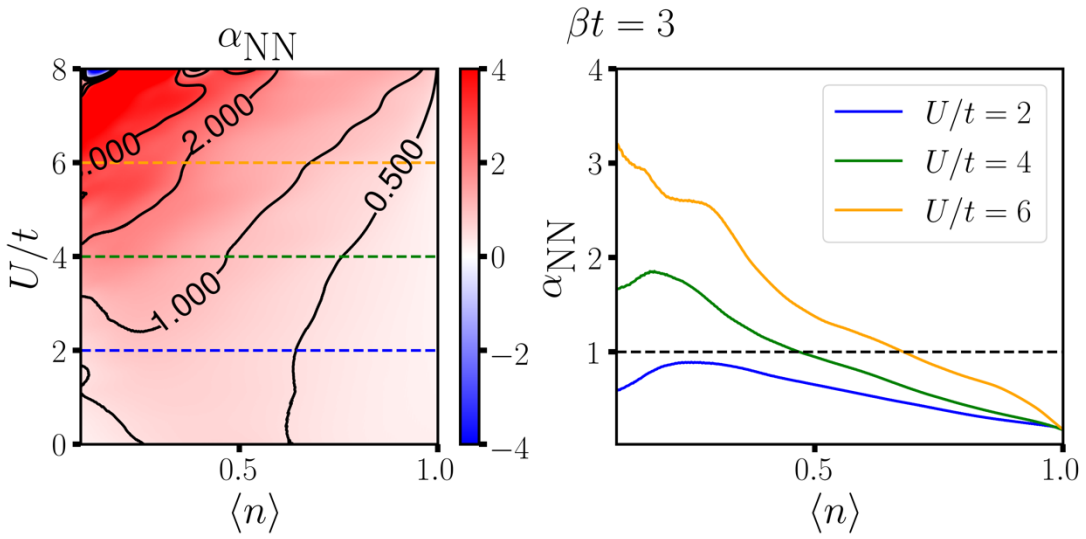

Figure 2: (left): Screening factor depending on local interaction strength and filling of the system. (right): Lineplots along the dashed lines in the left picture. This simulation has been performed on an 8-site dynamical cluster.

Our findings suggest that the screening of the local interaction by the non-local one is indeed considerably doping dependent. Figure 2 shows an exemplary plot at a fixed, rather high temperature; we obtained the same data for a larger set of different temperatures in order to investigate the scaling. In parameter regimes where the numerical sign problem is absent (e.g. at high temperature), we furthermore compare and benchmark our results with direct lattice approaches (Determinantal Quantum Monte Carlo).

While the refinement of the more challenging data sets is still ongoing, all data obtained so far hints that, when doping the system away from half filling towards the relevant fillings for superconductivity, the screening of the local interaction caused by the non-local one *increases.* Thus, great care must be taken in downfolding processes and the construction of effective low-energy model when choosing appropriate interaction parameters.

Outlook

After further refining the data and ascertaining our findings, we will summarize our results in a new paper. Our findings furthermore lead to new questions: What happens when longer-ranged interactions are included? How does this translate to other lattice systems? Additional calculations in the near future, either in a prolongation of the current project or in a new one may shed light on these problems.

References

[1] M. Schüler et al., Phys. Rev. Lett **111**, 036601 (2013)
[2] M. Schüler et al., SciPost Phys. **6**, 067 (2019)
[3] E. Kapetanovic et al., Phys. Rev. B **101**, 235165 (2020)

6.34 *nak00001:* Seamless sea ice prediction with AWI Climate Model

HLRN Project ID:	nak00001
Run time:	III/2020 – II/2021
Project Leader:	Dr. Helge Goessling[1]
Project Scientists:	Dr. Longjiang Mu[1], Dr. Lars Nerger[1]
Affiliation:	[1]Alfred-Wegener-Institut Helmholtz Zentrum für Polar- und Meeresforschung, Bremerhaven

Overview

The rencently developed climate model AWI-CM3.0 in the Alfred-Wegener-Institute (AWI), which is based on the finite volume sea ice-ocean model FESOM2.0 for the ocean component and the Integrated Forecasting System (OpenIFS) developed by European Centre for Medium-Range Weather Forecasts for the atmosphere component, has shown faster integrations and relatively reliable simulations in the polar regions than its ancestor AWI-CM1.1 which uses the finite-element sea ice-ocean model FESOM1.0 and the atmosphere model ECHAM from the Max Planck Institute for Meteorology. We have adapted our previous seamless sea ice prediction system based on AWI-CM1.1 to AWI-CM3.0. Given the increased computational efficiency, we can now run the assimilation system with 30 ensemble members and at the same time assimilate more observations. During the reporting period, the majority of the development and test runs of the new seamless sea ice prediction system have been performed at HLRN.

Results

The implementation of the Parallel Data Assimilation Framework (PDAF; Nerger and Hiller, 2013) in AWI-CM3.0 has been straightforward, based on the experiences gained with the first version based on AWI-CM1.0 (Mu et al., 2020). An efficient communication procedure is necessary considering the large parallelization of the ensemble climate models. The splitting of the communicators is done in the same way as in the first verison (see Nerger et al. 2020), enabling the system to do online data assimilation without restarts each assimilation step. Thereby a significant reduction of the computational demand is obtained. We use the Local Error Subspace Transform Kalman Filter (LESTKF) coded in PDAF.

Version 2 of the AWI seamless sea ice prediction system now has 30 ensemble members which is more than twice of that in the previous system (12), however, with almost the same computation costs. Figure 1 shows the design of the system. After 24 hours of model integration, the MPI communicator for one realization conducts the analysis and distributes the analyzed states to all the ensemble members. Every 3 months, the forecast system is restarted from the analyzed states and integrated for 1-year long forecasts. A forecast calibration procedure is applied afterwards to remove systematic drift due to model biases that generally remain in climate modles (including AWI-CM3) to achieve better forecast results. To start with, the calibration procedure has been conducted only for sea ice concentration states.

This system currently assimilates sea ice concentration, sea ice thickness, sea ice velocity, sea surface height, sea surface temperature, sea surface salinity, temperature and salinity profile observations. The assimilation of temperature and salinity profiles, however, gives rise to partly spurious results in the sea-ice states when using cross-covariance from the ocean profiles to update the sea-ice state. Therefore, we have modified the procedure such that these cross-updates are supressed. Finally, it's important to point out that the atmospheric states of the 30 ensemble members are evolving without any data constraints, except for what is

communicated from the ice/ocean state (SST and sea-ice concentration and thickness) through the coupling.

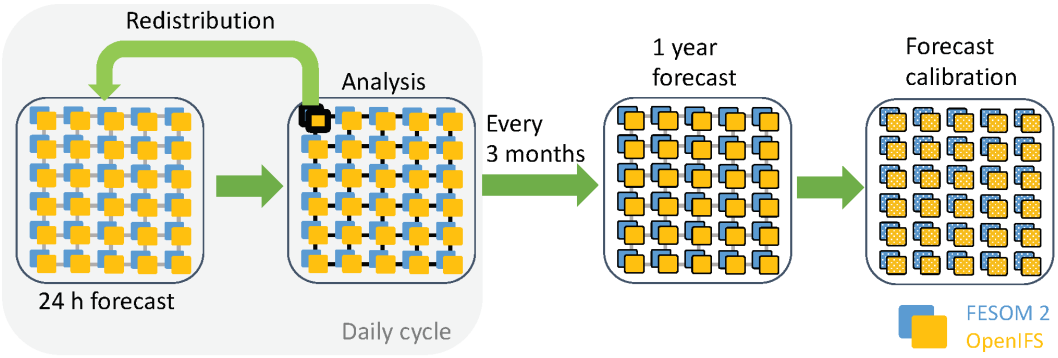

Figure 1: The design of the AWI Seamless Sea Ice Prediction System (version 2).

The system has mostly been developed with relatively short test simulations at HLRN for the first half of the current project phase. Therefore, we have unused resources left, but we plan to perform comprehensive sets of experiments during the next half of the project phase, as inidicated in the project proposal.

As mentioned above, we used the new system to conduct extensive sets of re-forecast experiments, initialized every third month between 2011 and 2019 (and 2003-2010 for calibration). As an example, Figure 2 shows the (uncalibrated) predicted sea-surface temperature (SST) in the Niño-3.4 region in the equatorial Pacific, compared with OSTIA observations. Even though our research focus is on sea-ice forecasts, the experiments with different lead-times demonstrate the ability of our system to predict ENSO.

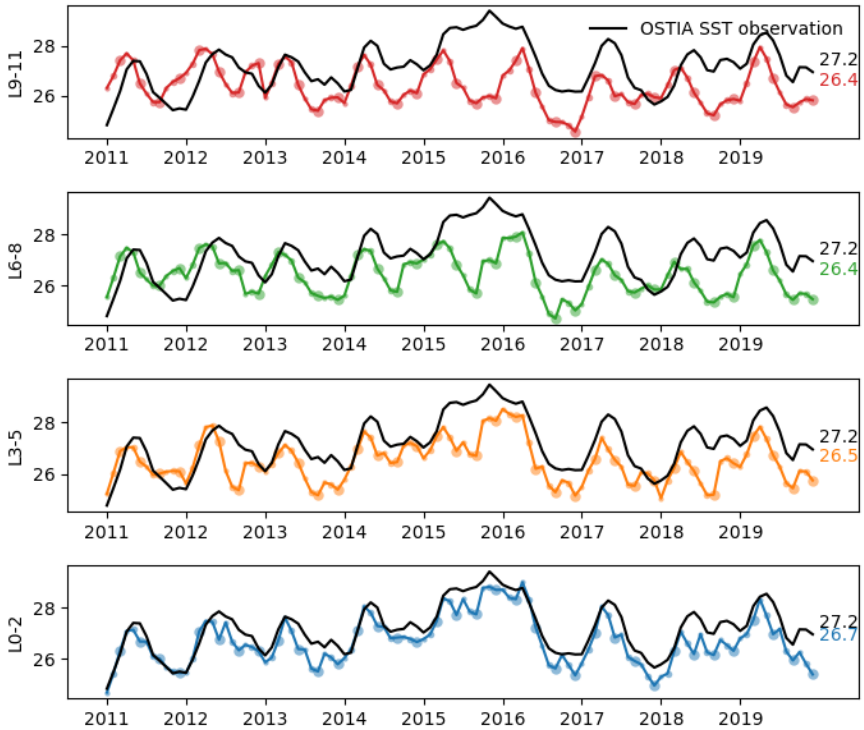

Figure 2: Comparison of the (uncalibrated) predicted SST (degrees C) and OSTIA observations in the Niño-3.4 region with lead-time 0-2 months, 3-5 months, 6-8 months, 9-11 months. Small (large) circles denote months with the shortest (longest) lead-time within the respective group of lead-times. Mean values of the time series are shown on the right.

Outlook

Thanks to the computational resources granted by HLRN, we have successfully completed the development of version 2.0 of the AWI seamless sea ice prediction system. A paper describing the system and discussing the performance of the system with respect to sea-ice prediction is in preparation.

Currently, we have not implemented PDAF also in the atmosphere model. We plan to use the nudging method to constrain the atmosphere with large-scale dynamics (winds) from reanalysis (ERA5). The nudging method is expected to significantly impact the ensemble spread in the ice/ocean assimilation system, which needs to be explored next. Furthermore, more development is needed to enable the use of the currently-supressed ocean-ice cross-updates, which should in principle contain valuable information for a consistent initialization of the forecast system.

Publications

1. L. Mu, L. Nerger, J. Streffing, Q. Tang, B. Niraula, L. Zampieri, H.F. Goessling, Verification of sea ice forecasts in the AWI Seamless Sea Ice Prediction System (version 2). In preparation.

References

1. L. Mu, L. Nerger, Q. Tang, S.N. Losa, D. Sidorenko, Q. Wang, T. Semmler, L. Zampieri, M. Losch, H.F. Goessling, Towards a data assimilation system for seamless sea ice prediction based on the AWI Climate Model. Journal of Advances in Modeling Earth Systems, p. e2019MS001937, https://doi.org/10.1029/2019MS001937
2. L. Nerger, Q. Tang, L. Mu, 2020. Efficient ensemble data assimilation for coupled models with the Parallel Data Assimilation Framework: example of AWI-CM (AWI-CM-PDAF 1.0). Geoscientific Model Development, 13(9), pp. 4305-4321.
3. L. Nerger and W. Hiller, 2013. Software for ensemble-based data assimilation systems—Implementation strategies and scalability. Computers & Geosciences, 55, pp. 110-118.